UNIVERSITY OF BERGAMO

DEPARTMENT OF ENGINEERING AND APPLIED SCIENCES

DOCTORAL PROGRAMME IN ENGINEERING AND APPLIED SCIENCES

CATHODIC PROTECTION AND HYDROGEN EMBRITTLEMENT

Doctoral dissertation of:

Diego Pesenti Bucella

Supervisor:

Prof. Marina Cabrini

Tutor:

Prof. Tommaso Pastore

The Chair of the Doctoral Program:

Prof. Valerio Re

2017/2018 – XXXI Cycle

SUMMARY

ACKNOWLEDGEMENTS

This research activity was financed by APCE Service Srl.

The period of internship carried out from June to September 2018 at the Corrosion Prevention Unit (TEC/NORTEC/ANTICOR) of the Technical Department of Snam Rete Gas S.p.A., allowed me to interface with the resources in the field of cathodic protection of underground metallic structures, along with those related to the anti-corrosive coatings of the assets both buried and above ground.

I would like to thank my Tutor Prof. Pastore Tommaso for all the great expertise, professional support and endless patience during these years and my Supervisor Prof. Cabrini Marina, who gave me great guidance and encouragement throughout this project work and allowed me to participate in several national and international conferences. A big thank goes to Eng. Lorenzi Sergio for all the time spent together in the laboratories and for the precious contribution in developing all the devices and equipment used in the performed tests, and thus for giving me the possibility to achieve better results.

Finally, I would like to thank my family and friends for their priceless help and moral support at any moment during this experience.

LIST OF SYMBOLS

E_{eq} = Equilibrium potential of the metal
E_{corr} = Corrosion potential
E_p = Protection potential
$E_{IR\text{-}free}$ = IR-free potential ($E_p = E_{IR\text{-}free}$), purified of the ohmic drops (IR)
E_r = Re-passivation potential
E_l = Critical limit potential
i_L = Limit current density of oxygen diffusion
i_P = Background passivity current density
$i_{P,\infty}$ = Background passivity current density at infinite time
i_c = Cathodic current density
i_a = Anodic current density
$i_{a,\infty}$ = Steady state anodic current density
$i_H = (i_a – i_P)$ = Hydrogen permeation current density
$i_{H,\infty} = (i_{a,\infty} – i_{P,\infty})$ = Steady state hydrogen permeation current density
H_l = Diffusible hydrogen in the lattice
$H_{t,r}$ = Trapped hydrogen in reversible traps
$H_{t,ir}$ = Trapped hydrogen in irreversible traps
L_e = Lattice site not occupied by hydrogen
$T_{e,r}$ = Empty reversible trap, not occupied by hydrogen
$T_{e,ir}$ = Empty irreversible trap, not occupied by hydrogen
C [mol/L] = Total concentration of the diffusible hydrogen
C_H [mol/L] = Diffusible hydrogen concentration in the lattice and in the reversible traps
C_{Hl} [mol/L] = Hydrogen concentration in the lattice
$C_{Ht,r}$ [mol/L] = Hydrogen concentration in the reversible traps
$C_{Ht,ir}$ [mol/L] = Hydrogen concentration in the irreversible traps
C_{el} [mol/L] = Concentration of the empty lattice sites
$C_{et,r}$ [mol/L] = Concentration of the empty reversible traps
$C_{et,ir}$ [mol/L] = Concentration of the empty irreversible traps
C_l [mol/L] = Total concentration of the lattice sites
$C_{t,r}$ [mol/L] = Total concentration of the reversible traps
$C_{t,ir}$ [mol/L] = Total concentration of the irreversible traps
Φ [mol/(m^{2}s)] = Flux of the diffusible hydrogen in the lattice
Φ_∞ [mol/(m^{2}s)] = steady state hydrogen permeation flux
Φ_r [mol/(m^{2}s)] = Flux in the radial direction of the diffusible hydrogen in the lattice
t [s] = Time
x, y, z [m] = Cartesian coordinates

$\vec{\iota}, \vec{J}, \vec{k}$ = Unit vectors of the Cartesian axes

r, φ, z = Cylindrical coordinates

$\overrightarrow{\iota_r}, \overrightarrow{\iota_\varphi}, \vec{k}$ = Unit vectors of the cylindrical coordinates

R(C) = Constant reaction contribution

D_l [m^2/s] = Hydrogen diffusion coefficient in the lattice

D_{app} [m^2/s] = Apparent hydrogen diffusion coefficient, in the presence of trapping sites

L [m] = Thickness

N_A [atoms/mol] = Avogadro’s constant = $6.023*10^{23}$

R [J/(mol*K)] = Gas constant = 8.314472

T [K] = Absolute temperature = T [°C] + 273.15

K = Equilibrium constant of the trapping reaction

k, k’ = Kinetic constants of the reaction in the direct or opposite direction, respectively

ΔG^0 [J/mol] = Standard molar Gibbs free energy of reaction

N_l [L^{-1}] = Number of lattice sites available for hydrogen absorption, per unit volume

N_{Hl} [L^{-1}] = Number of lattice sites occupied by hydrogen, per unit volume

N_{el} [L^{-1}] = Number of empty lattice sites available for hydrogen absorption, per unit volume

$N_{t,r}$ [L^{-1}] = Number of reversible traps available for hydrogen absorption, per unit volume

$N_{Ht,r}$ [L^{-1}] = Number of reversible traps occupied by hydrogen, per unit volume

$N_{et,r}$ [L^{-1}] = Number of empty reversible traps available for hydrogen absorption, per unit volume

θ_l [N_{Hl} / N_l] = Saturation degree of the lattice sites available for hydrogen absorption

$\theta_{t,r}$ [$N_{Ht,r} / N_{t,r}$] = Saturation degree of the reversible traps available for hydrogen absorption

α = Reversible trapping factor

τ = Reaction time in the presence of irreversible traps $= k_{ir} \cdot C_{Hl}$

LIST OF FIGURES

LIST OF TABLES

INTRODUCTION

The main topic of the research activity carried out at the Department of Engineering and Applied Sciences of the University of Bergamo during this 3-year PhD Program was the study of hydrogen embrittlement in high strength low alloy steels under cathodic protection.

The project of this PhD Thesis is entitled *"Cathodic Protection and Hydrogen Embrittlement"*, and the entire research activity was financed by APCE Service Srl (Associazione per la Protezione dalle Corrosioni Elettrolitiche). The necessity of deepening this very wide and complex theme was driven by the purpose of a more efficient prevention and control of the corrosion mechanisms that can verify, in particular operating situations, in underground steel pipelines and transport systems, in which the combined use of a cathodic polarization and a protective coating must be necessarily involved.

Cathodic protection (CP), along with the application of protective coatings, represents one of the main techniques for corrosion protection of submerged parts of metal structures exposed to the marine environment, buried structures, and equipment operating with natural and process waters. The extensive experience has made it one of the most reliable protection techniques, essential to guarantee full safety and long service lives in naval, offshore and underground structures, Oil&Gas equipment, transport systems and pipelines, etc. It is usually applied to protect carbon and low alloy steels in neutral or slightly alkaline solutions, in order to reduce the overall loss of metal and to enhance the corrosion-fatigue limits.

Protection is achieved by means of a cathodic current, flowing from the anode towards the structure to be protected, sufficient to lower the metal potential at any point of the surface below a protective limit, the so-called protection potential (E_p). To less noble potentials of E_p, the general corrosion rate reduces to less than 10 µm/year, or it becomes nil if the polarization leads to immunity conditions.

The effectiveness of this protection technique is indubitable. However, there may be particular conditions in which CP, especially if not correctly applied, can produce negative effects. The most important effect, analyzed in this PhD Thesis work, is that connected to Hydrogen Embrittlement (HE), a specific type of Environmental Assisted Cracking (EAC) connected to the absorption and consequent diffusion of atomic hydrogen through the metal matrix. The risk of such effect becomes evident mostly for excessive cathodic polarizations, when over-protection potentials (E_{op}) are reached, well below E_p, in which the polarization cathodic current density becomes high and the process of hydrogen development becomes relevant.

Therefore, the aim of this PhD Thesis was to better understand the process of hydrogen diffusion in a commercial pipeline steel, because the presence of hydrogen in metallic materials is well known to be detrimental for the mechanical properties in certain conditions, as it causes significant decrease in ductility and/or fracture strength, unexpected failure, etc.

Measurements of hydrogen permeation in metallic materials were carried out for nearly 40 years according to the electrochemical permeation technique proposed by Devanathan and Stachurski and used in the experimental tests, which probably provides the simplest and most flexible approach. However, even if many results were published since then and several methods were developed to evaluate hydrogen uptake and transport, the interpretation of the literature data and the correlation with the proposed models was not always satisfactory.

The structure of this PhD Thesis is organized in a general section (from Chapter 1 to Chapter 6) and in an experimental section (from Chapter 7 to Chapter 10).

As regards the general section, Chapter 1 illustrates the application of CP to buried pipelines in order to eliminate or reduce the corrosion rate of the coating defects exposed to the soil environment down to negligible values, along with the importance of the application of a protective coating on a steel pipeline, which must ensure the physical separation of the steel towards the environment. In fact, even the most efficient and high-performance coating present hidden or non-systematic defects, which the final qualification tests are often unable to detect. Consequently, the application of a cathodic polarization must be necessarily undertaken. However, in correspondence with very negative potentials, the steel is in over-protection conditions. Atomic hydrogen, developed from the cathodic reaction, diffuses through the steel and can lead to the formation and propagation of cracks; this risk increases with the increase in the mechanical strength of the steel. The most important national and international reference standards indicate precise limits for the application of CP to avoid the risk of embrittlement, especially in steels with a high Yield Strength (YS); the critical limit is generally indicated as the potential for the beginning of hydrogen development.

Chapter 2 explains the hydrogen induced failure mechanisms related to EAC, subsequent to hydrogen evolution and permeation into the metal matrix, when a metallic material is not protected against an aggressive environment, represented by different kinds of soil in the case of underground pipelines. A quite exhaustive overview of the main theories proposed as a possible explanation for Hydrogen Assisted Cracking (HAC) mechanisms is then reported.

In Chapter 3, after the explanation of the pure diffusion mechanism, in accordance with Fick’s first and second law, attention was paid to the effects of microstructure, temperature, sub-surface hydrogen concentration, applied mechanical stress, specimen thickness, and trapping sites.

In Chapter 4, the main mathematical models for hydrogen diffusion are presented, both in the case of ideal diffusion (absence of trapping sites) and non-ideal diffusion (presence of trapping sites, i.e. sites that affect hydrogen diffusion and can represent preferential paths or traps, which are usually classified as reversible or irreversible in relation to the binding energy).

Chapter 5 will provide an interesting examination of the mathematical models that try to explain the effect of elasto-plastic deformation on hydrogen permeability.

In Chapter 6, the electrochemical permeation technique, proposed by Devanathan and Stachurski for the evaluation of hydrogen diffusivity through steel, and used in the further tests, will be analyzed.

Chapter 7 describes the experimental permeation tests and procedures performed on one type of high strength low alloy carbon steel, catalogued as API 5L X65 grade steel, which is probably one of the mainly utilized in pipelines construction for the transportation of petroleum and natural gas.

The experimental results deriving from the permeation tests, realized in accordance with the International ISO 17081:2014 standard in the absence of an applied load and in the presence of cyclic and incremental step loading conditions, are presented in Chapter 8. The discussion of the results achieved is reported in Chapter 9. For the processing of the experimental curves, firstly the implementation of the pure diffusion model (according to Fick’s second law) was proposed; however, this resulted not accurate enough to simulate the permeation process of hydrogen, due to the existence of trapping sites. Therefore, another processing method, proposed by Grabke and Riecke, allowed to calculate diffusion parameters in a more accurate way than the previous model, also in the presence of residual plastic deformation or loading conditions beyond the yield limit.

In Chapter 10, the conclusions to this PhD Thesis work are drawn. From the analysis of the main international and national standards that regulate the application of CP, it was concluded that no criteria are standardized for the determination of the critical limit potential indicated to avoid the occurrence of HE phenomena. This limit should be experimentally determined by means of mechanical tests, but without any precise indication of the test methods to be adopted. As regards the permeation tests performed in the absence or in the presence of an applied load, the results allowed to better understand the variations in hydrogen transport mechanism into a X65 grade pipeline steel. In particular, with the application of cyclic loading conditions beyond the yield limit, it was observed:

- Significant decrease in the apparent diffusivity, due to the enhancement of trapping phenomena
- Sharp increase in the reversible trapping parameter, due to the contribution of the accumulation of new trapping sites in the plastic deformation field. The extent of the plastic deformation achieved in the tests is relatively low, thus the delaying effect related to the irreversible traps is small if compared to the multiplication of reversible traps
- Significant increase in the total hydrogen concentration, as a result of enhanced hydrogen

absorption and filling of an increasing number of trapping sites

- Appreciable mitigation of the stress field generated by a tensile stress after the application of a compressive stress, with a consequent less marked decrease in D_{app}
- Temporary reduction in hydrogen flux, determined by a variation of the applied maximum stress, due to an instantaneous reduction of the mobile hydrogen concentration in the lattice, caused by an increase in the number of trapping sites following local plasticization phenomena even for stresses lower than the yield limit.

Concerning the permeation tests performed in the presence of an applied incremental step load, for the X65 grade steel (sorbite) and heat treated (martensite) material, it was observed that:

- Failure occurred at stress values very close to those in air, and in a region very far from the permeation area, with no crack propagation during the constant deformation phase and, thus, no susceptibility to HE in accordance with the International ASTM F1624-12 standard
- Step duration, in the plastic deformation field, was not sufficient for the permeation transient to completely exhaust, even if the tested specimen was just 1-mm thick; therefore, the observation of the subsequent stabilization in the hydrogen permeation flux and the evaluation of the possible occurrence of embrittlement phenomena connected to the filling of new traps was not possible.

1

ACTIVE AND PASSIVE PROTECTION OF STEEL STRUCTURES

1.1 Active protection with cathodic polarization

1.1.1 Operating principle of cathodic protection

Cathodic protection (CP) represents an electrochemical technique that reduces the corrosion rate of an underground metal structure, or immersed in seawater, by lowering its potential thanks to the application of a continuous cathodic current towards the same structure. If well designed and realized, the application of CP to buried metal structures, such as pipelines, allows to minimize the corrosion rate to engineering negligible values, less than 10 μm/year. The UNI EN 12954:2002 [1] and ISO 15589-1:2015 [2] standards constitute the European and International technical reference, respectively. Those standards indicate the protection potential (E_P) values, net of ohmic drops, which must be guaranteed to protect the steel pipeline from different types of corrosion, due to galvanic coupling, differential aeration, Sulfate Reducing Bacteria (SRB), and electrical interference (deriving from electric systems operating both in direct current and alternate current).

Two CP techniques can be identified: impressed current system and galvanic anodes system. In order to reduce the potential of the pipelines that constitute the complex gas transport network, the CP technique with impressed current is the mainly implemented one. Instead, the CP technique with galvanic anodes is used only for the final user terminals (final user side for the only portion of the pipeline under the provider's jurisdiction), or for limited concentrated areas electrically isolated from the CP line systems. In general, the CP (impressed current or galvanic anodes) is implemented by the circulation of a direct current between the earth electrode (anode) and the structure to be protected.

In particular, the principle by which CP is applied is that the electrode potential of the cathode, i.e. the material to be protected and where the reduction reaction will occur, is pushed from the corrosion potential (E_{corr}) down to E_p, into the immune area in Evan's diagram *(Figure 1.1)*.

Thus, the oxidation reaction is forced to happen at the anode, and corrosion phenomena are avoided. As indicated in the reference standards, for the protection of subsea installations, E_p is usually pushed down at least to -0.80 V (Ag/AgCl/SW), which represents a commonly accepted limit where the hydrogen development and corrosion rate of steel are negligible.

Theoretically, to reduce the corrosion rate by an order of magnitude, the steel potential must be subject to a negative variation of at least 150 mV from E_{corr}; to make the risk of bacteria-induced corrosion negligible, instead, the negative variation must be at least 250 mV.

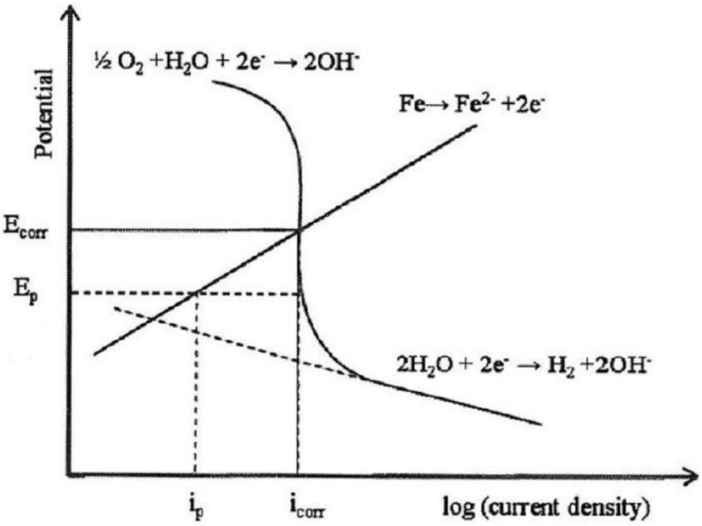

Figure 1.1. Basic principle for the application of cathodic protection. Current density vs electrode potential. Adaptation from the literature [3]

For onshore applications and underground pipelines, the cathodic current allows to eliminate or reduce the corrosion rate of the coating defects exposed to the soil environment. The amount of current required, therefore, depends on the corrosion rate (oxygen availability) of the steel in the soil. The charge balance of CP is summarized in *Figure 1.2*.

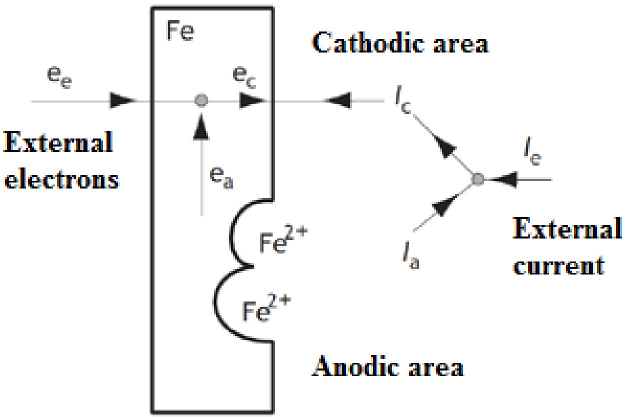

Figure 1.2. Electric scheme and charge balance of cathodic protection

From the above-mentioned electric scheme, following Kirkhoff's law, it is possible to write *(eq. 1)*:

$$I_e \text{ (external current/CP current)} = I_c \text{ (cathodic current)} - I_a \text{ (anodic current)} \quad \text{(eq. 1)}$$

Corrosion mechanisms are therefore eliminated ($I_a = 0$) if the external current is equal to the current of the cathodic process ($I_e = I_c$). From the graph reported in *Figure 1.1*, it is possible to identify the new working point of the pipeline in the presence of an external protection current: the potential to which the pipeline is pushed corresponds to that at which the afore-said charge balance is valid.

The corrosion rate is reduced (condition of quasi-immunity) if E_p, purified of the ohmic drops and indicated as the IR-free potential ($E_p = E_{IR\text{-}free}$), remains between E_{corr} and the equilibrium potential (E_{eq}) of the metal.

However, corrosion is eliminated if the potential is lower than E_{eq}, below which the protection conditions for immunity are established *(Figure 1.1)*. In soils and seawaters, the cathodic process is represented by oxygen reduction, so the protection current must be at least equal to the limit current density of oxygen diffusion (i_L); its value depends on the oxygen content, moisture content, temperature, level of aggressiveness of the environment, fluid-dynamic regime (only in seawater) and the presence of coatings that reduce the exposed metal surface. The reaction that takes place at the anode is instead its corrosion (soluble or galvanic anode) or oxygen development, in the case of insoluble anodes in impressed current systems.

1.1.2 Limit potentials for hydrogen embrittlement prevention

Shortly after the application of the fixed CP, close to the anode the potential can reach values ranging from -0.90 to -1.00 V (Ag/AgCl/SW), but most likely it will drop even lower. In correspondence with very low potentials ($E_p < -1.10$ V (Ag/AgCl/SW)), the steel is in over-protection conditions; as a result, on its surface the development of hydrogen must be considered in addition to the reaction of oxygen reduction. The quantity of hydrogen developed increases with the increase in the external current value and, thus, with the decrease in E_p *(Figure 1.1)*.

Even though, on one hand, the corrosion processes are absent (the potential is lower than E_{corr}), on the other hand the cathodic over-protection can determine:

- Cathodic disbonding of coatings. Hydrogen development tends to disbond the coating from the steel surface; this phenomenon can cause the onset of an anaerobic environment under the coating, with the development of a bacteria-induced corrosion mechanism, where the protection current hardly arrives. In addition to gaseous hydrogen development at the interface steel/coating, the phenomena of cathodic disbonding can be determined by an increase in the alkalinity, or induced by the electrophoretic transport through the coating
- Risk of hydrogen embrittlement (HE). Atomic hydrogen, developed from the cathodic reaction, diffuses through the steel and can lead to the formation and propagation of cracks. The risk

increases with the increase in the mechanical strength of the steel
- Increase in the risk of corrosion determined by induced alternate current.

Therefore, cathodic over-protection is particularly deleterious for the possible insurgence of HE phenomena, as reported in the design guidelines contained in the UK HSE Offshore Guidance Notes [4], adopted by DNV [5] and ISO [6]. To prevent the risk of Hydrogen-Induced Stress Cracking (HISC), in particular for susceptible steels with a high yield strength in over-protection conditions, the reference standards for CP regulation indicate precise limits for its application [1] [7] [2].

1.1.3 Regulatory requirements on cathodic protection

Nowadays, the field of CP avails itself of an extensive collection of rules, regulating its application, which includes 42 Italian and European standards; the latter are prepared by institutions which Italy directly collaborates with, such as the CEN (European Committee for Standardization) and the ISO (International Organization for Standardization). To these, International standards commonly adopted in specific areas, such as Oil&Gas, offshore, etc. must be considered, where often referred to NACE (interNational Association of Corrosion Engineering) and DNV (Det Norske Veritas) regulations.

Approximately one third of National, European and ISO standards includes the general aspects of CP, with reference to management, facilities and equipment, inspection and monitoring and anodic materials. Another third concerns the coatings used in conjunction with CP. Finally, just over one third specifically concerns the design and application of CP to marine and offshore structures (10 standards), underground structures (7 standards), equipment interiors and protection of reinforcement bars in concrete structures. Among these, the regulations with the indications concerning HISC phenomena. Other requirements are contained in the International standards DNV and NACE.

The current regulations have been developed over a long period; in fact, documents dating back more than fifteen years ago are still into force, along with others which have just entered. A noticeable difference in indications follows and, sometimes, true contradictions. These arise for two fundamental reasons. Firstly, the legislation concerning particular sectors of CP assumes a range of reference materials valid at the time of the document writing, with a usually implicit reference; especially in the case of older documents, the indications concern a relatively small number of alloys.

Secondly, over the last twenty years, cases of failures involving different alloys have been observed, and the results of studies carried out since the 1980s have become available. The most recent regulations have been updated on the basis of those results and the gained experience, with much more detailed requirements.

The main standards for the embrittlement risk prevention are UNI EN 12954:2002 [1], UNI EN 12473:2014 [7], ISO 15589-1:2015 [2], UNI EN 12499:2004 [8], UNI EN ISO 15589-2:2014 [9], DNV-RP-B401:2010 [10]. Other standards refer to these, which include the indications of the primary ones or make explicit reference to these. UNI EN 13636:2004 [7] refers to UNI EN 12954:2002 [1], while UNI EN 13173:2001 [11], UNI EN 12474:2001 [12], UNI EN 12495:2002 [13], UNI EN 16222:2012 [14], UNI EN ISO 13174:2013 [15] refer to UNI EN 12473:2014 [7].

The general approach followed in the HISC prevention regulations is based on three principles:

1. Identification of materials not susceptible to HISC, based on the type of alloy and the properties of mechanical strength or hardness; these materials can be used under cathodic protection in the common limits of potential assumed for the usual grade carbon steels (-1.10 V (Ag/AgCl/SW))
2. Indication of materials with potential risk of HISC, based on the type of alloy and the properties of mechanical strength or hardness; the protection is limited to potential values to which the formation of hydrogen is negligible (usually a limit around -0.90 V (Ag/AgCl/SW))
3. Evaluation, for materials with potential risk of HISC, of the usability limit by means of susceptibility tests to HE under CP (if this is not possible, the potential must be limited to "intrinsically safe" values).

However, nowadays none of the analyzed standards adopts an approach to HISC prevention based on stress limitation below the critical limit. The only indication attributable in some way to this approach, concerning the prescription of stress relieving treatments to reduce the material susceptibility (reduction of hardness and residual internal stresses), is included in some standards, such as in the DNV-RP-B401:2010 [10]. Reference is here made to general considerations for the use of materials with potential risk of HISC, because the standard underlines the susceptibility of non-tempered martensite and, therefore, the need to carry out post-welding heat treatments to reduce hardness and limit internal residual stresses.

For example, UNI EN 12954:2002 [1] reports the conditions for a correct protection, indicating that *"Some metals can be damaged by corrosion to very negative potentials. For these metals the potential must not be more negative than the critical limit potential* E_l*"*. It is added that for all the metals not included in the standard *"...the critical limit potential and the protection potential must be determined experimentally..."*, but without any indication on the test methods. However, also for the materials included, the standard does not establish a critical limit value. In fact, it indicates only a limit of -1.10 V vs CSE (for the CSE electrode, a potential of +0.32 V vs SHE is assumed), *"unless the coating manufacturer provides another documented value"* to avoid *"any detrimental effect on low-thickness insulation coatings with an average insulation resistance of less than* 10^8 Ωm^2*"*.

For steels with a high yield strength, the critical limit potential (E_l) is generally indicated under the potential for the beginning of hydrogen development, but without indicating how to estimate it. As the text of the standard is structured, the need to proceed to the experimental evaluation of the critical limit for these materials is not clearly indicated. A limit of -1.10 V (CSE) is expressly indicated only for steels in *“cement”* for pre/post-tensioning, with a YS > 700 MPa.

According to the International ISO 19902:2007 [6] standard, HE susceptibility increases for steels with a Specified Minimum Yield Strength (SMYS) in the range 460÷500 MPa. However, field experience has demonstrated that Thermo-Mechanically Controlled Processed (TMCP) steels with a SMYS in the range 450÷480 MPa are not susceptible to HE.

More recently, UNI EN 12473:2014 [7] specifies that, if the available documentation is not sufficient, the specific critical limit must be experimentally determined by means of a mechanical test conducted at E_l, in relation to the metallurgical and mechanical conditions of the particular material. In relation to these tests, the standard refers to the work of the UK Health and Safety Executive [16]. For carbon-manganese and low alloy steels, with a SMYS ≤ 550 MPa, the standard indicates that a limit of -1.10 V (Ag/AgCl/SW) prevents the phenomena of swelling or cathodic disbonding of coatings, the negative effect on fatigue properties and the risk of HISC phenomena. For steels with SMYS > 550 MPa, E_l is generally specified in the range from -0.83 to -0.95 V (Ag/AgCl/SW). The standard reports cases of HISC of high strength steels for the fabrication of hydraulic lifting jacks on offshore drilling platforms, in the areas near the welded points. The studies carried out in this case, by means of SSR tests, established that the damage caused by hydrogen is insignificant at potentials higher than -0.83 V (Ag/AgCl/SW) [17].

Moreover, ISO 15589-1:2015 [2] indicates that, for steels with a SMYS ≤ 550 MPa, the lower potential limits prescribed for an adequate protection are fixed to the common values of -0.85 (soils and waters in all the common operative conditions) and -0.95 V (SCE) (soils and waters in anaerobic conditions and with corrosion risks caused by the Sulfate Reducing Bacteria – SRB). An additional limit of -1.20 V (SCE) is specified uniquely for the prevention of damaging, disbonding and blistering of the coatings normally used in the present pipelines. On the contrary, for steels characterized by a SMYS > 550 MPa, it is indicated only that E_l shall be documented or determined experimentally to avoid the risk of hydrogen formation. Therefore, even in the updated test of this standard no specific tests for the determination of this limit are indicated.

The most detailed information regarding HISC phenomena, not only for carbon and low alloy steels but for all the main alloys, is reported in the DNV-RP-B401:2010 [10]. On the basis of practical experience, the standard reports that ferritic and ferritic-pearlitic steels with a SMYS of 500 MPa can be considered fully compatible with CP in the marine environment, as these steels showed susceptibility to HISC only during laboratory tests, under extreme yielding conditions. For these materials, the standard recommends realizing welds according to qualified procedures, with absolute maximum hardness limit below 350 HV. Moreover, for hardness values within this limit, but higher than 300 HV, the standard prescribes that measures must be taken during design to avoid local yield conditions, and that coating systems, capable of acting as a barrier to hydrogen absorption, must be necessarily applied. For low alloy carbon steels, the standard reports HISC failures on materials with a SMYS of about 700 MPa and 350 HV of hardness.

For HISC susceptible materials within the normal range of protection, the standard provides no potential limits, unless reporting that particular CP techniques, which limit E_p to less negative values, in the range from -0.80 to -0.90 V (Ag/AgCl/SW), were applied.

Table 1.1 summarizes the requirements for the HISC risk prevention reported in the main standards.

Table 1.1. Main requirements for HISC risk prevention in carbon or low alloy steels contained in the reference standards for cathodic protection

Main standard for HISC prevention	**Material**	**Main requirements**
UNI EN 12954:2002	Ferrous materials (SMYS < 800 MPa)	No limit
	Other ferrous materials (SMYS > 800 MPa)	Critical limit potential to be determined experimentally, in relation to the individual case. No indication of the type of test
	Pre/post-tensioning cables in concrete (SMYS > 700 MPa)	Critical limit potential to be determined experimentally, in relation to the individual case. Indication of criticality at potentials lower than -1.10 V (CSE)
UNI EN 12473:2014	Carbon steels (SMYS < 550 MPa)	Normal limit at -1.10 V (Ag/AgCl/SW)
	Carbon steels (SMYS > 550 MPa)	Determination of the limit by means of experimental tests [16]. Indication of the usual limit from -0.83 to -0.95 V (Ag/AgCl/SW). Indirect indication to: uni-axial tensile test with constant load, four-point bending test; C-ring test, DCB test, SSRT test
ISO 15589-1:2015	Carbon or low alloy steels (SMYS < 550 MPa)	Normal limit at -0.85 V (soils and waters in all the common operative conditions) and -0.95 V (SCE) (soils and waters in anaerobic conditions and with corrosion risks caused by SRB). An additional limit of -1.20 V (SCE) is specified uniquely for the prevention of damaging, disbonding and blistering of the coatings normally used in the present pipelines
	Carbon or low alloy steels (SMYS > 550 MPa)	Critical limit potential to be determined experimentally, in relation to the individual case. No indication of the type of test nor evaluation criterion
DNV-RP-B401:2010 (*)	Ferritic and ferritic-pearlitic construction steels	No limit: compatible with the cathodic protection systems in marine environment. Indication of susceptibility in extreme yielding conditions (in laboratory tests). Recommendation for welding procedures with a maximum hardness limit of 350 HV. For the range hardness 300÷350 HV, it is recommended avoiding local yield conditions or to provide barrier layers to hydrogen absorption
	Martensitic carbon steels (SMYS > 700 MPa and hardness > 350 HV)	Indication of possible failures
(*) The standard explicitly states that: a) there is no generally accepted test to evaluate compatibility with		

cathodic protection; the comparison between materials of the same type can be conveniently obtained by means of SSRT; uni-axial tensile tests with constant load, four-point bending, CTOD and other tests can be also used.

1.1.4 Compatibility tests for hydrogen embrittlement prevention

Many of the standards with recommendations for HISC prevention under CP refer to compatibility tests, but none of them reports experimental methods to achieve this result. In any case, tests are prescribed to evaluate the compatibility with the normal CP or to verify the maximum negative limit applicable to materials whose full compatibility is not known yet. In no case it is expected to estimate the usability limit in relation to the mechanical stress. In the case of a susceptible material, only in the case of the DNV-RP-B401:2010 [10], reference is made to general considerations for tests useful to identify the intrinsically safe exposure conditions, mainly of potential. However, no standard either prescribes particular tests or recommends criteria for evaluating the results.

The most detailed indications are given in DNV-RP-B401:2010 [10] and in UNI EN 12473:2014 [7]. DNV-RP-B401:2010 [10] indicates the SSR test to compare materials with similar microstructure, but it emphasizes that a comparison of different types of materials is more difficult; it also indicates that uni-axial tensile tests with constant load, four-point bending, CTOD and further tests must be carried out.

UNI EN 12473:2014 [7] refers to the Health and Safety Executive of 2003, Research Report 105 [16], which notes that the proposed tests to determine the behavior to embrittlement are not equivalent to each other, but each has its own role and gives a specific piece of information. Above all, therefore, the need to perform multiple types of tests for a reliable compatibility assessment arises.

In the absence of specific indications, it is possible to refer to UNI EN ISO 7539-1 [18] that, from part 2 to 11, reports the general indications on the implementation of stress corrosion tests for the assessment of susceptibility to environmental failure.

In addition to the different values of E_l fixed by the reference standards to avoid hydrogen development, another important question is the determination of the hydrogen quantity that enters a metal, and the time taken to saturate the entire matrix and cause embrittlement phenomena. All these uncertainties are generated by the fact that hydrogen flow strongly depends on the loading conditions. For this reason, the recent UNI EN ISO 7539-11 [19] standard, which provides the guidelines for the design and realization of tests for the evaluation of the resistance of a metal or alloy to HE and to Hydrogen Assisted Cracking (HAC), indicates that the main factors that must be considered are dynamic plastic deformation, test time and temperature. The effect of dynamic plastic deformation is developed in four additional sub-items, among which the role of hydrogen transport by dislocations during plastic deformation must be considered, which increases its contribution within the metal.

A fundamental aspect underlined by the standard is the relation between the test time and hydrogen supply, or rather the identification of the time necessary for the hydrogen supply to be sufficient to reproduce the operating conditions, in which the exposure time is in the order of years. This effect is especially important in the case of thick pipes that require a long time to reach the saturation condition in the center of the wall, where critical inclusions may occur and act as preferential sites for the initiation of HAC.

Moreover, the standard recommends the measurement of the hydrogen permeation flow for the evaluation of the time necessary to achieve steady state conditions, which it must eventually include a pre-charging period, to be estimated by applying the laws governing diffusion (Fick's second law). Operatively, the recommended approach is based on a selection of the test or hydrogen pre-charge time necessary to reach 80% of the stationary concentration at a certain depth, considering that the HAC phenomena generally trigger on the surface.

With regard to the load, the standard recommends that stress levels as close as possible to the operating conditions, including their slight variations, must be considered, as well as the fact that dynamic deformation conditions can intervene during operation, in situations such as thermal transients, soil and seabed settlement for the pipes, etc. Particular attention is to be paid to the deformation speed, as this intervenes both in the mechanism of environmental embrittlement and in determining the test duration. In fact, as the deformation speed decreases, the test time increases, as well as the time available for hydrogen to saturate the material. In order to separate these two effects, the standard recommends carrying out tests with a sufficiently long hydrogen pre-charge.

However, even in the text of this recent standard is reported only that *"A fundamental question is how long should a laboratory test be to ensure that hydrogen uptake is sufficient"* and again that *"...pre-charging may be pertinent to ensure that uptake of hydrogen is significant"*. The result is that, since hydrogen flow strongly depends on the loading conditions, this is not a useful indication for the estimate of the time necessary to reach steady state conditions and valid for the evaluation of the HE phenomena.

UNI EN ISO 7539-7 [20] standard, on SSR tests, usually reports the deformation speed of 10^{-6} s^{-1}, both to determine the environmental parameters critical for environmental failure and to compare different materials. Although no universally accepted criteria have been found, it provides some indications. In order to accelerate the tests, a rate higher than 10^{-6} s^{-1} in the elastic field could be adopted, and the strain rate should be decreased only in close proximity to the yield limit.

Typically, a 30-day test should lead to more than 2% of plastic deformation, which can be considered the upper limit of strain transients during operation. If fracture is not observed during this time, the specimens should be metallographically observed to determine the presence of micro-cracks.

In addition to the tests with MFLE notched specimens with an increasing apex, it is also possible to use incremental load tests as preliminary tests, in order to obtain an approximate value of the intensity factor of the threshold stresses. In this way, there is an indication of the initial K value from which to start, with the slow increase of the apex or the test load in the dynamic deformation tests. However, these tests require, subsequently, the definition of acceptance criteria of the obtained value of K_{ISCC}. The most rigorous approach involves the use of elasto-plastic fracture mechanics, by means of CTOD tests or the J-integral determination. Other International standards, universally recognized for the execution of stress corrosion tests, are NACE TM 0177-2016 [21], but related to sour environments, and different ASTM standards, which however were largely recovered in ISO 7539-1 [22].

1.1.5 Summary of limit potentials and compatibility tests

From what was presented in the previous paragraphs, it is clear that the regulatory framework is rather complex and sometimes contradictory. The requirements for the HISC risk prevention for carbon or low alloy steels, summarized in *Table 1.1*, can be simplified in the graph of *Figure 1.3*.

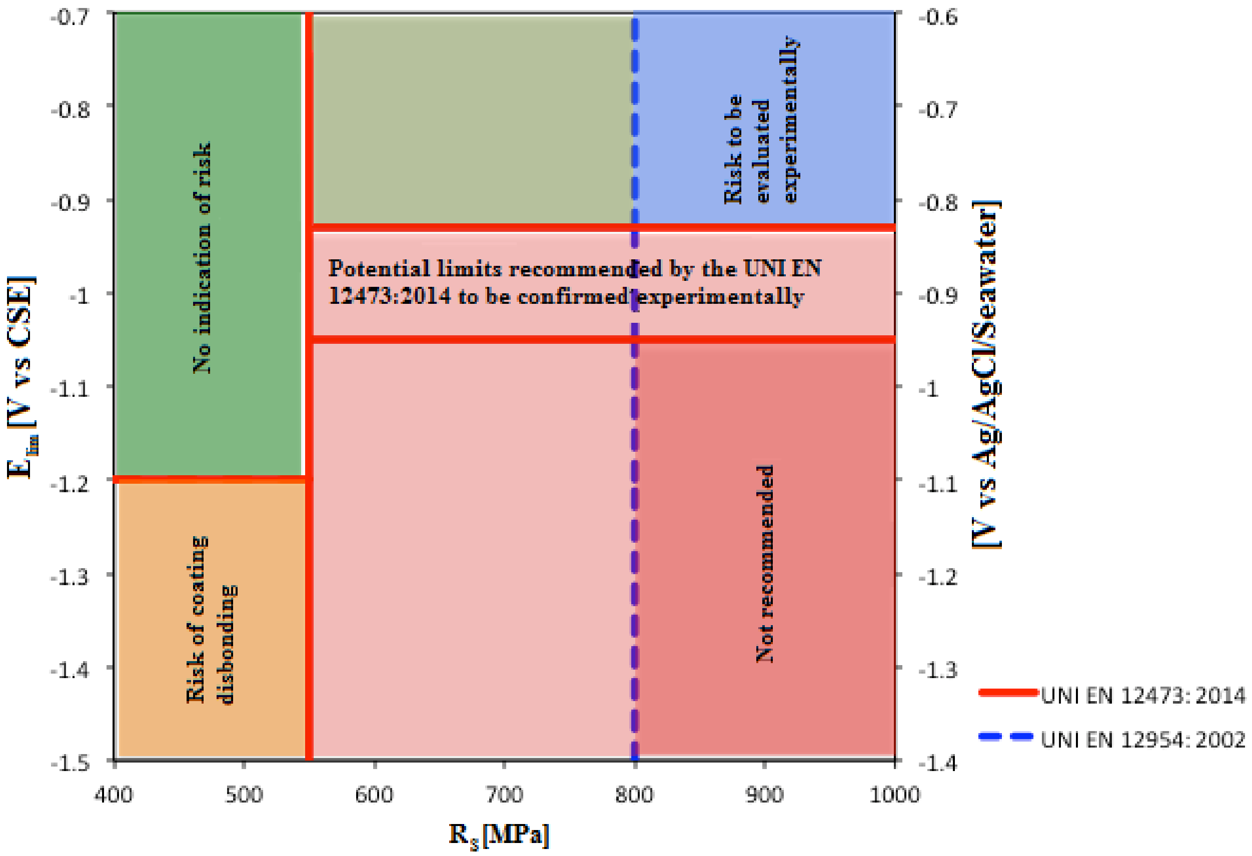

Figure 1.3. Summary of the prescriptions for the HISC risk prevention for ferritic-pearlitic carbon steels, in relation to the UNI EN standards on cathodic protection, as summarized in Table 1.1

The green area corresponds to no indication of risk by any standard. The dotted line above 800 MPa refers to the yield strength (YS) above which the UNI EN 12954:2002 [1] standard provides for the experimental verification of applicability. The red lines refer to the UNI EN 12473:2014 [7] standard. For YS below 550MPa, only the potential coatings disbonding for potentials below -1.10 V (Ag/AgCl/SW) is reported, while, above the YS of 550 MPa, the potential limit of CP application must be verified experimentally, in the range from -0.83 to -0.95 V (Ag/AgCl/SW).

In conclusion, for YS below 550 MPa, no risk of HISC is reported, but only of cathodic disbonding of the coating. Between 550 and 800 MPa, the limit protection potential to exclude the risk of HISC will fall in the range from -1.10 to -0.93 V (CSE) (from -0.95 to -0.83 V (Ag/AgCl/SW)), but should be verified experimentally. Over 800 MPa, this limit must also be verified even for protection potentials higher than -0.93 V (CSE), while it is not recommended to go below -1.10 V (CSE).

Regarding the experimental determination of E_l, if required, i.e. the pink and blue areas of the graph of *Figure 1.3*, the UNI EN standards give no indication, except for the UNI EN 12473:2014 [7] one, which provides an indirect indication of uni-axial constant load test, four-point bending test, C-ring test, DCB test and SSR test.

The first three methods, uni-axial constant load test, four-point bending test and C-ring test, must be considered not very conservative, and a positive response with these specimens (presence of cracks) must be considered as a high susceptibility index to HISC. On the other hand, useful indications can be drawn from the SSR tests; in fact, these tests allow to evaluate also the effect of the strain rate, and therefore of any stress transient during operation. The evaluation of susceptibility to HISC in SSR tests can be performed, with the same potential and strain rate, by comparing the behavior of the test material with that of materials of proven immunity to HISC, as suggested by DNV-RP-B401:2010 [10]. According to the standards, MFLE specimens, such as DCB and WOL, should be used only if there are conditions that justify the presence of notches with a sharp apex, such as welding.

The exposure time should be evaluated by means of hydrogen permeation tests, in order to ensure the achievement of steady state conditions of hydrogen flow at the center of the specimen or, alternatively for the cylindrical SSR specimens, upon reaching a permeation flow equal to 80% of the steady state, at a distance equal to 20% of the diameter.

1.1.6 Monitoring techniques of cathodic protection

With regard to the CP monitoring, this includes all the operations aimed at verifying, directly (on site) or indirectly (by remote terminal), the protection degree of metal structures.

In particular, a guiding factor in the installation of remote monitoring measurement units is the necessity to create a remote-controlled system: according to the UNI 11094:2004 [23] standard, those units must be installed in correspondence of power supplies, drainages, railway crossings, connections to third-party structures (minimum of measurement points indicated in the standard [23]) and in correspondence with those "characteristic" measurement points, considered significant, or even critical for the control and monitoring of the electrical condition of the pipeline.

Moreover, the technical criteria indicated in the UNI 10950:2001 [24] and UNI 11094:2004 [23] standards allow to establish whether each portion of a pipeline network is adequately protected by calculating the so-called "K_t indicator" of CP, whose key parameters refer to the technical data for the design, management and verification of the electrical parameters of CP. This K_t indicator is applicable to CP systems monitored both by operators and via a remote monitoring system, according to the criteria cited in the above-mentioned standards.

Anyway, the universal criterion for the CP verification of a structure is based on the measure of the real potential.

The electrochemical potential E_{corr}, referred to the CSE electrode, assumes a value between -0.4 (typical for well-aerated soils) and -0.65 V (CSE) (typical for wet soils). With the application of the CP, the potential undergoes a negative variation, settling in the range between -0.85 (or -0.95 V in the presence of bacteria-induced corrosion) and -1.2 V (CSE) to limit hydrogen development.

As mentioned in the previous paragraph, UNI EN 12954:2002 [1] reports these criteria in a more detailed manner, and considers also the risk of coating disbonding in over-protection conditions, for protection potentials more negative than -1.1 V (lowered to -1.2 V (CSE) in ISO 15589-1:2015 [2]). In particular, it is emphasized that, in order to prevent the risk of HE, the fixed E_l [1] must be documented or "experimentally" determined [2]. The measure of the potential can be affected by errors that must be eliminated, primarily the ohmic drop.

In order to maintain a suitable level of protection, it is necessary to keep the electrode-conducting potential below a preset value; therefore, the main function of the measure is to verify the effectiveness of CP on the pipeline. Secondly, the measures are also used to verify the proper functioning of the installed equipment.

1.1.7 Interpretation of the measured potential

The value of the potential measured while the protection current circulates, the so-called ON-potential (E_{on}), is a function of the position of the reference electrode (RE) with respect to the structure, and it represents the sum of two contributions: the IR-free potential ($E_{IR\text{-}free}$), which represents the true level of protection of the pipeline, and the ohmic drop in the soil (IR), which depends on the circulating current, the soil resistivity and the distance between the structure and the RE. The measurement of the potential of the pipeline without the ohmic drop is given by the following relation *(eq. 2)*:

$$E_{IR\text{-}free} = E_{on} - IR \qquad \textit{(eq. 2)}$$

This equation contains the following parameters:

- ON-potential (E_{on}), which represents the pipeline-RE potential, measured in the presence of the CP current. The electrode must be placed superficially on the vertical line of the pipeline, or buried laterally to it. E_{on} is a parameter whose measurement is strongly influenced by the stray currents present in the ground, as it contains the term related to the ohmic drop (IR). With a negligible contribution of electrical interference from direct current traction systems, a remote monitoring device, in accordance to UNI 10950:2001 [24] and connected on a bitumen coated pipeline, in the 24 hours returns the typical graph of the E_{on} potential shown in *Figure 1.4*. The E_{on} measurement performed on polyethylene coated steel pipelines (coating characterized by high efficiency, with absence of generalized porosity and minimal localized porosity) can be characterized by a non-negligible IR contribution, which depends on the effective distance separating the RE and the defect present on the coating. This condition leads to a considerable increase in the value of voltage drop in the soil, which becomes strongly influenced by the presence of stray currents (*Figure 1.5*)

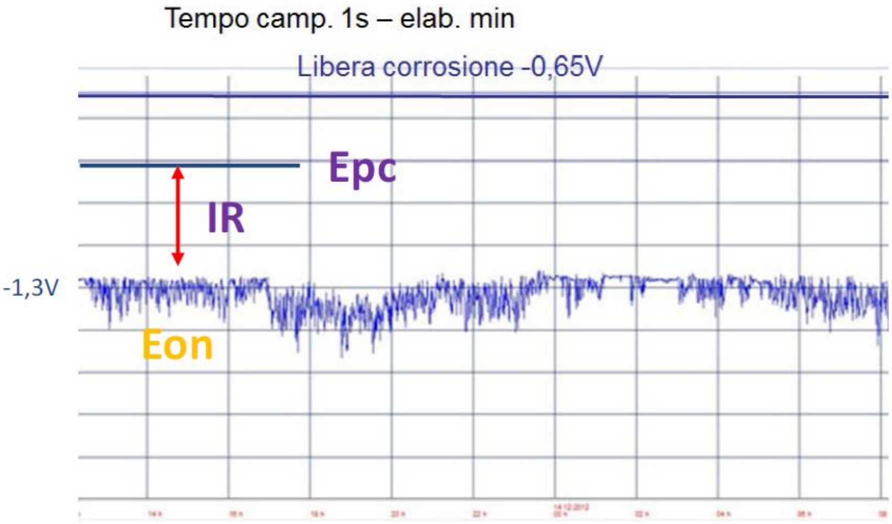

Figure 1.4. Example of monitoring in continuous on a bitumen coated pipeline in a non-interfered area

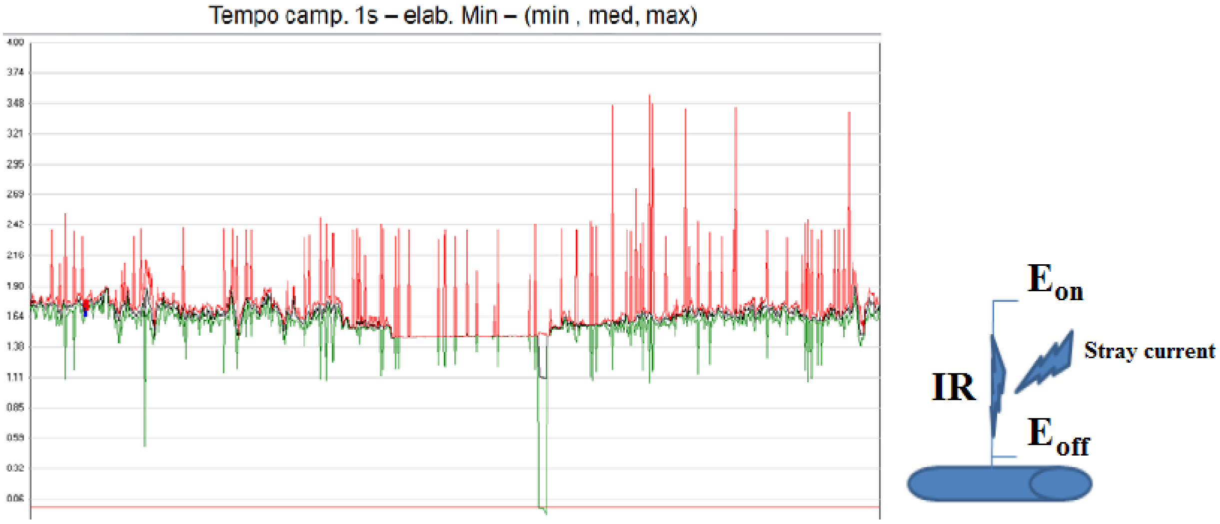

Figure 1.5. Example of monitoring in continuous on a polyethylene coated pipeline in an interfered area

- IR-free potential ($E_{IR\text{-free}}$), which indicates the potential, measured net of ohmic drops, due to the protection current, or to other currents circulating in the ground between the RE and the pipeline. The IR-free potential is measured in two ways: by positioning the RE as close as possible to the defect present on the pipeline coating; by the so-called ON-OFF technique. The first mode is the most correct one. It is performed by means of potential probes, i.e. sensors containing a steel coupon and an embedded RE, placed near the coupon itself. The coupon, connected to the pipeline under CP, allows to simulate a defect of known dimensions on the coating (*Figure 1.6*).

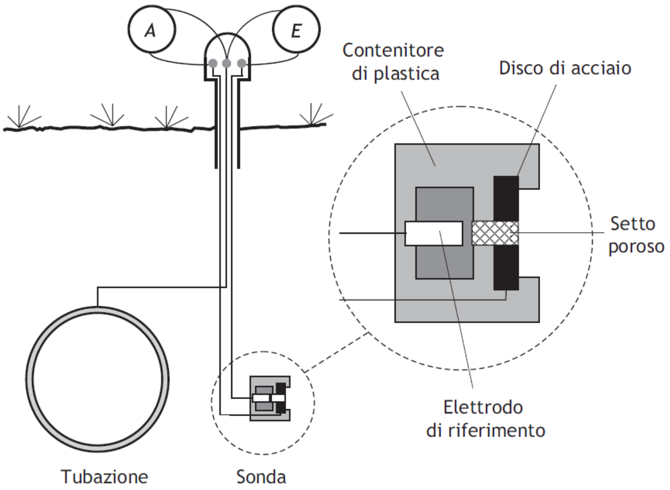

Figure 1.6. Schematization of a potential probe, with a steel coupon and an embedded RE

The International [2] and European [1] standards prescribe, in the monitoring criterion, the control of the CP potential with measurement techniques that exclude, from the measured values, the contribution of voltage drops in the soil *(Figure 1.7)*. The IR contributions can derive not only from dispersed currents, but also from the current supplied by the CP system, if the RE is laid between the pipeline and the anodic system *(Figure 1.8)*

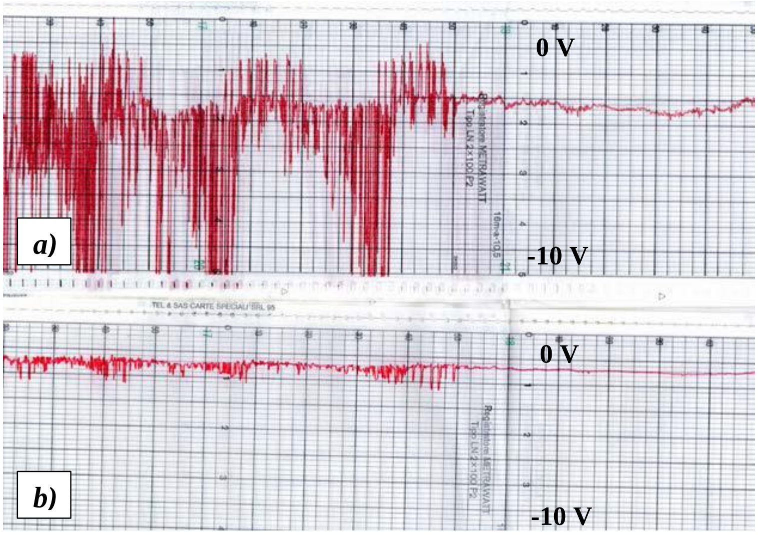

Figure 1.7. Potential measurement: a) Without the potential probe; b) With the potential probe

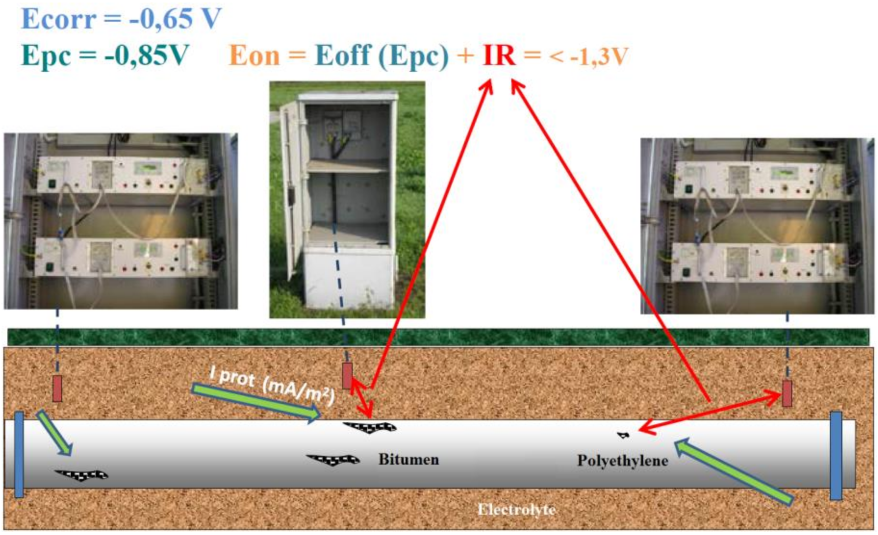

Figure 1.8. Schematization of the electric parameters of the electrochemical potential

- <u>OFF-potential (E_{off})</u>, which provides the pipeline-RE potential, measured with two possibilities: cyclical interruptions of the CP current (ON-OFF technique), or with potential probes that simulate a defect in the coating, by disconnecting them from the protected pipeline. It is important to underline that the OFF-potential does not always coincide with the IR-free potential; in particular, the ON-OFF technique measurement must be carried out in the absence of currents other than the protection current. Furthermore, it is possible to prove experimentally that the OFF-potential does not allow to identify conditions of cathodic over-protection. E_{off} becomes redundant if acquired indiscriminately in all the measurement points in which steel coupons are installed, but it can assume a remarkable valence only in the measurement points affected by a high electrical variability (electrical interferences according to EN 50162 [25]).

1.1.8 <u>Critical issues in the present protection systems</u>

This paragraph aims to identify the main critical issues encountered in the CP systems currently installed on the national territory, and in some cases tries to provide possible solutions.

In particular, concerning the analysis of the critical issues in the design and building phases, from a technical point of view, it is necessary to consider that:

- Design regulation related to insulating joints must be modified. When the joint is 150 m far from a grounding system of a high voltage pylon, the transversal spark-gap dischargers between the upstream and downstream of the joint towards earth must be omitted. On the contrary, the longitudinal spark-gap discharger must always be installed, connected in an underground way between the upstream and downstream of the joint itself. Spark-gap dischargers installed between upstream pipeline vs. ground, and downstream pipeline vs. earth, are always provided without taking into consideration the proximity of the grounding systems of the power lines

- Since the longitudinal spark-gap discharger, buried to protect the insulating joint, has a higher permanent regime trigger voltage than those in transversal connection with the pipeline, it is considered appropriate to install longitudinal spark-gap dischargers in a remote configuration, translated by maximum 2 m towards the ground surface
- In order to facilitate the achievement of low electrical resistance values, depending on the type of soil resistivity, lamellar grounding systems should be introduced
- During the design phases, it must be taken into account that the transversal grounding system must be omitted if the corresponding grounding system is located at a distance < 150 m from the ground system of a high voltage pylon > 30kV
- Given the high efficiency insulation of the new types of coatings and the reduction of the necessary current (even of one order of magnitude), the present distance of the anode with respect to the pipeline is excessive (the building flexibility would be increased and, therefore, horizontal anodes could also be used more often). Moreover, because the currents exchanged on very isolated pipelines have low average values, the use of drainage for non-stationary interferences is surpassed
- It is necessary to clarify the suitability and compatibility of the materials of the anode with respect to the laying bed. The current UNI standards are not clear. For deep anodes, the laying bed is generally realized with the same drilling mud, which is an improper practice. The magnesium anode is laid directly in bentonite, but the practice is not correct because the laying bed must consist of a suitable backfill, i.e. bentonite with chalk and/or sulfates. Venting pipes for deep anodes are rarely used and for low current values these are not necessary. The material currently used, Fe-Si or Fe [23] [26], does not facilitate the installation and has an environmental impact. Therefore, insoluble MMO-activated titanium anodes should be used
- Regarding the installation of the anodes, the acquisition of public and private permits is required, which is really demanding. Moreover, in particular for the vertical anodes, the installation (too often subject to budget logics) is entrusted to mechanical or instrumental companies, and not to drilling companies, which leads to a lengthening of the times
- In the case where it is expected that the gases generated by the anodic reaction may compromise the operation of the anode (gas-induced block) it is convenient to insert, during the laying phase, a synthetic resin pipe, with the walls properly drilled, to facilitate the escape of the gases, conveying them towards the outside of the hole. Unfortunately, this is currently rarely realized
- There is a lack of paper and photographic documentation of what realized on site, especially in

small projects. In particular, the as-built presentation of a small-scale planimetric section (for the archives) of the CP/remote monitoring systems is lacking in legislation. It is necessary to encourage and foresee, in the procedures, the delivery of detailed photos and drawings from the building site. With regard to the wiring activities for insulating joints and CP/remote monitoring systems, currently this is often carried out by external personnel, but the documentation transmitted for the operation is often not sufficient for a good understanding of the system

- The UNI 11094:2004 [23] standard does not apply to complex structures in concentrated areas. However, in the text there is reported that a superficial anode can be used only when it is possible to maintain a distance of at least 100 m from third-party structures and the structure to be protected (in case of impossibility, it is necessary to use deep anodes); a smaller distance can still be maintained by following appropriate measurements to evaluate the variations made to the electric field in the ground. In particular, Par. 7.9 of the EN 14505:2005 [27] standard indicates requirements for the laying beds, not specifying the anode-structure distances
- The OFF-potential (E_{off}) indicates the “effective value of CP”; thus, if this is not correctly acquired, can lead to the dangerous lowering of the CP current (against inconsistent data), with the consequent threat of a significant increase in the corrosion risk. Consequently, E_{off} must be measured after 80 ms from the opening of the cyclic switch; it would be sufficient to take only one measure, and over a period of 20 ms. As a result, the electronic devices employed on site for the remote monitoring of the CP parameters do not have to take measures with a high acquisition frequency, because there is the concrete risk of considering all the high/low electrical noise, also coming simply from installed unshielded cables. Surely, it must be considered the fact that the depolarization phenomenon is slow, and therefore the type of monitoring must be consistent with what must be measured. In fact, acquisition times of the E_{off} value after 80 ms from the opening of the electrical connection between the coupon and the structure, allow the coupon to settle on Tafel lines to follow the electrochemical depolarization. Moreover, it would not be correct even to insert a low-pass filter, because in this way alternate current interferences could be detected no longer. Concerning the activation of the cyclic switch, this must ensure the zeroing of the CP current, because any current leakage (even in the order of µA or nA) would lead to incongruent values of the measured potential. Therefore, the robustness of the measuring instrument must also be guaranteed, because, with the activation of the switch, this must completely disconnect the circuit in order to obtain the correct E_{off} value, without any residual circulating current, so that the working electrode is no longer polarized.

1.2 Passive protection with protective coatings

1.2.1 Common properties of coatings

The concept at the basis of passive protection (PP) is linked to the implementation of all the provisions, both during the design and construction phases, which allow to isolate all the metal parts constituting a structure from the surrounding environment. In fact, the application of a coating on a steel pipeline involves the physical separation of the steel towards the environment, physically limiting the access of oxygen in contact with the metal (barrier effect) and the transport of current in the ground. The optimization of the PP involves the reduction of the protection current, with the consequent reduction of energy consumptions, along with the reduction of the corrosion risks and the realization costs of the CP systems.

However, the use of protective coatings only is not sufficient to guarantee a complete protection of the pipeline from corrosion mechanisms, because every coating presents defects due to the handling of the pipes and to soil settlement after laying; moreover, it has a characteristic of water permeability and it is affected by a physiological degradation over time. In all the protective coatings currently applied to underground pipelines, corrosion phenomena are present in coating defects, with a generalized corrosion rate between 10 and 100 µm/year, depending on oxygen availability.

As a result, corrosion phenomena are absent where the coating is intact, but the risk of bacteria-induced corrosion (anaerobic) under the coating arises if the adhesion between coating and pipeline, or under wrinkles, is missing.

During the last ten years, the field of natural gas distribution has determined an increasing necessity of the development of innovative materials and application technologies, oriented to the evaluation and consequent resolution of the ageing and degradation problems in the protection of pipelines against corrosion. More generally, an insulating coating allows to:

- Avoid direct contact of the structure to be protected from environment and other metal structures, by giving an adequate mechanical protection and an electrical and chemical/physical insulation
- Reduce the total protection current (decreases the metal surface exposed to the soil, reducing itself only to the defects) and uniform the distribution
- Reduce the effects of electrical interference with other structures coexisting in the ground, the effects due to dispersed currents and the influence of any electric field in the surroundings.

In addition, in order to ensure the PP of an underground structure in every situation, an insulating coating must:

- Provide an effective electrical insulation, combined with a high and durable electrical resistivity
- Constitute an adequate barrier against humidity, water vapor and oxygen
- Be applicable with reliable methods that do not alter the properties of the structure

- Be characterized by an adequate resistance to the disbonding due to over-protection conditions
- Present a good and durable adhesion, in a wide temperature range, to the metal surface
- Resist to possible damage due to handling, storage and assembly
- Withstand the stresses due to the environment over time
- Be repairable with reliable and simple systems, also applicable on site.

By using materials that satisfy these requirements as much as possible, very positive results can be obtained from both a technical and economic point of view, by creating coatings able to withstand the typical stresses occurring during the different work phases: transport and storage of coated structure elements, laying, proof test, and operation.

1.2.1.1 Choice of the specific coating

The choice of a coating must be made by taking into account the conditions that will occur during the service life. Therefore, in addition to the type of environment, it will be necessary to consider:

- Characteristics of the structure to be protected and accessibility to it
- Presence of external electric fields
- Proximity to other structures, protected or not
- Environmental conditions during application, transport, storage, assembly, and hydraulic testing
- Handling, stacking, and storage conditions
- Operating temperature
- Expected life span of the structure and maintenance charges.

As regards the economic evaluation, it will be important during this phase to consider not only the purchase cost of the coating, but also the additional costs due to any particular treatment required during the period preceding the laying, or after it, to protect the applied coating. Also the cost of the repairs to be carried out on site must be considered carefully, because for some coatings (bitumen, cold-applied tapes) it affects a relevant percentage of the final costs.

1.2.1.2 Coatings currently present on pipelines in Italy

Nowadays, in Italy, the most used coatings on underground pipelines are essentially based on:

- Bitumen [28], usually hot-applied in factory and used until 1990. Unfortunately, this coating is characterized by a remarkable water permeability
- Polyolefins (polyethylene [29] and polypropylene [29], or epoxy resins [30]), applied by extrusion in factory and standardly used since 1990 on all the nominal diameters pipelines. These coatings are characterized by a low/negligible water and oxygen permeability, which allows to have a very low corrosion rate, less than 10 µm/year
- Self-adhesive polyolefin tapes [31] applied on site, both on pipes and on welding joints. These coatings are also used to rehabilitate short sections of pipelines

- Thermo-setting resins [30] [32] applied by machine or hand, in liquid form, in factory or on site
- Thermo-shrinkable sleeves [31] for coating of welding joints and repair of polyolefin coatings.

1.2.2 Products for the coating of pipelines and other elements

1.2.2.1 Coatings based on bitumen

Among the most used in Italy in the past, those coatings provided generally satisfying results, especially for small diameter pipelines. The bitumen was applied melted in factory, in combination with one or more reinforcing glass fabrics, depending on the nominal diameter; thus, the thickness could also result of several millimeters (from 3 to 8 mm).

Mainly due to the intrinsic fragility of bitumen at low temperatures and the tendency to softening at temperatures above 30 °C (303 K), in recent years that coating has been progressively abandoned, in favor of polyethylene-based coatings, which can maintain their characteristics unaltered over time.

The conditions in which the use of bituminous coatings [28] is critical are:

- Room temperature lower than 10 °C (283 K) during handling and laying
- Room or operating temperature higher than 35 °C (308 K), which is more than 50 °C (323 K) in the case of laying on sand bed or on other fine material
- Cold bending on site with pipe-bending machine
- Soil pollution with liquid hydrocarbons
- Laying in stony ground areas, with steep slopes or deep rooting plants.

Furthermore, particular precautions have to be observed during the storage of stacked pipes to prevent crushing and reduction of thickness, or tearing of the coating.

The problems that after years of service that coating involves are, above all, a relevant deterioration of the electrical insulation of the pipeline, with cracks and large areas of degraded coating and exposed material. This necessarily results in a considerable increase in the protection current consumption. Moreover, particular attention must be paid in the case of exposed material in operating pipelines: the areas repaired with cold-applied tapes and the pipe bends (re-taped on site) are the worst weak points of the insulation.

1.2.2.2 Coatings based on polyolefins, polyethylene or polypropylene

Over the last thirty years, these types of coating [29] have been developed at top quality levels, thanks to the technologies used for the realization of stationary systems in factory. Their main characteristics, maintained practically unaltered over time and in a wide temperature range, are mechanical strength, resistance to corrosion beneath them, electrical resistance and strong adherence to metal surfaces in a temperature field much wider than that of bitumen. With these coatings, almost all the problems due to the exposure to solar radiation, cold bending on site, storage, handling at low and high temperatures (in the range from -40 (233) to +60 °C (333 K)) have been solved, with excellent adhesion values up to +70 °C (343 K) for polyethylene and up to +100 °C (373 K) for polypropylene. The application usually takes place by extruding a layer of adhesive and one of polyolefin (mixture) over an epoxy primer layer; the composition of the layers has the function of maximizing the adhesion between the mixture and the metal surface.

In relation to the diameter of the pipe, the thickness assumes typical values ranging from about 2 mm to about 3.5÷4 mm. In some factories, the application is made using only powdered polyethylene (melted or sintered coating); this application method is currently reserved for small diameter pipes, and more rarely for bends and special pieces. The technical results are lower than those obtainable with the extrusion application.

At room temperature, polyethylene coatings present a mechanical strength from 5 to 10 times higher than that of the best bitumen coatings. The high performances offered by the polyolefins allow the laying of perfectly insulated pipes, as a technically safe result is obtained with a considerable reduction in the operational costs (maintenance, any rehabilitation, CP, etc.).

Only a few precautions must be adopted to fully achieve the afore-mentioned objectives:

- Careful handling of the coated elements
- Search for insulation defects with a Flaw-Detector Device (Holiday Detector), applied to the entire coated surface
- Care during the laying and backfilling phases.

With the use of these high quality coatings, it is convenient to search for and localize any flaw that may have formed on the already laid pipeline, and proceed with its repair. The search for insulation flaws takes place using well known methods, and currently very reliable, such as the Transversal Gradient method and the Pearson method. Therefore, that the need for effective PP now pushes users to completely abandon bitumen for more performing products, with higher characteristics.

By making a technical-economic evaluation, polyolefins are now more convenient than bitumen coatings; in fact, in addition to the pure factory cost, additional costs must be considered, due to:

- Particular precautions during transport
- Limited outdoor stacking times, which may require re-coating
- Coating of the welding joints more expensive, both for the surface preparation and application
- Greater number of repairs and more accurate laying bed
- Need to re-coat the cold-bent pipes on site
- Operational costs of the structure and greater complexity of the CP system.

Obviously, these are not exempt from the risk of damage during the construction of the line but, in addition to the good resistance, which allows the limitation of the damage without its propagation, these are also easily repairable.

1.2.2.3 Coatings based on liquid thermo-setting resins

These coatings are normally used for those parts that cannot be coated with other coatings in factory or in other plants (T-pieces, special pieces, insulating joints, bends, valves, and fittings). Those are also used on site to coat the underground parts of line systems and points emerging from the ground. These coatings are normally two-component, epoxy-based, solvent-free resins, applied by brush or airless spray in thicknesses higher than 1.5 mm, class C [30] [32].

The characteristics of these products are substantially good, because they achieve a compromise between an electrical insulation, comparable to that of bitumen coatings, and a satisfactory mechanical strength with a relative ease of application and repair, resistance to operating temperatures up to 80÷90 °C (353÷363 K), resistance to abrasion and penetration, and excellent adhesion to steel. Some problems arise for applications in particularly harsh environmental conditions, temperatures below 7÷8 °C (281÷282 K), in which case it is necessary to pre-heat the separate components, or to provide appropriate protections. There is also the concrete risk, when it is necessary to apply more layers to reach the required thickness, to cause delamination of the various layers if the periods of over-application are not respected.

1.2.3 Products for the coating of welding joints

With an increasing quality in the application of coatings in factory, the weak points of the pipeline coating are those performed on site on the welding joints and repairs. The research of materials and application technologies tend towards a type of coating very similar to that applied in factory, or with very close performances. Unfortunately, the environmental conditions on site do not allow to obtain those results that are standard in factory; therefore, it is fundamental the scrupulousness of qualified personnel in carrying out and controlling all the coating operations, accurately following the application instructions and specifications. In fact, a neglected execution of the operations and the non-respect of the fundamental parameters (surface cleaning, pre-heating temperature, etc.), or even the use of materials not suitable for the present operation conditions, can lead to serious problems, such as lack of adhesion, coating disbonding and consequent infiltration of water.

In order to overcome these drawbacks, it is therefore necessary to carefully analyze the previously listed conditions and choose the most reliable coatings from the point of view of application and performance.

1.2.3.1 Self-adhesive polyolefin tapes

These coatings [31] constitute a variant to what was previously said. In this case, the polyolefin is produced in the form of a tape, with one or both sides adhesiveized with a special adhesive, formulated to adhere to a layer of primer applied to the steel in advance. The application can be done in factory or manually on site; however, for the problems of mechanical fragility, low resistance to solar radiation and heat, it is better not to carry out the application in factory.

The typical use of cold-applied tapes is that on the welding joints of small and medium diameter pipes, and in any repair of degraded or damaged coating sections. In these areas, the small dimensions of the so-coated sections do not offer a large friction surface to the ground and, consequently, the typical defects of the tapes do not occur: wrinkles of variable length, often full of moisture, in which the presence of disbonded tape, even if intact, does not allow the protection current to reach the steel. These conditions are the most suitable for the development of localized and concentrated corrosive phenomena. Moreover, the cold-applied tapes do not offer great resistance to cathodic disbonding, adherence to steel and resistance to the tangential stresses applied by the soil both during laying and operation phases, and these products also require care during application.

1.2.3.2 Non-crystalline polymer tapes

These tapes [31] have been recently qualified, and are characterized by a polymer mass that remains permanently soft, by ensuring anti-corrosive protection; the mechanical protection is then provided by an external PVC tape. The most interesting feature is that of maintaining its properties and, above all, the ability to adhere to the metal even at temperatures below zero. It represents a rehabilitation coating for short pipe sections, with the possibility of winter applications (absence of surface condensation on exposed and operating pipes).

1.2.3.3 Thermo-shrinkable sleeves

These products [31] are normally used for the coating of welding joints, to coat insulating joints on site and to seal the cavity between the protection steel sleeve and the pipe, and frequently used also for repairs, especially on polyethylene-based coatings or for connecting different types of coatings.

Those coatings consist of a polyethylene support with a side adhesiveized with a suitable butyl, crystalline or semi-crystalline (elastomeric), mastic. When heated, the polyethylene support is activated and starts to shrink, forcing the melted mastic to flow on the steel surface and to cover it uniformly (forming the anti-corrosive protection layer).

The most common types of these products have a resistance up to an operating temperature of 50 °C (323 K), a variable resistance to cathodic disbonding, a relative ease of application and a great compatibility with the most used coatings. Thermo-shrinkable sleeves can be applied on special primers, normally epoxy-based, in order to increase the resistance to mechanical stresses, temperature, tangential stress and corrosion. Other types of heat shrinkable products, suitable for high operating temperatures (up to 120 °C, or 393 K) are available, but they involve more complex installation operations.

1.2.4 Coating rehabilitation on operating pipelines

In recent years, in Italy the interventions to restore the PP of pipelines have multiplied, as a consequence of the natural ageing process of coatings. The frequency and extent of such interventions on some pipelines are becoming so important that they must be faced with specific solutions, including both materials and application technologies, more efficient than those adopted so far.

The conditions of the subsoil and the equipment operating in this environment are now so relevant that any CP strengthening intervention is not always feasible. The most practical solution is therefore the rehabilitation of PP, together with an accurate use of inner inspection techniques and surface surveys, which also allow the intervention only where the magnitude of the detected flaw requires an effective restoration intervention. After the identification of the need, an efficient rehabilitation system must essentially allow two things: reduced excavation opening periods and long-term effectiveness of the new protection applied on site.

The loss of effectiveness of a coating, along with the operating temperature, is normally due to:

- Compatibility with CP
- Easiness to curtain-effect in the welding area
- Resistance to impact and abrasion
- Stresses applied by soil settlement and landslides
- Susceptibility to oxidation and bio-degradation
- Poor surface preparation of the steel and poor quality in the coating application, whether it is realized in factory or on site. The most common cases are connected to localized interventions, with a maximum length of a few hundred meters due to the territorial limits, the need for permits and the long periods required.

Therefore, a coating rehabilitation intervention should be usually performed taking into consideration the following points:

- Identification of the critical pipeline sections with regard to the coating: wrinkles, disbonding, tears, presence of corrosion beneath the same, etc.
- Definition of the sections to be subjected to rehabilitation (maximum length that can be exposed, free spans, sections to be treated, etc.) and the consequent duration of the operations
- Manual removal of the coating and subsequent preparation by sandblasting which, nowadays, are still the most practical and economical methods in short-segment reconditioning projects (on longer pipeline segments, automated surface preparation by means of high-pressure water-jetting equipment is to be preferred, thanks to the reduction of labor and abrasives costs per square meter, which result in higher production rates [33])
- Application of the new coating: epoxy-based thermo-setting resins by brush; polyurethane thermo-setting resins, in case a higher reticulation speed is required for logistics reasons; cold-

applied or non-crystalline polymer tapes, applied by hand in the sections subject to particular time constraints, such as for the excavation backfilling or low winter temperatures
- Application methodology of thermo-setting products, according to the time required for the excavation backfilling (mono- or two-component hot airless equipment)
- During excavation opening and reduction of the gas flow, by waiting for the reticulation of the new layer to the sufficient grade before the backfilling.

Thus, this system results:
- Extremely slow, due to the manual application and the long reticulation periods of the present resins (from 7 to 15 days)
- Subject to environmental conditions
- Time consuming, as it requires prolonged stops or reductions in the gas flow to avoid significant condensation during the reticulation time
- Technically effective only if the minimum reticulation times of the applied resin are respected.

Moreover, because of the lack of preparation of some maintenance companies to operate on coatings with specific equipment, some cases of rapid degradation of the rehabilitation coating have been reported, due to serious application shortcomings, which have required further interventions after only 2÷3 years from application. Any coating rehabilitation cannot be separated from the quality of the application, which is directly correlated with the preparation level of the executing company.

1.2.5 Qualification tests of the coatings on site

During coatings application, accurate qualification tests must be carried out by suitably qualified personnel in all the various phases in which the production itself is organized. Only a continuous presence and a careful observation of the different operations allow the detection of any non-conformity, for example of superficial cleaning, pipeline heating or processing of the product to be applied. Only regular checks can reasonably ensure that the coating does not present any hidden or non-systematic defect, which the final qualification tests are often unable to detect.

About the qualification tests on site, these must be accurately carried out on:
- Level of surface preparation for application (degree of surface finish, cleanliness and roughness)
- Process parameters (application temperature, time, speed, etc.), along with a particular attention to the environmental conditions (low or high room temperature and relative humidity)
- Coating products before use (state of conservation, technical indications of the producer, etc.)
- Coating application process and on the finished coating, by means of specific tests (adherence, thickness, integrity, insulation continuity, etc.)
- Ability of the operators and quality of all the equipment.

In particular, cleaning must be carried out by means of sandblasting with selected abrasives, with controlled particle sizes, not containing salts or other pollutants that may cause damage to metal structures over time. The minimum finish grade required is Sa 2 ½, according to ISO 8501-1:2007 [34] standard, and the level of surface roughness (normally indicated with the Rz scale) must allow an excellent anchorage of the coating to clean steel. The abrasive projection system can also be used to remove pre-existing non-compliant coatings.

The cleaning of the surfaces to be coated by mechanical brushing, with the finish grade St 3 [34], must be reduced only to the areas where it is impossible to intervene with sandblasting. In any case, the coating must be applied only on dry surfaces, free from dust.

The aim of these qualification tests is to avoid a series of problems occurring on coatings, such as:

- Insufficient surface preparation, which also includes problems due to environmental conditions
- Incorrect preparation of materials and application parameters
- Lack of effective controls.

The main tests in which the qualification procedure of a coating is divided, both in the factory and on site, are as follows:

- Thickness measurement, both wet and dry, according to a sampling plan, using special serrated calipers for the wet conditions, and magnetic or electromagnetic thickness gauges for the dry one
- Adhesion test, which is carried out with different procedures, depending on the type of coating involved. On coatings based on bitumen, a qualitative test is carried out, which consists in removing a coating strip and observing its behavior during disbonding, and also its surfaces. Adhesion is considered acceptable when there is no clear separation between the adhesion layer and the steel with which it is in contact. A fracture must be observed in the coating thickness, which is an index of cohesion of the same. For bitumen, the test is reliable in a temperature range between 10 (283) and 35 °C (308 K); below this limit the product becomes brittle while, beyond, it starts to soften, causing in both cases an unreliability of the results. On coatings based on cold-applied tapes, polyolefins or thermo-shrinkable sleeves, a quantitative determination of the stress necessary to disbond a coating strip from the substrate is performed. The test is carried out, after a period established by the application, using spring dynamometers or pressure transducers connected to displays or recorders. Also for these products, the direct observation of the type of disbonding from the pipe or the behavior of the adhesion layer is very important: a cohesive disbonding (with separation in the layer thickness) is generally a sign of good adhesion. In all cases, the complete coating of the steel must be produced by an anti-corrosive protection (primer or adhesion layer or mastic). On the coatings based on thermo-setting resins, the test is carried out by making a 45° V incision with a blade and trying to undermine the coating from the vertex. Adhesion is acceptable if the coating does not disbond from the pipe in large flakes (more than

2÷4 mm) or it does not rise up. As the adhesion test is a destructive test, it must be performed on samples, and the test areas must be immediately repaired

- Insulation continuity test, which must be performed on 100% of the coated surfaces, both during the qualification test in factory and on site (the test must also be performed immediately before the laying or operation of the pipeline). It is carried out with special devices called Holiday Detector or Flaw-Detector Device, which produce high voltage electric impulses or a high direct current voltage (generally in the range from 2.5 to 30 kV). For the use of such devices, the battery status is very important, and the test voltage must be correctly set, in order to adapt the instrument to the coating to be tested. Badly made settings and calibrations can lead to disputes with the supplier or, worse, to the non-detection of eventual defects. In order to correctly interpret the test results, it is important to consider that a defect may not be detected if the battery is low, or anomalous resistors are inserted in the test circuit. Moreover, the defect, to be considered such, must be visible, or the electric arc caused by the short-circuit must be visible; the appearance of superficial discharges is not a sign of flaws. For products made of materials with high electrical insulation characteristics, such as polyolefins and thermo-setting resins, a predefined test voltage can be set; therefore, the value depends only on the coating total thickness. The test voltages must therefore be set starting from the following values: for bitumen, 10 kV for thicknesses ≥ 3.5 mm (about 3 kV/mm); for extruded polyethylene, 25 kV for thicknesses ≥ 1.5 mm; for self-adhesive tapes and thermo-shrinkable sleeves, 20 kV for all the cycle thicknesses; for thermo-setting resins, 15 kV (about 5 kV/mm). The set test voltage must be checked several times during the day, with simulated defects, in order to control the efficiency of the equipment
- Verification of the composition, generally required for bitumen-based coatings, cold-applied tapes and thermo-shrinkable sleeves, is performed on the same specimens disbonded during the adhesion test. It consists in examining the complete thickness of the coating, in order to determine its composition layer by layer and their correct deposition on the pipe. During the test, the steel surface is also observed to detect any defects in cleaning or pollution of the surface
- Verification of the compactness, on bitumen-based coatings, is performed by lightly tapping the coating with a wooden stick and detecting the sound: a full sound is a sign of compact coating and without voids or disbonding from the pipe, while a soft and empty sound indicates the presence of defects, such as air inclusions between bitumen and steel, or between the different components of the coating. This is a quick and easy qualification test, to be carried out especially at the pipe extremities. It provides good results even when applied to thermo-shrinkable sleeves, in correspondence with the welding joints.

2

HYDROGEN EMBRITTLEMENT MECHANISMS

2.1 Environmentally Assisted Cracking

As well known, the term Environmentally Assisted Cracking (EAC) refers to all those forms of corrosion that necessarily involve the synergistic and concomitant action of a mechanical stress, applied to a susceptible material, and a promoter environment, which in the absence of stresses can be mildly aggressive or entirely not aggressive *(Figure 2.1)*.

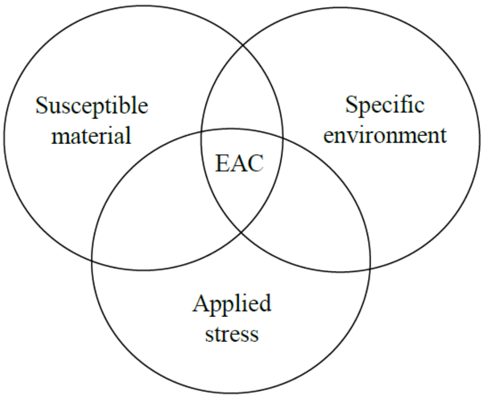

Figure 2.1. Schematic representation of EAC phenomena

The effect of these phenomena is the formation of cracks with a brittle morphology, which propagate under the combined action of stress and environment, and which can lead to the unexpected failure of the loaded element, due to stresses lower than the maximum strength of the metal in air.

The stress component able to determine the onset of Stress Corrosion Cracking (SCC) phenomena, deriving from both external loads and internal stresses, is always the tensile one. Cracks propagation is characterized by brittle morphology (intergranular, transgranular or mixed morphology), in a direction perpendicular to the tensile stress; it is not unusual to observe a ramification of the crack.

In particular, the mechanism of EAC manifests itself in two phases: triggering and crack propagation. Usually, the triggering phase is preceded by an incubation period, during which the formation of micrometric or even nanometric “crack embryos” occurs, i.e. very small defects or imperfections in correspondence of emerging inclusions, grain boundaries and interfaces between different phases. These defects are generally characterized by a similar probability of re-passivating, or continuing to propagate and turn into real cracks. The incubation period depends on the specific environment-metal coupling and the propagation mechanism.

The crack propagation phase can be stable or unstable. In the case of stable propagation, the crack advances by concomitant action of environment and applied stress, stopping if one of the two factors is lost and restarting the propagation if favorable conditions to the advancement are restored.

The propagation rate, if compared to the one with which a purely mechanical crack usually propagates, is significantly lower, with values that can vary between few mm/h and 10^{-6} mm/year, and sometimes even out of this range. By applying a constant load, the sub-critical crack propagation leads to the achievement of the critical size relative to the material tenacity, beyond which the unstable propagation occurs, due to a purely mechanical failure.

It is possible that this phase does not intervene if the crack propagation determines the discharge of the stress (for example in the presence of internal stresses or imposed deformations); in this specific case, the crack is stopped below a stress threshold. Moreover, the crack propagation can also be stopped even at areas of the material characterized by a different microstructure, such as in the case of cracks arisen in the welding area, when the propagation front exceeds the Heat Affected Zone (HAZ) to enter the base material, which is much more resistant to the EAC phenomena.

In order to explain the synergistic action between environment and stress condition at the base of stress corrosion (and, more generally, of EAC phenomena), several mechanisms are hypothesized, and this topic is still the subject of a heated debate. It is likely that more mechanisms can contribute, composing differently between one environment and another, and between one material and another. From a general point of view, two fundamental categories can be involved to represent the proposed mechanisms, one linked to the anodic process and the other one to the cathodic process.

The first category can be schematized with the sliding/dissolution process. In this case, the crack propagates by anodic dissolution, made possible by the continuous mechanical cracking of the passive film at the crack tip, due to the intense and continuous plastic deformation. The rest of the metal surface, including the crack walls, remains in passivity conditions and, as such, it constitutes the area for the cathodic process that supports dissolution.

The second category also foresees the presence of an anodic area at the crack tip and an adjacent cathodic area, but the propagation is directly linked to the cathodic process and, in particular, to the hydrogen development process. In this case, the propagation of the crack takes place due to the embrittlement of the material in the area with a high plastic deformation, placed before the crack tip, following the absorption of hydrogen from the cathodic areas adjacent to the tip.

As already said, the preferential mechanism of crack propagation due to EAC in steels used in marine environment under Cathodic Protection (CP) is that related to Hydrogen Embrittlement (HE), which is connected to the diffusion of atomic hydrogen inside the metallic material.

2.2 Mechanisms of hydrogen evolution

Hydrogen is the most common element in the universe and, in its electrically neutral atom state constituted by a single proton and electron, is also the smallest and the lightest. In fact, with an atomic radius of just 0.53 Å, it is much smaller if compared to the diameter of other metallic atoms, so it is readily soluble in the matrix. These features allow hydrogen diffusion through the lattice of metals and their alloys, along with the occupation of the interstitial sites inside the material.

Thanks to many studies, this phenomenon seems to be both beneficial for technologies involving hydrogen storage [35] and almost catastrophic for applications related to Oil&Gas industry, such as pipelines [36]. The latter is often connected to the degradation of metals determined by hydrogen, which can cause various severe problems. In fact, hydrogen is already made available from different treatments during production, processing, and service of metallic materials, such as, for example:

- Acid cleaning, also known as pickling
- Contact with water and other liquids or gases which contain hydrogen
- Electroplating, phosphating, and welding
- Refining, which leads to the formation of precipitates in the solidification phase, due to supersaturated concentrations
- Recombination poisons, such as hydrogen sulfide (H_2S). The effect of H_2S is not only that of increasing the concentration of available hydrogen ions for the cathodic reaction, but this recombination poison is able to increase the concentration of adsorbed hydrogen [37]. Therefore, an increase in hydrogen flux during the permeation process through the metal is observed, both to the corrosion potential (E_{corr}) and to cathodic polarizations [38].

It is also possible that hydrogen enters a metal during service conditions, in particular circumstances which can cause hydrogen development, including cathodic over-protection and any form of corrosion involving hydrogen evolution as the cathodic process, such as galvanic corrosion. The kinetics of hydrogen development differs from gaseous media to aqueous media [39].

As reported by De Luccia [40], in 1864 Cailletet was the first to state that, when an iron specimen is immersed in dilute sulfuric acid, a small part of the hydrogen released in the reaction is adsorbed on the surface and then absorbed into the metal [41]. Later in 1922, Bodenstein [42] found that the amount of “nascent” hydrogen (atomic hydrogen) absorbed into the metal could be modified with the application of a cathodic current. More recently, Crolet [43] affirmed that, since dissolved hydrogen is necessarily dissociated into a proton and a conduction electron, cathodic charging becomes a direct proton transfer, with the result that the proton (H^+) is transferred from the aqueous solution (H^+_{water}) to the metal (H^+_{metal}), adsorbed on the surface and then absorbed into the crystal lattice.

Therefore, as shown in *Figure 2.2* for aqueous solutions, two reduction reactions can generate adsorbed hydrogen on the metal surface, in dependence of the pH of the environment, which can be alkaline *(eq. 3)* or acidic *(eq. 4)*:

(In alkaline solutions) $H_2O + e^- \rightarrow H_{ads} + OH^-$ *(eq. 3)*

(In acidic solutions) $H_3O^+ + e^- \rightarrow H_{ads} + H_2O$ *(eq. 4)*

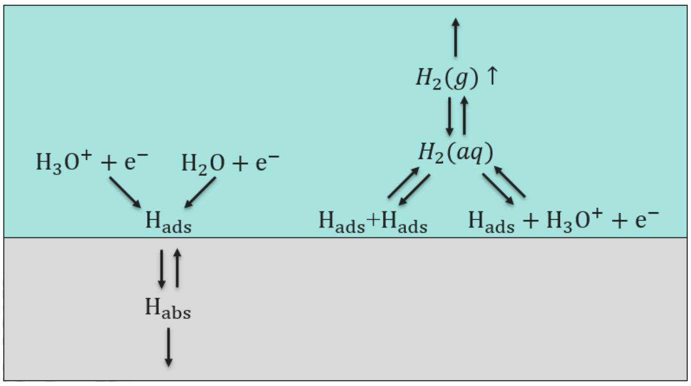

Figure 2.2. Reduction reactions for aqueous solutions that can determine hydrogen evolution

In acidic environments, corrosion takes place through an anodic dissolution reaction *(eq. 5)* of steel:

$$Fe \rightarrow Fe^{2+} + 2e^- \qquad \text{(eq. 5)}$$

This is supported by the cathodic process of hydrogen development for hydrogen ions reduction, according to the mechanism described by the following parallel reactions, namely the chemical recombination *(eq. 6)* of adsorbed hydrogen atoms (Tafel reaction) and the electrochemical recombination *(eq. 7)*, involving both the adsorbed hydrogen and the proton (Heyrovsky reaction).

$$H_{ads} + H_{ads} \rightarrow H_2 \qquad \text{(eq. 6)}$$

$$H_{ads} + H_3O^+ + e^- \rightarrow H_2 + H_2O \qquad \text{(eq. 7)}$$

Part of the hydrogen *(eq. 8)* adsorbed on the metal surface (H_{ads}) diffuses through the lattice (H_{abs}):

$$H_{ads} \rightarrow H_{abs} \qquad \text{(eq. 8)}$$

Absorbed hydrogen tends to concentrate in the areas of maximum tensile stress; once the critical concentration at the defect tip is reached, if the steel is susceptible to HE, the brittle propagation of the same defect takes place.

Molecular hydrogen evolution occurs only if its partial pressure reaches the external pressure [44].

2.3 Hydrogen induced failure mechanisms

Hydrogen embrittlement (HE) is a deleterious phenomenon, which happens when a metallic material is exposed to hydrogen atoms. This undesirable mechanism is particularly important for high strength steels, and represents a persistent problem for different material design processes and industries, such as offshore, aircraft, nuclear, and hydrogen storage.

Johnson [45] [46] first documented HE phenomena in 1875, reporting a reduction in ductility and fracture strength caused by hydrogen action. Since then, numerous theories have been formulated, although none of them is able to explain the phenomenon in all its aspects [47] [48] [49].

In the absence of stresses, the two types of damage that can be observed are blistering, or Hydrogen Blistering (HB), and Hydrogen Induced Oriented Cracking (HIOC), also called Hydrogen Induced Cracking (HIC) or Step Wise Cracking (SWC). In both cases, the main cause of damaging is provided by manganese sulfide (MnS) inclusions, elongated in the direction of hot rolling of the steel, perpendicular to the flow direction [50] [51] [52] [53].

The interface between the inclusion and the crystal lattice acts as an irreversible trap for hydrogen. Its recombination, from atomic to molecular, causes an increase in the internal pressure, which induces a lattice distortion and a separation of the interface and the formation of the blistering [54] [55], as represented in *Figure 2.3*.

In the presence of internal/external stress fields, the type of damage called Stress Oriented Hydrogen Induced Cracking (SOHIC) causes the formation of small cracks along a direction perpendicular to the stress (external or internal). This mechanism involves the achievement of a critical concentration of atomic hydrogen in the areas with a maximum intensification of these tensile stresses, causing cracks nucleation and propagation [56] [57] [58].

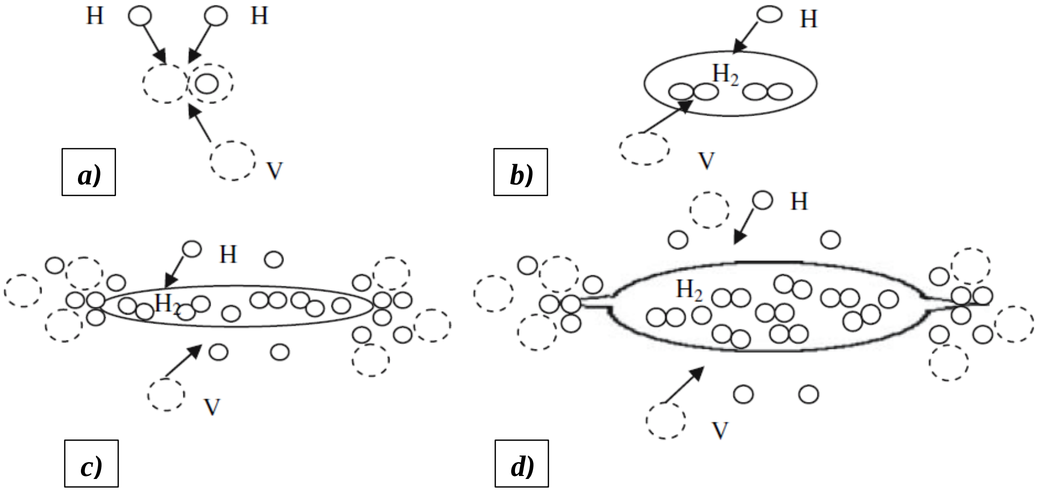

Figure 2.3. Illustration of hydrogen blister nucleation: a) Aggregation of superabundant vacancies and hydrogen atoms into a vacancy-hydrogen cluster; b) Transformation of hydrogen atoms in hydrogen molecules; c) Cluster growth through gathering vacancies; d) Crack initiation from the cavity wall due to the internal hydrogen pressure when the blister nucleus reaches a critical size, C_{cr} [55]

2.3.1 Hydrogen Induced Cracking

In 1986, during the first discussion on pipeline integrity and reliability organized by CANMET and

C-FER Atlantic, it was established that HIC represented the main cause of failure of underground cathodically protected pipelines in Canada, Italy, Russia, The Netherlands and the USA in the period 1987-2000 [59] [60] [61] [62] [63] [64] [65] [66] [67] [68]. According to Kim et al. [69], this kind of HE cracking manifests itself in the form of superficial blisters and/or internal cracks in the absence of an applied stress, and it is generated by a sulfide corrosion process occurring on the steel surface in the presence of H_2S in the solution.

In HIC, the internal tensions generated by hydrogen cause cracks propagation between two or more nearby inclusions that lie on different planes. The material around the cracks becomes highly strained, and this determines the connection of nearby cracks to form HIC; the cracks arrays linked to this type of damage have a peculiar stepped appearance. Although isolated small blisters or hydrogen induced cracks do not influence the load bearing capacity of a component, these represent a manifestation of a cracking problem, which can continue to develop *(Figure 2.4)* unless the corrosion mechanism is blocked [70].

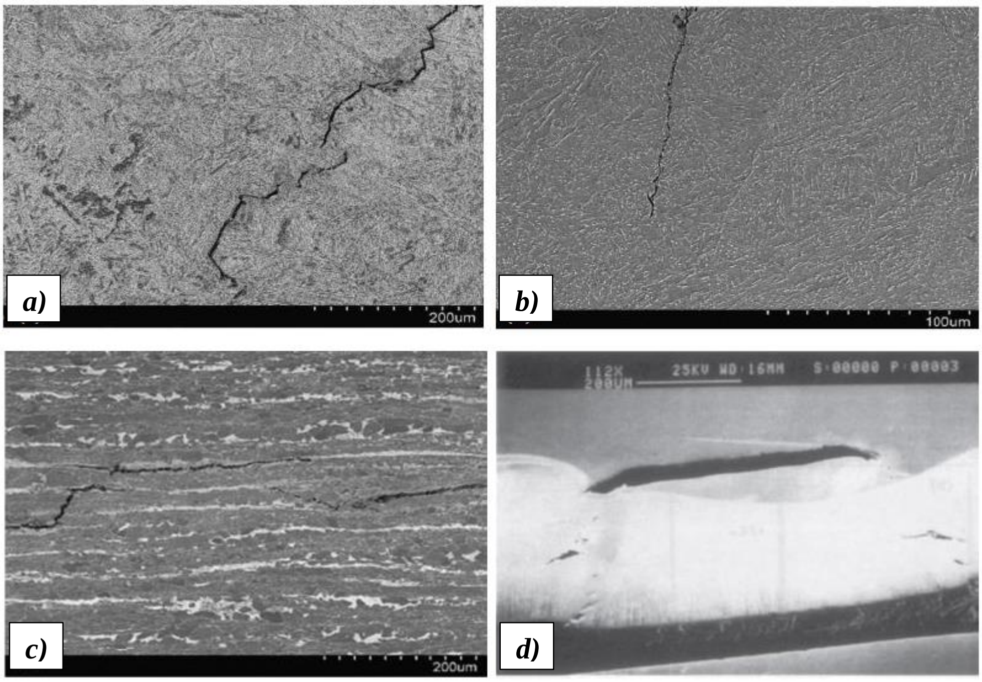

Figure 2.4. Internal cracking in the weld of an X70 grade steel, showing: a) Propagation with SOHIC mode; b) Morphology of SSC cracks; c) HIC cracks; d) Blistering [71]

The onset of this phenomenon is dependent not only on the steel microstructure, but also on its mechanical strength and on any residual internal stresses; its onset is favored by the presence of large MnS inclusions, oriented perpendicular to the hydrogen flow, by elongated oxides and by segregation bands containing perlite, bainite or martensite [72].

To limit HIC phenomena, materials with low inclusions content should be used, especially without MnS elongated inclusions. Thus, the production of steels to be used in sour environments must provide very low contents of sulfur and phosphorous, as well as particular treatments with calcium or rare earths to obtain spheroidal inclusions.

2.3.2 Stress Oriented Hydrogen Induced Cracking

Related to both HIC and SSC, Stress Oriented Hydrogen Induced Cracking (SOHIC) involves the formation of staggered small cracks along a direction approximately perpendicular to the stress (external or internal), resulting in a “ladder-like” crack array [73]. This particular cracking mechanism, observed in longitudinally welded pipelines, may be classified as SSC, and it is caused by a combination of applied stress and local strain around HIC sites *(Figure 2.5).*

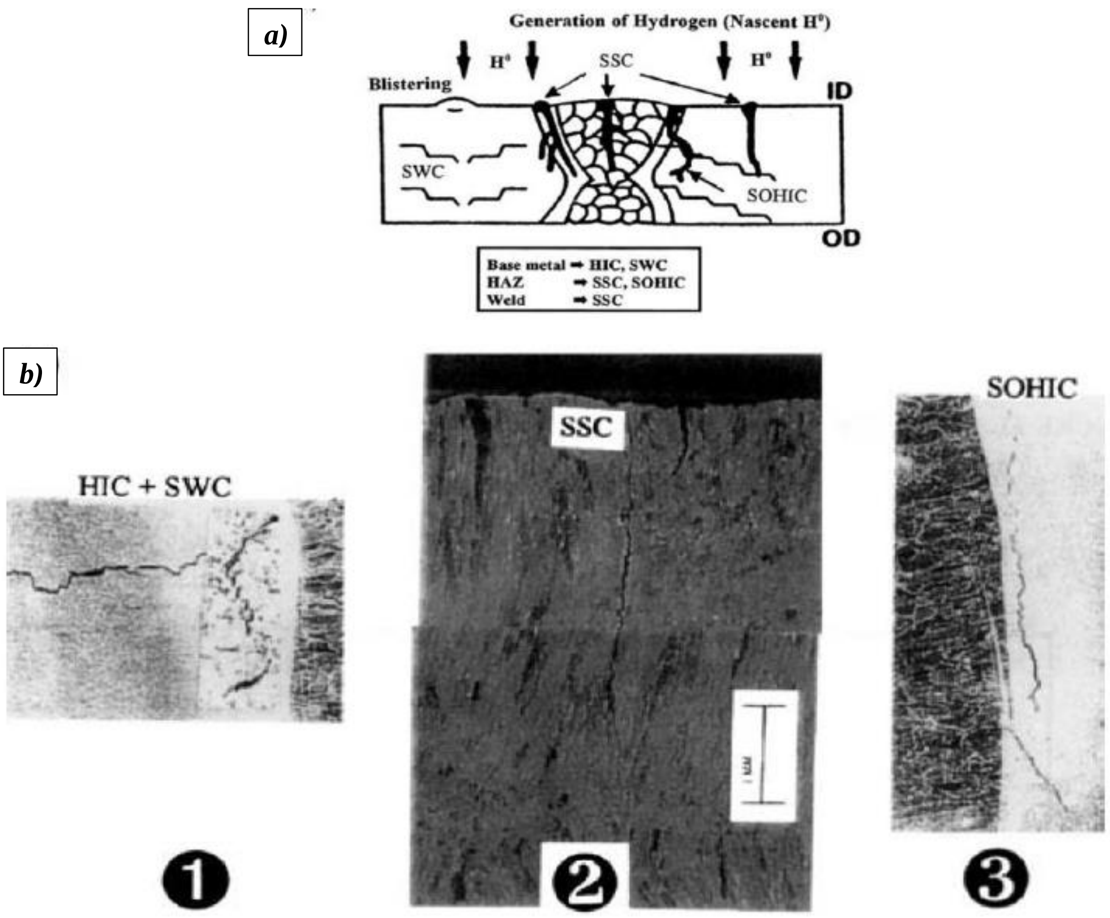

Figure 2.5. a) Types of hydrogen damage in H2S service; (b) Metallographic sections of welded pipes, showing: (1) SWC in the base material; (2) Apparent SSC in the weld zone; (3) SOHIC and SSC in the Heat Affected Zone (HAZ) [74]

In the case of rolled plate steels, presenting softened heat affected zones in correspondence of welds, a similar phenomenon occurs, called Soft Zone Cracking (SZC). The susceptibility of these areas to SZC seems to derive from a combination of micro-structural effects due to temperature cycling during welding procedure and local softening in the HAZ. The result consists in strains within a narrow zone, which can reach or even exceed the YS.

2.4 Theories for hydrogen assisted cracking mechanisms

2.4.1 Pressure theory

In relation to the pressure theory, probably the oldest proposed for the analysis of Hydrogen Assisted Cracking (HAC), hydrogen is charged within unloaded specimens. As a result, hydrogen precipitation and recombination in molecular hydrogen generates high internal pressures into the defects (flakes, micro-voids, and inclusions), even higher than 10^5 atm, causing blisters and internal cracking. In correspondence of inclusions, Louthan [75] estimated by means of a precise mathematical method that a pressure of even 10^6 atm could be reached. However, this theory does not explain the ruptures occurred in the presence of weak hydrogen activity; moreover, in the presence of a high fugacity, the crack should propagate until failure, that not always takes place. This theory is in contrast with the brittle behavior observed of the crack surface [76].

Zapffe and Sims [77] stated that the main fraction of absorbed hydrogen into iron consists of atomic hydrogen contained into these pre-existing defects. In the analysis of these authors, a relevant hydrogen super-saturation may derive by cathodic electrolysis and pickling, because of the production of significant concentrations of hydrogen on the steel surface, equal to or greater than those taking place at high temperatures in pure hydrogen. Once this super-saturation exceeds certain limits, hydrogen recombines into molecular form into these defects. Even at low temperatures, hydrogen high pressure exceeds the YS *(Figure 2.6)* and, consequently, breaks the lattice bonds.

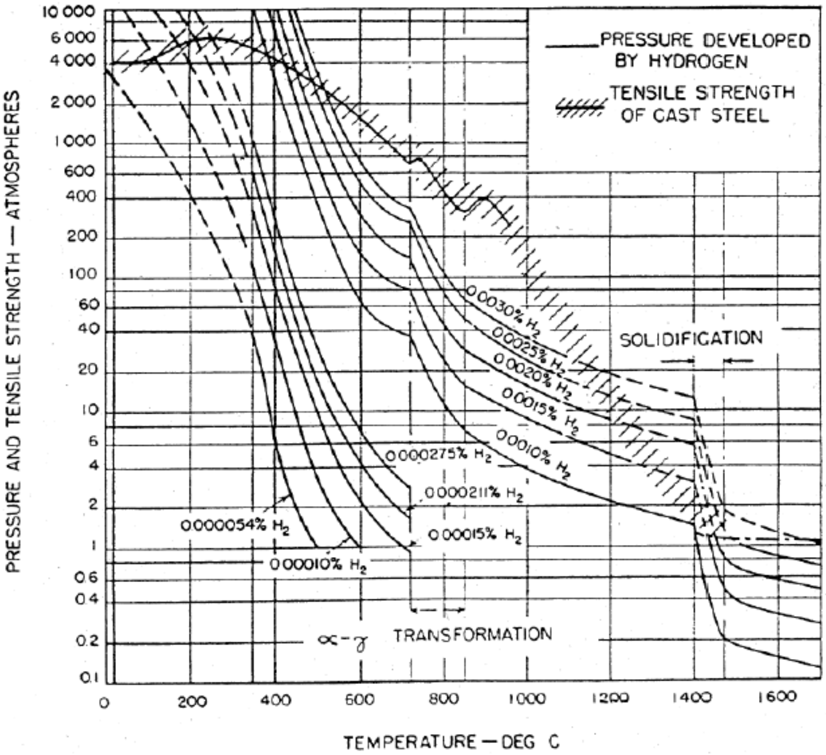

Figure 2.6. a) Temperature variation at equilibrium pressure for molecular hydrogen precipitated within the steel, as a function of hydrogen concentration [77]

Consequently, many authors adjusted this theory. For example, De Kazinczy [78] suggested that, as the crack propagates, hydrogen diffusing to pre-existing voids or cracks is necessary to maintain internal stresses.

2.4.2 Surface energy theory

With reference to the surface energy theory proposed by Pitch [79], adsorbed hydrogen on the metal surface causes a reduction in the surface energy, which is directly proportional to adsorbed hydrogen concentration. Once absorbed on the internal surfaces of cracks or micro-voids, hydrogen decreases the energy for creating new surfaces during crack propagation, lowering the energy needed for fracture initiation.

In relation to the model of brittle fracture of a perfectly elastic material developed by Griffith [80], this surface energy is directly proportional to the material maximum strength.

After an exhaustive investigation of crack growth in hydrogenated high strength steels, Troiano et al. [81] [82] [83] [84] [85] suggested that hydrogen diffused towards regions of high tri-axial stress, and then acted to reduce the theoretical cohesion or fracture strength of the material. With these concepts, a different set of experimental observations, such as the existence of reversible incubation periods for crack initiation, the variation of crack initiation site with notch sharpness, and the effect of post-hydrogenation plastic strain upon ductility, were brought together in a self-consistent framework.

However, Griffith's theory mainly presents two weak points. The energy required *(eq. 9)* to form new surfaces during crack propagation (γ) is represented by the sum of thermodynamic superficial energy (γ_S) and plasticization energy (γ_P):

$$\gamma = \gamma_S + \gamma_P \qquad \textit{(eq. 9)}$$

For a ductile material, the plasticization energy is much higher than the thermodynamic one and, since hydrogen adsorption leads to a reduction of the thermodynamic energy only, the surface energy γ is not significantly affected. Therefore, for these materials, the increase in the steel brittleness is not justified. Furthermore, embrittlement does not occur for gases with higher absorption energies compared to hydrogen, such as oxygen, nitrogen and water. According to this theory, these substances should favor the embrittlement mechanism, while actually it was demonstrated that this does not happen at all [76].

2.4.3 HEDE theory

The decohesion theory, or Hydrogen Enhanced DEcohesion (HEDE), also called Hydrogen Induced Decohesion (HID), is one of the earliest models proposed for HE. This theory was postulated in 1926 by Pfeil [86], who observed in both single-crystal and poly-crystalline iron pre-charged with hydrogen the occurrence of a brittle fracture surface.

This theory hypothesizes the accumulation of hydrogen in solid solution at the crack tip that lowers the cohesive interatomic bonding energy required to separate the lattice along a crystallographic plane *(Figure 2.7)*. This leads to a weakening and a reduction of the fracture toughness [81] [84] [85] [87], encouraging more cleavage-like failures [88]. Both the surface energy and decohesion theory mechanisms explain the fragile fracture observed in metals subject to HE.

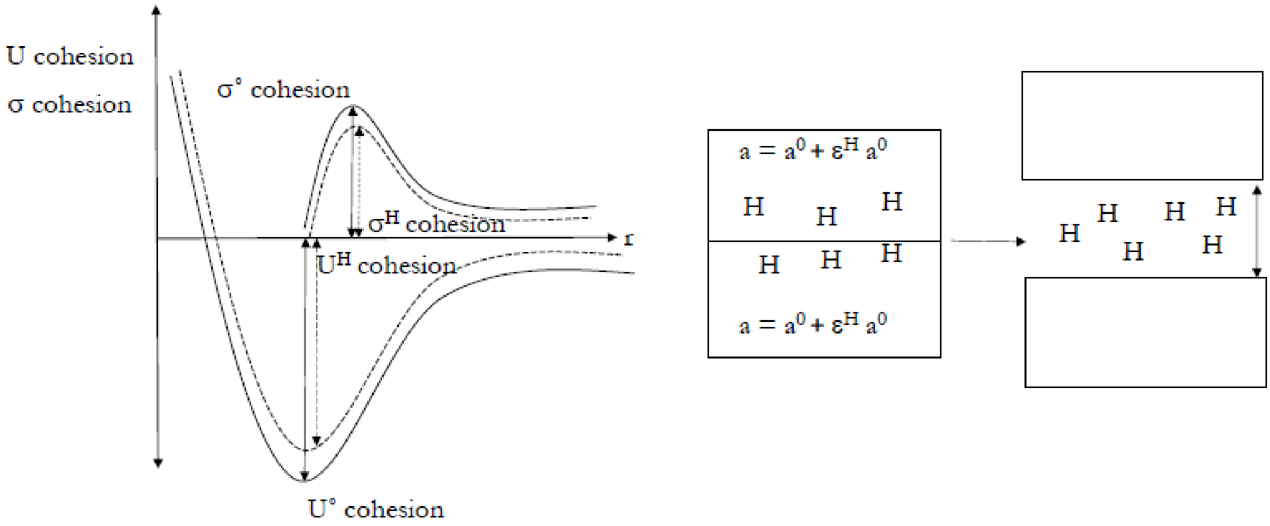

Figure 2.7. Hydrogen effect on cohesive energy (U) and stress (σ) of a metal, where: $U^{0}_{cohesion}$ *is the cohesive energy (energy required to separate the crystal along the crystallographic plane, to a separation larger than the critical distance, r, in the absence of hydrogen);* $U^{H}_{cohesion}$ *is the cohesive energy in the presence of hydrogen in solid solution;* $\sigma^{0}_{cohesion}$ *is the cohesive stress (stress to disrupt the atomic bonds) in the absence of hydrogen;* $\sigma^{H}_{cohesion}$ *is the cohesive stress in the presence of hydrogen in solid solution; a is the lattice parameter;* ε^{H} *is the strain induced by hydrogen in solid solution [85] [89] [90] [91]*

The HEDE mechanisms were then studied by Troiano [85] and Gerberich et al. [92], in order to try to explain the significant increase in the crack tip opening angle, which represents a consequence of reduced cleavage toughness with increasing hydrogen content. Moreover, Oriani [93] stated that, as a result of the elastic-hydrostatic stress field, hydrogen exceeds the solubility limit within the lattice due to its dimensional dilatation. Further studies identified trapping sites as a preferential location for the segregation of hydrogen atoms, such as grain boundaries, locally decreasing the cohesive strength between metal atoms. According to Oudriss et al. [94], the grain boundaries seem to act as irreversible trapping sites for hydrogen atoms; in fact, these researches observed a slowdown of hydrogen diffusion probably due to the increase in the density of hydrogen traps.

In particular, when a metal is pre-strained, the density of dislocations increases, therefore the Ultimate Tensile Strength (UTS) also increases. In particular, it has been found that high pre-strain leads to HEDE being dominant, decreasing the UTS value in the presence of hydrogen, which in high concentrations can be linked to a resistance reduction to HE [95].

However, the aim of this theory is to analyze crack propagation in the presence of hydrogen, which can occur if the local maximum tensile component of the stress, normal to the crack plane and beyond the crack tip, results equal to the maximum resisting stress of the metal. The concentration of stresses at the crack tip favors higher hydrogen accumulation in this area. HEDE theory affirms that HE phenomena occur within the crack tip fracture process area in which the tensile stresses exceed the maximum local atomic cohesive strength, which is reduced in the presence of hydrogen.

Therefore, this theory is applicable to fractures with a brittle morphology, in which hydrogen accumulates at the interface with the solution or in correspondence with grain boundaries and reaches high critical concentrations, sufficient to cause brittle fracture. On the contrary, it is not applicable to fractures accompanied by plasticity. Even if HEDE theory is still unproven by direct experimental techniques, it has been used to justify brittle intergranular fracture surfaces observed in high strength steels.

2.4.4 Dislocation blockage

Considering hydrogen effect on the occurrence of brittle fracture, two contradictory theories are reported, based respectively on a hardening and a softening effect.

Regarding the hardening effect, or Dislocation Blockage, Stroh [96] stated that hydrogen interacts with the field of high tensile stresses around the dislocation to form a Cottrell-atmosphere [97], which can strongly reduce dislocation mobility and make the deformation at the crack tip more difficult. Consequently, more dragging forces are necessary for dislocations movement.

This theory is supported by Louthan et al. [98], who affirmed that hydrogen association and movement with dislocations can be degradative for the properties of the material. This would be due to the interaction between hydrogen and dislocations, which stabilizes micro-cracks and determines a hardening effect. However, this theory is contradicted by Beachem [47], who stated that hydrogen enhances the movement of dislocations, facilitating the plasticity of material (softening effect).

2.4.5 HELP theory

The effect of hydrogen on the ductile fracture is explained by the Hydrogen Enhanced Localized Plasticity (HELP) theory [99], which is based on direct observations [100] of small dimples in correspondence of fracture surfaces, normally present in ductile fractures because of the coalescence of micro-voids. According to this theory, local plasticity is due to the stress distribution, which leads to a higher hydrogen concentration at the crack tip rather than the walls. Hydrogen is redistributed around dislocations and seems to decrease the barriers to dislocations motion and, thus, to favor their mobility (*Figure 2.8*, tests performed on α-Ti), reducing their elastic interaction energy [99] [101].

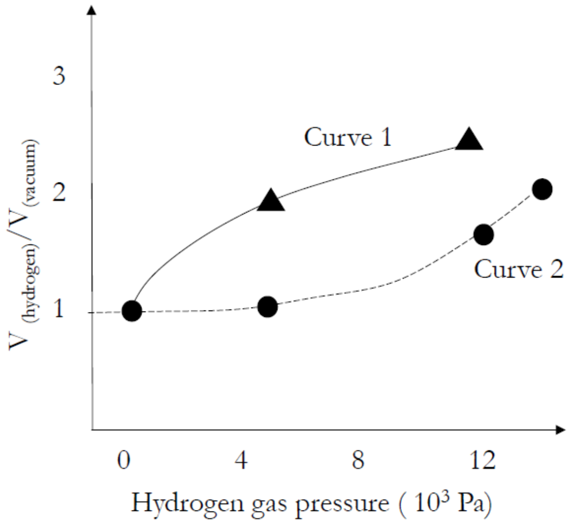

Figure 2.8. Hydrogen effect on dislocations velocity, which increases if hydrogen pressure increases. The ratio between the dislocation velocity in hydrogen and in vacuum is here reported, highlighting the effect of introducing hydrogen for the first time (Curve 1) and re-introducing it after its removal (Curve 2) [47]

The strain distribution generated in the lattice takes place in the presence of stress conditions significantly lower than those occurring in the absence of hydrogen.

However, this energy reduction promotes planar slip and increases pile-up phenomena, which can determine damage initiation. Consequently, the shear stress needed to activate dislocations movement decreases and the material softens [102]. Therefore, the presence of hydrogen increases the amount of deformation that occurs in a localized region adjacent to the fracture surface [103] [104] [105] [106] [107].

The reasons why the presence of hydrogen would favor dislocations mobility and facilitate slip have not been identified yet with certainty, and are still the subject of research. It was only proved the existence of interactions between hydrogen atoms and dislocations. The experimental tests carried out by Cottrell [108] on pure iron induced to hypothesize that hydrogen atoms present in the metal lattice are subject to the action due to a local electronic density near the lattice sites occupied by iron atoms. The interaction would cause a migration of hydrogen atoms towards grain boundaries, dislocations and vacancies, characterized by a lower electronic density.

2.4.6 HESIV theory

According to the Hydrogen-Enhanced Strain-Induced Vacancy (HESIV) formation theory, in the presence of plastic deformation, hydrogen increases the creation and agglomeration of vacancies, facilitating the formation and coalescence of micro-voids during the fracture process [109], which may combine to form larger voids that lead to a decrease in the ductile crack growth strength. This phenomenon can be observed during tensile tests and fracture toughness tests on hydrogen pre-charged specimens [110]. HESIV formation theory was firstly postulated by Nagumo [109], who clarified hydrogen influence on the stress-deformation relationship and fatigue life of a Ni-based Alloy 625 and pure iron, which were pre-charged with hydrogen *(Figure 2.9)*. The result was that, after the same fatigue cycles as the uncharged specimens, hydrogen-charged specimens were characterized by a higher void density (as predicted by the HESIV formation theory).

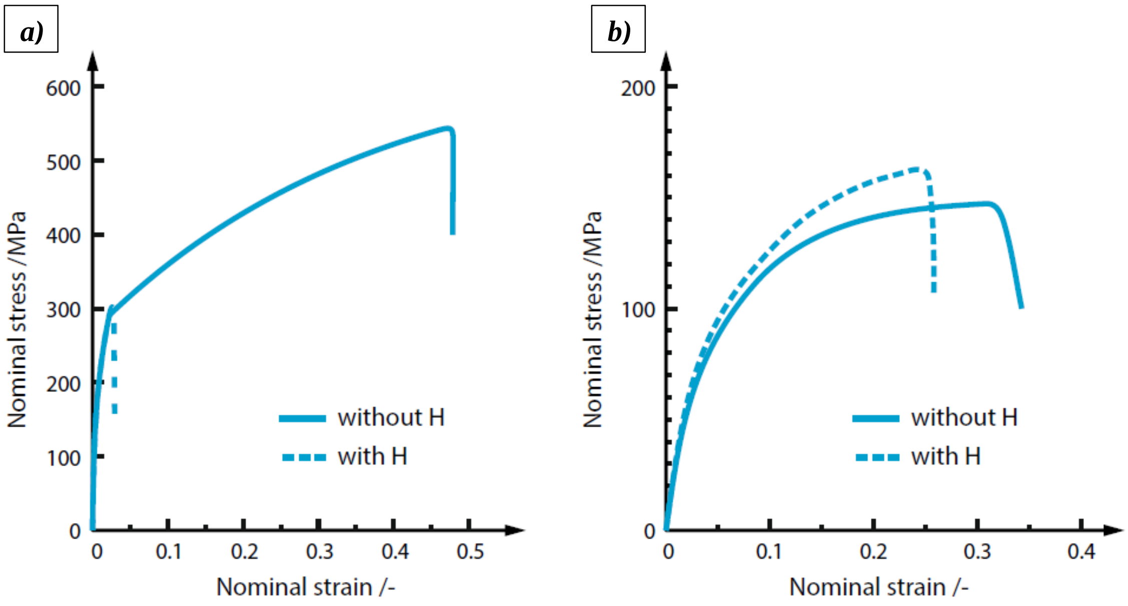

Figure 2.9. Stress-deformation data from tensile testing of hydrogen-charged and uncharged specimens of: a) Ni-based alloy 625; b) Pure iron. Adaptation from the literature [109]

According to Srinivasan et al. [57], the different theories (HELP, HEDE and HESIV) can coexist; in fact, they proposed a combination mechanism of HELP, HESIV, and nano-void coalescence to explain the fracture path-ways of both X65 and X80 grade steels, which failed by quasi-brittle fracture. The transition between one mechanism and another, which changes the fracture mode from ductile to an almost fragile one, occurs at the increase in the YS and/or the tri-axial stress condition.

2.4.7 Surface mobility theory

This theory brings together theories based on the sliding-dissolution mechanism, characteristic of SCC, and others typical of HE. The model involves a migration of metal atoms from the crack tip, with a higher concentration of stresses, towards the walls, where the stress field is less intense. This migration induces a vacancy in the crystal lattice at the crack tip, causing the propagation of the crack of an atomic dimension. This mechanism is determined by the ease of sliding of the metal atoms on the crack walls, dependent on the type of environment and reactions occurring on the metal surface; the greater the potential, the greater the speed at which vacancies form at the crack tip [111]. Hydrogen facilitates the removal of the surface oxide film that hinders the mobility of metal atoms, and thus interacts with vacancies, which constitute hydrogen traps.

2.4.8 Defactants theory

Moreover, recent studies found a new theory called Defactants Concept, which well describes HE as a decrease in the defect formation energy. On the basis of an experimental approach, the results may be interpreted as both HELP and HEDE.

The name for this new concept, exhaustively summarized by Haga [112] in her Master thesis, derives from DEFect ACTing AgeNTS (Defactants), which covers the action of atoms segregating near defects in solids and reducing their creation energy, similarly to the way by which surfactants reduce surface energy in liquids. In the case of HE, these defactants are represented by solute hydrogen into the metal lattice. Every material is characterized by an activation energy of Homogeneous Dislocation Nucleation (HDN), related to the specific parameters of the material, such as the shear modulus (μ), the dislocation core-radius (ρ), the Stacking Fault Energy (SFE, or γ). Some experiments discovered that hydrogen, through the effect of the above-mentioned parameters, reduced the activation energy for HDN. In particular, a local reduction in μ was noted consequently to the enrichment with hydrogen of a small volume of the strained metal lattice.

This was sufficient to reduce the activation energy for dislocations nucleation. Hydrogen can influence interatomic binding forces and dislocation line energy in the dislocation core, as well as SFE in the case of partial dislocations in crystalline fcc-structure. Therefore, HE mechanism is controlled by a reduction in defect deformation and interatomic bonding energy.

2.4.9 Hydrides formation

In fcc-alloys, such as austenitic stainless steels, a large hydrogen super-saturation can create relevant structural modifications in the specimen surface layer; this is the so-called Hydrogen-Induced Phase Transformation (HIPT). One of the two types of phase transformations is hydrides formation. In addition to stainless steels, hydride formation under cathodic charging was reported also in the case of nickel [113].

For metals that form stable hydrides, such as niobium [114] [115], titanium [116] [117], vanadium [118] [119] and zirconium [120], HE occurs through repeated formation and fracture of fragile hydrides at the crack tip [49], even at hydrogen concentrations as low as few parts per million.

In fact, the formation of metal hydrides may occur ahead of the crack tip [121] [122], which is a region characterized by a high tri-axial stress field. The presence of a stress field can stabilize these hydrides. The propagation of this crack might occur due to cracking of the brittle phase.

A metal-hydrogen system exhibits a very wide range of behaviors. In these systems, hydrogen solid solubility can be significant and up to values of metal-hydrogen ≈ 1, while the heat of solution from the gas phase is negative, as reported in *Table 2.1* [123]. Contrary to these systems, non-hydride formers have limited ranges of solid solubility, with positive heats of solution from the gas phase.

Some metals, such as nickel, exhibit an intermediate behavior, characterized by stable hydrides at high hydrogen fugacities, but not at the condition for embrittlement occurrence.

Table 2.1. Thermodynamic properties of some metal-hydrogen systems [123]

Element	**Hydrides**	**ΔH solution from gas phase [kJ/mol]**	**ΔH formation of hydrides [kJ/mol]**	**H solid solubility at 300 K (metal/hydrogen)**	**Comments**
Li	LiH		-90.7	Very small	Hydride has a ionic bonding
Cu	CuH	+54.8		<$8.0*10^{-7}$ (*)	Hydride has not been reported to form from metal
Ag		+56.9		<$5.0*10^{-6}$ (*)	
Au		+27.6		Extremely small (*)	
Mg	MgH_2		-74.5	<0.02	
Zn	ZnH_2				Hydride has not been reported to form from metal
Cd	CdH_2				Hydride has not been reported to form from metal
Al	AlH_3	+25.2	-46.0	$2.4*10^{-8}$ (*)	Hydride has not been reported to form from metal
Y	YH_2, YH_3		-235.0 (YH_2)	≈0.2 (**)	
Ti (α)	TiH_2 (γ)	-45.2	-123.5	0.0014 (**)	Metastable hydrogen formation
Ti (β)	TiH_2 (γ)	-58.2		≈1.0 (**)	Solubility at T ≥ 700K
Zr (α)	$ZrH_{1.5}$ (γ)	-51.1	-94.1	<0.01 (**)	Metastable hydrides formation Solubility at T ≥ 700K
Zr (β)	$ZrH_{1.5}$ (γ)	-64.5		≈1.0 (**)	Metastable hydrides formation Solubility at T ≥ 700K
V	$VH_{0.5}$, VH, VH_2	-31.1	-17.3 ($VH_{0.5}$)	0.05 (**)	
Nb	NbH,	-36.0	-29.3 (NbH)	0.05 (**)	

	NbH_2				
Ta	TaH	-34.0	-20.0	0.2 (**)	
Cr	CrH, CrH_2	+47.7		$<0.1*10^{-4}$ (*)	
Mo		+51.5		$<0.1*10^{-4}$ (*)	
W				Extremely small (*)	
Mn (α)		-8.0		$1.0*10^{-4}$ (*)	
Fe (α)		+28.0		$3.0*10^{-8}$ (*)	
Co (hcp)		+20.5		$<4.0*10^{-5}$	
Ni	NiH	+16.7		$<7.6*10^{-5}$	NiH has been formed by electrolytic charging and under hydrostatic pressures of about $5.7*10^{-4}$ Pa
Pd	PdH	-9.6	20 (Pd_2H)	0.03 (**)	
Pt		+18.8		$<1.0*10^{-5}$	
(*) Solubility in equilibrium with H_2 gas at p = 1 atm					
(**) Solubility in equilibrium with the hydride					

3

MECHANISMS OF HYDROGEN DIFFUSION

3.1 Hydrogen absorption and diffusion

Hydrogen absorption and diffusion mechanisms can occur in a metallic material in particular circumstances during service conditions, such as cathodic over-protection, or because hydrogen is already made available from different treatments during production, processing, and operation of metallic materials, as already mentioned in Par. 2.2.

In aqueous solutions, two reduction reactions in alkaline *(eq. 3)* or acidic *(eq. 4*) environment can generate adsorbed hydrogen on the metal surface (H_{ads}), which then becomes absorbed (H_{abs}) in the metal matrix, and tends to concentrate in the areas of maximum tensile stress. The diffusion mechanism of hydrogen can follow different laws, depending on the concentration and the boundary conditions.

In Fick's first law, first proposed in 1855 [124] [125], the flux of a diffusible species, such as hydrogen, under steady state conditions, is related to the concentration of the same species. In particular, hydrogen flux moves from regions with a high concentration to regions with a low concentration, with a magnitude directly proportional to the concentration gradient [126]. In one dimension, Fick's first law can be written as *(eq. 10)*:

$$\Phi_\infty = -D_l \cdot \left(\frac{\partial C}{\partial x}\right) \qquad \textit{(eq. 10)}$$

With: Φ_∞ = steady state hydrogen diffusion flux; C = hydrogen concentration, i.e. density of the diffusing hydrogen; D_l = hydrogen diffusion coefficient, or diffusivity, for lattice diffusion. As soon as the diffusion process determines an equalization of the concentration, the previous equation requires a negative sign, which indicates the opposite direction of the diffusion flux in respect to the concentration. Unfortunately, this equation is only applicable under steady state conditions. Since steady state conditions cannot be determined, Fick's second law must be used instead [124] [125], according to the following equation *(eq. 11)*:

$$\left(\frac{\partial C}{\partial t}\right) = D_l \cdot \left(\frac{\partial^2 C}{\partial x^2}\right) \qquad \text{(eq. 11)}$$

Therefore, a transient diffusion mechanism involves the variation in the concentration of hydrogen in any position *(Figure 3.1)*, as a function of time, and according to Fick's second law [127].

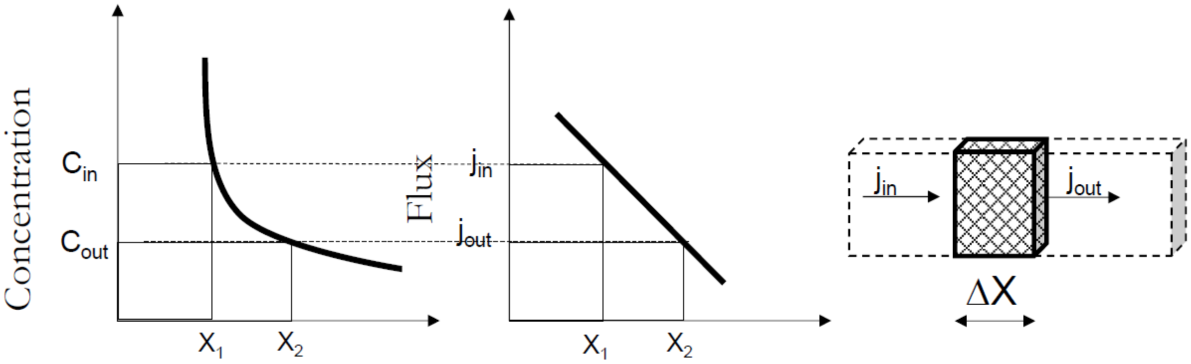

Figure 3.1. Illustration of the principle of the diffusion theory based on Fick's second law [127]

This second law is at the basis of the plot of Fick's permeation curve, which represents a theoretical permeation transient for pure (lattice) diffusion into metals *(Figure 3.2)*. The solutions of Fick's second law are strictly dependent on a set of boundary conditions.

For a semi-infinite medium, a classic analytical solution is provided under the following conditions *(eq. 12)*:

$$\begin{cases} C = C_0 \; at \; x = 0 \\ C = 0 \; at \; x = \infty \end{cases} \qquad \text{(eq. 12)}$$

With: C_0 = sub-surface concentration (constant on the entry surface of the specimen, x = 0). On the exit surface of the specimen (x = ∞), instead, C_0 is equal to zero. The relation between C and C_0 can also be written in the form *(eq. 13)*:

$$C = C_0 \cdot erf\left(\frac{x}{2\sqrt{D_l \cdot t}}\right) \qquad \text{(eq. 13)}$$

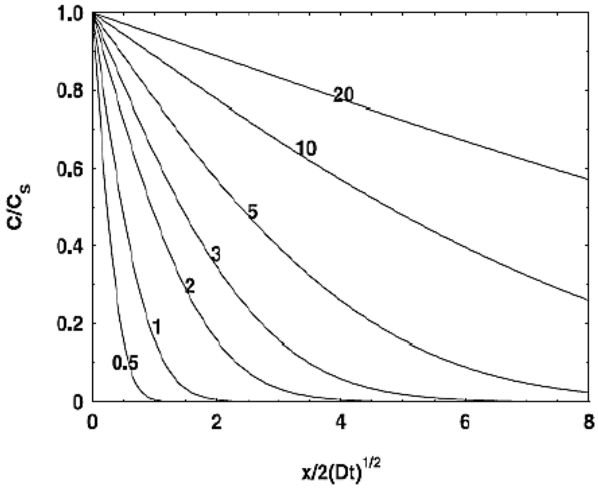

Figure 3.2. Solution of Fick's second law. Semi-infinite medium

For a membrane of finite thickness (x = L), and in-plane dimensions (y, z) much larger than L, the boundary conditions *(eq. 14)* that can optimally simulate the electrochemical method used to measure hydrogen diffusion coefficient into metallic materials are, for any value of time (t):

$$\begin{cases} C = C_0 \; at \; x = 0 \\ C = 0 \; at \; x = L \end{cases} \qquad \textit{(eq. 14)}$$

Hydrogen flux can then be derived, as a function of time (t). In a mono-dimensional flux, the absolute value of hydrogen flux through a surface (S) normal to the x-axis is expressible as *(eq. 15)*:

$$\Phi(t) = D_l \cdot \iint_S \left(\frac{\partial C}{\partial x} \cdot dS\right) \qquad \textit{(eq. 15)}$$

Under the latter boundary conditions, hydrogen flux can be derived, at the exit side and in an adimensional numerical form, from two different solutions (*(eq. 16)* and *(eq. 17)*):

(Fourier solution)

$$\frac{\Phi(t)}{\Phi_\infty} = 1 + \sum_{n=1}^{\infty} (-1)^n \, exp(-n^2\pi^2\tau) \qquad \textit{(eq. 16)}$$

(Laplace solution)

$$\frac{\Phi(t)}{\Phi_\infty} = \frac{2}{\sqrt{\pi\tau}} \cdot \sum_{n=0}^{\infty} exp\left[-\frac{(2n+1)^2}{4\tau}\right] \qquad \textit{(eq. 17)}$$

With: $\Phi(t)$ = time dependent flux; Φ_∞ = steady state hydrogen flux; $\tau = D_l{*}t/L^2$, dimensionless time parameter, where: L = membrane thickness; t = elapsed time; D_l = lattice diffusion coefficient. Both the solutions should provide similar results if enough steps in the summation are used. The reference ISO standard reports that a summation from n = 1 to 6 is sufficiently accurate. In particular, the theoretical hydrogen permeation curves assume the form of the Fourier solution when: $D_l{*}t/L^2 > 0.3$ [128], while these curves assume the form of the Laplace solution when: $D_l{*}t/L^2 < 0.3$ [53].

3.2 Effect of microstructure

The crystal microstructure of metallic materials influences in a relevant way the diffusion of atomic hydrogen through their lattice and, consequently, the susceptibility to embrittlement [113] [129]. Therefore, the different characteristics of the basis crystal microstructure of a metal matrix must be outlined, i.e. bcc-structure for ferritic steels and fcc-structure for austenitic steels, due to the peculiar behavior of the different interstitial sites towards foreign smaller atoms, such as hydrogen.

These interstitial positions can be divided into two categories, the first one including a tetrahedral interstice with a co-ordination number of 6, and the second one including an octahedral interstice with a co-ordination number of four.

In particular, regarding the first category, the fcc-structure is characterized by two kinds of interstitial sites. The larger one is represented by the space at the center of the cube faces or at the center of the cube, the latter surrounded by 6 atoms positioned at the corners of a regular octahedron *(Figure 3.3a)*.

The smaller one, instead, is represented by the tetrahedral interstice surrounded by four atoms *(Figure 3.3b)*. The maximum radius of the atom that can be placed in the lattice interstitial positions without spatial distortion is equal to 0.410*r (octahedral interstice) or to 0.225*r (tetrahedral interstice), where "r" indicates the radius of metal atoms (≈1.26Å).

Concerning the second category, i.e. the bcc-structure, also containing two kinds of interstitial sites, is less packed than the fcc-structure. The octahedral interstice, surrounded by 6 atoms placed at the corners of an irregular octahedron *(Figure 3.3c)*, is the smaller one, and is represented by the space at the center of the cube edge or at the center of the face. The tetrahedral interstice is the larger one, and is surrounded by four atoms of the bcc-structure, positioned at the corners of an irregular tetrahedron *(Figure 3.3d)*. In this case, the maximum radius of the atom that can be accommodated in the lattice interstitial positions without spatial distortion is equal to 0.291*r (tetrahedral interstice) or to 0.154*r (octahedral interstice).

Summarizing, the fcc-structure is characterized by a packing fraction of 0.74, a lower density of interstitial positions per atom and the largest one with a radius of 0.41*r. The bcc-structure, instead, has a lower packing fraction, equal to 0.68, a larger density of interstitial positions per atom, but the largest one has a radius of only 0.291*r, which is lower than the largest of the fcc-structure. Thus, hydrogen solubility in fcc-structure is much larger than that in the bcc-structure, mainly due to different interstitial spacing. The larger availability of interstices in the bcc-structure (ferrite) explains why the diffusion coefficient in this structure is greater than that in the fcc-structure (austenite).

However, the geometry of the interstitial positions is not the only parameter to be taken into account to outline hydrogen solubility. In fact, Smialowski [130] stated that hydrogen solubility in the metal lattice is directly proportional to the quantity of austenite (fcc-structure). Fukai et al. [131] affirmed that the maximum number of hydrogen atoms trapped by vacancy is 6 in both fcc- and bcc-structure. Both in the fcc- and in the bcc-structure, the tetrahedral interstice is a more stable absorption position for atomic hydrogen than the octahedral one.

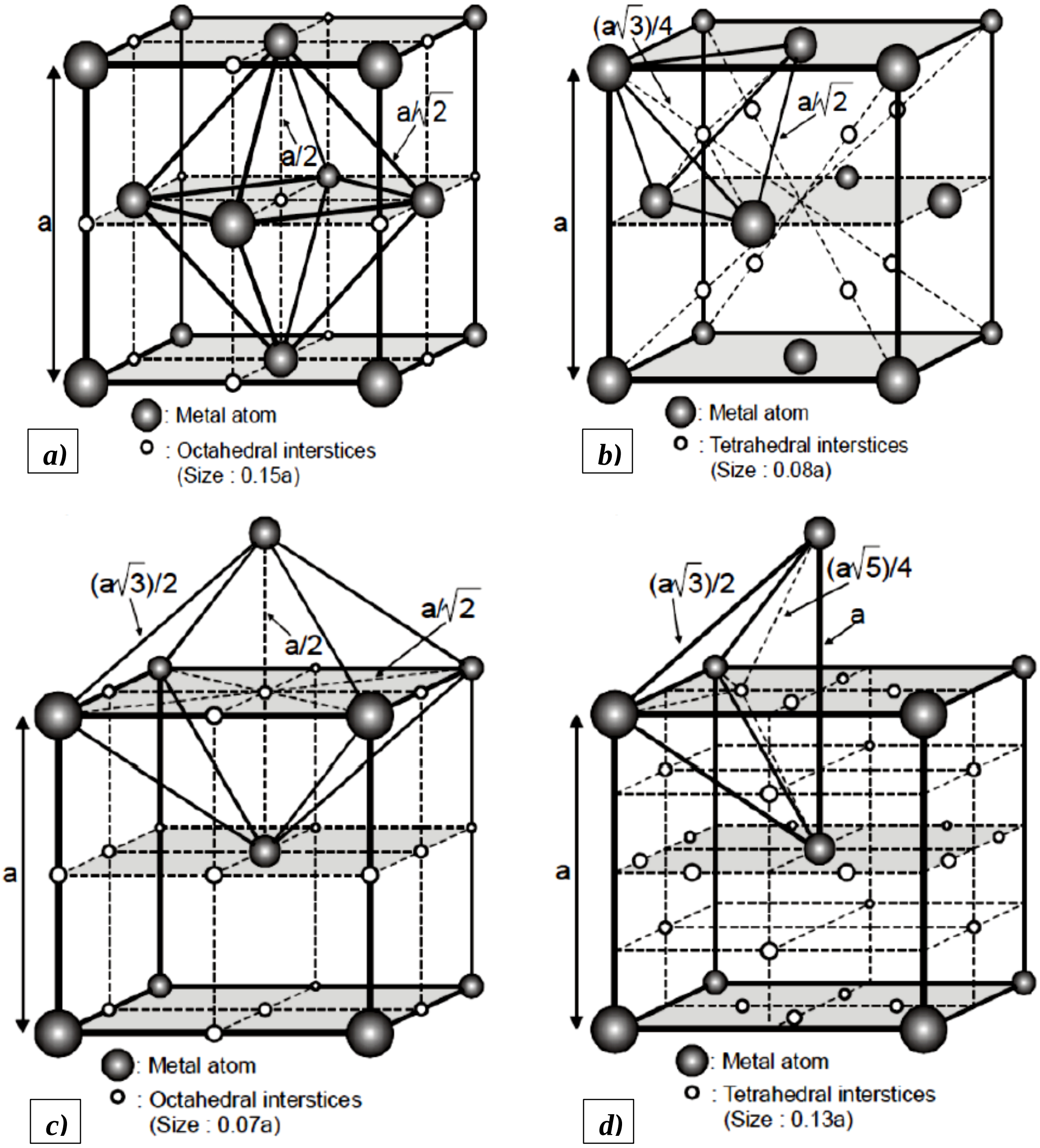

Figure 3.3. Interstitial positions for foreign smaller atoms in iron matrix. Octahedral and tetrahedral sites for γ-iron system (fcc-structure): a) and b); for α-iron system (bcc-structure): c) and d), respectively [130]

According to Krom and Bakker [132], the density of lattice sites (N_L), per unit volume *(eq. 18)*, is linked to the atoms constituting the host lattice, i.e. the iron lattice:

$$N_L = \frac{N_A \cdot \beta \cdot \rho}{A_r} \qquad \textit{(eq. 18)}$$

With: β = density of the interstitial sites per atom *(Table 3.1)*; N_A = Avogadro's constant = $6.023*10^{23}$ atoms/mol; ρ = density of iron = $7.87*10^3$ kg/m^3 (T = 20 °C, or 293 K); A_r = atomic weight of the atoms constituting the iron lattice = 55.845 $*10^{-3}$ kg/mol.

In the case of α-iron, indirect evidence denotes tetrahedral site occupancy of hydrogen atoms at room temperature, thus β is equal to 6. The resulting value is: $N_L = 5.10*10^{29}$ atoms/m^3.

Table 3.1. Density of interstitial sites per atom for fcc-structure and bcc-structure [132]

Structure	**Geometry**	**Density of sites per unit cell**	**Density of atoms per unit cell**	**β**
fcc	Octahedral	4	4	1
fcc	Tetrahedral	8	4	2
bcc	Octahedral	6	2	3
bcc	Tetrahedral	12	2	6

The available data, reported in the literature and referred to similar microstructures, are very dispersed and the values of the hydrogen diffusion coefficient presented appear to be very variable, but always in the order of magnitude of 10^{-11} m^2/s. For the ferritic-pearlitic structures, in fact, these values range between 1.5 and $9*10^{-11}$ m^2/s; for bainitic and martensitic microstructures, however, the values found are comparable with the previous ones. On the assumption of the same microstructure, it is widely accepted that HE phenomena increase with an increase in diffusivity. However, moving from the ferrite/pearlite bands microstructure to the less susceptible one of sorbite, with the same diffusivity, the embrittlement effects are lower [133] [134].

In particular, hot-rolled X60 steel is characterized by a ferritic-pearlitic coarse microstructure, with the presence of MnS inclusions, oriented along the rolling direction. The diffusion mechanism takes place along ferritic grain boundaries and in correspondence of ferrite-pearlite interfaces, while the interfaces between inclusions and the matrix constitute hydrogen trapping sites.

Some researchers [135] affirm that the pearlitic bands in the ferrite may hinder hydrogen transport.

Therefore, the diffusion mechanism in the X60 steel depends on the orientation of ferrite and pearlite, and on the inclusions present. A marked difference exists between the diffusion coefficients in the direction parallel to the lamination plane (i.e. planar section) and in the direction perpendicular to the rolling direction (i.e. transversal section). In fact, in the planar section hydrogen is forced to cross layers of pearlite, which slow down its diffusion, while, in the transversal section, the ferrite/pearlite interfaces are aligned to the direction of hydrogen diffusion, promoting its transport.

A quenching and tempering (Q&T) treatment produces a martensitic microstructure, in which the carbides, round and small, are distributed uniformly on the grain boundaries. The X65M and X85M steels, with a similar chemical composition, are characterized by this type of microstructure and have almost equal diffusivity values. An accelerated cooling after a controlled rolling produces grain refinement, and favors martensitic and bainitic transformations; the X80 steel shows the presence of pearlite and bainite, while the X100 steel has a microstructure characterized by ferrite and martensite. The latter, concerning hydrogen diffusion, exhibits a perfectly isotropic behavior.

A high dislocation density is expected in the acicular ferrite phase [136] and, generally, in the whole steel matrix after cold work [53].

Serna et al. [137] affirmed that the fine grain acicular ferrite deriving from the Q&T process after rolling in micro-alloyed steels may present uniformly distributed fully tempered second phase constituents (preferentially in grain boundaries), such as carbides, nitrides or carbonitrides. Those constituents represent more irreversible traps than dislocations and, if more uniformly distributed, can reduce the hydrogen amount in dislocations and, therefore, the effects of HE phenomena.

Park et al. [138] investigated, through optical and scanning electron microscope, an X65 steel produced by means of TMCP, and indicated a primary phase consisting of elongated ferrite, while the secondary phase varied depending on the Start Cooling Temperature (SCT) and on the Finish Cooling Temperature (FCT), as shown in *Figure 3.4.*

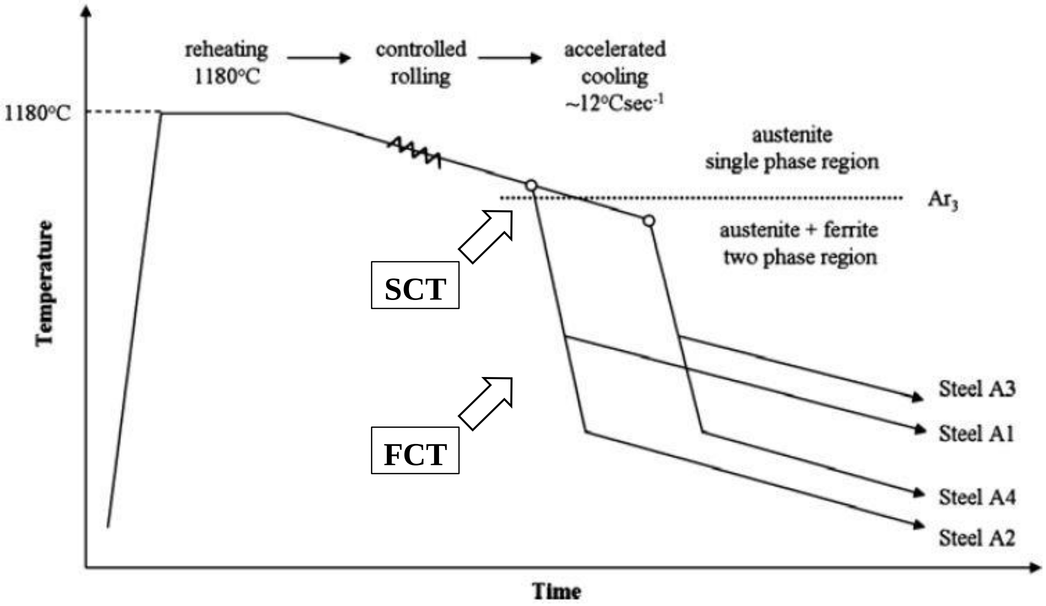

Figure 3.4. Schematic representation of TMCP conditions. Adaptation from the literature [138]

These researchers finally proposed the influence on the diffusion properties of the steel determined by the second microstructure phase. The ranking of the different phases was made on the basis of their hydrogen diffusivity, solubility, and permeability, in addition to the quantity of trapped hydrogen in correspondence of irreversible trapping sites. In particular, compared to degenerated pearlite and bainite, acicular ferrite exhibited the lowest diffusivities and the highest solubilities, therefore it was assumed to be characterized by the highest trapping efficiency, as well as martensite-austenite (M/A) constituents. Thus, they reached the conclusion that acicular ferrite and M/A constituents act as reversible trapping sites for diffusing hydrogen atoms.

As affirmed by Chatzidouros et al. [139], the presence of M/A constituents may represent favorable hydrogen trapping sites [138] [140], and can determine the insurgence of HIC phenomena [138].

Although several valid studies, which concern the estimate of the apparent hydrogen diffusivity (D_{app}), i.e. in the presence of trapping sites, were carried out until now, a variation of that parameter of many orders of magnitude points out several problems during experimentation *(Table 3.2)*.

Table 3.2. Review of hydrogen apparent diffusivities (D_{app}) in different pipeline steels [53]

Material	**Experimental method**	**D_{app} at T = 25°C [cm²/s]**	**Reference no.**
X65	Permeation	$9.49*10^{-7}$	[141]
X52 X70	Permeation	$0.1÷0.9*10^{-7}$ $0.1÷0.3*10^{-7}$	[142]
X100	Permeation	$1.04*10^{-8}$	[143]
X80	Permeation	$5.32*10^{-9}$	[144]
X70	Permeation	$2.63*10^{-7}$	[145]
X65	Permeation	$1.5*10^{-6}$	[146]
X120	Permeation	$2.0÷2.8*10^{-7}$	[147]
X65	Permeation	$0.8÷2.7*10^{-9}$	[148]
X52	Permeation	$7*10^{-7}÷3.2*10^{-5}$	[149]
X60 X65* X80 X100 X65* X85	Permeation	$5.6÷11.5*10^{-7}$ $0.9÷4.6*10^{-7}$ $4.7*10^{-7}$ $3.9*10^{-7}$ $4.2*10^{-7}$ $4.0*10^{-7}$	[150]
X60	Permeation	$3.5*10^{-6}$	[151]

In fact, the complexity of the experimental procedures for the calculation of D_{app} seems caused by the low hydrogen solubility and the lack of knowledge of the interactions between hydrogen and microstructure [53] because, in too many works, the effect of both reversible and irreversible trapping sites on D_{app} after subsequent hydrogen charging and discharging cycles was not even considered. Moreover, in many studies involving the electrochemical permeation technique, test conditions to ensure bulk diffusion control were not always verified [138].

3.3 Effect of temperature

The temperature at which a permeation test is carried out represents a fundamental parameter for the evaluation of hydrogen diffusion coefficient in the lattice (D_l). In fact, it has been proved several times that an increase in temperature determines an increase in D_l [137] [152]. The dependence of D_l

on temperature can be described *(eq. 19)* by the Arrhenius equation [153] [130] [154] [155]:

$$D_l = D_0 \cdot e^{\left(\frac{-E_l}{R \cdot T}\right)} \qquad \textit{(eq. 19)}$$

With: D_0 [m^2/s] = pre-exponential factor (frequency factor) in the normal state; E_l = activation energy for pure lattice diffusion (energy required for hydrogen atoms to jump from one lattice site to another); R [J/(mol*K)] = gas constant = 8.314; T [K] = absolute temperature.

Kiuchi and McLellan [155] analyzed a wide group of data of D_l for α-iron (ferrite). They found that, for temperatures ranging from -40 (233) to +80 °C (353 K), a quite accurate representation *(eq. 20)* for bcc-structure is given by: $D_0 = 7.23*10^{-4}$ m^2/s and E_l = 5.69 kJ/mol [156] [157]:

$$D_l = 7.23 \cdot 10^{-4} \cdot e^{\left(\frac{-E_l}{R \cdot T}\right)} \qquad \textit{(eq. 20)}$$

At 23 °C (296 K), the common room temperature, a value of $D_l = 7.2*10^{-9}$ m^2/s can be obtained.

More recently, Grabke and Riecke [158] developed a similar correlation *(eq. 21)* for very pure iron:

$$D_l = 5.12 \cdot 10^{-4} \cdot e^{\left(\frac{-E_l}{R \cdot T}\right)} \qquad \textit{(eq. 21)}$$

They considered a lower value for the activation energy for pure lattice diffusion (E_l = 4.15 kJ/mol), affirming that this is due to hydrogen movement through the interstitial lattice sites as a proton.

Thus, the value of the diffusion coefficient in the lattice was slightly higher ($D_l = 9.5*10^{-9}$ m^2/s) than that obtained by Kiuchi and McLellan [155], but identical to the value calculated by Bruzzoni et al. [159] a couple of years before ($D_l = 9.6*10^{-9}$ m^2/s).

Furthermore, from the permeation curves obtained by Addach et al. [160] at different temperatures for pure iron, an increase in the temperature corresponds to an increase in the steady state hydrogen permeation current *(Figure 3.5)*.

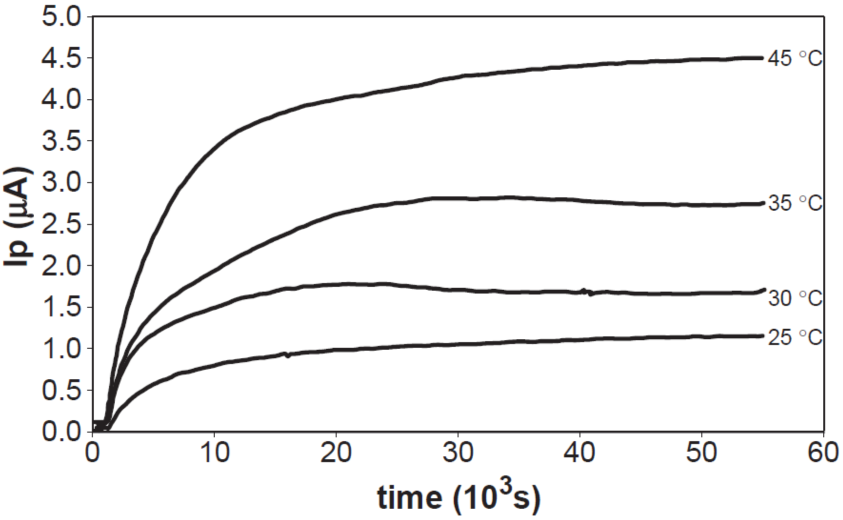

Figure 3.5. Effect of temperature on hydrogen permeation curves [160]

In addition, considering the apparent hydrogen diffusion coefficient (D_{app}), this exhibits the same trend highlighted before over temperature *(Table 3.3)*.

Table 3.3. Apparent hydrogen diffusion coefficients (D_{app}) at different temperatures for pure iron. Adaptation from the literature [160]

	Electrochemical permeation results			**Thermal desorption results**
T perm [°C]	V [mol/m*s]	D_{app} [m^2/s]	C_{app} [mol/m^3]	H_2 desorbed [ppm]
25	$0.9*10^{-10}$	$5.8*10^{-10}$	0.15	3.5
30	$1.4*10^{-10}$	$6.5*10^{-10}$	0.21	5.7
35	$2.1*10^{-10}$	$7.6*10^{-10}$	0.28	8.2
45	$3.3*10^{-10}$	$9.3*10^{-10}$	0.35	14.5

Smialowski [130] provided an exhaustive collection of published results for hydrogen diffusion coefficient in iron and steels in a wide range of temperatures *(Figure 3.6)*. In particular, at temperatures above 200 °C (473 K) and for ferritic steels, hydrogen diffusivity is in agreement with the accepted value of D_l for bcc-iron. Instead, for temperatures below 200 °C (473 K), both the scattering of the values and the difference from lattice diffusivity becomes relevant; this behavior is caused by hydrogen trapping phenomena.

The necessity of including the trapping effect in the evaluation of the apparent hydrogen diffusivity involved the introduction of an apparent diffusion coefficient (D_{app}), related to hydrogen diffusion in ferritic steels; in accordance with Oriani [153], this is given by the following equation *(eq. 22)* [130]:

$$D_{app} = \frac{D_l}{1 + K \cdot e^{\left(\frac{E_b}{R \cdot T}\right)}} = \frac{2.0 \cdot 10^{-7} \cdot e^{\left(\frac{-6950}{R \cdot T}\right)}}{1 + 4.4 \cdot 10^{-3} \cdot e^{\left(\frac{26000}{R \cdot T}\right)}} \left[\frac{m^2}{s}\right] \qquad \textit{(eq. 22)}$$

With: D_l = hydrogen diffusion coefficient in the lattice (in bcc-iron); K = trapping sites density (i.e. number of trapping sites per number of lattice sites); E_b = binding energy between hydrogen and trapping site. *Figure 3.6* provides a graphical representation of the previous equation *(eq. 22)*.

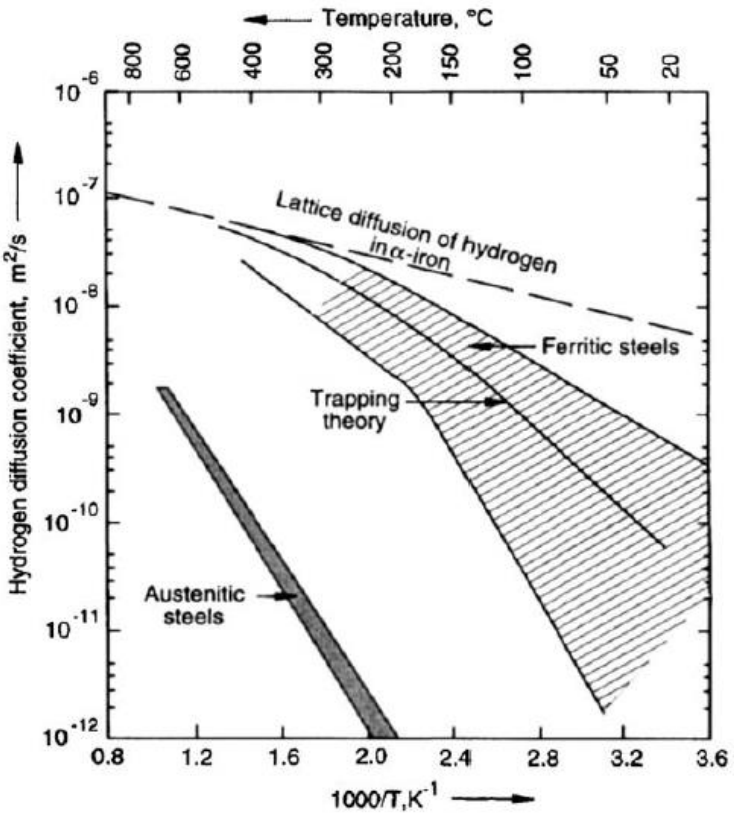

Figure 3.6. Collection of published results for hydrogen diffusion coefficient in iron and steels [130]

In the graph on the following page *(Figure 3.7)*, the values collected in the literature by Babu et al. [161], which highlight the relationship between the values of hydrogen diffusion coefficients and the inverse of temperature, are summarized. It is evident a relevant dispersion of the coefficient values for temperatures lower than 80 °C (353 K). At room temperature, the dispersion band is of several orders of magnitude.

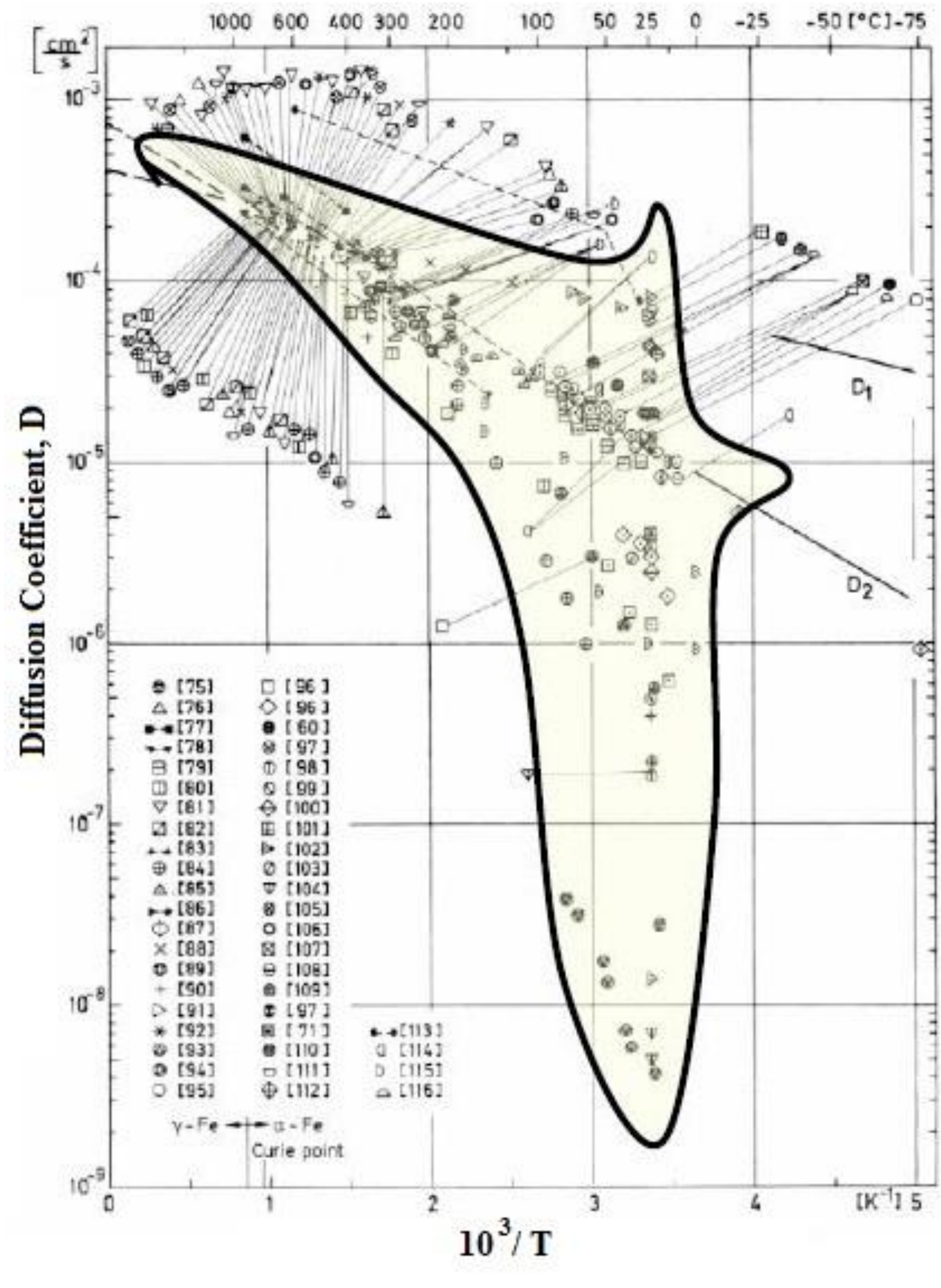

Figure 3.7. Correlation between hydrogen diffusion coefficients and temperature [161]

3.4 Effect of sub-surface hydrogen concentration

As clearly proposed by McNabb and Foster [162] and Oriani [153] in their works, the dependence of the apparent diffusivity on hydrogen content is caused by the variation of trap occupancy. The predicted data [163] shown in *Figure 3.8* can be estimated using both the NPL diffusion-trapping model [164], or from a more accessible analytical equation, as demonstrated by Johnson [165].

The sub-surface hydrogen concentration in lattice sites (C_0) on the specimen charging side can be obtained from the following equation *(eq. 23)* of the steady state hydrogen permeation current:

$$\Phi_{\infty} = D_l \cdot \frac{C_0}{s} \qquad (eq.\ 23)$$

With: Φ_{∞} [mol/(m^{2}s)] = steady state hydrogen flux; s [m] = specimen thickness; D_l [m^2/s] = hydrogen diffusion coefficient in the lattice.

The deriving relevant aspect is that the apparent diffusivity can change by more than one order of magnitude in relation to the environment aggressiveness, with respect to hydrogen uptake. In fact, values around $C_0 = 10^{-3}$ ppm (in mass) are typical of steels under CP in near-neutral environments, whereas values around $C_0 = 10^{-1}$ ppm (in mass) are typical of steels under CP in acidic environments. The atomic hydrogen that enters the steel during cathodic charging is subdivided between interstitial lattice sites and microstructural defects. Hydrogen atoms are mobile and can jump between lattice sites, and also those atoms in the reversible traps can become mobile by de-trapping towards lattice sites [166]; thus, both lattice and reversibly trapped hydrogen (at weak traps) contribute to the diffusible hydrogen content in steels [53]. Instead, irreversibly trapped hydrogen (at strong traps) cannot escape and, therefore, is less mobile and do not contribute to the diffusible hydrogen content.

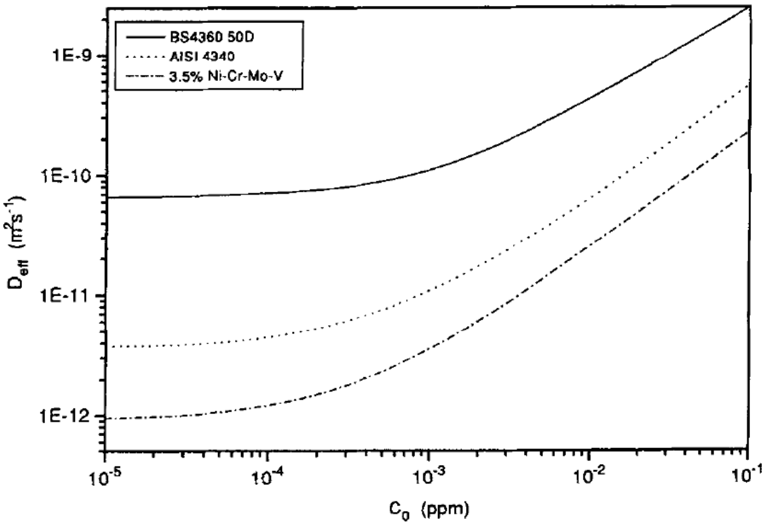

Figure 3.8. Simulated effect of sub-surface hydrogen concentration (C_0) on the apparent diffusivities (D_{app}) of three different low alloy steels [163]

3.5 Effect of applied mechanical stress

It has already been explained that the damaging phenomena related to absorption and consequent diffusion of hydrogen through the steel matrix differ significantly in the presence or absence of internal residual stresses and/or external stresses. For example, cracking phenomena due to HE in API X70 grade steel were found to initiate in correspondence of inclusions [167], propagating transgranularly along a direction perpendicular to that of the applied tensile stress [142] [167] [168]. This synergistic action of atomic hydrogen and applied stress field is at the basis of all the works and efforts made for the evaluation of the effect of an applied stress field on hydrogen permeation through steel membranes, using the gas phase charging procedure [169] [170], the electrochemical permeation technique [171] [172] [173] [174] or the hydrogen microprint technique [100] [111] [175].

In particular, no relevant effects on hydrogen diffusivity have been reported for applied tensile stresses in the elastic field, but only an increase in the steady state hydrogen permeation flux due to lattice expansion [172] [174] [176]. Some works in the literature report that a constant elastic tensile stress does not affect hydrogen diffusivity [174] [177], while other authors [170] stated that the apparent diffusivity is affected both in the elastic and plastic domain by an applied stress field. In particular, Bockris et al. [178] [179] found that an elastic stress produces no variations in hydrogen apparent diffusivity, but that the effect of stress acts only on hydrogen solubility and, thus, on its chemical potential.

Instead, for example in a bcc-structure crystal lattice under a tensile stress field in the plastic domain, a significant decrease in the permeation flux and a considerably slower diffusion rate have been reported, which were assumed to be linked to the enhanced hydrogen trapping phenomena in the newly created traps [171] [172].

In fact, when the stress value is close to the YS, so still in the elastic region, the effect of a tensile stress on hydrogen diffusion is that of inducing a decrease in the permeation flux and a slight decrease in D_{app}, instead of causing an increase in the flux connected to a stronger lattice expansion [180].

Moreover, it is necessary to consider the difficulty of following the conventional analysis method for hydrogen diffusion, because, in the presence of an applied stress field, the trap density dynamically modifies during the permeation test, due to the presence of newly generated surfaces and internal cracks as trapping sites for atomic hydrogen.

3.6 Effect of specimen thickness

The thickness of the steel membrane significantly influences hydrogen diffusivity through the metal matrix. *Figure 3.9* reports the effect of an increase in the specimen thickness in an AF1410 steel, used for the permeation tests under the same charging current [181].

It is evident how the steady state hydrogen permeation flux is significantly higher for lower thicknesses. Too thin walls make the permeation test to be a function only of the superficial reactions occurring on the specimen surface; thus, the diffusivity constant depends on the wall thickness through which hydrogen is diffusing [182].

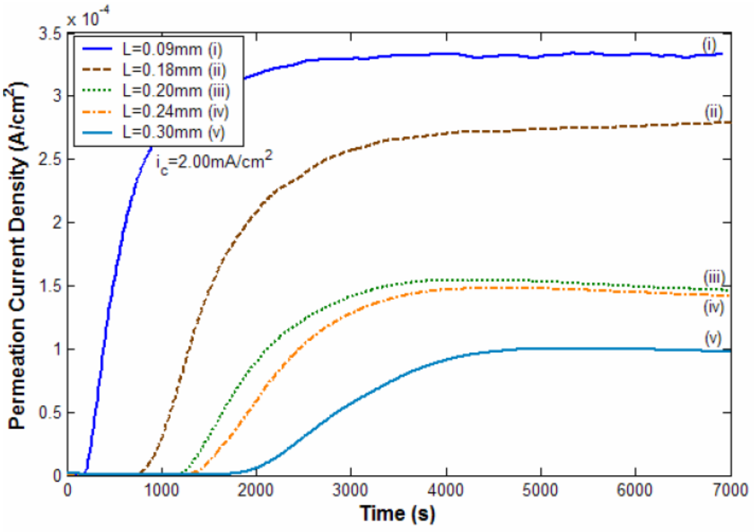

Figure 3.9. Hydrogen permeation transients for different thicknesses under the same charging current [181]

Those observations were confirmed by Ha et al. [53] in their work, in which they affirmed that, in thin foils, the hydrogen permeation current began to increase earlier and at faster rates, if compared to thick foils, and with higher values of the steady state current *(Figure 3.10a)*.

Moreover, they found that the steady state current was strongly dependent on the foil thickness in the case of thick foils (when 1/L was small) and, instead, it was weakly dependent on the foil thickness in the case of thin foils (when 1/L was large), as shown in *Figure 3.10b*.

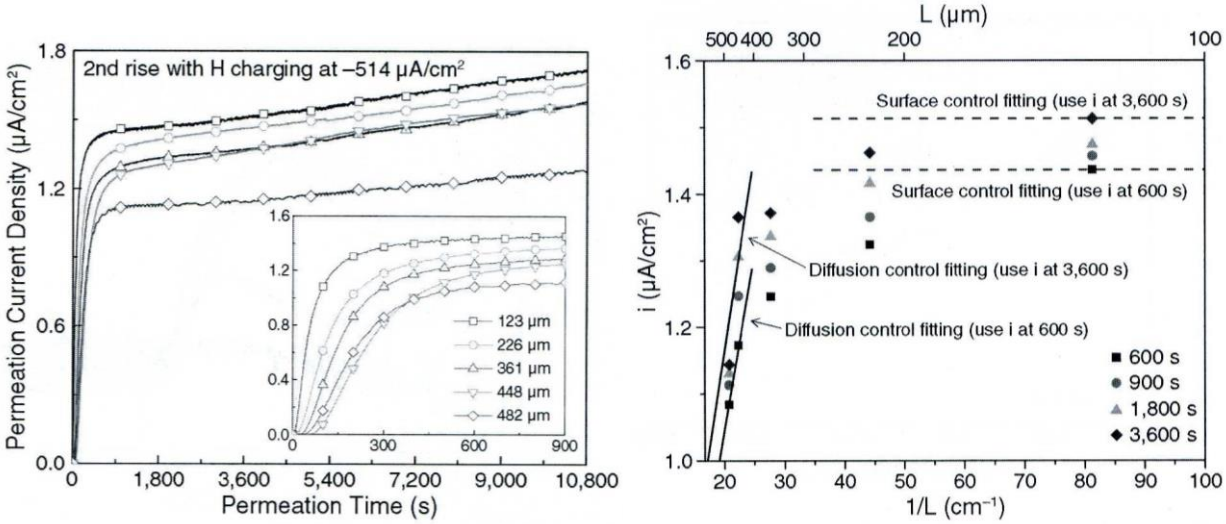

Figure 3.10. a) Comparison of the permeation currents on the as-received API X70 grade steel of different thickness; b) Permeation current i(t) vs. 1/L of the as-received API X70 grade steel. Adaptation from the literature [53]

The graph shown in *Figure 3.11* indicates the variation in the steady state permeation current when changing the specimen thickness, in addition to the variation in the hydrogen diffusion coefficient [160].

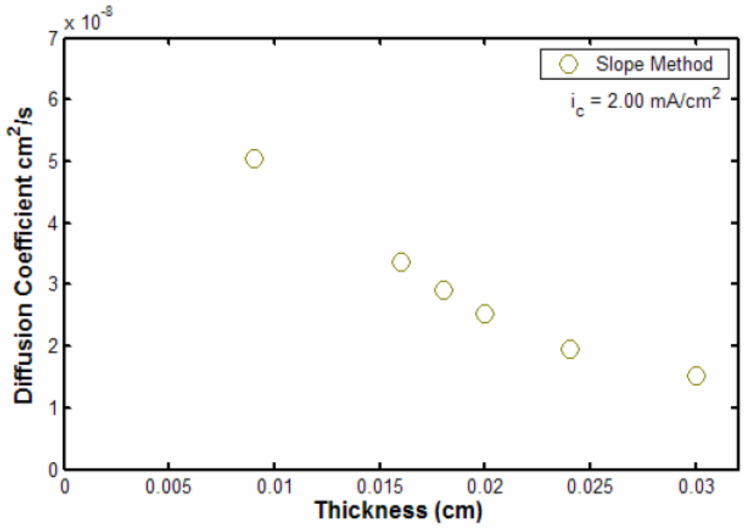

Figure 3.11. Relation between hydrogen diffusion coefficient and specimen thickness. Adaptation from the literature [160]

3.7 Effect of trapping

All the metallic materials present imperfections in their crystal lattice that can bond hydrogen inside them. For hot-rolled steels, these trapping sites can be represented by inclusions of various types of oxides or sulfides, such as those of manganese, very widespread in old-manufactured steels and much rarer in the most recent ones.

The presence of traps inside a metal or on its surface involves the following deleterious effects [183]:

- Increase in hydrogen total solubility and hydrogen local concentration
- Decrease in hydrogen apparent diffusivity
- Dependence of the diffusion phenomenon from hydrogen penetration paths in the material, an unpredictable factor on the basis of Fick’s equation.

A trapping site, or more simply a trap, represents a region that causes a delay in hydrogen diffusion through a metallic material, because in here a hydrogen atom can be placed in a more stable way compared to an interstitial lattice site, where the physical space is significantly lower. The probability that a hydrogen atom jumps into a trap should not be lower than that related to a jump into an interstitial lattice site.

It is generally accepted the existence of two main reasons for the modification of jump probabilities into the crystal lattice, as concluded by Bernstein and Pressouyre [184].

According to this model, an attractive force of unknown origin may act on a hydrogen atom in a preferential direction, either because its condition of screened proton, or because its small size and consequent high mobility. In this case, the lattice physical space is not altered, but it is more probable for hydrogen to jump in the force direction *(Figure 3.12a)* and be attracted towards the force origin.

However, a distortion of the lattice physical space could also happen, which causes a modification of the average jump height of the hydrogen atom, consequently making the de-trapping process more difficult *(Figure 3.12b)*. Thus, the two researchers divided traps into attractive or physical, considering a mixed behavior for most real traps.

3.7.1 Attractive traps

A schematic representation of an attractive trap is shown in *Figure 3.12c*. The classification of the forces acting on the hydrogen atom in the crystal lattice is here reported:

- Electronic force. When hydrogen dissolves into the iron lattice, it releases its excess electron and gives it to the metal electron cloud [185]; thus, hydrogen is attracted by any imperfection that provides an electron vacancy in order to reach a more stable condition
- Force due to a stress field. A distortion of the lattice physical space has occurred. For example, hydrogen migrates towards tensile stressed region instead of moving towards a compressive stressed one, as in that region there is more space available to stay
- Force due to a temperature gradient. An increase in temperature determines an increase in hydrogen solubility; hence, hydrogen is attracted in the regions with a higher temperature, such as, for example, the inner regions of a solidifying ingot.

The magnitude of an electronic force should be small if compared to the other two categories, as here it should scale proportionally to the stress field or the temperature gradient.

3.7.2 Physical traps

According to Oriani's theory [153], hydrogen can occupy interstitial sites of the metal lattice or be trapped in physical discontinuities. Typical examples include microstructural defects, like vacancies [186], dislocations [170], grain boundaries [94] [187], interfaces [188] [189], voids [190] and carbides [56]. As schematized in *Figure 3.12d*, a hydrogen atom is not effectively attracted in a purely physical trap, but, once trapped, the de-trapping process becomes more difficult. In contrast to the hydrogen diffusing through the lattice, reversibly trapped hydrogen atoms likely resided at the afore-mentioned microstructural defects.

3.7.3 Mixed traps

Provided that a distortion in the lattice physical space is certainly followed by an electronic disorder, for most real traps both characteristics are likely to coexist. An edge dislocation represents a valid example of a mixed trap, because the attractive behavior derives from the tensile stress field, while the physical one is provided by the core region. A schematic representation of a mixed trap is given in *Figure 3.12e*.

For real traps with a mixed behavior, two different kinds of traps exist: reversible and irreversible.

The reversibility of traps cannot be understood in an absolute way, as for each one a characteristic trapping energy is associated, which depends on temperature. Normally, reversible traps release hydrogen more easily. Irreversible traps, instead, are those that do not allow hydrogen to escape. This results in a retarding effect on diffusion, because those traps will bond a hydrogen fraction within them that differently would increase the total hydrogen flux.

There are still conflicting opinions regarding the classification of reversible and irreversible traps at room temperature. Hydrogen entrapment in steels is generally attributable to grain boundaries and interfaces between matrix and second phase particles. In steels in which the carbon content and the production process involves the formation of ferrite/pearlite bands, the possible traps for hydrogen consist of [191]:

- Grain boundaries between pre-eutectoidic ferrite grains
- Interfaces between ferrite and pearlite bands, and between piles of pearlite
- Interfaces with metallic and non-metallic phase particles present in the matrix.

The most influencing inclusions for hydrogen diffusion are those of iron (FeS) and manganese sulfide (MnS), which in the recently manufactured steels are however very limited. As an example, Razzini et al. [58] [192] analyzed hydrogen diffusion by means of an in-situ scanning photoelectrochemical microscopy (SPEM) technique, and found that the sulfide inclusions generated by the quenching processes during production determine the creation of micro-voids at the inclusion-matrix interface, due to the different thermal expansion coefficients of the two materials. Therefore, wide amounts of hydrogen atoms can precipitate and be trapped in these micro-cracks.

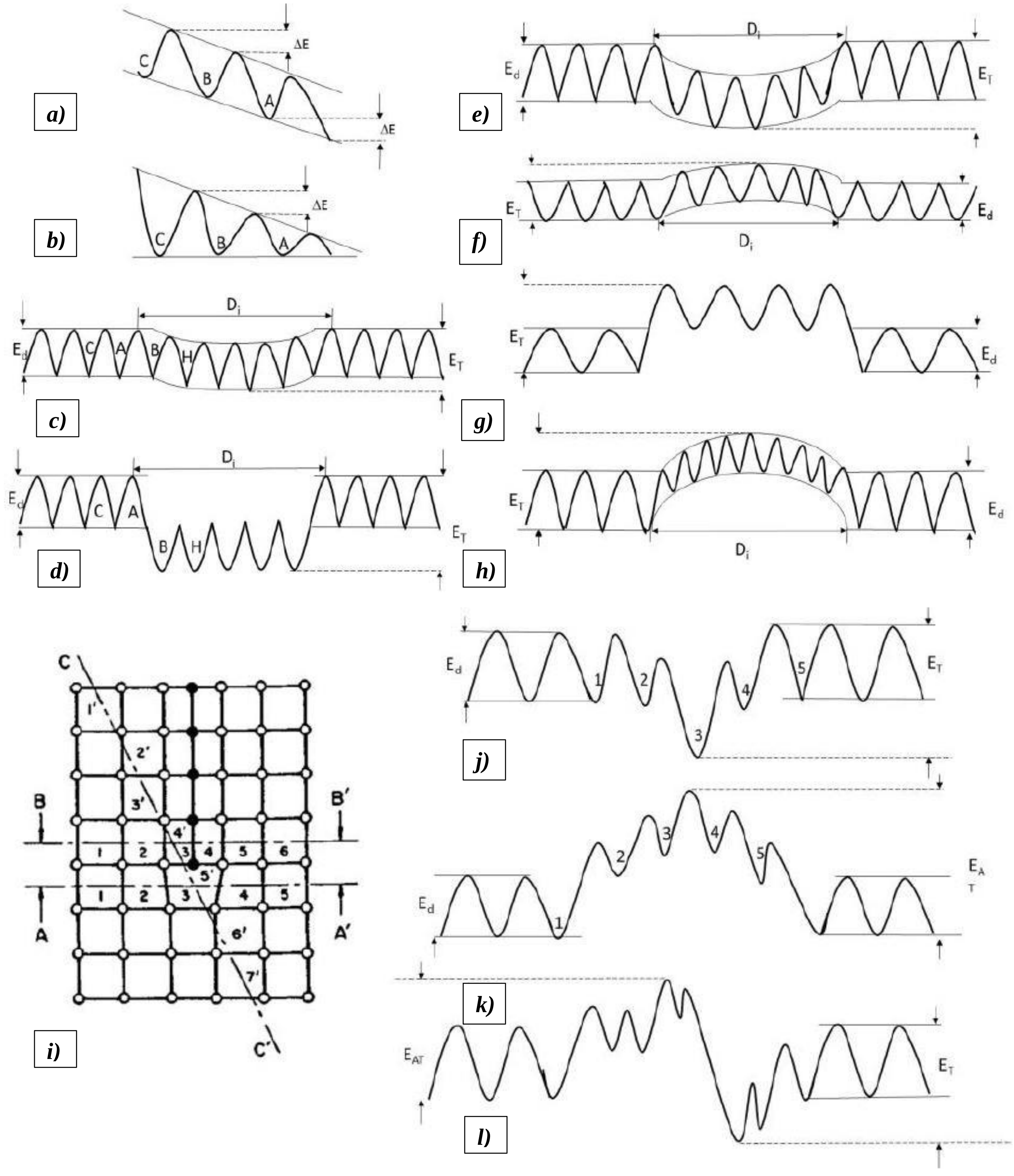

Figure 3.12. Schematic representation of energy gaps which characterize hydrogen traps, repellers and obstacles in metallic materials. In order: a) Attractive force on hydrogen diffusion; b) Lattice space distortion on hydrogen diffusion; c) Attractive trap; d) Physical trap; e) Mixed trap; f) Repeller; g) Obstacle; h) Mixed anti-trap; i) Edge dislocation; Hydrogen diffusion: j) along A-A' (Attractive trap); k) along B-B' (Repeller); l) along C-C' (Obstacle-Repeller-Trap) [184]

3.7.4 Repellers and obstacles

Repellers, whose schematic illustration is provided in *Figure 3.12f*, are the counterpart of attractive traps, because of the action of repulsive forces within these regions. In particular, one or more of the following features are necessary for the existence of a repulsive force:

- Solute atoms, lying on the right of iron in the Periodic Table, which introduce an excess electron
- Compressive stress field generated in the lattice by the defect, if it represents an interstitial or substitutional atom, particle, inclusion, or a compressive region adjacent to an edge dislocation
- Region of the material concerned by the defect and subject to a reduction of hydrogen solubility.

Obstacles, whose schematic representation is given in *Figure 3.12g*, are the counterpart of physical traps, because of the presence of a lattice physical gap through which hydrogen has no relevant mobility. Incoherent precipitates constitute an example of this kind of defects, as these do not dissolve hydrogen atoms and do not generate a local stress field.

As occurred for real traps, it is difficult to find pure repellers or pure obstacles, as both behaviors are likely to take place simultaneously, generating a mixed behavior, as shown in *Figure 3.12h*. Some defects, such as edge dislocations, may have this mixed behavior, presenting both trapping and repeller/obstacle features. Moreover, considering particles with incoherent interfaces that do not dissolve hydrogen, the surface represents a physical trap, while the bulk represents an obstacle.

In *Figure 3.12*, from i to l, the movement of a hydrogen atom along the direction C – C’ is hypothesized; this has to cross a mixed repeller/obstacle region (sites 1’ to 4’) before being trapped (sites 5’ and 7’).

4

MATHEMATICAL MODELS FOR HYDROGEN DIFFUSION

4.1 Ideal and non-ideal diffusion

Hydrogen diffusivity through the metal lattice can be considered at different levels. A first approach considers a perfect lattice, through which hydrogen diffuses by jumping between interstitial sites. These jumps involve the overcoming of a certain activation energy, which can be explained as the activation energy of the hydrogen diffusion process.

On the other hand, in a theoretically homogeneous lattice, the depth of the potential wells and the activation energy between adjacent sites should be the same. In fact, inside the lattice, preferential paths for the diffusion process with less activation energy are present, and hydrogen traps, i.e. sites with very low energy, where hydrogen remains trapped in metastable conditions, slowing the diffusive flux. Grain boundaries, dislocations, interfaces of different phases affect hydrogen diffusion and can represent preferential paths or traps, which are usually classified as reversible or irreversible [193] [166] [194], in relation to the binding energy.

Reversible traps are associated with low binding energies and can release hydrogen at room temperature when the surface concentration goes to zero, whereas irreversible traps, associated with high binding energies, can only release hydrogen at temperatures higher than the room one [195]. Traps can also be classified as saturable, if they can retain only one hydrogen atom (or a defined finite number) or not saturable, if they can accommodate any quantity of hydrogen (blisters) [188] [195] [196] [197] [198].

In the absence of traps or preferential paths, the diffusion of hydrogen atoms through the lattice can be derived from the resolution of Fick's second law, where the diffusion is defined as the lattice diffusion coefficient parameter D_l (diffusion without trapping). In the presence of defects, such equation must be modified by inserting, in the boundary conditions, the presence of hydrogen "sources" (preferential paths or sites with a lower energy than the NILS) and "wells" (hydrogen trap sites). Fick's second law can also be used to describe the diffusion process in the presence of traps and preferential paths, by entering an apparent diffusion coefficient D_{app} [153] [199].

The most utilized method for the experimental measurement of hydrogen diffusion parameters is the electrochemical method originally suggested by Devanathan and Stachurski [200], standardized in 2004 in the ISO 17081 [201] [202] International standard.

Changes to this method are hereafter proposed to take into account the effect of the traps and the kinetics of hydrogen reduction on the cathode surface [154] [188] [203] [204] [205] [206].

The absorbed atomic hydrogen tends to concentrate in the areas of maximum tensile stresses in the steel, in correspondence of defects or micro-cracks. Once a critical concentration at the tip of the defect is reached, if the steel is susceptible of HE, a brittle propagation occurs, which can determine the failure of the element for stresses much lower than those which would lead to failure in air [207].

4.2 Fick's laws for ideal diffusion (absence of trapping)

The results obtained from the electrochemical permeation tests, carried out in accordance with the Devanathan and Stachurski method, reported in the ISO 17081 [201] [202] International standard, must be examined in order to measure the hydrogen diffusion coefficient. In particular, steady state and transient permeation currents can be analyzed only once the background current, generally related to the passivity current density (i_P) detected by the potentiostat in the oxidation cell, has been subtracted from the total anodic current density (i_a).

Different methods are available to calculate hydrogen diffusion coefficient based on the test results, usually if hydrogen diffusion correctly follows Fick's second law for pure (ideal) diffusion or, anyway, if only reversible trapping is significant, and the permeation transient can still be accurately represented by this law. Hydrogen diffusivity can vary even by one order of magnitude in relation to the method implemented for its derivation [163] [208]. The principal methods provided are:

- Time-lag
- Breakthrough, inflection point and half-rise time
- Fourier
- Laplace
- CANMET.

The time-lag method is certainly the simplest and diffused method. As reported by Devanathan and Stachurski [200], the time-lag (t_{lag}) is defined as the necessary period to reach a current density equal to 63% of the steady state permeation flux (Φ_∞), using a graphical extrapolation to the time axis of the total amount of hydrogen that has diffused through the metal specimen *(Figure 4.1)*. The value of the diffusion coefficient can be easily obtained from the following equation *(eq. 24)*:

$$D_l = \frac{L^2}{6 \cdot t_{lag}} \qquad \text{(eq. 24)}$$

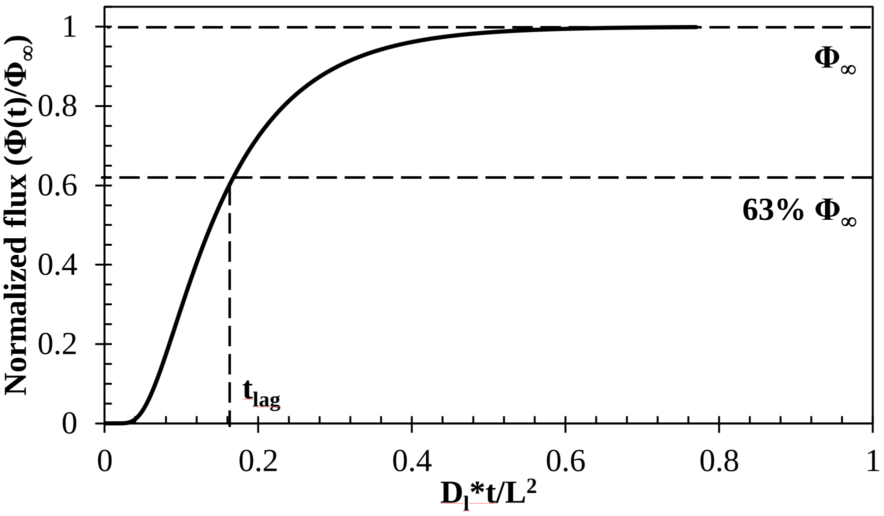

Figure 4.1. Graphic method for the extrapolation of the time-lag (t_{lag})

The breakthrough time method is based on the identification of the necessary time (t_b) for diffusing hydrogen to be detected in the oxidation cell, at the exit surface of the specimen. The ISO 17081:2014 [201] standard indicates that the breakthrough time (t_b) represents the *"elapsed time measured by extrapolating the linear portion of the rising permeation current transient"*. In other words, this value is an approximation of the intersection between the time axis and the tangent to the permeation curve at the inflection point *(Figure 4.2)*. The equation that relates t_b and D_l is as follows *(eq. 25)*:

$$D_l = \frac{L^2}{15.3 \cdot t_b} \qquad \text{(eq. 25)}$$

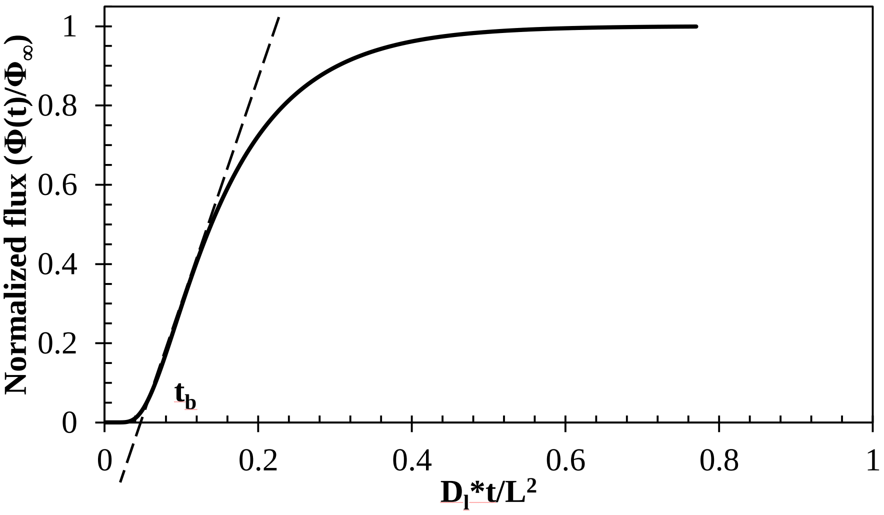

Figure 4.2. Graphic method for the extrapolation of the breakthrough time (t_b)

The inflection point time method is based on the graphic determination of the inflection point present in the transient of the permeation curve *(Figure 4.3)*. The equation correlating t_{ip} and D_l is (eq. 26):

$$D_l = 0.024 \cdot \frac{L^2}{\pi^2 \cdot t_{ip}} \qquad \textit{(eq. 26)}$$

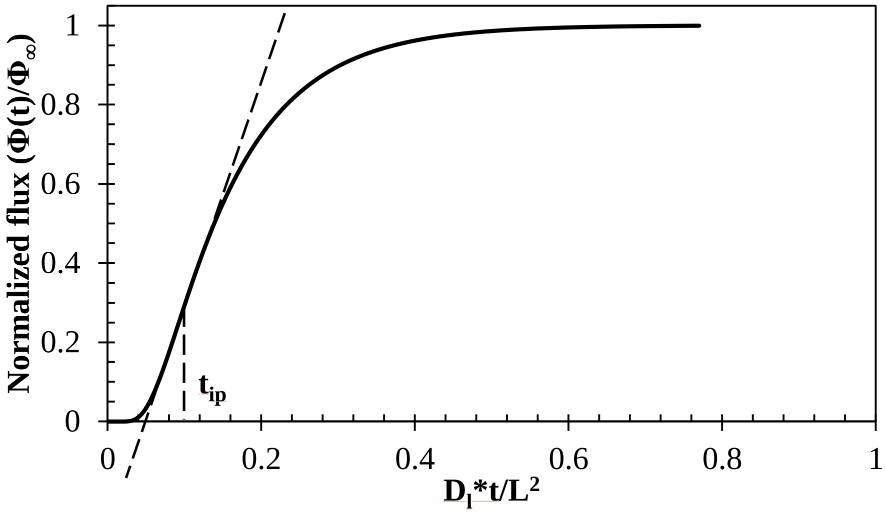

Figure 4.3. Graphic method for the extrapolation of the inflection point time (t_{ip})

The half-rise time method takes into consideration the necessary time for the current density to reach a value equal to 51% Φ_∞, so that the first half of the transient is completed *(Figure 4.4)*. The equation utilized in this case is the following *(eq. 27)*:

$$D_l = \frac{0.04 \cdot L^2}{t_{hr}} \qquad \textit{(eq. 27)}$$

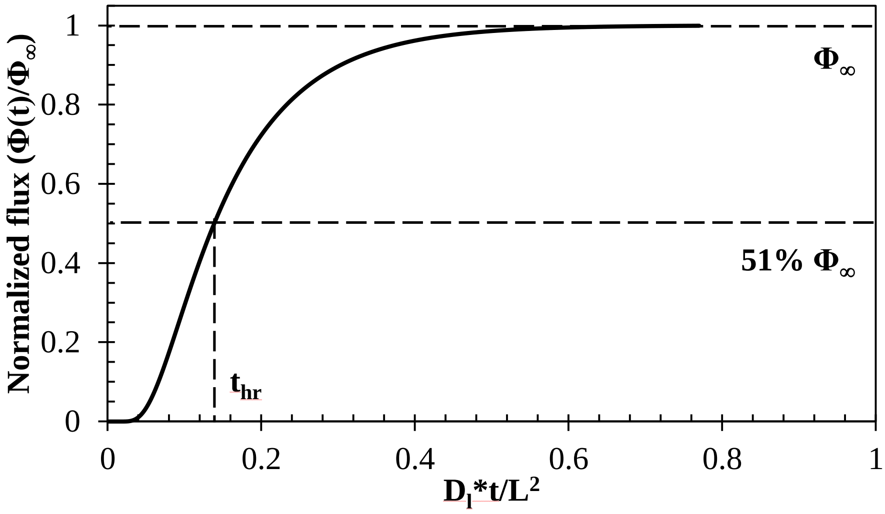

Figure 4.4. Graphic method for the extrapolation of the half-rise time (t_{hr})

Concerning the Fourier method, it is necessary to consider the Fourier solution previously exposed *(eq. 16)*, in order to obtain *(eq. 28)*:

$$\frac{\Phi(t)}{\Phi_\infty} = 1 - exp\left(\frac{\pi^2 D_l t}{L}\right) \qquad \textit{(eq. 28)}$$

From this equation, D_l can be derived from the slope of the plot of: ln(1-Φ(t)/Φ∞) against time (t), for

$\Phi > 0.3*\Phi_\infty$ *(Figure 4.5(a))*.

As regards the Laplace method, it is necessary to consider the Laplace solution previously exposed *(eq. 17)*, in order to have *(eq. 29)*:

$$\frac{\Phi(t)}{\Phi_\infty} = \frac{2}{\sqrt{\pi}} \cdot \frac{L}{\sqrt{D_l \cdot t}} \cdot exp\left(-\frac{L^2}{4 \cdot D_l \cdot t}\right) \qquad \textit{(eq. 29)}$$

Then *(eq. 30)*:

$$ln\left(\Phi(t) \cdot \sqrt{t}\right) = Constant - \frac{L^2}{4 \cdot D_l \cdot t} \qquad \textit{(eq. 30)}$$

From this relation, D_l can be derived from the slope of the plot of: $\ln(\Phi(t)*t^{0.5})$ against time (t^{-1}), for $\Phi < 0.965*\Phi_\infty$ *(Figure 4.5(b))*.

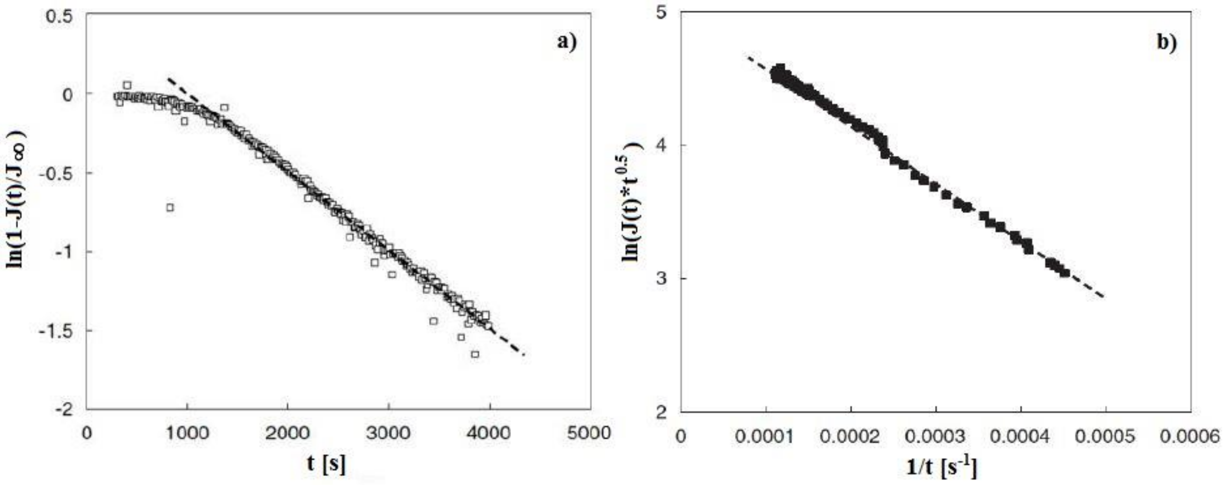

Figure 4.5. Fourier (a) and Laplace (b) methods for the determination of hydrogen diffusion coefficient [141]

Finally, the method proposed by Canadian CANMET researchers [128] differs from the previous methods because the calculation of D_l does not refer to a single point of the permeation curve, but uses any two points of this. In agreement with McBreen and other researchers [128], it is possible to affirm that the effect of factors that can vary the value of Φ_∞ is negligible in the first part of the permeation transient, allowing an estimate of the diffusion coefficient that is valid for any test condition.

The CANMET method is based on this theoretical assumption and has to be applied to the initial portion of the permeation curve, as shown in *Figure 4.6*.

The hydrogen diffusion coefficient is derived from the following *(eq. 31)*:

$$\frac{\Phi(t_1)}{\Phi(t_2)} = \sqrt{\frac{t_2}{t_1}} \cdot exp\left[-\frac{L^2}{4 \cdot D_l} \cdot \left(\frac{1}{t_1} - \frac{1}{t_2}\right)\right] \qquad \textit{(eq. 31)}$$

According to this method, four values of current density, corresponding to 5, 10, 15 and 20% of the maximum value, and the related times are identified, which are entered in pairs in the previous equation to obtain the value of the diffusion coefficient. From the arithmetical average of the six values thus obtained, the average value of the diffusion coefficient is then obtained.

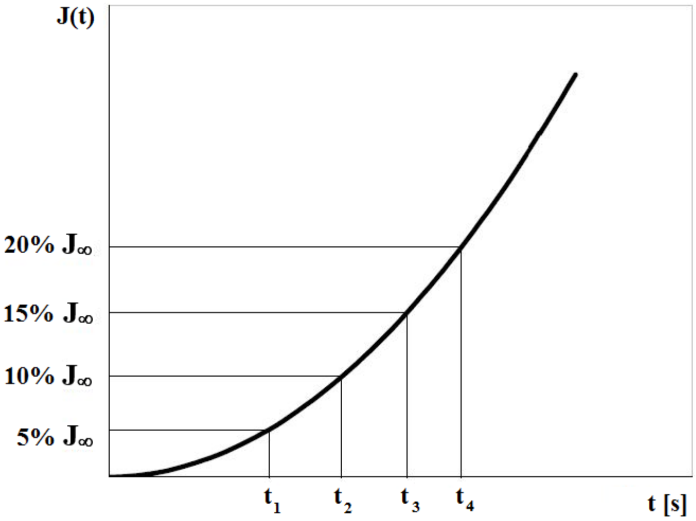

Figure 4.6. CANMET method for the determination of hydrogen diffusion coefficient

4.3 Non-ideal diffusion (presence of trapping)

In the presence of trapping, Fick’s second law does not describe adequately the phenomenon of hydrogen diffusion through a specimen, since this phenomenon is inevitably delayed. Many theories, based on different assumptions for the modelling of hydrogen transport and developed in order to take into consideration the trapping effect, have permitted a deeper analysis of hydrogen diffusion through a metal membrane in the presence of traps. Since its first discovery, hydrogen trapping has been validated with both experimental and theoretical results. Nowadays, trapping phenomena in metals and the connection with hydrogen embrittlement have not been fully understood yet.

Probably, the existence of trapping phenomena was firstly proposed by Darken and Smith in 1949 [209], who stated that the delayed hydrogen diffusion in cold worked steels, evaluated by means of measurements on the permeation transient, was due to attractive interactions between dissolved hydrogen in the lattice and imperfections in the microstructure, i.e. trapping sites.

The two main effects related to trapping are that of decreasing the apparent diffusivity and that of increasing the hydrogen solubility. When in equilibrium with a constant external source of hydrogen, an iron-base alloy will absorb hydrogen until the lattice solubility limit, and then the trapping sites are occupied by additional hydrogen. Finally, only when hydrogen populations of lattice and trapping sites are simultaneously balanced to each other and to the external source of hydrogen, equilibrium has been reached. Therefore, the total hydrogen concentration (C_{TOT}) may be significantly higher than the hydrogen concentration in the lattice (C_0) [165] [170] [210] [163]. Consequently, considering these trapping sites acting substantially as sources or “sinks” for hydrogen atoms, Fick’s second law is no longer valid and a deeper analysis with the implementation of mathematical models in essential.

4.3.1 McNabb and Foster

The effect of trapping on hydrogen diffusion was first formally modelled by McNabb and Foster [162]. The approximation developed by the two researchers stated that hydrogen trapping sites can be catalogued into two different groups, in accordance with the tenacity with which these retain the captured hydrogen atom. The traps included in the first group are shallow enough to have an irrelevant delaying effect, while those included in the second group are so deep that their trapped hydrogen can be considered as permanently removed from the diffusion process.

The first step consisted in considering the density of reversible traps (N), per unit volume, and the occupied fraction of the reversible traps (θ). It was then supposed that these active trapping sites could be expressed by the two parameters p and k.

The parameter p represents the average probability that a reversible trap, included in the first group, which is retaining a hydrogen atom, will release it before 1 second has passed. This probability of release is dependent on temperature and nature of the trap, but not dependent on the local concentration of trapped and diffusing hydrogen. The number of hydrogen atoms released in 1 second in the small volume δV is directly proportional to the number of occupied trapping sites; therefore, this is given by the relation: p*θ*N*δV. The probability that the active trapping sites in the volume δV will capture a hydrogen atom is proportional to the diffusible hydrogen concentration (C) and to the number of empty traps (N*(1-θ)) available for hydrogen absorption, per unit volume.

The parameter k represents a trapping coefficient, so that the number of hydrogen atoms retained every second in a small volume δV is equal to: k*C*N*(1-θ)*δV.

The solutions obtained by McNabb and Foster define hydrogen diffusion through a medium that contains reversible trapping sites, as presented in the following *(eq. 32)*:

$$\left(\frac{\partial C}{\partial t}\right) + N \cdot \left(\frac{\partial \theta}{\partial t}\right) = D_l \cdot \left(\frac{\partial^2 C}{\partial x^2}\right) \quad \textit{(eq. 32)}$$

In the small volume δV, the increase rate in the number of hydrogen atoms *(eq. 33)* among the trapped population can be equalized to the difference between the capture rate and the release rate; therefore:

$$\frac{\partial \theta}{\partial t} = k \cdot C \cdot (1 - \theta) - p \cdot \theta \qquad \textit{(eq. 33)}$$

Considering non-dimensional variables for a slab of finite thickness (L), it is possible to write:

$$u = \frac{C}{C_0}; \quad \omega = N \cdot \frac{\theta}{C_0}; \quad \nu = C_0 \cdot k \cdot \frac{L^2}{D_l}; \quad \tau = D_l \cdot \frac{t}{L^2}; \quad \lambda = N \cdot k \cdot \frac{L^2}{D_l}; \quad \mu = p \cdot \frac{L^2}{D_l}$$

Thus, *(eq. 32)* and *(eq. 33)* become *(eq. 34)* and *(eq. 35)*:

$$\left(\frac{\partial u}{\partial \tau}\right)+\left(\frac{\partial \omega}{\partial \tau}\right)=\left(\frac{\partial^2 u}{\partial x^2}\right) \qquad \text{(eq. 34)}$$

$$\frac{\partial \omega}{\partial \tau}=\lambda \cdot u-\nu \cdot u \cdot \omega-\mu \cdot \omega \qquad \text{(eq. 35)}$$

If C_0 is small enough, compared to N, the behavior is governed by the linear system *(eq. 36)*:

$$\frac{\partial \omega}{\partial \tau}=\lambda \cdot u-\mu \cdot \omega \qquad \text{(eq. 36)}$$

Moreover, in relation to the steady state hydrogen flux (Φ_∞), McNabb and Foster demonstrated that the ratio between the average hydrogen content (Q_0) with the concentration varying linearly throughout the membrane, and the average quantity (Q_1) necessary for the saturation of the same membrane to a uniform concentration C_0, is not equal to 0.5 as stated by the classical theory, but:

$$0.5 \ll \frac{Q_0}{Q_1} \ll 1$$

From this relation, the ratio is equal to 0.5 if $k \ll p$, while it tends to a maximum value between 0.5 and 1 if k/p increases and, finally, it decreases to 0.5 again if $k \gg p$.

In addition, the two researchers also showed that the hydrogen flux ($\Phi(t)$), at any instant time τ and through a surface of area S_0, is governed by the following *(eq. 37)*:

$$F(\tau)=\frac{C_0 \cdot D_l}{L} \cdot \iint_S \left(\frac{\partial u}{\partial \theta} \cdot dS\right) \qquad \text{(eq. 37)}$$

For $\tau \rightarrow \infty$, the hydrogen flux reaches a constant value; therefore, the total amount of hydrogen that has diffused through the surface S_0 in the time τ, expressed by its integral over time, tends to an asymptote. Then, the intercept of the asymptote *(eq. 38)* on the time axis (τ) permits to determine D_l:

$$t_{lag}=t_L \cdot \frac{D_l}{L^2}=\frac{1}{6}+\frac{\alpha}{2\beta}+\frac{\alpha}{\beta^2}-\frac{\alpha}{\beta^3} \cdot (1+\beta) \cdot log(1+\beta) \qquad \text{(eq. 38)}$$

With: $\alpha=\frac{N \cdot k}{p}$ and $\beta=\frac{C_0 \cdot k}{p}$ *(eq. 39)*

Finally, in order to obtain D_l from the previous equation, it is necessary the measurement or estimate of the following parameters: n, k, p and C_0.

In the case of thick membranes and low hydrogen concentrations, D_{app} is linked to D_l by *(eq. 40)*:

$$\frac{D_l}{D_{app}}=1+\frac{k}{p} \cdot N \qquad \text{(eq. 40)}$$

In relation to the variation of the diffusion coefficient during the permeation test, these two authors affirmed that D_{app} in the previous *(eq. 40)* is not only smaller than D_l, but also decreases as N increases. Anyway, a relevant concept they highlighted is that the values of D_{app} determined from the initial transient are likely to be closer to the actual values of D_l than the values calculated from the end of the desorption curve.

4.3.2 Oriani

In 1970, Oriani [153] affirmed that the local hydrogen equilibrium, at any stage of hydrogen diffusion, exists between two kinds of available sites: interstitial sites of the metal lattice (Normal Interstitial Lattice Sites, or NILS) and reversible trapping sites (lattice imperfections, such as dislocations [170], vacancies [186], grain boundaries [187], interfaces [188] [189], voids [190] and carbides [56]), which represent an energetically favored environment for hydrogen occupancy [56] [188] [166] [211].

He stated also that, although dislocations are tenacious trapping sites, solid-solid interfaces represent the most significant microstructural sites in non-cold worked steels for hydrogen trapping. Thus, with an increase in the cold working, micro-crack surfaces become much more important over the expanded dislocation net.

Therefore, Oriani modified Fick's first law for pure diffusion assuming that, in the majority of the experimental tests, D_l and C_0 can no longer be deemed sufficient to analyze hydrogen transport.

The following equation was proposed *(eq. 41)*:

$$\Phi = -D_{app} \cdot \frac{dC_{TOT}}{d_x} \qquad \textit{(eq. 41)}$$

With: D_{app} = apparent diffusion coefficient; C_{TOT} = total hydrogen concentration. The correlation between D_l and D_{app} was made possible by the assumption of local equilibrium between lattice and trapping sites. Thus, the two finite populations occupy a fraction θ_i of the available sites, and the equilibrium between these is defined by the constant: $k = a_t / a_l$, where a_t represents the hydrogen activity in the trapping sites and a_l the hydrogen activity in the lattice sites.

In addition, assuming no interactions between the occupied sites, both a_t and a_l can be written in terms of fractional occupancies: $a_i = \theta_i / (1-\theta_i)$; the reference state is: $a_i = \theta_i$ when $\theta_i \rightarrow 0$.

Because he assumed only very low lattice hydrogen concentrations, the result is that $\theta_i<1$; the equilibrium constant for hydrogen reaction in lattice and trapping sites was expressed as *(eq. 42)*:

$$k = \frac{1}{\theta_l} \cdot \left(\frac{\theta_t}{1-\theta_t}\right) \qquad \textit{(eq. 42)}$$

The lattice and the apparent diffusivity can be related by the following *(eq. 43)*:

$$D_{app} = \frac{D_l}{\left[1 + \frac{k \cdot N_l \cdot N_t}{(N_l + k \cdot C_0)^2}\right]} = \frac{D_l}{\left[\frac{C_0}{C_0 + C_t \cdot (1-\theta_t)}\right]} \qquad \textit{(eq. 43)}$$

This model involves the necessary assumptions of the presence of only reversible trapping sites, the low trap occupancy and the stability of the domain of local equilibrium for the analyzed system [153] [151] [212]. Moreover, this model considers only one type of trapping site, and each trap is considered saturable and able to hold only one hydrogen atom [153] [151]. Under these conditions, the equation for the calculation of D_{app} *(eq. 44)* can be written as [153] [53] [213] [214]:

$$D_{app} = \frac{D_l}{\left[1 + \frac{N_r \cdot k_r}{p_r}\right]} = \frac{D_l}{\left[1 + \frac{N_r}{N_l} \cdot e^{\left(\frac{-E_b}{R \cdot T}\right)}\right]} \qquad \textit{(eq. 44)}$$

With: k_r = capture rate; p_r = release rate for each reversible trap; N_l [sites/cm^3] = number of lattice sites; N_r [sites/cm^3] = number of reversible traps.

Considering the Arrhenius equation, the binding energy (E_b) and the lattice activation energy (E_l), a modification of the expression is provided *(eq. 45)*:

$$D_{app} = D_l \cdot \frac{N_l}{N_r} \cdot e^{\left(\frac{-E_b}{R \cdot T}\right)} = D_0 \cdot \frac{N_l}{N_r} \cdot e^{\left(\frac{-(E_t + E_l)}{R \cdot T}\right)} \qquad \textit{(eq. 45)}$$

Since atomic hydrogen primarily occupies tetrahedral interstitial sites in bcc-iron at common room temperatures ($T < 100$ °C [157]), with a corresponding value of $N_l = 5.23 * 10^{23}$ sites/cm^3, *(eq. 44)* can be modified [143] [214] [215] [216] [217] to give the following *(eq. 46)*:

$$ln\left(\frac{D_l}{D_{app}} - 1\right) = ln\left(\frac{N_r}{N_l}\right) + \frac{E_b}{R \cdot T} \qquad \textit{(eq. 46)}$$

In particular, when the D_{app} values are obtained for a certain material at different temperatures (at least for three different temperatures), a plot of the left value of the previous equation against the inverse of the temperature (T^{-1}) should fit to a straight line, characterized by the known values of slope (a) and intercept (b). Thus, D_{app} can be plotted against the inverse of temperature, allowing the estimate of the Arrhenius line by means of regression, and the reversible trap density ($N_{t,r}$) and binding energy (E_b) can be easily derived [3] [151] [218].

4.3.3 Caskey and Pillinger

In the work proposed in 1974, Caskey and Pillinger [219] found an approximate solution of the McNabb and Foster's non-linear partial differential equations [162] in the presence of reversible traps. They applied the finite difference method to these equations; thus, as to describe the rates of trapping and releasing atoms from the traps, three non-dimensional parameters were used in *(eq. 34)*. In particular, if all these parameters are equal to zero, *(eq. 34)* reduces to that valid for pure diffusion, governed by the lattice diffusivity, while, if μ is equal to zero, *(eq. 34)* describes irreversible trapping. *Figure 4.7* shows how the increase in both the k/p ratio and the trap density (N) determines a significant decrease in the permeation rate, governed by D_{app}, and delays the achievement of the steady state, which is reached even after long periods. It can also be seen that the trapping phenomena produce no variations in the steady state flux, which is comparable to the steady state value (i_∞) reached in the case of pure diffusion. Anyway, in the presence of reversible trapping phenomena, D_{app} is undoubtedly lower than D_l.

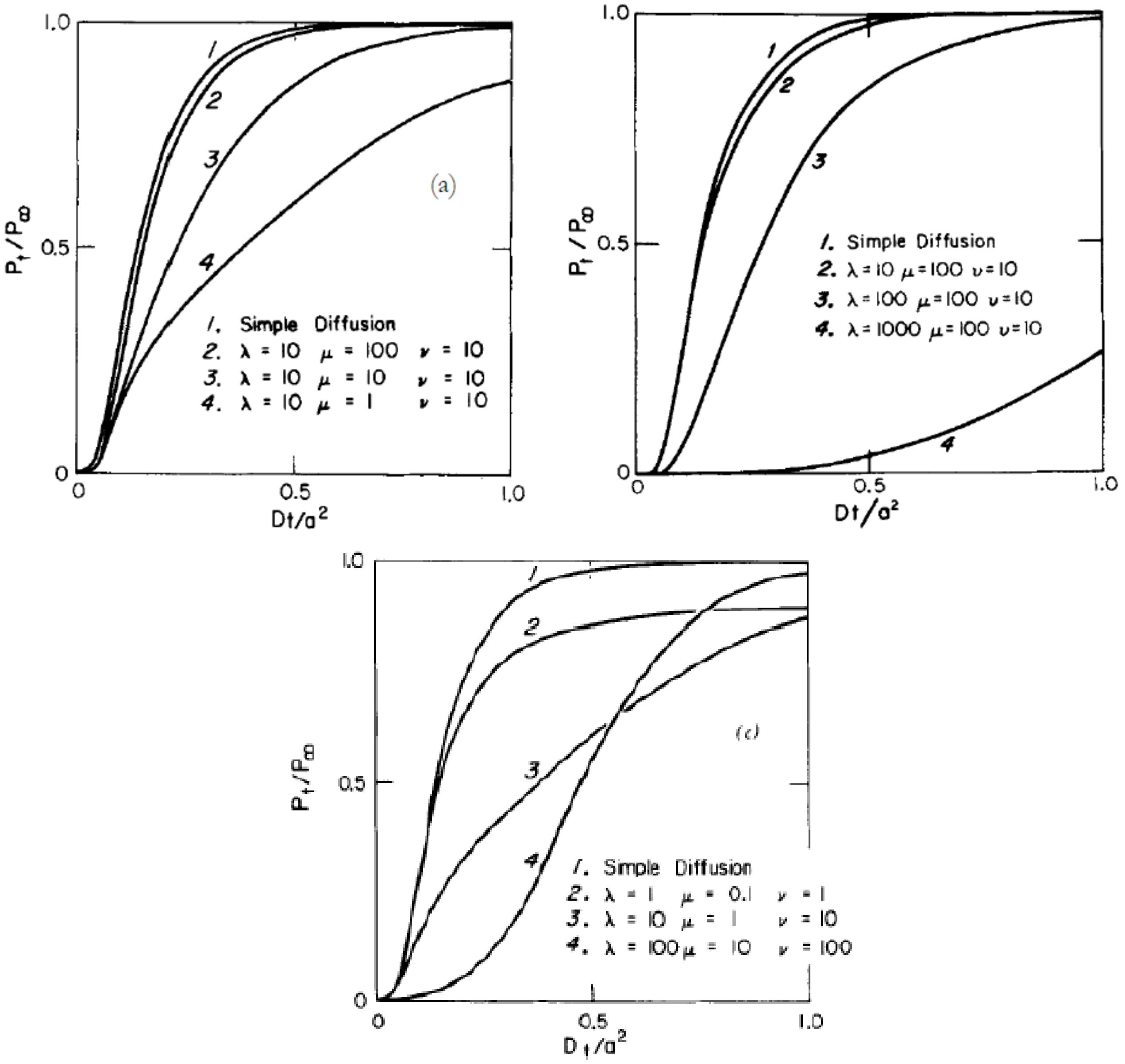

Figure 4.7. Hydrogen permeation transients for: a) Increasing λ/μ ratio (Constant trap density); b) Increasing trap density (Constant trap and release rates); c) Increasing λ, μ and ν (Constant λ/μ ratio) [219]

4.3.4 Thomas and Stern

The numerical model developed by Thomas and Stern [220] aimed to make the previous system introduced by McNabb and Foster [162] as efficient as possible, also by optimizing the computing time. They considered the method determined by Caskey and Pillinger [219]; their approach involved other dimensionless equations (*(eq. 47)* and *(eq. 48)*), starting from the model of McNabb and Foster:

$$\left(\frac{\partial u}{\partial \tau}\right) + \beta \cdot \left(\frac{\partial \gamma}{\partial \tau}\right) = \left(\frac{\partial^2 u}{\partial x^2}\right) \qquad \textit{(eq. 47)}$$

$$\frac{\partial v}{\partial \tau} = \nu \cdot u - v \cdot u \cdot \gamma - \mu \cdot v \qquad \textit{(eq. 48)}$$

With the non-dimensional parameters: τ, u, μ, ν defined by the previous equations, respectively, while the newly-introduced parameter β represents the number of traps per each hydrogen atom *(eq. 49)*:

$$\beta = \frac{N}{K} \qquad \textit{(eq. 49)}$$

λ has been replaced by β*ν and ω has been replaced by β*γ, where the parameter γ can be determined from the previous equation using the following *(eq. 50)*:

$$\gamma = K \cdot \frac{\theta}{C_0} \qquad \textit{(eq. 50)}$$

The two researchers affirmed that these dimensionless parameters reflect with very good accuracy the physical parameters N, ρ, and k. The previous equations (*(eq. 47)* and *(eq. 48)*) were substituted by the following finite-difference system (*(eq. 51)* and *(eq. 52)*):

$$u_m^{n+1} - u_m^n + \beta \cdot (v_m^{n+1} - v_m^n) = \frac{r}{2} \cdot (u_{m-1}^{n+1} - 2 \cdot u_m^{n+1} + u_{m+1}^{n+1}) + \frac{r}{2} \cdot (u_{m-1}^n - 2 \cdot u_m^n + u_{m+1}^n) \qquad \textit{(eq. 51)}$$

$$v_m^{n+1} - v_m^n = \frac{a}{2} \cdot (\nu \cdot u_m^{n+1} - \mu \cdot v_m^{n+1} - \nu \cdot u_m^{n+1} \cdot v_m^{n+1}) + \frac{a}{2} \cdot (\nu \cdot u_m^n - \mu \cdot v_m^n - \nu \cdot u_m^n \cdot v_m^n) \qquad \textit{(eq. 52)}$$

Where u_m^n, v_m^n represent u(mh, na), v(mh, na) in the range: m ϵ M = {1, …M-1}, n = {0, 1, …}. M = 1/h, where h represents the x-step, a is the time-step and φ is the mesh ratio provided by the following *(eq. 53)*:

$$\varphi = \frac{a}{h^2} \qquad \textit{(eq. 53)}$$

Thomas and Stern removed the non-linearity parts of u_m^{n+1} *(eq. 51)* using Taylor expansions. The boundary conditions for u are given as follows *(eq. 54)*:

$$n = \{0,\ 1,\ \ldots\} \qquad u_0^n = 1; \quad u_m^n = 0 \qquad \textit{(eq. 54)}$$

The initial conditions for u and v are *(eq. 55):*

$$m \in M = \{1,\ \ldots M\text{-}1\} \qquad u_m^0 = v_m^0 = 0 \qquad \textit{(eq. 55)}$$

A consequent variation in the previous finite-difference system (*(eq. 51)* and *(eq. 52)*), similar to that performed by Caskey and Pillinger [219], was then applied as follows (*(eq. 56)* and *(eq. 57)*):

$$-\frac{r}{2} \cdot u_{m-1}^{n+1} + K_m \cdot u_m^{n+1} - \frac{r}{2} \cdot u_{m+1}^{n+1} = C_m \qquad \textit{(eq. 56)}$$

$$v_m^{n+1} = R_m \cdot u_m^{n+1} + S_m \qquad \textit{(eq. 57)}$$

With:

$$R_m = \frac{z_m}{d_m} \qquad \textit{(eq. 58)}$$

$$d_m = 2 + a \cdot (\mu + \nu \cdot u_m^n) \tag{eq. 59}$$

$$z_m = a \cdot \nu \cdot (1 - v_m^n) \tag{eq. 60}$$

$$K_m = 1 + r + \beta \cdot R_m \tag{eq. 61}$$

$$C_m = \frac{r}{2} \cdot (u_{m-1}^n + u_{m+1}^n) + (2 - K_m) \cdot u_m^n + \frac{2 \cdot a \cdot \beta \cdot \mu \cdot v_m^n}{d_m} \tag{eq. 62}$$

$$S_m = \frac{(2 - a \cdot \mu) \cdot v_m^n + a \cdot \nu \cdot u_m^n}{d_m} \tag{eq. 63}$$

With the use of the boundary conditions *(eq. 54)* of the equation it is possible to simplify the previous equation *(eq. 56)* as follows *(eq. 64)*:

m = {1, ...M} $$u_m^{n+1} = A_m \cdot u_{m-1}^{n+1} + B_m \tag{eq. 64}$$

Finally, the equations describing the system by Thomas and Stern (*(eq. 65)* and *(eq. 66)*) can be directly obtained by inserting *(eq. 64)* in *(eq. 57)*:

m ϵ M = {1, ...M-1} $$A_m = \frac{r}{2 \cdot K_m - r \cdot A_{m+1}} \tag{eq. 65}$$

m ϵ M = {1, ...M-1} $$B_m = \frac{2 \cdot C_m + r \cdot B_{m+1}}{2 \cdot K_m - r \cdot A_{m+1}} \tag{eq. 66}$$

In their work, this system is claimed to provide more accurate results using approximately only 20% of the computing time; the results of the normalized flux against time are shown in *Figure 4.8*.

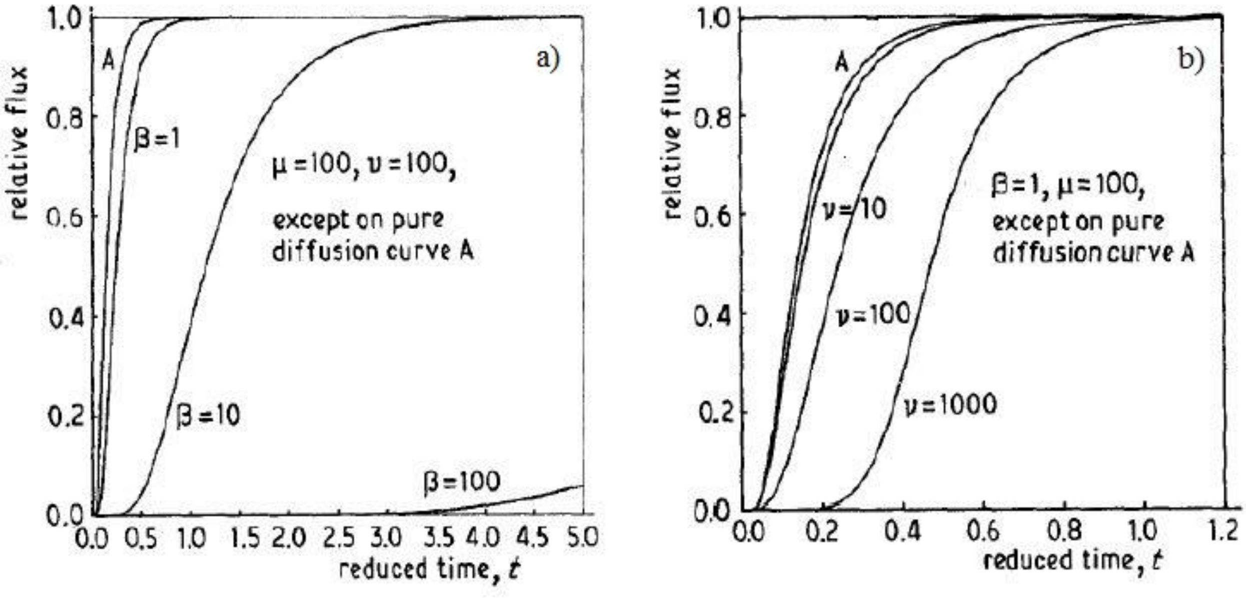

Figure 4.8. Normalized flux against reduced time, with: a) Increasing β in the graph on the left; b) Increasing v in the graph on the right. Adaptation from the literature [220]

4.3.5 Iino

In 1982, Iino [221] [222] proposed a model for describing hydrogen diffusion in the presence of trapping sites, including parameters for both reversible and irreversible traps. He modified the McNabb and Foster [162] equation, which considered only reversible trapping sites, and he introduced other terms in the equation describing irreversible trapping sites.

Thus, the following equations (*(eq. 67)* and *(eq. 68)*) in a non-dimensional form were presented:

$$\frac{\partial u}{\partial \tau}+\frac{\partial \omega}{\partial \tau}+\frac{\partial v}{\partial \tau}=\frac{\partial^2 u}{\partial x^2} \qquad \textit{(eq. 67)}$$

$$\frac{\partial v}{\partial \tau}=k \cdot u \cdot (1-\theta_{ir}) \qquad \textit{(eq. 68)}$$

With:

$$u=\frac{C}{C_0}; \quad \omega = N_{ir}\cdot\frac{\theta_{ir}}{C_0}; \quad v=C_0\cdot k_{re}\cdot\frac{L^2}{D_l}; \quad \tau = D_l\cdot\frac{t}{L^2}; \quad k=N_{ir}\cdot k_{ir}\cdot\frac{L^2}{D_l}$$

The solution for hydrogen diffusion in a medium with homogeneously distributed traps through the exit surface of a metal membrane [221], in the case of low hydrogen concentrations, is *(eq. 69)*:

$$j(0,\tau)=\frac{\sqrt{k}}{sinh\sqrt{k}}+\sum_{n=1}^{\infty}(-1)^n\frac{2n^2\pi^2}{s_n^-\cdot\left[1+\frac{\lambda\cdot\mu}{(s_n^- -\mu)^2}\right]}\cdot e^{-s_n^-\cdot\tau} \qquad \textit{(eq. 69)}$$
$$+\sum_{n=1}^{\infty}(-1)^n\frac{2\cdot n^2\cdot\pi^2}{s_n^+\cdot\left[1+\frac{\lambda\cdot\mu}{(s_n^+ -\mu)^2}\right]}\cdot e^{-s_n^+\cdot\tau}$$

Where:

$$s_n^{\pm}=\frac{1}{2}\cdot\left[n^2\cdot\pi^2+k+\lambda + \mu \pm\sqrt{(n^2\cdot\pi^2+k+\lambda-\mu)^2+4\cdot\lambda\cdot\mu}\right] \qquad \textit{(eq. 70)}$$

$$\lambda = N_{re}\cdot k_{re}\cdot\frac{L^2}{D_l} \qquad \textit{(eq. 71)}$$

$$\mu = p_{re}\cdot\frac{L^2}{D_l} \qquad \textit{(eq. 72)}$$

From hydrogen permeation transients reported in *Figure 4.9*, it is possible to see how the irreversible trapping phenomena, affecting the first transients, lead to an increased break-through time (t_b).

The “double-plateau” behavior, which in this model is claimed to be an effect of the reversible trapping phenomena, can be observed in transient number 4 in the graph on the right. This curve exhibits an increase at a high rate, then flattens out for a while before increasing again at a high rate. Iino stated that this behavior is due to sufficiently small values of μ. In both graphs, the “Fourier” curves represent the Fourier solution to Fick’s second law.

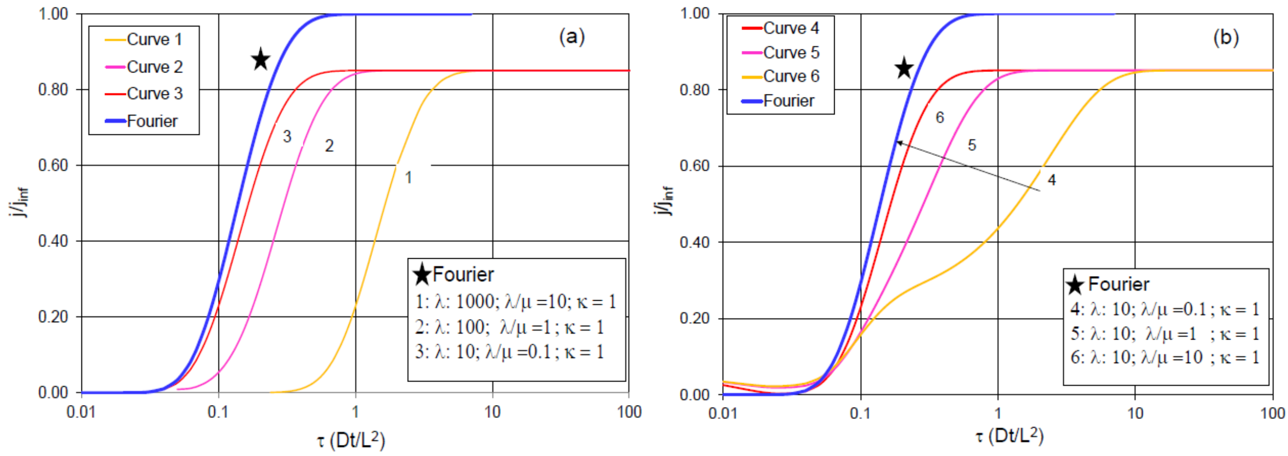

Figure 4.9. Hydrogen permeation transients in a medium containing both reversible and irreversible trapping sites. Adaptation from the literature [221]

4.3.6 Leblond and Dubois

A further general equation for hydrogen diffusion, based on a statistical treatment of the random movements of hydrogen atoms, was obtained by Leblond and Dubois [223] [224] [177]. They took into consideration the probability g(r, r', t) that an atom of hydrogen, located in a certain site r at the time t, will jump into another site r' (located in a volume d^3r' around r') during the period [t, t + dt]. Therefore, they catalogued the traps in m classes, where class 1 included ordinary sites, while the other classes (from 2 to m) consisted of different trapping sites, each one identified by a specific volume (p_l) and hydrogen concentration (n_k).

Anyway, the resulting equation depended on too many unknown parameters, so they affirmed that: *"The physical interpretation of the different terms of the equations is not obvious and, moreover, that for practical purposes, equations contain too many parameters, and that one must look for simplified assumptions to reduce their number."*

They came to a simplified equation *(eq. 73)* only after the application of mathematical operations:

$$\frac{\partial n_k}{\partial t} = -\frac{n_k}{\tau_k} + \sum_{l=1}^{m} \frac{p_l \cdot n_l}{\tau_l} + \sum_{l=1}^{m} \nabla\left[D_l \cdot S_l \cdot \nabla\left(\frac{p_l \cdot n_l}{S_l}\right)\right] \qquad \textit{(eq. 73)}$$

If lattice diffusivity and hydrogen solubility are assumed uniform in the whole material (the latter hypothesis will not be valid if a stress gradient is present), the transport equations (from *(eq. 74)* to *(eq. 76)*) proposed by Leblond and Dubois [223] [224] [177] can be simplified ad follows:

$$\frac{\partial n_1}{\partial t} = D_1 \cdot \frac{\partial^2 n_1}{\partial x^2} + p_2 \cdot \frac{n_2}{\tau_2} - p_2 \cdot \frac{n_1}{\tau_1} \cdot \left[1 - \frac{n_2}{n_2^s}\right] - p_3 \cdot \frac{n_1}{\tau_1} \cdot \left[1 - \frac{n_3}{n_3^s}\right] \qquad \textit{(eq. 74)}$$

$$\frac{\partial n_2}{\partial t} = \frac{n_1}{\tau_1} \cdot \left[1 - \frac{n_2}{n_2^s}\right] - n_2 \cdot \tau_2 \qquad \textit{(eq. 75)}$$

$$\frac{\partial n_3}{\partial t} = \frac{n_1}{\tau_1} \cdot \left[1 - \frac{n_3}{n_3^s}\right] \qquad \textit{(eq. 76)}$$

With: n_1 = hydrogen concentration in diffusion sites; n_2, n_3 = number of hydrogen atoms in trapping sites of type 2 or 3 divided by the volume of those sites; p_2, p_3 = volumetric proportion of trapping sites of type 2 or 3, respectively; τ_2, τ_3 = average transfer times from a site of type 2 or 3 to another site, related to the residence time in each site if the time spent in jumping to another site is comparatively short; n_3^s = saturation concentration of hydrogen atoms in sites of type 3.

Under steady state conditions, the time derivatives are equal to zero; consequently, equation *(eq. 74)* reduces itself to Laplace equation *(eq. 77)*:

$$\frac{\partial^2 n_1}{\partial x^2} = 0 \qquad \textit{(eq. 77)}$$

The solution to this equation produces a linear relationship between n_1 and x. An analytical solution to the previous equations (from *(eq. 74)* to *(eq. 76)*) is not possible, mainly due to the characteristic of non-linearity of *(eq. 76)* for the product of n_1 and n_3, but a numerical analysis is currently studied.

5

EFFECT OF DEFORMATION ON HYDROGEN PERMEABILITY

5.1 Analysis of literature works

A generic stress field into a metallic material may influence hydrogen diffusivity in different ways, depending on the fact that the stress can be tensile or compressive, and that the material can remain in the elastic deformation field or undergo plastic deformation.

In particular, it is well known from thermodynamics that a tensile stress determines a decrease in hydrogen chemical potential and an increase in hydrogen solubility. A compression stress, instead, causes an increase in hydrogen chemical potential [178] [179] and a decrease in hydrogen solubility [225]; therefore, as stated by Bockris et al. [179], this fact suggests the possibility of reducing or eliminating HE phenomena.

In elastic deformation conditions, hydrogen diffusivity and the related permeation flux are expected to increase, due to the lattice expansion.

In plastic deformation conditions, the newly formed dislocations act as trapping sites; thus, as the number of trapped hydrogen atoms increases [226], hydrogen diffusivity significantly decreases [169] [227], while hydrogen solubility and break-through time (t_b) considerably increase.

The steel considered in this Thesis work is immune to HE under static load conditions, but this condition may be less under slow continuous plastic deformation or during corrosion-fatigue tests, in the presence of a cathodic over-protection. In particular, susceptibility to HE increases with decreasing E_P and strain rate. Under slow deformation conditions, the hydrogen permeation flux decreases as the strain rate increases, because of the prevailing of the trapping effect [67].

The effect of stress fields and elasto-plastic deformations on hydrogen diffusivity parameters was first analyzed by Troiano [85], who stated that hydrogen diffusion towards regions characterized by a high tri-axial stress is of major relevance in the failure mechanism due to HE of high strength steels. De Kazinczy [228] found that a uni-axial tensile stress increased the steady state hydrogen permeation flux in mild steel; a similar effect was discovered in 1966 by Beck et al. [174].

Later, Oriani [229] affirmed that the application of a compressive stress should determine an increase in hydrogen chemical potential and, consequently, a decrease in its solubility. This result was confirmed by Bockris et al. [179] who showed that, for Armco iron and AISI 4340, a compressive stress determined a decrease in the steady state permeation flux of the same magnitude as the increase detected after the application of an equivalent tensile stress. Thanks to these studies, an elastic tensile stress was observed to increase hydrogen "permeability", represented by the product: $P = D_l * S$ between hydrogen diffusion coefficient (D_l, both in lattice sites and reversible trapping sites) and a solubility coefficient (S), leaving the diffusion coefficient unaltered.

According to Blundy et al. [230], if a tensile stress lower than YS is applied to a steel, an increase in the permeation flux and the achievement of a new steady state value occurs; if that stress is removed, a completely reversibility is observed, with a decay to the initial steady state value. Instead, with the application of a tensile stress higher than YS, there is an initial decrease in the permeation flux, due to the newly generated trapping sites by plastic deformation, followed by an eventual decrease to a new different steady state value, higher than the previous one; in this case, with the removal of that stress, completely reversibility cannot be observed anymore.

In 1985, Zakroczymski [176] affirmed that the effective diffusivity of Armco iron (low carbon steel) was not influenced by elastic deformation, whereas a significant decrease in the effective diffusivity was determined by plastic deformation. The newly generated dislocations enhanced hydrogen trapping and, even if hydrogen transport phenomena occurred, these were inevitably overtaken by trapping phenomena. With regard to the hypothesis of hydrogen transport by mobile dislocations, which involves rapid dislocation sweeping of hydrogen atoms at room temperature [193], he carried out experimental tests on low-carbon iron, pure Ni, and 17Cr-12Ni austenitic stainless steel membranes subject to simultaneous straining at room temperature; the results obtained did not support the assumption that moving dislocations would accelerate hydrogen transport in iron.

Moreover, from further literature results [113] [170] [231] [232] [233], it is fully accepted that a plastic deformation causes an increase in hydrogen solubility and a decrease in D_{app}, due to the creation of new trapping sites or the enlargement of the existing ones. Indeed, common mathematical models, which consider diffusion in the presence of trapping, assume that hydrogen permeability depends both on lattice and trapping sites.

However, on a plastically deformed A508Cl3 steel at room temperature, Leblond et al. [177] obtained a slight dependence of hydrogen permeability upon an applied stress, both in the elastic and plastic deformation field. In contradiction with the results of Beck et al., they affirmed that, even with a variation of the plastic strain from 1% to 2%, D_{app} remained in the same order of magnitude. This fact is probably related to the existence of irreversible trapping sites that are filled with hydrogen with a much lower rate compared to lattice sites (which are in equilibrium with reversible trapping sites).

Instead, Dietzel et al. [231] found in their work a relevant effect of plastic deformation on hydrogen diffusivity in a FeE690T ferritic steel. These researchers reported the apparent diffusivity as a decreasing function of plastic strain, whilst the steady state hydrogen permeation flux remained almost unaltered. In particular, a variation in the plastic strain from 0.2% to 60% involved a decrease of more than two orders of magnitude in D_{app}. In order to explain this behavior, an increase in the number of dislocations acting as "sinks" for diffusing hydrogen atoms was hypothesized.

Huang and Shaw [227], in their study on the effect of hydrogen transport on type 1020 steel exposed in a sour environment, reported a decrease in hydrogen diffusion coefficient with increasing cold work, and a flattening within the interval 30%-40% of cold work. Unfortunately, also the fracture toughness decreased with increasing cold work, leading to hydrogen damage after reaching steady state conditions.

Andenna and Torella [234] analyzed the effect of stress on the permeability of X65 pipeline steels, reporting no effects for the base material, characterized by a ferrite-pearlite microstructure, while for quenched material, characterized by a bainitic microstructure with martensite-austenite islands, the hydrogen diffusivity and permeation flux decrease with an increase in the stress level.

Cabrini et al. [67] analyzed the singular case of HE occurrence in a 24-inch pipeline subject to slow deformation conditions in the plastic field, caused by landslides [235] [61] [236] [67]. Similar results were reproduced in real-scale laboratory tests, with an applied cathodic protection of -1.05V and -2V vs SCE and a strain rate from 10^{-5} to 10^{-6} s^{-1} [236], in which a constant value of the hydrogen permeation flux was observed for strain rates of less than 10^{-6} s^{-1} [235], as previously highlighted by Frankel and Latanision [237]. In fact, these authors found that the hydrogen permeation flux strongly depended on the strain rate; at fast strain rates, a decrease in the hydrogen flux occurred as a consequence of dynamic trapping phenomena by newly generated dislocations, while, at slow strain rates, the creation of new trapping sites is much slower during time, so the lattice has more time and chances to be refilled with atomic hydrogen from the entry surface.

Moreover, Cabrini et al. proposed a useful correlation [232] between D_{app} and the results obtained by Slow Strain Rate (SSR) and Stress Corrosion Cracking (SCC) tests, in which the crack growth rate was measured by means of corrosion-fatigue tests. The results highlighted that the effect of HE became more evident with the increase in the apparent diffusivity; in fact, doubling in crack growth rates was observed as the diffusivity increased from $2.7*10^{-11}$ to $5*10^{-11}$ m^2/s.

Réquiz et al. [238] analyzed the effect of heat treatments and plastic deformation on hydrogen diffusivity in a common API 5L X52 low carbon steel (0.09C0.9Mn) seamless pipe. The apparent diffusivity, estimated using the time-lag method (t_{lag}), decreased about 2.6 times comparing the quenched ($3.76*10^{-11}$ m^2/s) and the normalized microstructure ($9.84*10^{-11}$ m^2/s). From the dislocation density analysis by means of TEM, these authors associated a larger dislocation density value in the quenched material, with a lower hydrogen diffusivity. Based on their results, these researchers came up with the assumption that, on one hand, cold work may increase hydrogen-induced damage by means of matrix-particle separation, and cavities initiation and growth. On the other hand, cold work may decrease this kind of damage, as hydrogen diffusion may be slowed down in response to the compression stresses in the metal sub-surface.

Figure 5.1 provides a summary of the relationship proposed in the analyzed literature works between apparent diffusivity (D_{app}) and level of cold work (ε).

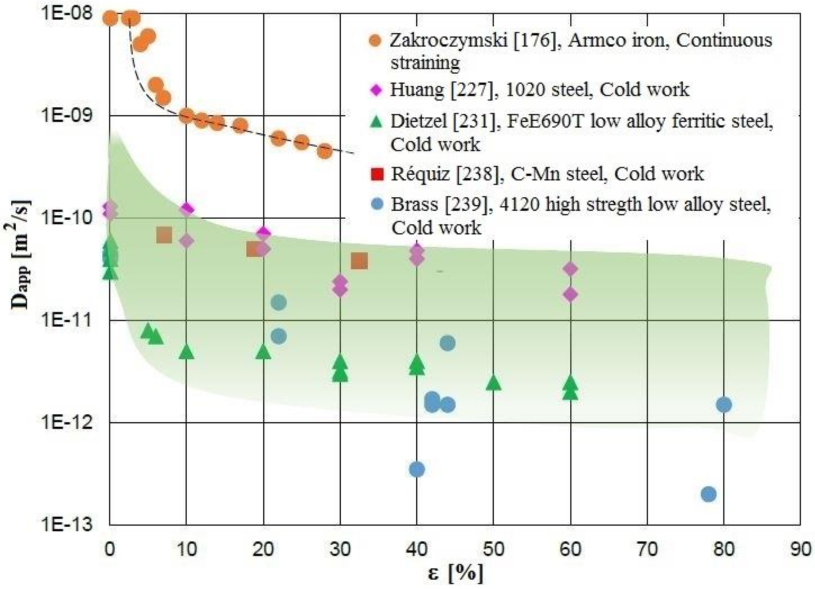

Figure 5.1. Relationship between apparent diffusivity (D_{app}) and cold work (ε). Adaptation from the literature [176] [227] [231] [238] [239]

5.2 Hydrogen transport models in an elasto-plastically strained metal

In 1980, Kumnick and Johnson [170] managed to analyze trapping phenomena in deformed iron by the measurement of the hydrogen permeation transient, but the first mathematical model that could evaluate the effect on non-linear diffusion phenomena due to elasto-plastic deformation was proposed by Kitagawa and Kojima [240] in 1983. A few years later, Turnbull et al. [154] performed a mathematical analysis for modelling hydrogen diffusion phenomena in steel and suggested a numerical solution in the presence of irreversible trapping sites with a finite trapping rate, thus not in local equilibrium conditions. Later, Sofronis and McMeeking [241] studied the permeation transients linked to hydrogen diffusion and trapping phenomena in correspondence of microstructural defects in the area around a blunting crack tip. In particular, their diffusion model considered the deviation caused by the hydrostatic stress and the new trapping sites generated by plastic deformation. In 1998, Lufrano and Sofronis [242] extended the model developed by Sofronis and McMeeking by including the effect of hydrogen-induced dilatation on the material constitutive laws. This dilatational effect becomes relevant at high hydrogen concentrations, in media characterized by a large hydrogen solubility, e.g. niobium, because it influences both the diffusion paths and the stress relaxation. Furthermore, Krom [243] introduced a strain rate factor in the diffusion equation modelled by Sofronis and McMeeking, in order to consider, in a more precise way, the equilibrium between hydrogen in NILS and in trapping sites, and to estimate permeation transients at high strain rates.

Later, Taha and Sofronis [244] took the equation governing the transient of hydrogen permeation and considered, in addition to reversible trapping sites, the deviation due to hydrostatic stress and the newly generated traps by plastic deformation.

Contrarily to what affirmed by Turnbull et al. [154], Castaño Rivera et al. [151] developed a numerical finite difference method (FDM) to solve the diffusion equation, considering the case of a local equilibrium and a high fraction of occupied trapping sites, such as irreversible traps, characterized by a high binding energy, but with no limits for the trap filling rate.

Just a couple of years later, Kim et al. [180] defined a numerical model in order to determine hydrogen diffusion parameters of a sour-resistant ferritic steel subject to a tensile stress in the plastic field, and solved the modified diffusion equation by means of a numerical finite difference method (FDM).

Anyway, the contribution given by all these diffusion models is very relevant, and fundamental to explain HIC failure mechanism. However, no accurate models have been presented yet that can be applied to the majority of actual situations, where diffusing hydrogen through a steel and loading conditions are simultaneously present.

5.2.1 Kumnick and Johnson

Kumnick and Johnson [170] analyzed hydrogen trapping phenomena in deformed iron by the measurement of the hydrogen permeation transient, using the gas phase charging procedure and the electrochemical technique for the evaluation of the steady state permeation flux. The two authors calculated the trap site density and the binding energy implementing the time-lag method (t_{lag}) taken from the work by McNabb and Foster *(eq. 38)* and from Sievert's law ($C_0 = S(T) * P^{1/2}$).

The new equation *(eq. 78)* enabled them to extrapolate the trap site density from permeation transient experimental data, as reported below:

$$\frac{t_T}{t_L} = 1 + \frac{3N_T}{S(T) \cdot \sqrt{P}} \qquad \textit{(eq. 78)}$$

With: t_T = time-lag in the presence of trapping sites; t_L = time-lag in the absence of trapping sites; S(T) = Sievert's constant; P = hydrogen pressure during the gas phase charging.

Trap site density and binding energy were obtained from the measurement at different levels of deformation and at different temperatures. In this work, the binding energy seemed not to be dependent on plastic deformation and temperature, probably because a single trap site density is represented in the results. The binding energy seemed to be the same for both annealed and deformed iron, while the trap site density, as expected, was not dependent on temperature. These two parameters increased considerably with deformation at low strain levels, and more gradually with the increase in the deformation level. The result they came up with was a binding energy of 59.9 ± 4.6 kJ/mol H (14.3 ± 1.1 kcal/mol H), and a trap site density ranging from just under 10^{20} m^{-3} for the annealed material to just over 10^{23} m^{-3} for heavily deformed iron, as shown in *Figure 5.2*.

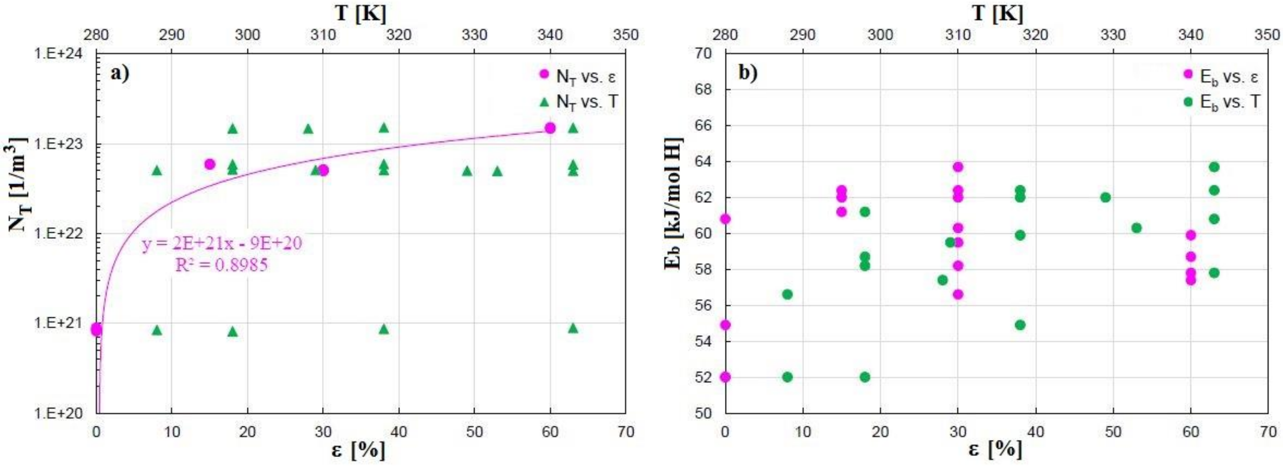

Figure 5.2. a) Trap site density; b) Trap binding energy derived from measurements at different levels of deformation and at different temperatures. Adaptation from the literature [170]

5.2.2 Hashimoto and Latanision

Hashimoto and Latanision [245] analyzed hydrogen transport in Armco iron during plastic deformation with the implementation of a new model, which took into account macroscopic diffusion in describing the interaction between diffusing hydrogen atoms and dislocations. They suggested that hydrogen diffusion parameters, during the deformation processes, are influenced by trapping phenomena, due to newly generated dislocations, and transport, due to mobile dislocations. In a previous work [246], they observed that hydrogen permeation flux, influenced by moving dislocations, strongly depended upon the kinetic interaction between hydrogen in the lattice and that in these moving dislocations. They also found that the trapping phenomena associated with the increasing dislocations population, i.e. dynamic trapping, should be considered to model hydrogen transport and to estimate the parameters that govern the Fe-H system in a more accurate way.

Firstly, with regard to the static trapping effect, they used the method proposed by Kumnick and Johnson [170] to obtain the total dislocation density (N_t) and the binding energy (E_b). In the case of non-deformed material, the average values were: $N_t = 6*10^{21}$ sites/m^3 and $E_b = 0.53$ eV. In the case of heavily deformed iron (17.5%), they could only estimate the value of the total dislocation density, equal to: $N_t = 5*10^{24}$ sites/m^3; thus, the binding energy was the same as for the annealed specimens, and equal to: $E_b = 0.53$ eV (Kumnick and Johnson [170] suggested that, in deformed specimens, this parameter remains constant).

Hashimoto and Latanision accurately calculated the three parameters λ, μ, ν of the McNabb-Foster equations, used to characterize the trapping effect (*(eq. 79)* and *(eq. 80)*):

$$\frac{\lambda}{\mu} = \alpha = \frac{N_t}{N_l} \cdot e^{\left(\frac{E_b}{k_b \cdot T}\right)} \qquad \textit{(eq. 79)}$$

$$\frac{\nu}{\mu} = \beta = \frac{C_0}{N_l} \cdot e^{\left(\frac{E_b}{k_b \cdot T}\right)} \qquad \textit{(eq. 80)}$$

The absolute values of λ, μ, ν are connected to the redistribution rate between lattice hydrogen and trapped hydrogen. In particular, two situations must be identified. The first one, called "fast kinetics", occurs when the values of the three parameters are large and, with the reliable assumption of local equilibrium, only two parameters (E_b, N_t or α, β) are sufficient to characterize the trapping effect. The second one, instead, called "slow kinetics", occurs when the values of the three parameters are small; thus, a long period is necessary to reach equilibrium between lattice hydrogen and trapped hydrogen. In this case, the third parameter can be called the kinetic parameter, which may be estimated from the best fit of the theoretical permeation curve derived from the solution of the McNabb-Foster equations to the experimental results.

As regards the dynamic trapping effect, new trapping sites are generated by plastic deformation during hydrogen diffusion, causing a further trapping effect and resulting in a dynamic interaction between diffusing hydrogen and the newly created trapping sites. Therefore, the McNabb-Foster equations were modified by substituting the static trapping constant (N_t) with a time dependent ($N_t(t)$) trapping sites density, as follows (*(eq. 81)* and *(eq. 82)*):

$$\left(\frac{\partial u_l}{\partial \tau}\right) + \left(\frac{\partial u_t}{\partial \tau}\right) = \left(\frac{\partial^2 u_l}{\partial x^2}\right) \qquad \textit{(eq. 81)}$$

$$\frac{\partial u_t}{\partial \tau} = \lambda(\tau) \cdot u_l - \nu \cdot u_l \cdot u_t - \mu \cdot u_t \qquad \textit{(eq. 82)}$$

With: u_l = normalized lattice hydrogen concentration; u_t = normalized hydrogen concentration in the traps; x = normalized distance; τ = normalized time.

In addition, they found that the applied stress determines an increase in hydrogen solubility, which should be considered in the modelling. The concentration of hydrogen at the entry surface can be expressed by the following equation *(eq. 83)*:

$$C(\sigma) = C(\sigma = 0) \cdot e^{\left(\frac{\sigma_h \cdot \Delta V}{k_b \cdot T}\right)} = C(\sigma = 0) \cdot \left(1 + \frac{\sigma_h \cdot \Delta V}{k_b \cdot T}\right) \qquad \textit{(eq. 83)}$$

Moreover, during plastic deformation, the possibility of hydrogen transport by mobile dislocations is also indicated, as clearly shown by Tien et al. [193] and Hwang and Bernstein [247] in the case of iron single crystals. Thus, the McNabb-Foster equations are again modified to model the profile of hydrogen concentration in a medium containing a large dislocation density (from *(eq. 84)* to *(eq. 87)*):

$$\left(\frac{\partial u_l}{\partial \tau}\right)+\left(\frac{\partial u^{m+}}{\partial \tau}\right)+\left(\frac{\partial u^{m-}}{\partial \tau}\right)+\left(\frac{\partial u^{S}}{\partial \tau}\right) = \frac{\partial}{\partial x}\left(\frac{\partial u_l}{\partial x}\right)-v^{+}\cdot\left(\frac{\partial u^{m+}}{\partial x}\right)+v^{-}\cdot\left(\frac{\partial u^{m-}}{\partial x}\right) \qquad \textit{(eq. 84)}$$

$$\frac{\partial u^{m+}}{\partial \tau}=\lambda^{+}\cdot u_l-\nu\cdot u_l\cdot u^{m+}-\mu\cdot u^{m+}-v^{+}\cdot\left(\frac{\partial u^{m+}}{\partial x}\right) \qquad \textit{(eq. 85)}$$

$$\frac{\partial u^{m-}}{\partial \tau}=\lambda^{-}\cdot u_l-\nu\cdot u_l\cdot u^{m-}-\mu\cdot u^{m-}+v^{-}\cdot\left(\frac{\partial u^{m-}}{\partial x}\right) \qquad \textit{(eq. 86)}$$

$$\frac{\partial u^{S}}{\partial \tau}=\lambda^{S}\cdot u_l-\nu\cdot u_l\cdot u^{S}-\mu\cdot u^{S} \qquad \textit{(eq. 87)}$$

With: u_l = normalized lattice hydrogen concentration; u^i = normalized hydrogen concentration in the trapping sites, where the exponent (i) changes for: stationary traps (S) and moving traps (m+, in positive direction, and m-, in negative direction); v = normalized velocity; D_l = lattice diffusion coefficient; τ = normalized time. When the trapping site density increases over time, in the above-mentioned equations λ should be replaced with the time dependent parameter λ(t), as previously said. When both the dynamic trapping effect and hydrogen transport by mobile dislocations (faster than that of lattice diffusion [193]) influence hydrogen permeation flux, the impact of mobile dislocations is significant only at short periods. However, when the lattice hydrogen represents the majority of the total hydrogen concentration, as commonly occurs in the experimental conditions of the hydrogen permeation technique, the effect of mobile dislocations becomes insignificant, as the hydrogen quantity trapped in these sites is by orders of magnitude smaller than that in the lattice sites.

5.2.3 Taha and Sofronis

Taha and Sofronis [244], in accordance with the work by Sofronis and McMeeking [241], presumed that hydrogen remains in the NILS or in new reversible traps, formed by plastic deformation. Following Oriani’s theory [153], both populations are constantly in balance, such that *(eq. 88)*:

$$\frac{\theta_T}{1-\theta_T}=\frac{\theta_L}{1-\theta_L}\cdot K \qquad \textit{(eq. 88)}$$

With: θ_T = occupancy of the trapping sites; θ_L = occupancy of the NILS; K = equilibrium constant, defined as follows *(eq. 89)*:

$$K=e^{\left(\frac{W_B}{R\cdot T}\right)} \qquad \textit{(eq. 89)}$$

With: W_B = trap binding energy; R [J/(mol*K)] = gas constant = 8.314; T [K] = absolute temperature.

The hydrogen concentration per unit volume in reversible trapping sites *(eq. 90)* can be expressed as:

$$C_T = \theta_T \cdot \alpha \cdot N_T \qquad \textit{(eq. 90)}$$

With: α = number of sites per trap; N_T = density of reversible trapping sites, measured as the number of traps per unit volume *(eq. 91)*, defined as follows [218] [248]:

$$logN_T = 23.26 - 2.33 \cdot e^{(-5.5 \cdot \varepsilon_p)} \qquad \textit{(eq. 91)}$$

The density of reversible trapping sites can be determined only as a function of the measure of plastic deformation, i.e. the equivalent plastic strain (ε_p) [249].

The hydrogen concentration in NILS can be indicated as *(eq. 92)*:

$$C_L = \theta_L \cdot \beta \cdot N_L \qquad \textit{(eq. 92)}$$

With: β = number of NILS per solvent atom; N_L = density of solvent lattice atoms per unit lattice volume. If the available number of reversible trapping sites per unit volume is small compared with the available NILS per unit volume, then N_L can be written as *(eq. 93)*:

$$N_L = \frac{N_A}{V_M} \qquad \textit{(eq. 93)}$$

With: N_A [atoms/mol] = Avogadro's constant = $6.023 * 10^{23}$; V_M = lattice molar volume, measured in units of volume per lattice mole.

Hydrogen conservation in a random material volume, combined with the previous equations (from *(eq. 88)* to *(eq. 92)*), gives the governing equation for the hydrogen permeation transient, considering reversible trapping sites and the deviation caused by the hydrostatic stress and the trapping sites generated by plastic deformation *(eq. 94)*:

$$\frac{D_l}{D_{app}} \cdot \frac{dC_L}{dt} = D_l \cdot C_{L,ii} - \left(\frac{D_l \cdot V_H \cdot C_L}{3 \cdot R \cdot T} \cdot \sigma_{kk,i}\right)_{,i} - \alpha \cdot \theta_T \cdot \frac{\partial N_T}{\partial \varepsilon_p} \cdot \frac{d\varepsilon_p}{dt} \qquad \textit{(eq. 94)}$$

With: $(\ )_{,i} = \partial (\ ) / \partial x_i$; d / dt = time derivative; D_l = lattice hydrogen diffusion coefficient through NILS; D_{app} = apparent hydrogen diffusion coefficient, defined as follows *(eq. 95)*:

$$D_{app} = \frac{D_l}{\left(1 + \frac{\partial C_T}{\partial C_L}\right)} \qquad \textit{(eq. 95)}$$

With: V_H = partial molar volume of hydrogen in solid solution; σ_{ij} = Cauchy stress (the standard summation convention over the range is implemented for a repeated index). The last term of equation *(eq. 94)* represents the strain rate factor defined by Krom [243].

In Oriani's model, it is clear that trap filling kinetics occurs very fast, so that D_{app} is lower than the average NILS diffusion coefficient, either because the trapping sites are not saturated and because always new traps are generated, due to increasing plastic deformation. On the contrary, if plastic deformation finishes and no more traps are generated, NILS hydrogen populations can reach equilibrium with the local stress field. The previous equation *(eq. 94)* shows that the evaluation of hydrogen distribution in a medium depends on hydrostatic stress and effective plastic deformation.

5.2.4 Kim et al.

Kim et al. [180] defined a numerical model for the calculation of hydrogen diffusion parameters in a sour-resistant ferritic steel subject to loading conditions in the plastic field. They started from the modified equation proposed by Oriani [153], which was simplified under the assumption of local equilibrium and very low fraction of occupied trapping sites *(eq. 96)*:

$$\frac{\partial C}{\partial t} = D_{app} \cdot \frac{\partial^2 C}{\partial x^2} \qquad \textit{(eq. 96)}$$

With:

$$C = C_L + C_r \qquad \textit{(eq. 97)}$$

$$D_{app} = \frac{D_l}{(1 + K_r \cdot N_r)} \qquad \textit{(eq. 98)}$$

With: D_{app} = apparent hydrogen diffusion coefficient; C_r = hydrogen concentration in reversible trapping sites. Thus, the analytical solution of the permeation transient can be expressed as *(eq. 99)*:

$$\Phi_H = \left(\frac{D_{app} \cdot C_0}{L}\right) \cdot \left\{1 + 2 \cdot \sum_{n=1}^{\infty} (-1)^n \cdot e^{\left[-n^2 \cdot \pi^2 \cdot \left(\frac{D_{app} \cdot t}{L^2}\right)\right]}\right\} \qquad \textit{(eq. 99)}$$

With: Φ_H = permeation transient; C_0 = sub-surface hydrogen concentration at NILS plus reversible trapping sites at the entry surface.

Therefore, the researchers considered the governing equation proposed by Turnbull et al. [154] in the presence of both reversible and irreversible trapping sites, with no stress fields applied to the steel membrane; the irreversible trapping sites were supposed to be characterized by a finite trapping rate, not in local equilibrium (*(eq. 100)* and *(eq. 101)*):

$$\frac{\partial C}{\partial t} = D_l \cdot \frac{\partial^2 C_L}{\partial x^2} - N_r \cdot \frac{\partial \theta_r}{\partial t} - N_{irr} \cdot \frac{\partial \theta_{irr}}{\partial t} \qquad \textit{(eq. 100)}$$

$$\frac{\partial C}{\partial t} = D_{app} \cdot \frac{\partial^2 C}{\partial x^2} - N_{irr} \cdot \frac{\partial \theta_{irr}}{\partial t} \qquad \textit{(eq. 101)}$$

$$= D_{app} \cdot \frac{\partial^2 C}{\partial x^2} - N_{irr} \cdot [K_{irr} \cdot C \cdot (1 - \theta_{irr})]$$

With: N_{irr} = irreversible trap density; θ_{irr} = fractional occupancy of irreversible traps; K_{irr} = transition probability for hydrogen transport from lattice sites to irreversible traps.

Consequently, the modified diffusion equation was solved by means of a numerical finite difference method (FDM), which proceeds from an initial condition in a succession of cycles, proposed below (*(eq. 102)* and *(eq. 103)*):

$$C_j' = C_j + D_{app} \cdot \left[\frac{C_{j+1} + C_{j-1} - 2 \cdot C_j}{(\Delta x)^2}\right] \cdot \Delta t - N_{irr} \cdot K_{irr} \cdot C \cdot (1 - \theta_{irr}) \cdot \Delta t \qquad (eq.\ 102)$$

$$\theta_{irr}' = \theta_{irr} + K_{irr} \cdot C \cdot (1 - \theta_{irr}) \cdot \Delta t \qquad (eq.\ 103)$$

With: C_j and C_j' = number of diffusing atoms per unit volume, at time (t) and (t + Δt), respectively; θ_{irr} and θ_{irr}' = fraction of occupied traps, at time (t) and (t +Δt), respectively; Δt = time interval.

In the absence of load, the permeation curves were fitted by the use of the following two equations (*(eq. 104)* and *(eq. 105)*), with the aim of minimizing the deviation between the experimental and calculated data:

$$Min\left[\sigma^2 = \sum_{i}^{n} \frac{\left(j_{exp}^{i} - j_{cal}^{i}\right)^2}{n}\right] \qquad (eq.\ 104)$$

$$\frac{\partial \sigma^2}{\partial D_{app}} = 0 \qquad (eq.\ 105)$$

With: j_{exp} and j_{cal} = experimental and calculated permeation current density, respectively; n = number of experimental data.

Instead, in the presence of an applied load, and more precisely under a loading condition generating local/generalized plasticity, the previous equations cannot be applied directly, because of the combined effect of additional hydrogen trapping at expanded interfacial gaps between matrix and second phase particles, and generation of blister cracks. Therefore, the modification introduced is as follows (*(eq. 106)* and *(eq. 107)*):

$$C' = C + D_{app} \cdot \left[\frac{C_{j+1} + C_{j-1} - 2 \cdot C_j}{(\Delta x)^2}\right] \cdot \Delta t - N_{irr}^{total} \cdot K_{irr} \cdot C \cdot (1 - \theta_{irr}) \cdot \Delta t \qquad (eq.\ 106)$$

$$N_{irr}^{total\prime} = N_{irr} + \Delta N \cdot F_{crack}^{blister} \qquad (eq.\ 107)$$

With:

$$F_{crack}^{blister} = \frac{1}{1 + e^{[-R\cdot(\theta_{irr}\cdot N_{irr} - C_{thres}) + ln(99.0)]}} \qquad (eq.\ 108)$$

$$\theta_{irr}' = [\theta_{irr} + K_{irr} \cdot C \cdot (1 - \theta_{irr}) \cdot \Delta t] \cdot \frac{N_{irr}^{total}}{N_{irr}^{total\prime}} \qquad (eq.\ 109)$$

With: $\mathrm{F_{crack}^{blister}}$ = fraction of newly generated blister crack induced by the local or generalized plasticity, which ranges from 0 to 1; R = parameter indicating how rapidly the crack propagation is; C_{thres} = hydrogen concentration with an increase in $\mathrm{F_{crack}^{blister}}$ to 1%; $\mathrm{N_{irr}^{total}}$ and $\mathrm{N_{irr}^{total\prime}}$ = total number of irreversible trapping sites, at time (t) and (t + Δt), respectively; ΔN = increased trap density, as a result of crack formation.

6

ELECTROCHEMICAL HYDROGEN PERMEATION TECHNIQUES

6.1 Hydrogen charging with electrochemical techniques

Hydrogen charging involves many experimental methods and techniques that can be used in order to estimate hydrogen diffusion coefficient in many metallic materials *(Figure 6.1)*.

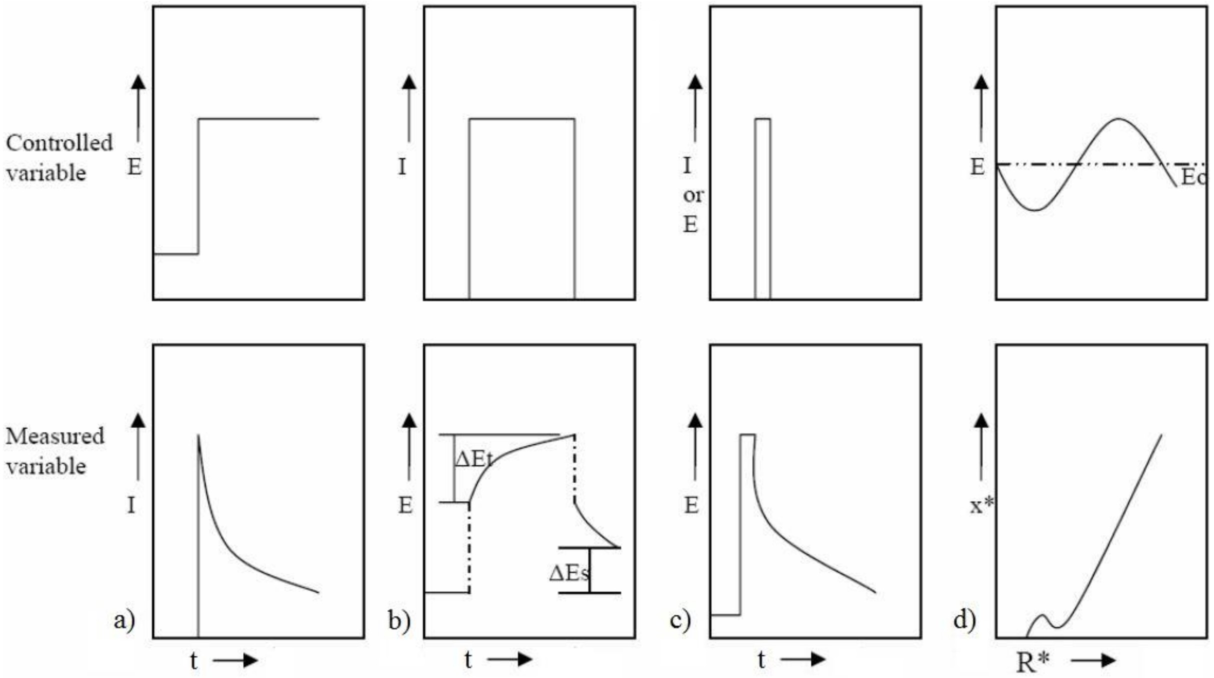

Figure 6.1. Electrochemical hydrogen charging techniques: a) Potentiostatic; b) Galvanostatic; c) Potentiometric; d) Steady state alternate current [250] (E = Potential; I = Current; R = Impedance Real part; x* = Impedance Imaginary part)*

These electrochemical techniques are reported as follows:

- Potentiostatic: the metal surface is characterized by an initial hydrogen concentration with an equilibrium potential *(Figure 6.1(a))*. At t = 0, a constant potential between specimen and electrode is applied, with a subsequent variation in hydrogen concentration. Then, at t > 0, current evolution is measured, while the concentration is maintained constant

- Galvanostatic: the controlled parameter is the current, while the measured parameter, on the specimen surface (x = 0), is the potential *(Figure 6.1(b))*. Since the potential represents a variable, a variation in hydrogen concentration is controlled by Fick's first law
- Potentiometric: the initial hydrogen concentration is assumed as a constant, which corresponds to an equilibrium potential. A high current impulse is applied and, after current interruption, the potential variation as a function of time is measured, at t < 0
- Steady state alternate current: as in the potentiometric technique, the initial hydrogen concentration is assumed as a constant, which corresponds to an equilibrium potential. A small sinusoidal alternate current signal (E_{max}*sin(2πft), where E_{max} is the alternate current voltage amplitude and f is the frequency) is then imposed upon the direct current equilibrium potential, and the response impedance parameters (R* and x*) are monitored.

Nowadays, although many methods are available to measure the amount of absorbed hydrogen into the metal, the electrochemical methods [200] [251], based on the oxidation of the absorbed atomic hydrogen, are still valid methods for these studies at room temperature.

According to Xie and Hirth [169], the electrochemical permeation technique presents a disadvantage: the chemical potential of hydrogen, which represents the boundary condition at the charging surface, can be estimated only after an analysis of the obtained data, rather than being fixed as in the gas phase charging procedure. However, the data found in the literature, concerning hydrogen permeation and obtained by means of this procedure, may be more representative of service conditions [113], which involve high hydrogen activities than the results derived from gas phase permeation, characterized by low pressures of ultrapure hydrogen.

The following paragraphs will provide a quite exhaustive overview of the available procedures for the electrochemical hydrogen permeation technique, such as Devanathan-Stachurski and ISO 17081 methods.

6.2 Devanathan-Stachurski technique

In 1962, Devanathan and Stachurski developed an electrochemical method to accurately measure the instantaneous rate of hydrogen permeation through a metallic membrane, which is positioned between two halves cells, or compartments [200]. All the details are described in *Figure 6.2.*

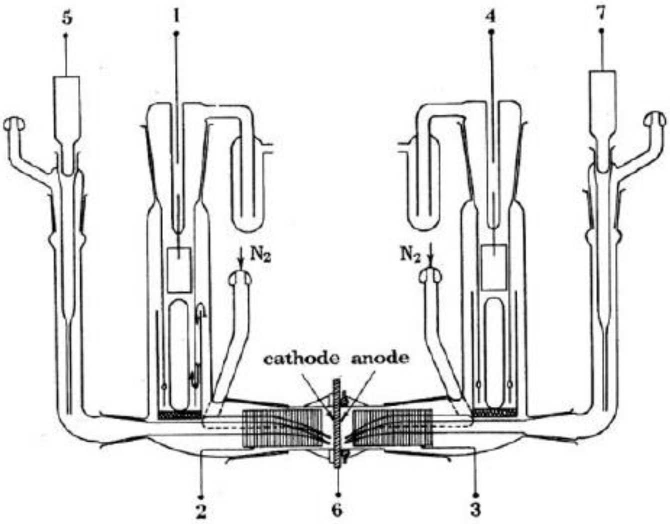

1. Pt counter electrode in the cathodic side
2. Cathodic side
3. Anodic side
4. Pt counter electrode in the anodic side
5. Reference electrode in the cathodic side
6. Sample membrane
7. Reference electrode in the anodic side

Figure 6.2. Set-up of the Devanathan-Stachurski's hydrogen permeation cell

This permeation technique can be properly performed if the concentration of adsorbed hydrogen in correspondence of the entry surface (cathodic side of the membrane) is maintained constant at a certain fixed level, while on the exit surface (anodic side of the membrane) this concentration is equal to zero. The two scientists obtained these conditions utilizing potentiostatic circuits, which imposed a cathodic polarization to the entry surface and an anodic polarization to the exit surface of a Pd membrane. In particular, in correspondence of the cathodic side (entry surface), hydrogen is reduced from the ion form (H^+) to the atomic form (H) and, once adsorbed on the surface, is able to diffuse through the membrane. When hydrogen reaches the exit surface on the anodic side, it is again oxidized from the atomic form (H) to the ion form (H^+). The background anodic current, in the anodic potentiostatic circuit, which maintains zero coverage on the exit surface, represents a direct measure of hydrogen instantaneous permeation rate *(eq. 110)*, according to Faraday's law:

$$\Delta W = \frac{M_w}{z \cdot F} \cdot I \cdot t \qquad \textit{(eq. 110)}$$

With: ΔW = mass of a produced species (hydrogen ion in this case) during electrochemical reaction

M_w = molecular weight of hydrogen atom

z = valence of electrochemical reaction (equal to 1 in the present situation)

F = Faraday's constant (≈ 96.500 C)

I = anodic current required to oxidize all the atomic hydrogen on the exit surface

t = time.

Therefore, it is possible to continuously record hydrogen instantaneous permeation rate with very high sensitivity. However, when this permeation technique is applied, the test results can be significantly influenced by the hydrogen surface concentration and the analytical procedure chosen to derive diffusion parameters.

In fact, for the first factor, in this technique surface hydrogen activity is assumed to remain always constant during the entire test over time, although, except in the presence of a thin Pd layer, it reaches constant values only after a long stabilization period [252] [253] [254] [255] [256].

For the second factor, it is necessary to consider the trapping effect, as it generates variations in the apparent diffusivity [201].

6.2.1 Specimen thickness

In order to choose the right specimen thickness, two important factors should be considered:

- Hydrogen diffusion must be controlled by transport through the metal bulk and not by surface processes. The thickness of the specimen must be higher than a critical minimum value [201]
- Greater the thickness, the longer the test duration is, and it is harder to keep constant conditions.

The decision should finally be a compromise between these factors. Moreover, in relation to the correct choice of the thickness, also the area radius exposed to both the solutions should be considered; in fact, only a sufficiently large radius/thickness ratio ensures a one-dimension diffusion.

6.2.2 Charging solution

The cathodic compartment can be filled either with a gaseous environment or with an aqueous solution, which is usually chosen in order to best simulate real operating conditions, or just to gather the easiest way to favor permeation conditions. The charging electrolyte, which can be maintained stagnant or in recirculation conditions, can be the same of the anodic compartment [200] [206] [257], or be formed sometimes by acetic solutions [255], NaCl solutions [154] [255] [258], borate buffer solutions [259] [260], or solutions containing recombination poisons [143] [145] [154] [255] [261].

The charging environment should be chosen with particular consideration. For example, for austenitic, martensitic, and duplex stainless steels, and nickel alloys, the use of a 0.1 M NaOH solution seemed to be satisfactory; however, for carbon, carbon-manganese and low alloy steels, the choice requires more careful attention. In fact, under cathodic charging conditions, the use of a 0.1 M NaOH solution results in an apparent film formation on the surface over time, resulting in a permeation transient much more prolonged and shallower than that predicted from Fick’s law.

Whichever charging environment is chosen, it is fundamental to maintain constant conditions of the environment during the whole test duration, and hence the pH and the concentration of recombination poisons should be frequently checked, as these can be consumed during the test.

6.2.3 Galvanostatic or potentiostatic charging

The charging current and the recombination rate must be constant, because a constant value of C_0 must be maintained during the whole test period. Even if a galvanostatic charging ensures a constant value of C_0, a variation in the surface condition or in the environment during a test usually determines a change of the electrode potential, which theoretically should be always monitored.

Other research studies reported that, either in alkaline or acidic solutions, during galvanostatic charging the cathodic potential reached more negative values [253] [254] [256] [262]. In fact, in most cases, this potential variation indicated that C_0 at the entry side did not stabilize immediately.

Many studies [131] [263] [264] even suggested that hydrogen charging may favor the creation of super-abundant vacancies (SAVs), which can also behave as hydrogen trapping sites. For example, Fukai et al. [131] proposed that the decrease in the vacancy creation energy, due to the trapping phenomena of hydrogen atoms, should determine the SAV formation.

However, the ISO 17081:2014 [201] reference standard affirms that *"For characterization of hydrogen transport in the bulk of the material, galvanostatic charging is preferred"*, and again that *"Significant variations in potential usually indicate a changing surface state and unsteady boundary conditions which can render uncertain the interpretation of the permeation transients. Potentiostatic charging may also be used provided there are no significant variations in the current"*.

Consequently, galvanostatic charging seems to represent the best option to maintain constant conditions, only if a continuous monitoring of potential variations is ensured during the whole test.

As previously mentioned, constant concentration or constant flux conditions on the charging surface will be reached depending on the relative values of the recombination flux and the diffusion flux.

6.2.4 Applied potential in the detection compartment

The electrode potential of the specimen area exposed to the oxidation solution should be potentiostatically monitored to ensure bulk transport-limited kinetics for hydrogen atoms oxidation.

As reported in the ISO 17081:2014 standard [201], suitable potential values for most of the applications are around +300 mV vs SCE. In particular, for carbon, carbon-manganese and low alloy steels, the ISO standard specifies that a solution from *"0,1 mol/l to 1 mol/l NaOH is recommended for the environment in the oxidation cell with the electrode potential set to +300 mV vs SCE"*.

A passivating solution is usually adopted during tests on iron or steel alloys, and a constant potential value is imposed in order to create and maintain a stable passive film on the anodic surface of the specimen, and to oxidize H to H^+. The passive film ensures that only a very low corrosion current, i.e. background current or passivation current (i_P), is recorded, however without disturbing the hydrogen permeation current measures, which are at least one order of magnitude higher.

The validation technique should involve a monitoring of steady state permeation current values at a fixed potential, and then an increase in the potential to a well-defined value. After an initial sharp increase, the oxidation current should return to the previous values, indicating that the current is potential-independent and transport-limited.

6.2.5 Application of a thin Pd layer on the exit surface

One of the questions most discussed about experimental conditions is represented by the role played by a thin Pd layer applied on the exit surface of the metal specimen, as the necessity of such an electroplated coating is not unanimously accepted. The application of this Pd layer, deposited on the specimen exit surface in galvanostatic conditions at a relatively large current density, is considered by many references as a fundamental requirement in order to analyze the diffusion through the metal of hydrogen coming from external sources, to eliminate surface effects and to obtain reliable results [205] [265] [266] [267] [268] [269] [270] [271]. Therefore, the use of steel specimens coated with a thin layer of palladium represents the method usually applied for the elimination of surface hindrances. The majority of the analyzed literature works report an increase in the steady state hydrogen permeation current due to the deposition of a thin Pd layer [205] [265] [269] [272] [273], but there are some authors [274] who underline that the break-through time (t_b) is much wider, and hydrogen permeability much lower (even of two order of magnitude), for an uncoated iron specimen. Unfortunately, after the application of the Pd layer on the surface, the metal specimen is no longer considered as a single layer, and this fact may influence the observation of hydrogen permeation through the metal [272] [273]. In fact, as reported in the observations of Züchner et al. [272] and Chen et al. [273], hydrogen diffusion through the metallic material under investigation may be effectively affected by the presence of deposited surface layers, such as palladium.

In particular, Zoltowski and Makowska [275] stated that the Pd deposition operations could probably determine a sub-surface incoherence of the substrate, and generate new sub-surface hydrogen traps, due to the temporary formation and subsequent decomposition of the Pd-H β-phase under the surface. Electrochemical Impedance Spectroscopy (EIS) should be applied to study metal-hydrogen systems during electrochemical hydrogen permeation, in order to subtract hindrances linked to relatively fast processes from the global ones.

The problems linked to a Pd layer application seem to worsen with the application of a uni-axial tensile stress [276], since the stability of the Pd layer depends of the strength and elongation level of the metal substrate. In fact, in the case of an applied external stress above the tensile yield strength (TYS) of palladium (< 205 MPa), the Pd coating is plastically deformed and damaged, with the result of unstable background currents during the permeation test. Thus, for high strength steels, the reliability of permeation data cannot be ensured, due to the rupture of the Pd coating.

As an example, Kurkela et al. [171] reported relevant current spikes caused by the failure of the Pd layer on the exit surface of Cr-Mo steel (TYS = 496 MPa) specimens, after the application of a plastic strain. Therefore, from this work it remains unclear whether the decrease in hydrogen permeation current under plastic strain is caused by hydrogen trapping, due to newly generated dislocations, or to the combined action of the reduced hydrogen oxidation rate, caused by the damage of the Pd layer, and the subsequent passivation of the bare substrate steel under a high anodic polarization.

Moreover, Brass and Chene [173] performed a permeation test without the presence of a Pd layer and, even if reporting very low permeation currents due to the low efficiency of hydrogen oxidation, they avoided any porosity associated to the failure of the layer of palladium, which was electrodeposited on a high strength Cr-Mo steel during plastic deformation.

Finally, Park et al. [277] [278], in order to replace the Pd coating and to avoid its inevitable rupture, obtained consistent permeation results by developing an iron oxide film, grown with the application of an anodic polarization in a 0.1 M NaOH solution.

6.3 ISO 17081:2014 method

In 2004, Devanathan and Stachurski's electrochemical technique was standardized by ISO 17081, thus revised and updated in 2014 [201]. This standard provides a laboratory technique to measure hydrogen permeation flux and to determine the amount of hydrogen atoms uptaken and transported through the lattice of metals and alloys. Specifically, it gives:

- A method to calculate the apparent hydrogen diffusivity and separate reversible and irreversible trapping sites
- Requirements for specimens' preparation, test procedures, monitoring and control of the environmental variables, and analysis of the results
- Suggestions concerning the composition of the charging solution: this means that it permits to choose solution, charging method (galvanostatic or potentiostatic charging, etc.) and to deposit or not a thin Pd layer on the metal surface. The only conditions demanded to be satisfied are to ensure proper hydrogen oxidation and reduction seen above, as well as the bulk transport-limited kinetics for oxidation of hydrogen atoms.

The test device consists of a two-compartment permeation cell (charging compartment and detection compartment), necessarily realized using inert materials, with reliable reference electrodes and auxiliary (counter) insoluble electrodes. The test procedure indicated in the standard provides:

- Preparation of the specimen to the required surface finish (usually 1200 grit), preparation of the charging solution and the oxidation solution, verification of the reference and auxiliary electrodes and assembling of the test device
- Inlet of the oxidation solution in the detection compartment and application of the anodic polarization
- Formation of a passive film on the metal surface and subsequently decrease in the passivation current, until low and stable values are reached (usually under 0.1 $\mu A/cm^2$), addition of the

hydrogen charging solution (in stagnant or under recirculation conditions) in the cathodic compartment and beginning of the galvanostatic or potentiostatic charging

- Monitoring of the total oxidation current (including the passivation current and the current related to atomic hydrogen oxidation) until steady state conditions are reached
- Reducing the charging current to zero in order to separate the contributions of irreversible and reversible traps on hydrogen permeation flow. Before repeating the charging procedure, enough time should be provided to hydrogen atoms still present in interstitial lattice sites and reversible traps to exit.

The last suggestion, in accordance with Turnbull [154] considerations, provides a technique to distinguish reversible and irreversible trapping effects; in fact, during the first charging transient, hydrogen atoms permeate through the metal bulk and occupy both reversible and irreversible traps.

As the charging current is switched off, the discharging transient takes place, in which hydrogen atoms present in the lattice sites and reversible traps come out, while hydrogen atoms present in the irreversible sites remain trapped.

To determine hydrogen diffusion coefficient from the permeation curves, the standard indicates two time methods, the break-through (t_b) method and the time-lag (t_{lag}) method, and, if Fick's second law is applicable, underlines that the resulting values of both methods should be similar.

Moreover, permeation transient should be plotted in the form of normalized flux ($\Phi(t)/\Phi_\infty$) against the logarithm of the normalized time ($\tau = D^*t/L^2$), with $\Phi(t)$ obtained from the following *(eq. 111)*:

$$\Phi(t) = \frac{i_P}{F} \qquad \textit{(eq. 111)}$$

This calculation aims to make the permeation transients data independent of the specimen thickness, and to directly compare these transients with the ones foreseen from Fick's law, (*Figure 6.3.* In this graph, the effect of C_0 variation on the permeation transient is highlighted; as C_0 value decreases of about one order of magnitude, the first permeation transient appears to be slower.

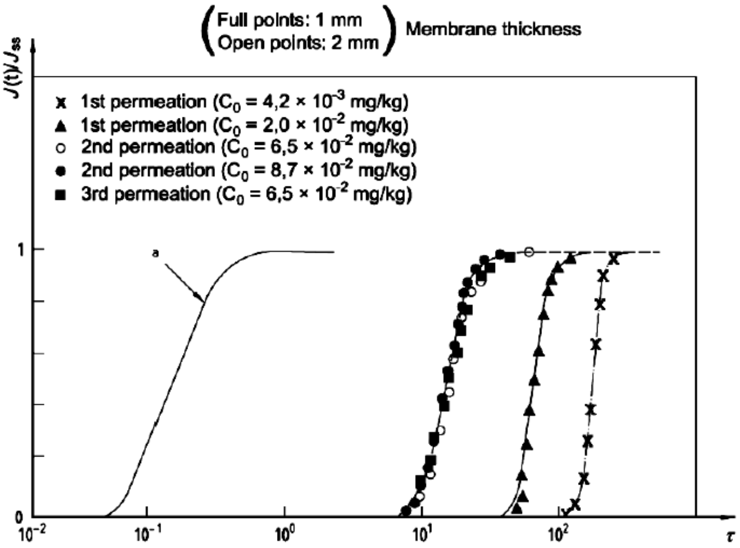

a Lattice diffusion.

Figure 6.3. Rising permeation transients for BS 970 410S21 stainless steel in acidified NaCl at 77°C. Results show irreversible trapping (first transient) and dependency on charging conditions (C_0 value). To be noted: time delay and steeping of the curves relative to lattice diffusion, similarity of second and third transients and independence of thickness [201]

If the normalized permeation transient appears steeper than predicted by Fick's second law, this indicates a significant trapping effect, while a transient less steep is often the manifestation of unsteady surface conditions. In addition, the possible presence of peaks in the transients represents variations over time of the effective diffusivity value, which inevitably makes the analysis uncertain. *Figure 6.3* also allows to evaluate the extent of reversible and irreversible trapping sites, as the first and second permeation transients are compared: if the first transient takes longer time than the second one, as shown by the normalized permeation curves, then irreversible trapping phenomena exist and influence hydrogen permeation.

In conclusion, it seems that the ISO 17081:2014 [201] standard did not explain clearly two fundamental aspects of this method:

- Electrochemical conditions of the specimen entry surface during the whole permeation test, due to its cathodic polarization. In fact, the standard assumption is that hydrogen activity on the entry surface remains constant during the test, but the electrochemical conditions cannot be considered as constant in most of the applications, because these change over time
- Diffusion transport in many industrial steels and metal alloys that do not follow pure diffusion. This aspect, already remarked by many researchers in the past, deals with the impossibility of obtaining the concurrence of the theoretical solution of Fick's second law and experimental permeation curves, and the real hydrogen charging profile of industrial steels and metal alloys.

7

EXPERIMENTAL PERMEATION TESTS AND PROCEDURES

The experimental section of the present work describes the materials and the testing procedures used to analyze hydrogen permeation, in terms of diffusivity and interaction with the defects inside the steel. The tests were performed on one type of high strength low alloy carbon steel, catalogued by the American Petroleum Institute [279] as API 5L X65 grade steel, which is probably the mainly utilized in pipelines construction for the transportation of petroleum and natural gas.

The grade designation of pipeline steels is attributed by the nominal yield strength (σ_y or TYS), expressed in ksi (1 ksi ≈ 6.9 MPa); for example, for the considered X65 grade steel, the designation indicates a TYS of 65 ksi (≈ 448 MPa).

7.1 Materials

The choice to deal with a metal structure as homogeneous as possible led to the adoption of the API 5L X65 grade steel, characterized by a microstructure typical of quenched and tempered (Q&T) martensite, i.e. ferritic-bainitic microstructure – sorbite *(Table 7.1)*. The microstructure of this steel was confirmed by metallographic etching with Nital 2% *(Figure 7.1)*.

Table 7.1. Characteristics of the pipes made of API 5L X65 grade steel used in the permeation tests

Grade	**OD x WT (mm)**	**Internal production order**	**Heat number**	**Actual YS (MPa)**
X65QS	360 x 57	1013741/1	936118	488 – 509

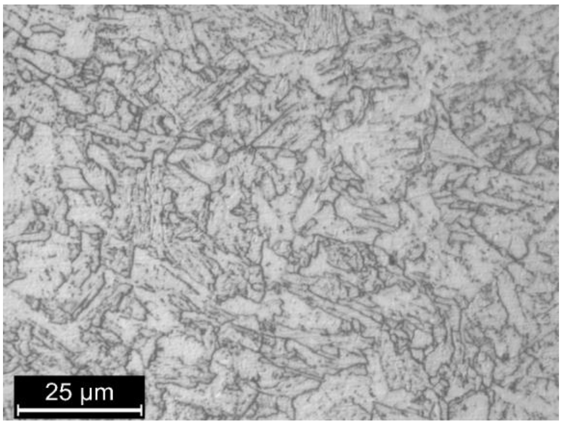

Figure 7.1. Microstructure of the tested X65 grade steel after etching with Nital 2%

All the specimens used in the permeation tests were extracted from commercial thick wall seamless pipes. These specimens were all obtained from the center of the pipe thickness, along the longitudinal direction of pipe segments, so that hydrogen permeation could occur always at the same thickness depth. Different specimen geometries were prepared, depending on the specific test condition.

7.2 Specimens

7.2.1 Specimens for tests on unloaded material

For the tests on the unloaded material, the specimens were obtained by cutting thin steel foils (dimensions: 30x30x5 mm), which were then shaped and milled in order to ensure a uniform thickness of 1 ± 0.01 mm in correspondence of the exposed area *(Figure 7.2)*.

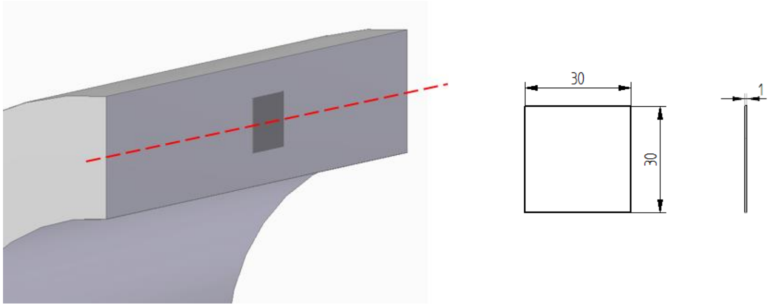

Figure 7.2. Specimen geometry for the tests on unloaded material

The tests on these specimens were carried out in order to characterize hydrogen diffusion behavior in the unstrained material in the absence of an applied load, and to compare the results obtained with those present in the literature for this kind of steel microstructure (sorbite).
In the results, reference will be made to the unloaded condition with the acronym *"U"*.

7.2.2 Specimens for tests on stretched material

For the tests on the stretched material, i.e. pre-strained by the achievement of a tensile stress, the specimens were obtained from thick slices (dimensions: 30x200x5 mm), then again shaped and milled to a uniform thickness of 1 ± 0.01 mm in correspondence of the exposed area *(Figure 7.3)*.

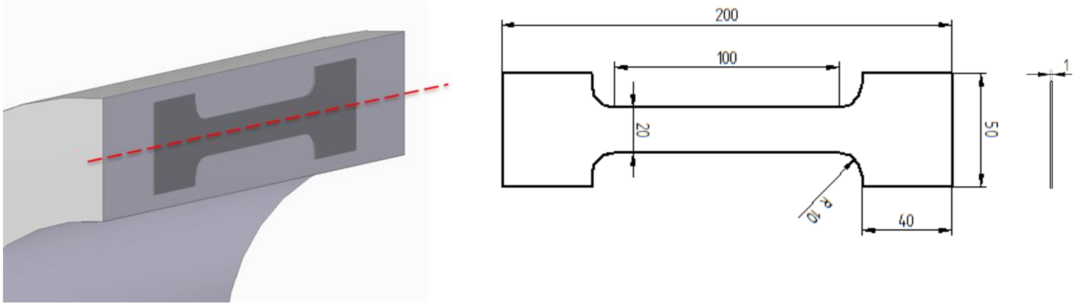

Figure 7.3. Specimen geometry for the tests on stretched material, tests on cyclically loaded material and tests on incremental step loaded material

After the application of the tensile stress, corresponding to the values 100/110% TYS, the pre-strained specimens were completely unloaded and removed from the testing machine. As a result, hydrogen permeation could occur through the metal only in the presence of a residual plastic strain, and without the elastic strain contribution due to the maintenance of an applied load.

In the results, reference will be made to the stretched condition with the acronym *"PT"*.

7.2.3 Specimens for tests on compressed material

For the tests on the compressed material, i.e. pre-strained by the achievement of a compressive stress, samples were milled to obtain compact prismatic samples (dimensions: 30x30x20 mm) with flat and planar surfaces *(Figure 7.4)*, in which the occurrence of instability phenomena can be excluded.

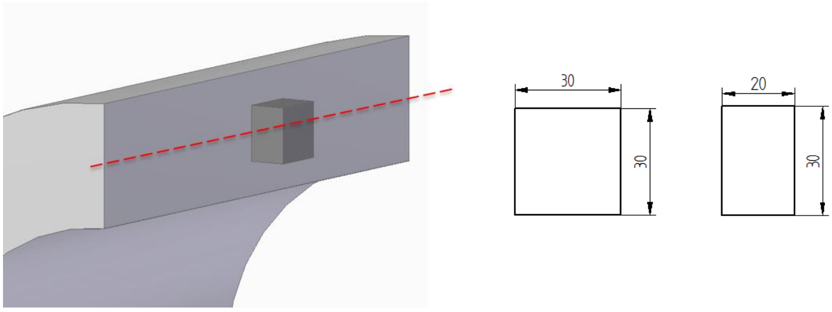

Figure 7.4. Specimen geometry for the tests on compressed material

After the application of a compressive stress, corresponding to the values 100/110% TYS, along a direction parallel to the longitudinal axis of the pipe, i.e. the same direction of the previous tensile stress, the width of these samples was reduced to 20 mm to exclude confinement effects during compression. The specimens were again shaped and milled to achieve a thickness of 1 ± 0.01 mm in correspondence of the exposed area.

In the results, reference will be made to the compressed condition with the acronym *"PC"*.

7.2.4 Specimens for tests on stretched/compressed material

These tests, performed on the stretched/compressed material, first involved the achievement of a certain tensile stress value, which was followed by the achievement of the same stress module but in compression, across the unloaded condition and in continuous, i.e. without ever removing the specimen from the testing machine.

The specimens used in these tests were obtained from elongated thick prismatic samples (dimensions: 30x200x30 mm), then milled in order to obtain flat and planar surfaces *(Figure 7.5).*

The significant dimensions of the square section involved relevant loads applied to reach the desired homogeneous stress distribution in the material, but allowed to avoid the occurrence of any instability phenomenon when crossing from a tensile stress to a symmetric compressive one.

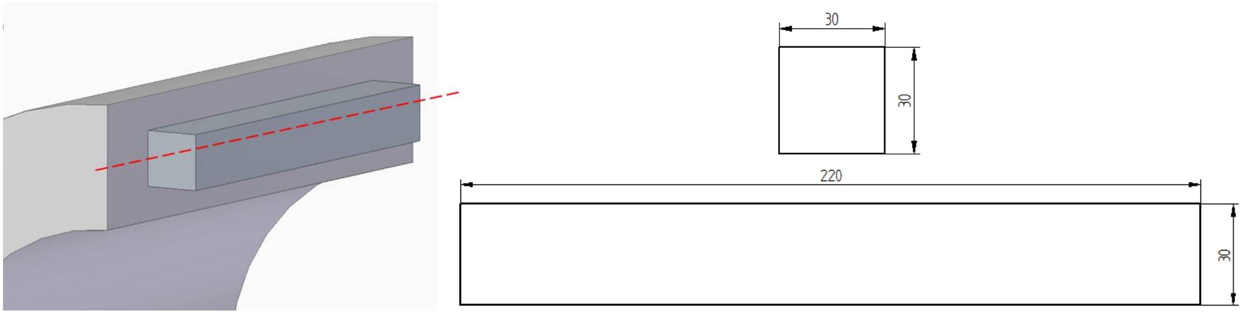

Figure 7.5. Specimen geometry for tests on stretched/compressed material

In the results, reference will be made to the stretched/compressed condition with the acronym *"PTC"*.

7.2.5 Specimens for tests on cyclically loaded material

For the tests on the cyclically loaded material, i.e. involving cyclic loading conditions, the specimens were obtained of the same dog-bone shape described for the tests on stretched material *(Figure 7.3).* These specimens were subject to a cyclic load with a sine waveform. Variations to the maximum value (55÷110% TYS), amplitude (±10/20% TYS), and frequency (10^{-2}÷1 Hz) were applied to:

- Analyze eventual transients occurring in the current induced by instant load variations, both on the steady state anodic current ($i_{a,\infty}$) and on the background passivity current ($i_{P,\infty}$)
- Evaluate the response to subsequent variations of the maximum stress on already stretched specimens (but still in the elastic field)
- Study the short-term response on the steady state anodic current ($i_{a,\infty}$) and on the background passivity current ($i_{P,\infty}$).

In the results, reference will be made to the cyclically loaded condition with the acronym *"C"*.

7.2.6 Specimens for tests on incremental step loaded material

This kind of tests refers to a standard test method for the measurement of HE susceptibility, indicated in the International ASTM F1624-12 [280] standard and prescribed for fasteners. This method, used to evaluate HE susceptibility in steels of different composition or in the same steel but with different heat treatments, is performed to measure the effect of hydrogen into the steel either in air, caused by the presence of residual hydrogen (IHE) due to the mainly manufacturing operations, or in a controlled environment, caused by the introduction of hydrogen due to the main external hydrogen sources (EHE), as detailed in the ASTM STP 543 [281] standard. However, in the performed experimental tests, only the incremental step load profile reported in the standard was applied.

This test method is based on the measurement of the load (P_{th}) necessary to determine the onset of a subcritical crack growth by means of a step modified, incrementally increasing, Slow Strain Rate (SSR) test under displacement control, according to Practice G129 [282].

By progressively decreasing the loading rate, a threshold stress (σ_{th}) can be evaluated for specimens with different geometries and different environmental conditions. In particular, the loading rate must be sufficiently slow in order to allow hydrogen to diffuse and induce cracking. The minimum stress of the threshold stress intensity represents the threshold for the onset of crack propagation due to HE.

As a result, the testing procedure described in the reference standard is as follows:

- Determination of the fast fracture strength (P_{FFS}) by means of a tensile test in air, in accordance with the ASTM E8 [283] standard, which represents the maximum load (P_{MAX}) of the first incremental step loading test. In particular, these tensile tests were carried out with an INSTRON oleo-dynamic universal testing machine (with MTS electronics) under displacement control, with a jack speed equal to 2 mm/min
- Choice of the specific load profile, depending on the material hardness (HRC). The analyzed steel in the tests carried out in this PhD Thesis work, even after the heat treatment, presents low mechanical characteristics, not included in the reference standard; therefore, the load profile relative to the lowest hardness value (HRC) was adopted. This load profile involves a first phase characterized by 10 steps, each with a load increase equal to 5% P_{MAX} maintained for 2 hours, and a second phase characterized by 10 steps, each with a load increase equal to 5% P_{MAX} maintained for 4 hours *(Figure 7.6)*
- Evaluation, at the end of the test, of the load at which the crack propagation occurred (P_{i1})
- Execution of the following tests, starting from a maximum load corresponding to the load value of the previous step (P_{th-1}) to that which led to crack propagation, increased by 10% ($1.10*P_{th-1}$). The threshold value (P_{i1}) was calculated from the load at the last step such as to maintain the load for the entire duration of the same step; any load decrease, represented by a descending convex-shape curve, is considered to be due to the subcritical crack propagation in the specimen
- Interruption of the execution of the loading ramps when the value of the threshold load variation (ΔP_{th}) was less than 5% of the maximum load in air (P_{FFS}), or in the absence of failure for the tested specimen
- Determination of the threshold stress value (σ_{th}) from the P_{th} load thus identified.

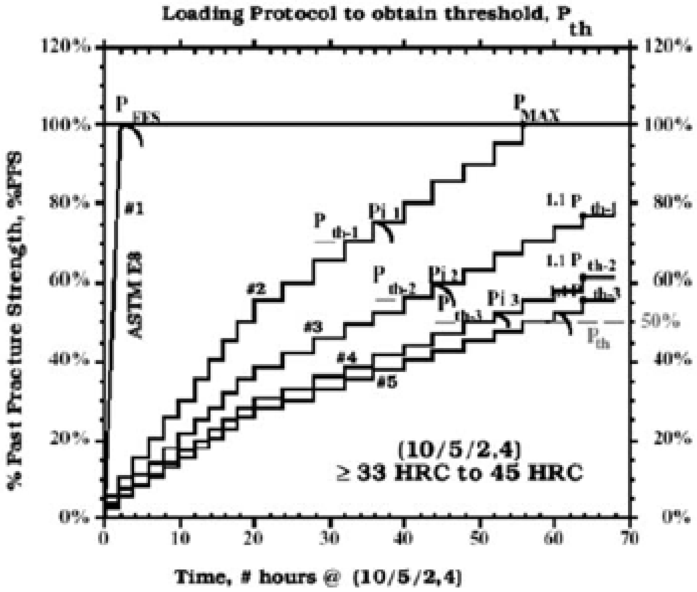

Figure 7.6. Specific load profile to be adopted, as a function of the material hardness (HRC) [280]

For the tests on the incremental step loaded material, the specimens were obtained of the same geometry described for the tests on stretched and cyclically loaded material *(Figure 7.3)*.

These tests were performed both on the X65 steel and on the same material after a heat treatment, which consists of an austenitization at 920 °C for 10 minutes, followed only by water quenching. The obtained structure is martensite, which is one of the hardest and most resistant microstructures, but at the same time the most fragile one and, thus, more susceptible to HE.

Thus, the aim of these tests was to compare, on one hand, the effect of this heat treatment on hydrogen diffusivity and, on the other hand, to analyze the possible occurrence of embrittlement phenomena at long periods in a much more susceptible steel microstructure (martensite).

It is important to specify that the incremental step load was applied only when the $i_{a,\infty}$ value was achieved, and after the same time for all the specimens and both the microstructures.

In the results, reference will be made to the incremental step loaded X65 steel with the acronym *"S"*, while, to the heat treated material but with the same load profile, with the acronym *"S_TT"*.

7.3 Hydrogen permeation test device

The test device for hydrogen permeation used in the tests on the unloaded and pre-strained material consisted of a standard Devanathan-Stachurski cell, constituted by two different compartments and realized in accordance with the International standard [201].

Instead, the device used in the tests on the material under cyclic or incremental step loading conditions consisted of a modified Devanathan-Stachurski cell, developed and assembled in the laboratories of the Department of Engineering and Applied Sciences of the University of Bergamo during this PhD Thesis *(Figure 7.7)*. Modifications to the original permeation cell and test procedures allowed to study hydrogen diffusion in the presence of different loading conditions.

The whole test apparatus is composed of poly-methyl-methacrylate (PMMA) components, with junction caps and contoured flanges used between the two compartments to hold the specimen in place with threaded bars, and flat neoprene gaskets applied for sealing.

The metal specimen acted as a bi-electrode for the two solutions, because one side (entry surface) was galvanostatically controlled, while the other side (exit surface) was potentiostatically controlled. Both the sample areas, one exposed to the charging solution (cathodic compartment) and one to the anodic solution (detection compartment) were 1.76 cm^2, considering the neoprene seal deformation after the tightening of the threaded bars. The ratio between radius and thickness of the membrane was greater than 5:1, as recommended by the standard [201].

The variability of the results obtained in the very preliminary tests, due to numerous factors, was significantly reduced thanks to a strict control of the specimen thickness and test temperature.

The specimen thickness was measured by means of a Mitutoyo high-accuracy micrometer, with a resolution in the measurement of one hundredth of a millimeter (± 0.01 mm). Instead, as the solution temperature can have a significant effect on the test results, the temperature regulation of both the solutions at the constant value of 23 ± 0.5 °C was made possible by a temperature control device, developed and assembled in the laboratories of the Department of Engineering and Applied Sciences of the University of Bergamo during this PhD Thesis.

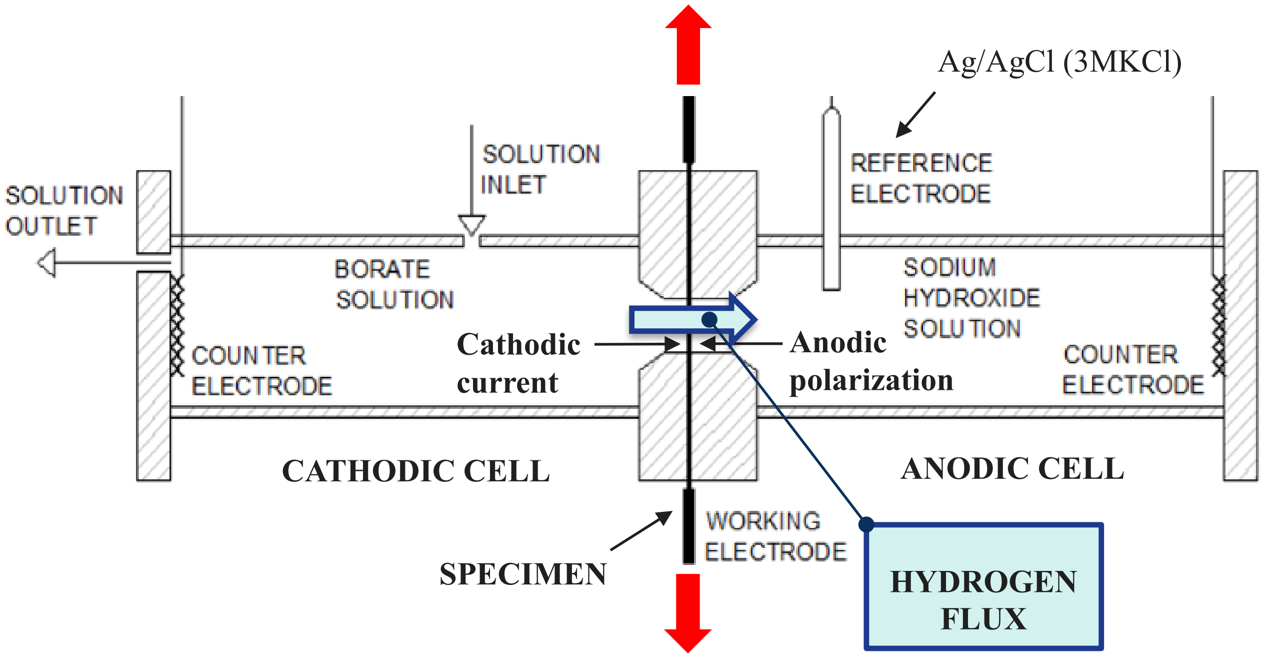

Figure 7.7. Modified Devanathan-Stachurski cell for electrochemical permeation tests in loading conditions

7.3.1 Charging compartment

The charging solution used in all the experimental procedures was an aerated borate buffer solution at pH=8.4 (0.3M H_3BO_3 + 0.075M $Na_2B_4O_7$) [259]. As stated by Nagumo and co-workers [284]

[285], this borate buffer solution is able to maintain the pH at a constant value during the whole test. Moreover, some authors [286] hypothesized that also boric acid can represent a poison for hydrogen recombination reaction, in addition to sulfur, phosphorous, arsenic, and tin.

An immersion brushless pump guaranteed a continuous replacement of the solution on the cathodic surface of the specimen from a 1-liter reservoir, with a solution velocity at the tip of the inflow tube of about 1 m/s, so to minimize the alkalization effect of the metal surface.

In this compartment, hydrogen charging was galvanostatically controlled, using an AMEL Multiple Potentiostat/Galvanostat (Model 1480/A). The counter electrode was a MMO-activated titanium net, cut into a rectangular shape (dimensions: 20x30 mm) and placed at the bottom of the compartment.

7.3.2 Detection compartment

The detection compartment was filled with a 0.1 M NaOH solution, aerated and under stagnant conditions. The condition of this side of the specimen was potentiostatically controlled, using an AMEL General Purpose Potentiostat/Galvanostat (Model 2049). The choice of using the same type of potentiostat/galvanostat for both the charging and detection compartment was fundamental for the measurement stability of such little current density values; in fact, during the development of the setup of the permeation test device, many problems linked to signal noise and instruments grounding systems occurred when coupling different type of potentiostats/galvanostats, inevitably delaying the obtainment of consistent and reliable data.

The anodic surface was polarized with an anodic potential by means of an Ag/AgCl (3MKCl) reference electrode (E ≈ +200 mV vs. SHE at T = 20 °C, or 293 K), in order to form a stable oxide film on the exit surface, and sufficient to oxidize any hydrogen atom that reaches the surface after passing through the metal. Once anodic current densities lower than 0.05 µA/cm^2 were recorded, the cathodic surface of the specimen was polarized with a constant current density to start hydrogen charging into the specimen. The counter electrode was the same used for the cathodic compartment.

7.3.3 Anodic/cathodic surface conditions

The surface preparation of both anodic and cathodic surfaces for all the X65 steel specimens included the following steps:

- Mechanical grinding of both surfaces, with the use of emery papers of decreasing SiC particles dimensions from 180 to 1200 grit, with a roughness of about 15 µm (ISO/FEPA grit designation)
- Electrical connection through the spot welding of an MMO-activated titanium wire
- Specimen cleaning with acetone and hot dry airflow.

The anodic surface in the detection compartment was not Pd-coated, in accordance with those works in the literature that suggested avoiding the electro-deposition of a thin Pd layer because of the unreliability of permeation data caused by the rupture of this coating during specimen deformation, especially in the plastic field. The works of Park et al. [277] [278] were then followed, in which consistent permeation results were obtained by developing a simple iron oxide film, grown with the application of an anodic polarization in a 0.1 M NaOH solution.

7.3.4 Hydrogen permeation procedure

The procedure adopted in the permeation tests for the evaluation of atomic hydrogen diffusion in the in all the test conditions considered is as follows:

- Assembling of the complete cell, with the specimen held in place by the two contoured flanges, positioned between the two compartments
- Filling of the anodic compartment with the 0.1 M NaOH solution and polarization with an anodic potential of +340 mV vs. Ag/AgCl (3MKCl)
- Measurement in continuous of the anodic current density (i_a), which decreases over time. The reference standard ISO 17081 [201] suggests waiting until i_a is lower than 0.1 µA/cm^2; even if this value was reached after only 3 hours of polarization, it was decided to wait 15 hours for the achievement of a more stable oxide film and lower background current densities ($i_{P,\infty}$). In this phase, in the case of tests with an applied load, different conditions of cyclic or incremental step loading were applied to observe any variation in the background passivity current. During the passivation of the anodic surface, the charging compartment was left in air
- After 15 hours, while the i_a in the anodic compartment was continuously measured, the charging compartment was filled with the borate buffer solution (0.3M H_3BO_3 + 0.075M $Na_2B_4O_7$) [259] at pH = 8.4. Once current density values lower than 0.05 µA/cm^2 were recorded, the cathodic surface of the specimen was galvanostatically polarized with a constant cathodic current density (i_c) of -0.50 mA/cm^2. This phase lasted until the exhaustion of the transient related to hydrogen diffusion and the achievement of the steady state anodic current ($i_{a,\infty}$), i.e. the stabilization of the anodic current density at values linked to the oxidation of diffusing hydrogen atoms. In the case of tests under cyclic loading conditions, different loading conditions were applied after the same periods, to observe any variation in the value of i_a, before the beginning of the charging transient or after the achievement of $i_{a,\infty}$. Instead, in the case of the tests with an incremental step load profile, the loading procedure was begun after the achievement of the steady state condition, always respecting the same periods.

A schematic representation of the mechanism of hydrogen diffusion acting during the application of the electrochemical permeation technique is reported in *Figure 7.8*.

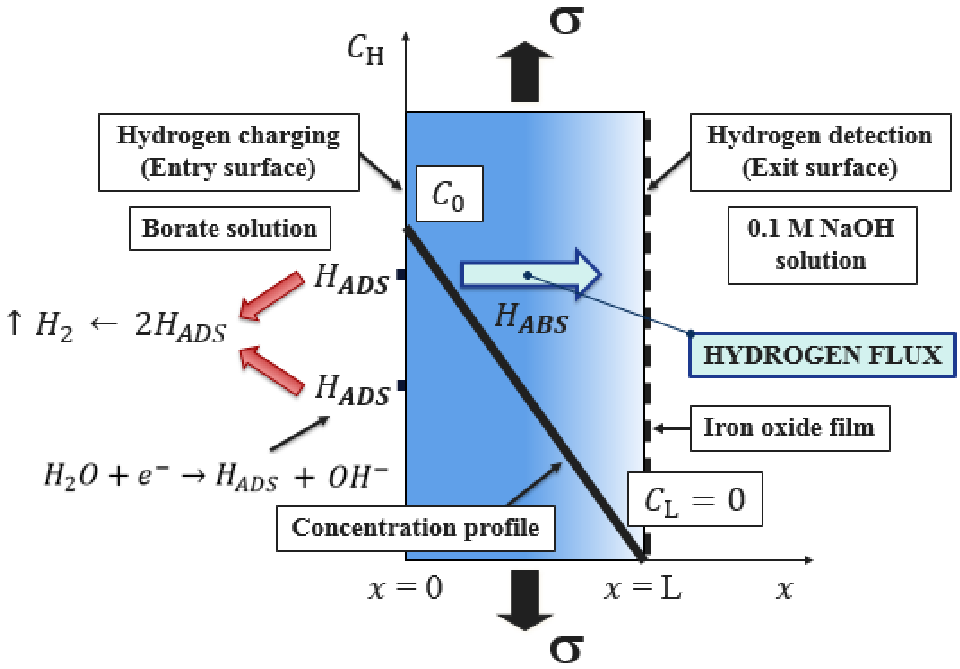

Figure 7.8. Schematic representation of hydrogen diffusion mechanism during the permeation tests

8
EXPERIMENTAL RESULTS

In this chapter, the experimental results of the permeation tests performed on the X65 grade steel in the absence of an applied load and in the presence of different loading conditions, will be presented. In the following graphs, the anodic current density (i_a) is depurated from the background passivity current (i_P); thus, $i_H = (i_a - i_P)$ represents the value, reported on the y-axis label, related only to hydrogen permeation flux. For the tests with an applied load, the increase in the ratio between the considered stress value and the tensile yield strength (σ/TYS), in percentage, is considered.

8.1 Tests in the absence of an applied load

8.1.1 Tests on unloaded material

Figure 8.1 shows that i_P decreases at similar rates in all the tests performed on the unloaded material (U); values lower than 0.1 µA/cm² [201] were reached after 10000 s of polarization.

Figure 8.2, the steady state hydrogen permeation current ($i_{H,\infty} = i_{a,\infty} - i_{P,\infty}$) was reached after about 6000 s for all the tests.

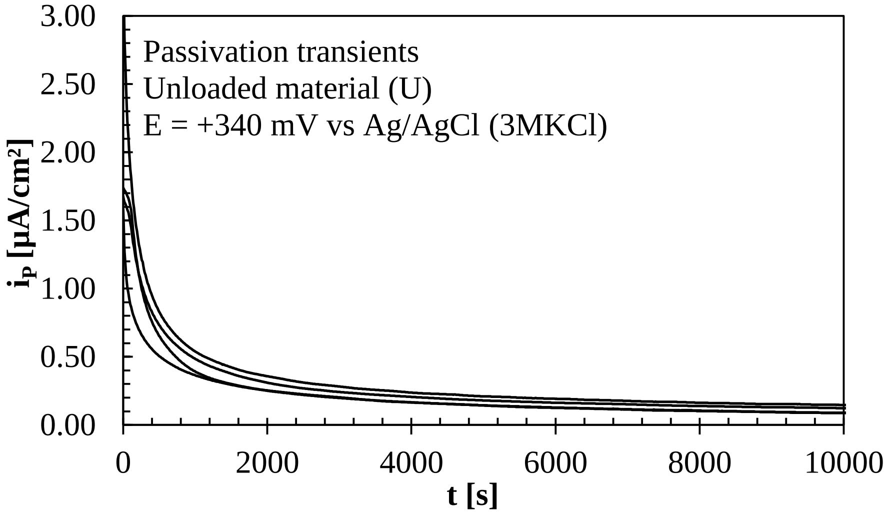

Figure 8.1. First passivation transients of the unloaded material (U)

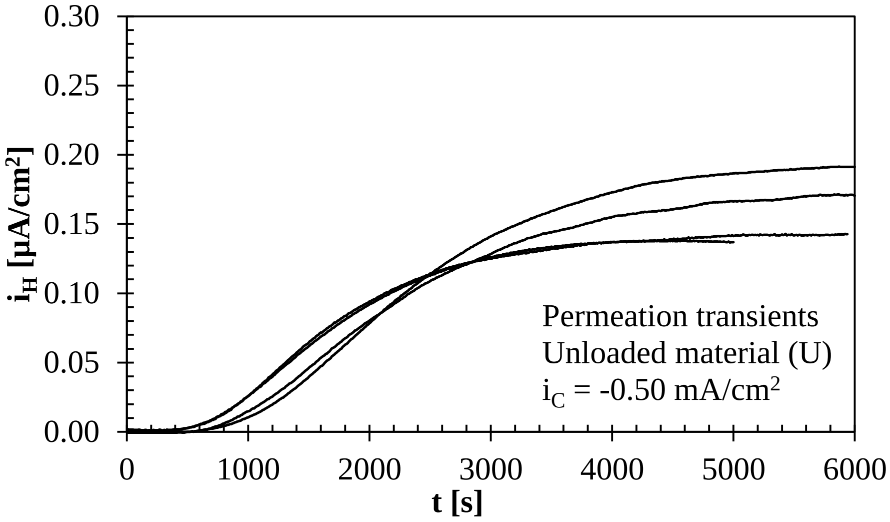

Figure 8.2. First permeation transients of the unloaded material (U)

From *Table 8.1* it is possible to see that the permeation current densities are quite reproducible and included in the range 0.14 ÷ 0.19 µA/cm^2. The average value of the time-lag (t_{lag}), previously defined as the necessary period to reach a current density equal to 63% of the steady state permeation current ($i_{H,\infty}$), and which was assumed as a reference for the comparison with the other data, is about 2100 s.

Table 8.1. Passivity and permeation current densities: unloaded material (U)

Specimen condition	**Thickness [mm]**	**Passivation time [s]**	**$i_{P,\infty}$ after 60000s [µA/cm^2]**	**$i_{H,\infty}$ after 6000s [µA/cm^2]**
U	1.03	60000	0.05	0.17
U	1.05	60000	0.02	0.14
U	1.05	60000	0.05	0.19
U	1.04	60000	0.03	0.14

During the tests, some permeation curves did not exhibit a stable and monotonic behavior, but presented a maximum at the end of the initial permeation transient, followed by a decrease in the steady state permeation flux *(Figure 8.3)*. The International ISO 17081 [201] standard reports that, for some permeation systems, a peak in the transient may be observed, and a steady state permeation current may not be obtained. This fact can be due to the development of voids in the metallic material, or caused by changes in the surface film, for example consequently to the buildup of corrosion products on the specimen charging side. The presence of peaks in the permeation transients implies that the value of the apparent diffusivity is changing with time, thus analysis is uncertain and difficult.

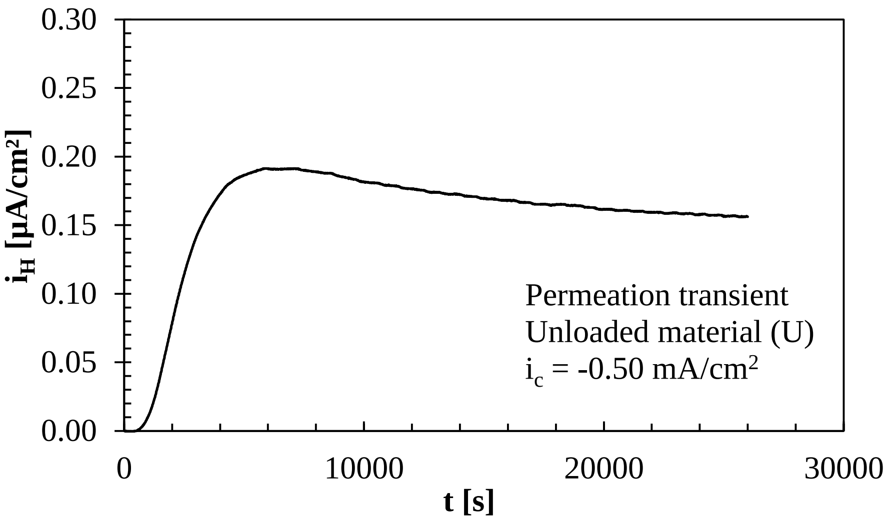

Figure 8.3. Permeation curve of the unloaded material (U) without a monotonic behavior

Bockris et al. [174] retained that the tests presenting this behavior were not valid for the purposes of the estimation of the apparent diffusion coefficient (D_{app}).

Moreover, other researchers stated that the immediate slight decrease in the steady state permeation current is a phenomenon probably ascribable to the formation and thickening of films of different nature [262] that, in alkaline solutions, cover the metal surface and may hinder the entry of H_{ads} [287]. These products can be constituted by Fe_3O_4 [288] [289] [290], γ-Fe_2O_3 [290] [291] [292], γ-FeOOH [291], δ-FeOOH, α-FeOOH [289] [290], and other oxide-hydroxides [293], which may replace atomic hydrogen at adsorbed sites. In the literature, there are works affirming that O-monolayers on intermetallic compounds significantly reduce the rate of hydrogen adsorption and desorption [184] [294] [295]. In fact, the formation of an oxide layer on the exit surface seems to act as a barrier to hydrogen evolution, not allowing the stabilization of hydrogen concentration on this side of the specimen. This seems to prevent the achievement of stable stationary conditions, thus affecting the steady state hydrogen flux.

In addition, more recent works reported this phenomenon [174] [222] [296] [297]. For example, Beck et al. [174] showed the existence of a first hydrogen permeation peak on Armco iron, in which hydrogen charging was carried out in a sulfuric acid solution at room temperature. Amiot et al. [296] affirmed that this phenomenon is due to the loss of hydrogen flux caused by the breakage of surface blisters. Similar results were obtained by Iino et al. [222] where, instead, no blisters were observed. These authors indicated void nucleation as an explanation of this phenomenon, which in their case was represented by an aggregate of dislocations [221].

8.1.2 Tests on stretched material

Figure 8.4 shows that, also in this case, i_P decreases at similar rates in all the tests performed on the stretched material (PT). Current density values lower than 0.1 µA/cm² [201] were again reached after

10000 s of polarization, as previously observed on the unloaded material (U).

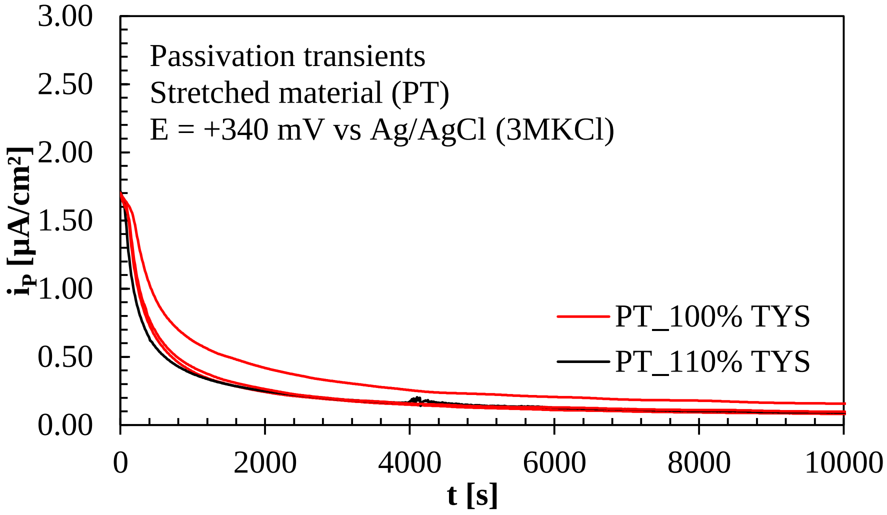

Figure 8.4. First passivation transients of the stretched material (PT)

As shown in *Figure 8.5*, $i_{H,\infty}$ is reached after a long period, much longer if compared to the previously presented results related to the unloaded material (U).

In fact, in the case of the "PT_100% TYS" specimens, previously loaded with a tensile stress of 100% TYS, $i_{H,\infty}$ was achieved after about 15000 s, which is twice the time of the unloaded material (U). Instead, for the "PT_110% TYS" specimen, previously loaded with a tensile stress of 110% TYS, $i_{H,\infty}$ was achieved only after a period of about 60000 s, which is one order of magnitude higher.

A similar behavior was observed by Ha et al. [53], in which the permeation current density increased and reached the steady state value more slowly with an increase in the strain extent.

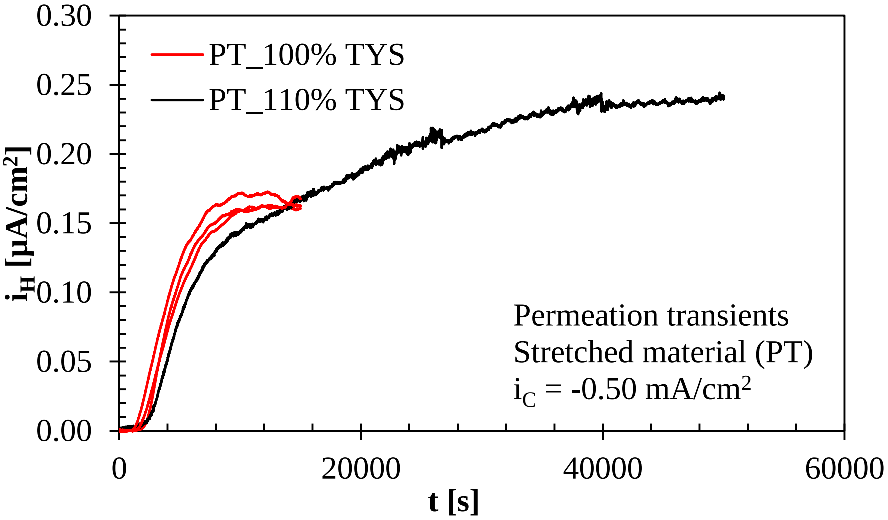

Figure 8.5. First permeation transients of the stretched material (PT)

Table 8.2 shows that, concerning the "PT_100% TYS" specimens, the current density values are quite reproducible and included in the range 0.16 ÷ 0.17 µA/cm^2, while, for the specimen identified as "PT_110% TYS", the obtained value is appreciably higher, and raises up to 0.24 µA/cm^2. The t_{lag}, for the “PT_100% TYS” specimens, was about twice the value of the unloaded material (U), with an average value of 4270 s; instead, for the “PT_110% TYS” specimen, it was equal to 5160 s.

Table 8.2. Passivity and permeation current densities: stretched material (PT)

Specimen condition	**Thickness [mm]**	**Passivation time [s]**	**$i_{P,\infty}$ after 60000s [μA/cm^2]**	**t_{lag} [s]**	**$i_{H,\infty}$ after 60000s [μA/cm^2]**
PT_100% TYS	1.04	60000	0.03	4390	0.16
PT_100% TYS	1.05	60000	0.05	4360	0.17
PT_100% TYS	1.04	60000	0.03	4055	0.16
PT_110% TYS	1.05	60000	0.04	5160	0.24

8.1.3 Tests on compressed material

As regards the compressed material (PC), i_P decreases again at similar rates *(Figure 8.6)*. Current density values lower than 0.1 μA/cm^2 [201] were again reached after 10000 s, as previously observed on the unloaded material (U).

Figure 8.7 reports that $i_{H,\infty}$ is reached after more or less the same time of the previously presented results related to the unloaded material (U). In fact, in both the cases of the “PC_100% TYS” and “PC_110% TYS” specimens, previously loaded with a compressive stress of 100% and 110% TYS, respectively, $i_{H,\infty}$ was achieved after about 8000 s.

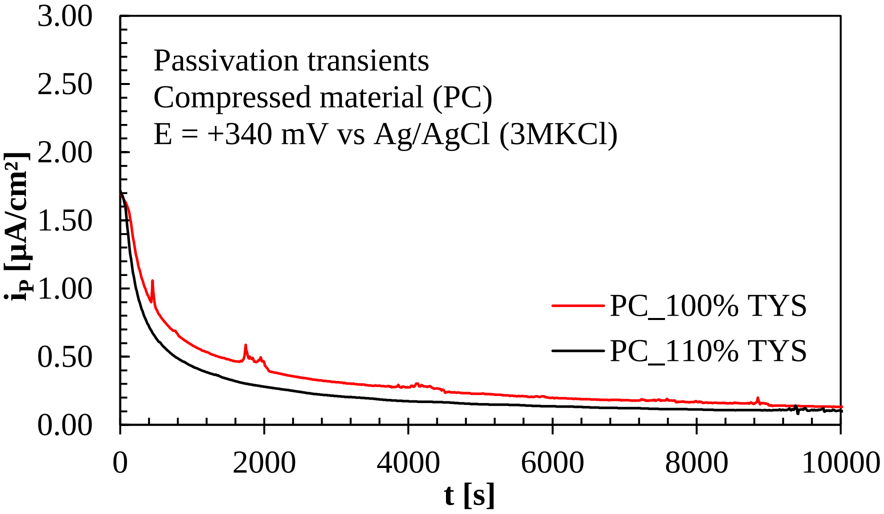

Figure 8.6. First passivation transients of the compressed material (PC)

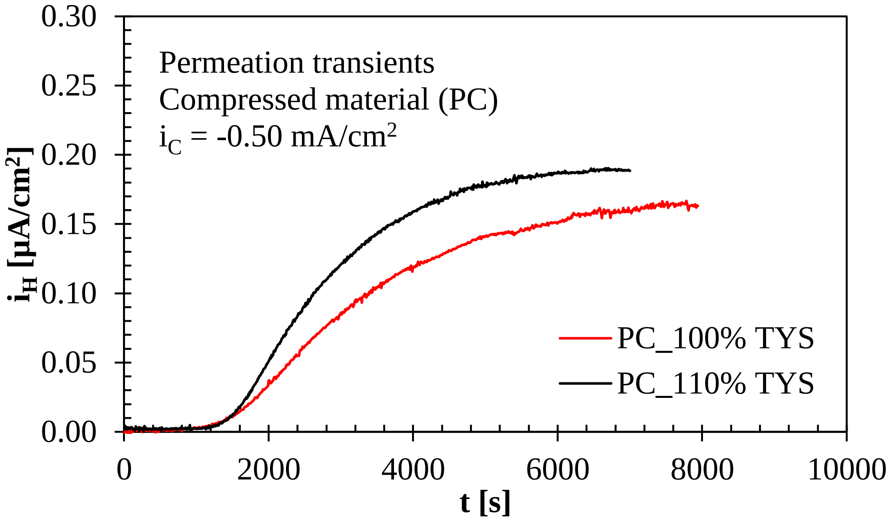

Figure 8.7. First permeation transients of the compressed material (PC)

The t_{lag} values and the permeation current densities *(Table 8.3)* are similar to those obtained on the unloaded material (U); in particular, concerning the "PC_100% TYS" specimen, the value is around 0.16 µA/cm^2, while, for the specimen identified as "PC_110% TYS", the obtained value is slightly higher (0.19 µA/cm^2), but again lower than 0.20 µA/cm^2.

Table 8.3. Passivity and permeation current densities: compressed material (PC)

Specimen condition	**Thickness [mm]**	**Passivation time [s]**	**$i_{P,\infty}$ after 60000s [µA/cm^2]**	**t_{lag} [s]**	**$i_{H,\infty}$ after 8000s [µA/cm^2]**
PC_100% TYS	1.05	60000	0.04	2865	0.16
PC_110% TYS	1.02	60000	0.03	2555	0.19

8.1.4 Tests on stretched/compressed material

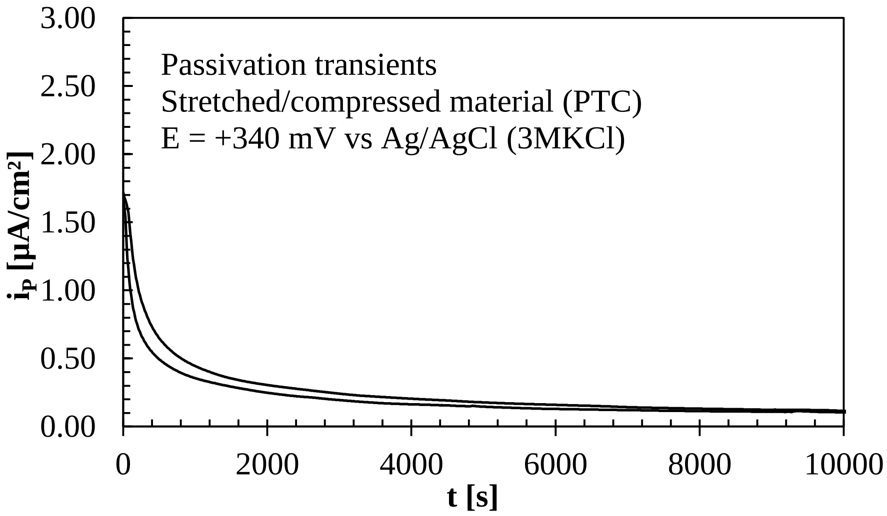

Figure 8.8. First passivation transients of the stretched/compressed material (PTC)

From *Figure 8.8* it can be seen that, also in the case of the tests performed on the stretched/compressed material (PTC), i_P decreases at similar rates, and that current density values lower than 0.1 µA/cm^2 [201] were again reached after 10000 s of polarization.

As shown in *Figure 8.9*, the $i_{H,\infty}$ values are achieved after twice the time related to the previously presented results on the unloaded material (BM), i.e. after about 15000 s. This period is instead comparable to that obtained in the case of the "PT_100% TYS" specimens.

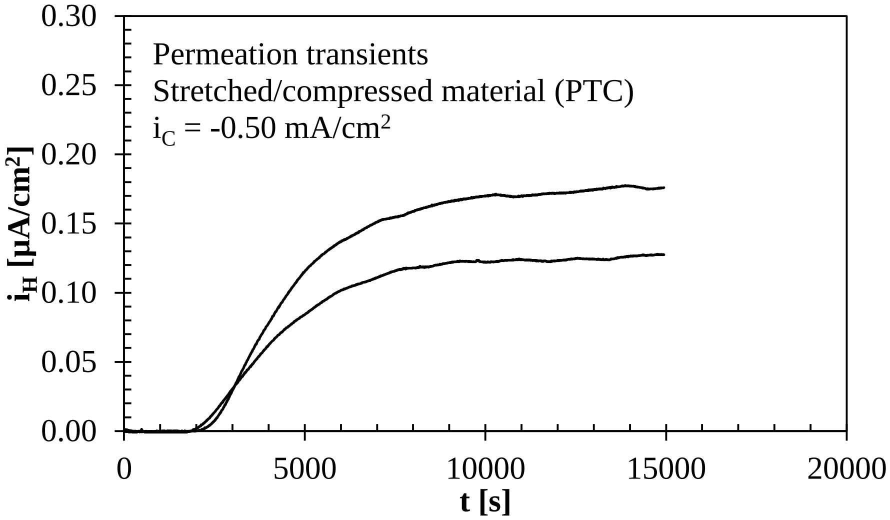

Figure 8.9. First permeation transients of the stretched/compressed material (PTC)

As occurred for example in the case of the unloaded material (U), the permeation current densities are again lower than 0.20 µA/cm^2 *(Table 8.4)*; the two values are equal to 0.17 and 0.18 µA/cm^2. For both the specimens, the t_{lag} was more or less twice the value of the unloaded material (U), with an average value of about 4000 s, which is lower than in the case of the "PT_110% TYS" specimen, and comparable to that obtained on the "PT_100% TYS" specimens.

Table 8.4. Passivity and permeation current densities: stretched/compressed material (PTC)

Specimen condition	Thickness [mm]	Passivation time [s]	$i_{P,\infty}$ after 60000s [µA/cm^2]	t_{lag} [s]	$i_{H,\infty}$ after 15000s [µA/cm^2]
PTC_110% TYS	1.04	60000	0.04	4165	0.17
PTC_110% TYS	0.96	60000	0.03	3835	0.18

8.2 Tests in the presence of an applied cyclic load

8.2.1 Influence of the applied maximum load

In these tests, the cyclic load was applied immediately at the beginning of the test, so that both the passivation of the anodic surface and the hydrogen permeation transient could occur under the specific loading condition. All these tests were performed at the lowest amplitude (±10% TYS) and frequency (10^{-2} Hz) of the load considered for the tests under cyclic loading conditions.

Figure 8.10 shows that, also in the tests performed on the cyclically loaded material (C), i_P decreases at similar rates. In fact, current density values lower than 0.1 µA/cm^2 [201] were again reached after 10000 s of polarization, as previously observed on the unloaded material (U).

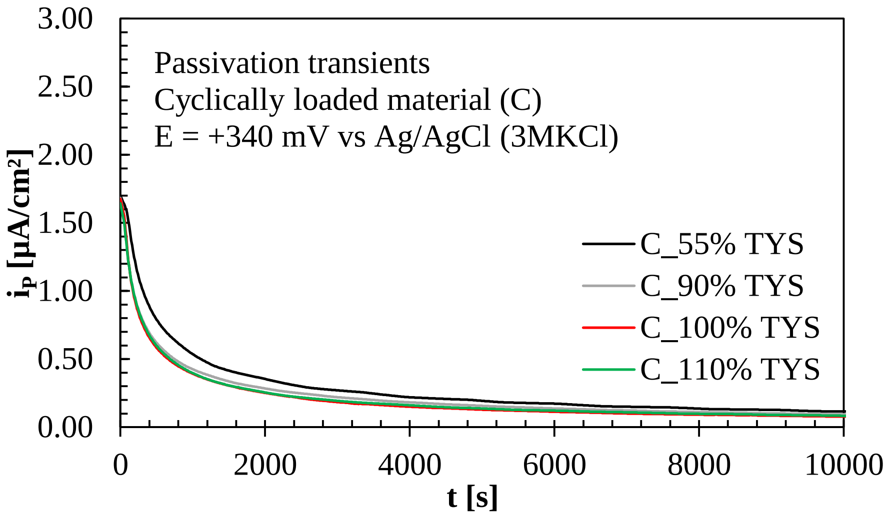

Figure 8.10. First passivation transients of the cyclically loaded material (C)

As shown in *Figure 8.11*, $i_{H,\infty}$ is reached after a long period, much longer if compared to the previously presented results related to the unloaded material (U). Unfortunately, due to acquisition problems, both the tests on the "C_55% TYS" and "C_90% TYS" specimens finished too early to appreciate the transient exhaustion, and consequently to observe the steady state permeation flux that would have been reached. Therefore, those flux values can only be simulated with a data processing method; the estimate of those values will be further presented (Par. 11.1.3).

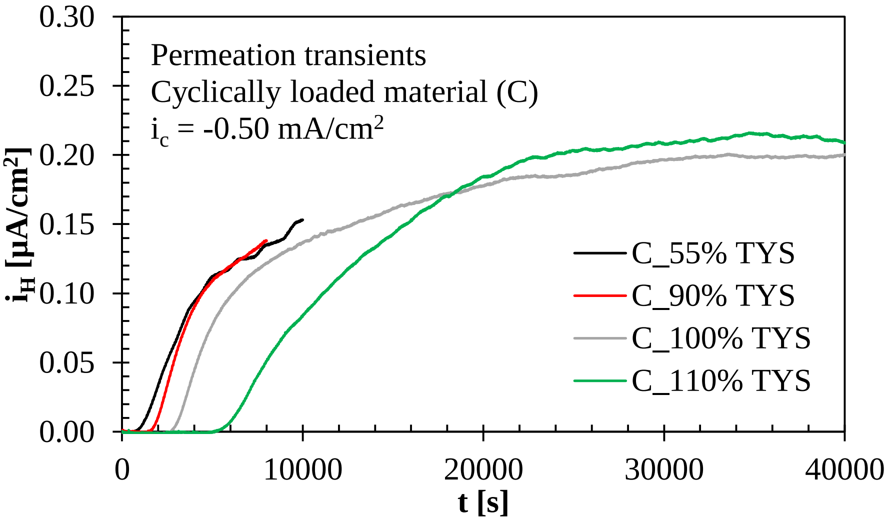

Figure 8.11. First permeation transients of the cyclically loaded material (C)

Anyway, for both the specimens "C_100% TYS" and "C_110% TYS", $i_{H,\infty}$ is reached after a period about one order of magnitude higher than the previous time of the unloaded material (U), i.e. only after about 40000 s. As in the case of the stretched material (PT), i_H reaches the steady state value more slowly as the strain extent increases [53].

The values of $i_{H,\infty}$ are again around 0.20 μA/cm^2 *(Table 8.5)*, and almost identical for both the conditions of 100% and 110% TYS. It is interesting to observe the trend of the t_{lag}, which passes from a value of ≈3400 s for the "C_55% TYS" specimen to a value of ≈11600 s for the "C_110% TYS" one, which is about 5.5 times higher than the value on the unloaded material (U).

Table 8.5. Passivity and permeation current densities: cyclically loaded material (C)

Specimen condition	**Thickness [mm]**	**Passivation time [s]**	**$i_{P,\infty}$ after 60000s [μA/cm^2]**	**t_{lag} [s]**	**$i_{H,\infty}$ after 40000s [μA/cm^2]**
C_55% TYS	1.05	60000	0.03	3405	-
C_90% TYS	1.05	60000	0.03	4375	-
C_100% TYS	1.05	60000	0.02	8455	0.21
C_100% TYS	1.05	60000	0.02	7100	0.20
C_110% TYS	1.05	60000	0.02	11975	0.20
C_110% TYS	1.05	60000	0.02	11410	0.21

8.2.2 Variation of amplitude and frequency of the load

In these tests, different cyclic loading conditions, fully included in the elastic domain, were applied for a short period (≈600 s) only after the exhaustion of the permeation transient and the achievement of a stable steady state anodic current ($i_{a,\infty}$). The aim of these tests was to observe any variation in the hydrogen flux due to the application of the above-mentioned loading conditions.

As shown in *Table 8.6*, the average value of the load was always equal to 45% TYS, while the two amplitude values considered were ±10% and ±20% TYS; moreover, for each load amplitude, three significant values of the frequency were considered (10^{-2}, 10^{-1}, 1 Hz).

Table 8.6. Effect of the amplitude and frequency of the load on the steady state permeation current

σ / TYS [%]	**Δσ / TYS [%]**	**f [Hz]**	**$\Delta i_{a,\infty}$ [μA/cm^2]**	**$\Phi(i_{a,\infty})$ [°]**	**Φ(σ) [°]**	**$\Delta(\Phi(\sigma) - \Phi(i_{a,\infty}))$ [°]**
45	10	0.0122	0.002	-120	17	136
45	10	0.1221	0.004	-146	-22	128
45	10	1.2207	0.022	42	143	123
45	20	0.0122	0.002	172	-60	120
45	20	0.1221	0.008	156	-84	101
45	20	1.2207	0.046	104	-155	101

For greater accuracy, slightly different values of the load frequency were applied. Moreover, the reported values of the current amplitude ($\Delta i_{a,\infty}$) are referred to the steady state value of the anodic current ($i_{a,\infty}$), thus not depurated from the contribution of the background passivity current ($i_{P,\infty}$).

From *Table 8.6* it is possible to see that, to an increase in the amplitude and frequency of the load, an increase in $\Delta i_{a,\infty}$ corresponds. In addition, there is a difference between the phase of the current signal ($\Phi(i_{a,\infty})$) and the phase of the load signal ($\Phi(\sigma)$), which seems to decrease with the increase in the amplitude and frequency of the load. This phase shift, identified as $\Delta(\Phi(\sigma) - \Phi(i_{a,\infty}))$, represents the delay between the load sinusoid and its effect on $i_{a,\infty}$.

As an example, *Figure 8.12* shows the effect of the alternate component of the load in the worst condition considered (A = ±20% TYS; f = 10^{-2} Hz) on $i_{a,\infty}$. It is possible to better appreciate how, at short periods (≈600 s), the average value exhibited no variations, and how the behavior of the current signal changes to a sine waveform, following the load sinusoid in a uniform way.

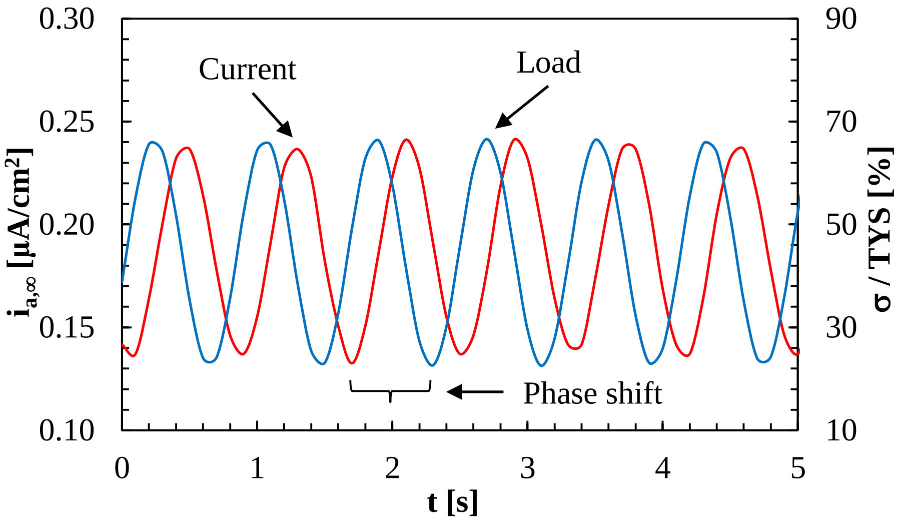

Figure 8.12. Effect of the alternate component of the load in the worst considered condition (A = ±20% TYS; f = 1 Hz) on the steady state anodic current

As a consequence, in order to verify if the variations in the current previously observed were indeed caused by the presence of diffusing hydrogen through the metal or due to other factors, the same cyclic loading conditions were applied for a short period (≈600 s) also on $i_{P,\infty}$.

Also in this case (*Table 8.7*), to an identical increase in the amplitude and frequency of the load, an increase in the current amplitude ($\Delta i_{P,\infty}$) corresponds, which is very similar to that on $i_{a,\infty}$ ($\Delta i_{a,\infty}$). Thus, the current variation previously observed was not due to the presence of diffusing atomic hydrogen.

Instead, the phase shift, identified in this case as $\Delta(\Phi(\sigma) - \Phi(i_{P,\infty}))$, seems to remain almost constant, or at least to slightly increase with an increase in the amplitude and frequency of the load.

As an example, *Figure 8.13* shows the effect of the alternate component of the load in the worst condition considered (A = ±20% TYS; f = 10^{-2} Hz) on $i_{P,\infty}$.

Table 8.7. Effect of the amplitude and frequency of the load on the background passivity current

σ / TYS [%]	**Δσ / TYS [%]**	**f [Hz]**	**$\Delta i_{P,\infty}$ [μA/cm^2]**	**$\Phi(i_{P,\infty})$ [°]**	**Φ(σ) [°]**	**$\Delta(\Phi(\sigma) - \Phi(i_{P,\infty}))$ [°]**
45	10	0.0122	0.001	-30	69	99
45	10	0.1221	0.004	79	179	99
45	10	1.2207	0.025	-98	13	111
45	20	0.0122	0.001	-16	89	105
45	20	0.1221	0.007	46	146	99
45	20	1.2207	0.050	-146	-35	111

The average value of $i_{P,\infty}$ exhibited no variation again at short periods (≈600 s), and the behavior of the current signal changes again to a sine waveform, following the load sinusoid in a uniform way.

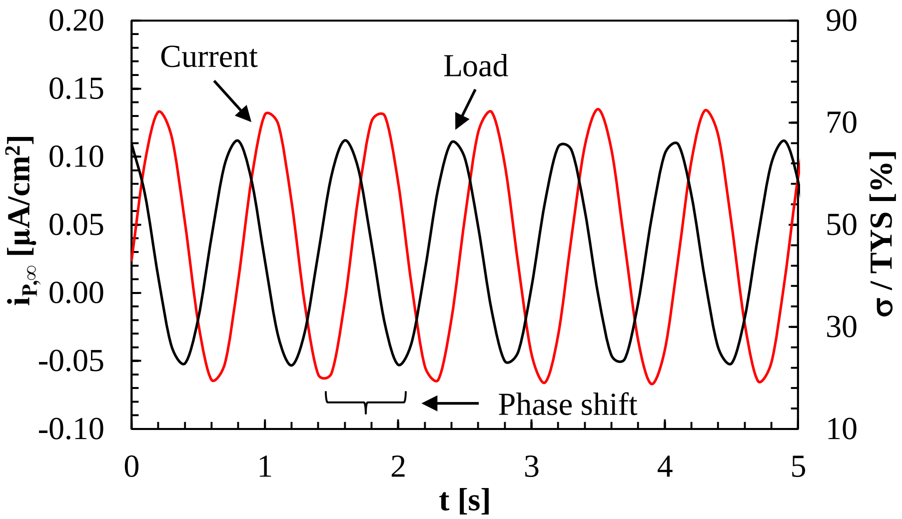

Figure 8.13. Effect of the alternate component of the load in the worst considered condition (A = ±20% TYS; f = 1 Hz) on the background passivity current

8.2.3 Variation of the maximum load

Another analysis performed under cyclic loading conditions, at the lowest frequency (10^{-2} Hz) and with an amplitude of the cyclic load equal to ±10% TYS, is represented by the response to instant variations of the maximum stress on $i_{a,\infty}$ *(Figure 8.14)*. In this graph, the test time is still expressed in seconds (s) while, for each test, the anodic current density (i_a) is normalized to the steady state value ($i_{a,\infty}$) of the corresponding permeation curve, in order to compare the different current responses.

For example, the curve indicated as “C_100-110” refers to a variation in the applied maximum stress from 100 to 110% TYS; this variation was applied only after the achievement of a stable value of $i_{a,\infty}$ under cyclic loading conditions with a maximum stress of 100% TYS.

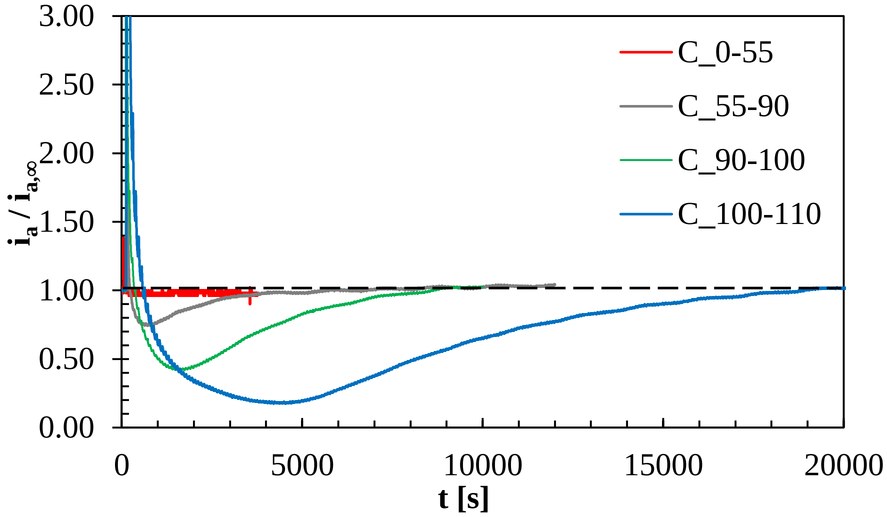

Figure 8.14. Effect of instant variations of the maximum stress (A = ±10% TYS; f = 10^{-2} Hz) on the steady state anodic current

For the stress variation from 0% to 55% TYS (fully in the elastic field), no appreciable variations in the hydrogen flux are detected. However, with stress variations closer to the yield limit (from 55% to 90% TYS and from 90% to 100% TYS), and even beyond this value (from 100% to 110% TYS), after an instantaneous peak in correspondence of the variation, the current is subject to an increasing steep drop, down to values well below the steady state flux, and then to a transient, after which, once exhausted, the current returns to the steady state values prior to the variation.

To verify that the above-mentioned response was entirely due to the variation in hydrogen flux, the same stress variations were applied on specimens without hydrogen charging, therefore only on $i_{P,\infty}$ *(Figure 8.15)*. The fact that the instantaneous peak, in correspondence of the stress variation, occurred also on $i_{P,\infty}$, suggests that this phenomenon is due to the instant local rupture of the oxide film, and not to a variation in the hydrogen flux. Therefore, after the rupture of the oxide film, a reformation of the same takes place, along with a temporary reduction in the permeation flow, due to the creation of new trapping sites that reduce temporarily the concentration of diffusing hydrogen in the lattice. This effect seems to be quite negligible for load variations almost in the middle of the elastic field; instead, it becomes greater for load variations closer to the YS, and much more beyond this limit.

Thus, from the steady state anodic current ($i_{a,\infty}$), an increasing contribution connected to i_P must be necessary subtracted; this contribution is due to the instant exposition and gradual re-passivation of ever larger areas of the bare substrate steel.

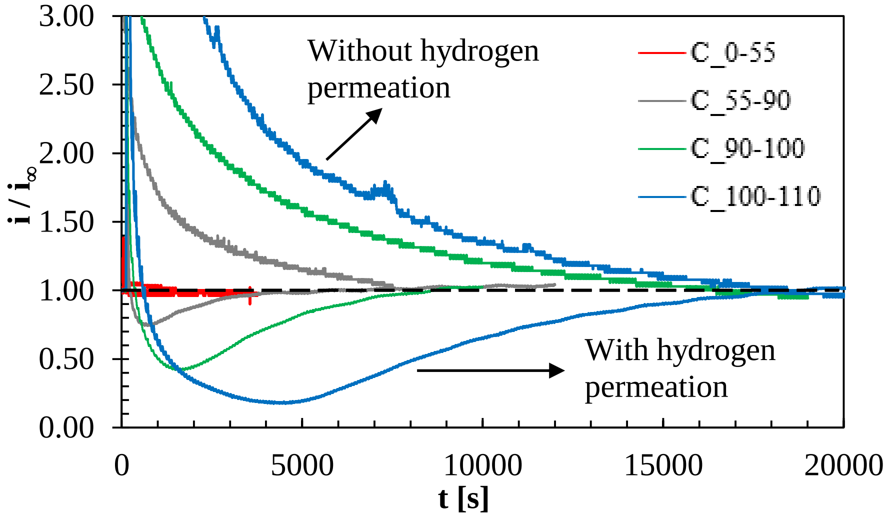

Figure 8.15. Effect of instant variations of the maximum stress (A = ±10% TYS; f = 10^{-2} Hz) on the background passivity current (compared to the steady state anodic current)

Consequently, for example for the stress variation from 55% to 90% TYS, always at the lowest load frequency (10^{-2} Hz) and with an amplitude of the cyclic load equal to ±10% TYS, once the flow transient had run out and the current had returned to the previous steady state values, a stress variation to the same maximum stress was applied on the same specimen (from 0% to 90% TYS).

As a result, no transient reductions in the permeation flow were detected *(Figure 8.16)*, probably because of the local strain-hardening of the material and no creation of new trapping sites.

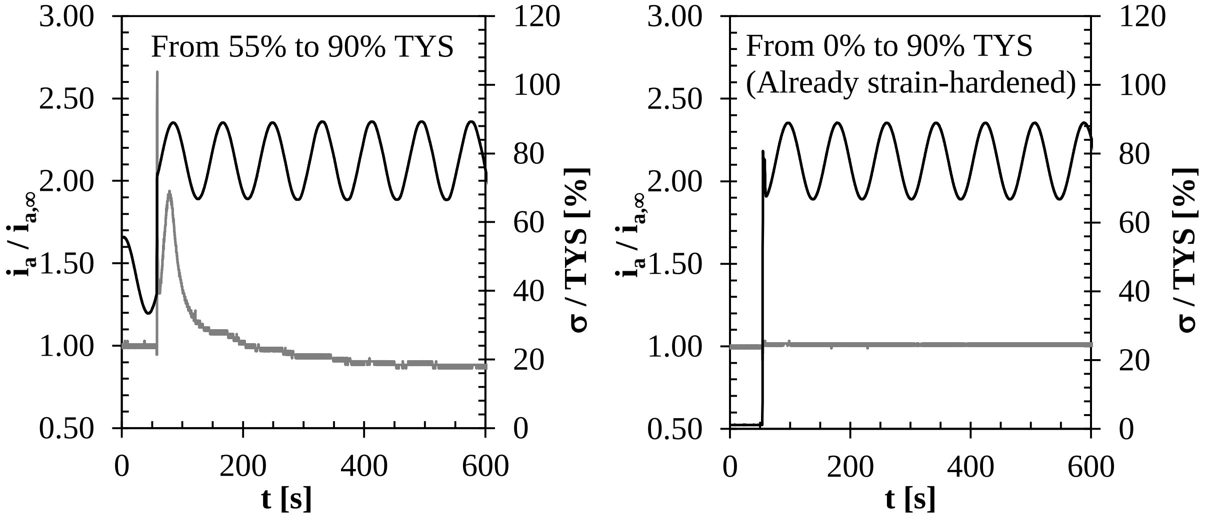

Figure 8.16. Response to subsequent variations of the maximum stress (A = ±10% TYS; f = 10^{-2} Hz) on the steady state anodic current (locally strain-hardened steel)

8.3 Tests in the presence of an applied incremental step load

8.3.1 Incremental step loading technique

In this section, the results obtained from the application of the incremental step load profile, reported in the test method for the measurement of HE susceptibility [280], will be presented. Provided that it is well known that the sorbitic microstructure that characterizes the tested X65 steel is not susceptible to HE, the aim of these tests was to:

- Evaluate any difference between the behavior of the tested steel without hydrogen charging, in which only the anodic polarization on the exit side of the specimen was activated, and during hydrogen permeation, in which the entry side was polarized by means of a fixed cathodic current
- Analyze the effect of the instant stress variation on the steady state hydrogen permeation flux in correspondence of the step changing, both in the elastic and plastic field, and on the kinetics related to the oxide film failure/reformation and to the creation/filling of new trapping sites
- Compare hydrogen diffusivity in the heat treated material (TT) to that in the unloaded material (U), and observe the possible occurrence of HE phenomena at long periods in a much more susceptible microstructure (martensite).

8.3.2 Determination of the fast fracture strength

The testing procedure described in the International standard [280] indicates that, before applying this load profile, it is necessary to determine the fast fracture strength (P_{FFS}) by performing a tensile test in air according to the ASTM E8 [283], in order to obtain the maximum load (P_{MAX}) for the first incremental step load test.

Figure 8.17 reports the results obtained from the tensile test on the X65 steel, which was conducted in air on the same specimen geometry used for the subsequent permeation test.

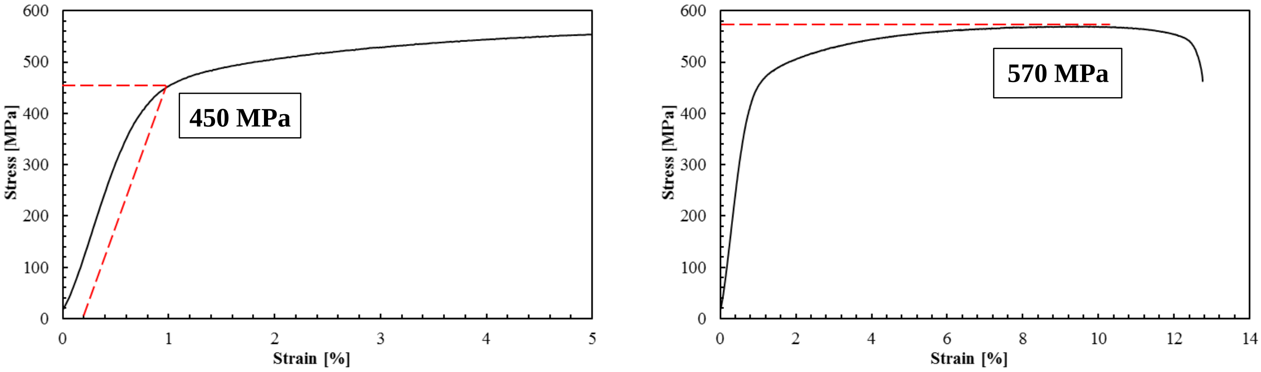

Figure 8.17. Results of the tensile test on the X65 steel for the determination of P_{MAX}

The specimen exhibited a tensile yield strength (TYS) of about 450 MPa and a maximum tensile strength (UTS) of about 570 MPa; the latter is taken as P_{MAX} for the incremental step loading technique on the X65 steel. The ratio TYS/UTS is around 0.8, while the elongation at break is about 11%, both in line with the mechanical properties commonly accepted for this steel.

Instead, *Figure 8.18* reports the results obtained from the tensile test on the heat treated material (TT). The specimen exhibited a TYS of about 1150 MPa and a UTS of about 1315 MPa; the latter is again taken as P_{MAX} for the incremental step loading technique. The ratio TYS/UTS is slightly higher, around 0.9, while the elongation at break (in percentage) is considerably lower, about 3%.

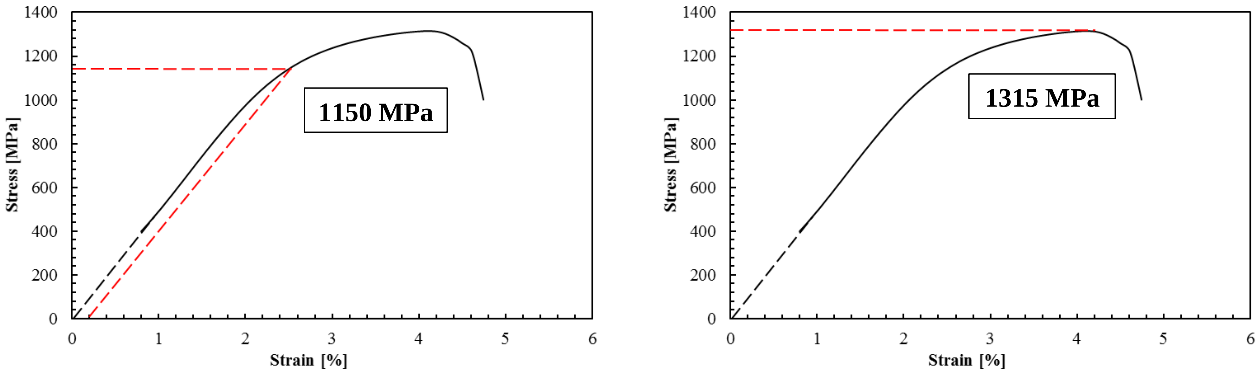

Figure 8.18. Results of the tensile test on the heat treated material (TT) for the determination of P_{MAX}

8.3.3 Choice of the specific load profile

As already said in Par. 7.2.6, the choice of the specific load profile depends on the material hardness (HRC). From the hardness tests carried out to evaluate the average hardness value at the core of the material, the tested steel is characterized by low mechanical characteristics, even after the heat treatment, not included in the reference standard. In fact, the average hardness value of the X65 steel is around 207 HV1, which corresponds to a value below the minimum limit of 20 HRC of significance of the Rockwell C scale, and below the threshold of 22 HRC, considered by the NACE MR0175/ISO 15156 [298] as the susceptibility limit to Sulfide Stress Corrosion Cracking (SSCC).

Even after the heat treatment of water quenching, the average hardness value is around 330 HV1, which corresponds to a value of 32 HRC.

Therefore, the load profile relative to the lowest hardness value (HRC) was adopted, which involves a first phase characterized by 10 steps, each with a load increase equal to 5% P_{MAX} for 2 hours, and a second phase characterized by 10 steps, each with a load increase equal to 5% P_{MAX} for 4 hours.

Because P_{MAX} assumed for the X65 steel in the incremental step load technique is 570 MPa, the increase for each step is about 28.5 MPa. Instead, concerning the heat treated material (TT), the P_{MAX} assumed is 1315 MPa, with an increase for each single step of about 65.5 MPa.

However, the results will be presented as a ratio between the considered stress value and the tensile yield strength (σ/TYS), in percentage; thus, the increase for each step was about 22.5 MPa for the X65 steel and about 57.5 MPa for the heat treated material (TT).

In the following paragraphs, this load profile will be applied both to the steady state anodic current ($i_{a,\infty}$) and to the background passivity current ($i_{P,\infty}$).

8.3.4 Heat treated material

Before the beginning of the incremental step loading, which was applied only after the achievement of a stable value of $i_{a,\infty}$ (for all the tests, after 15000 s from the activation of i_c), it was decided to analyze both the passivation and permeation transients of the heat treated material (TT) in the absence of an applied load.

As a result, from *Figure 8.19* it can be seen that, also in this case, i_P decreases at rates comparable to those previously analyzed for the unloaded material (U), as current density values again lower than 0.1 µA/cm^2 [201] were reached after 10000 s.

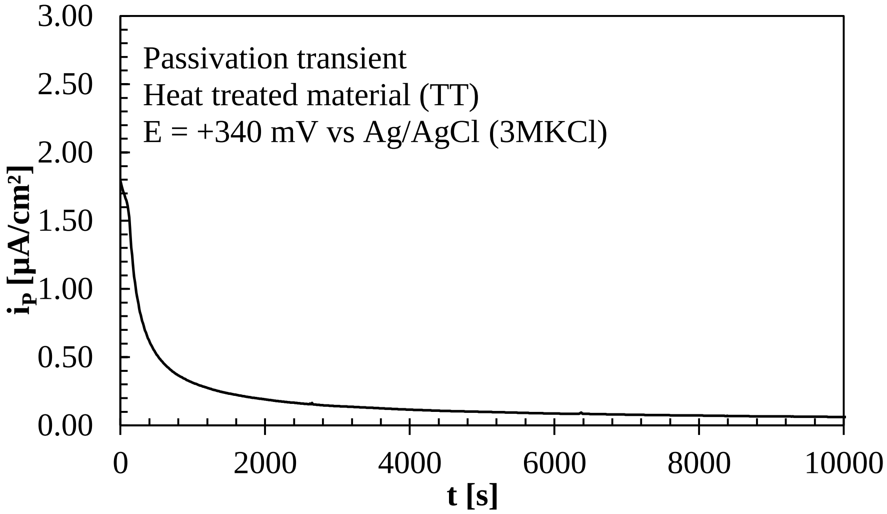

Figure 8.19. First passivation transient of the heat treated material (TT)

Figure 8.20 shows that $i_{H,\infty}$ was reached after 6000 s, which is more or less the same time if compared to the unloaded material (U).

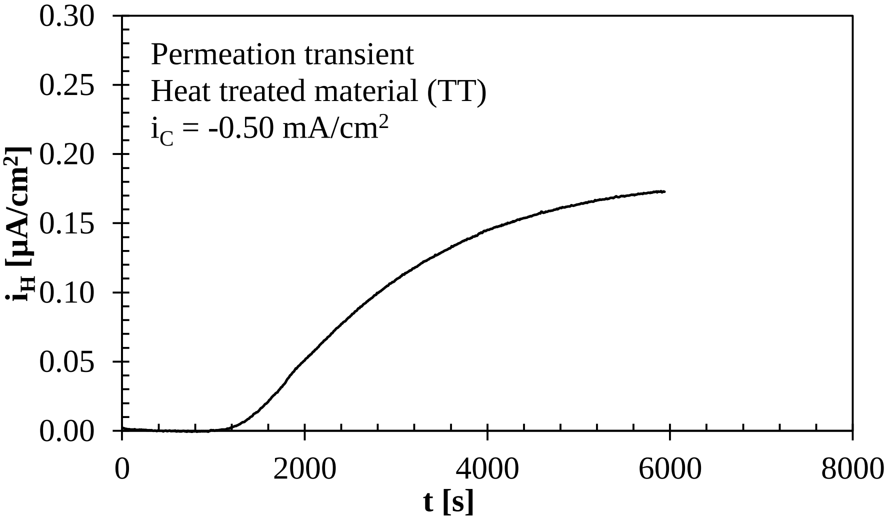

Figure 8.20. First permeation transient of the heat treated material (TT)

Also in this case *(Table 8.8)*, the t_{lag} value (≈2900 s) and the passivity and permeation current densities are similar to those detected on the unloaded material (U); the depurated value of $i_{H,\infty}$ is again below 0.20 µA/cm^2.

Table 8.8. Passivity and permeation current densities: heat treated material (TT)

Specimen condition	**Thickness [mm]**	**Passivation time [s]**	**$i_{P,\infty}$ after 60000s [μA/cm^2]**	**t_{lag} [s]**	**$i_{H,\infty}$ after 6000s [μA/cm^2]**
TT	0.98	60000	0.02	2920	0.18

8.3.5 Steady state anodic current

Figure 8.21 reports a comparison between the effects of different incremental step load tests on $i_{a,\infty}$; two tests (red and green curves) were performed on the X65 steel, while one (light blue curve) on the heat treated material (TT). The dashed curves represent the scheduled load profiles required by the reference standard (10 steps with a load increase equal to 5% P_{MAX} for 2 hours, and 10 steps with a load increase equal to 5% P_{MAX} for 4 hours), where the black one is applied on the X65 steel and the orange one on the heat treated material, respectively.

In this graph the test time is expressed in seconds (s); the anodic current density (i_a) is that directly obtained from the experimental permeation tests, thus it is expressed in μA/cm^2 and not depurated from the contribution of i_P.

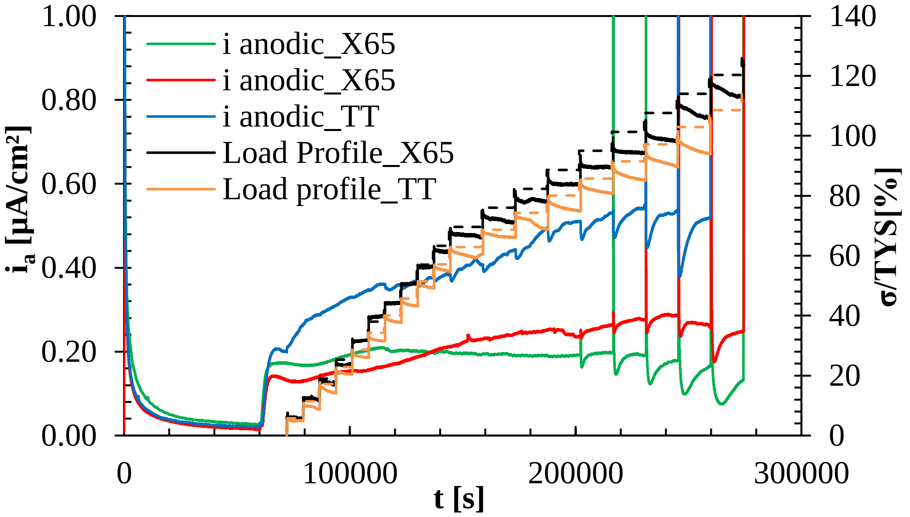

Figure 8.21. Results of different incremental step load tests on the steady state anodic current

Both the load profiles reflect the scheduled load profile up to a stress corresponding to the step around 63% TYS (50% UTS). For further increases of the applied stress, both for the X65 steel and the heat treated material (TT), a relevant decrease in the load step can be observed, which settles later during the maintenance at the imposed deformation. According to the reference standard ASTM F1624-12 [280], this behavior is uniquely due to the local plastic deformation of the specimen *(Figure 8.22)*, thus not to a subcritical crack propagation.

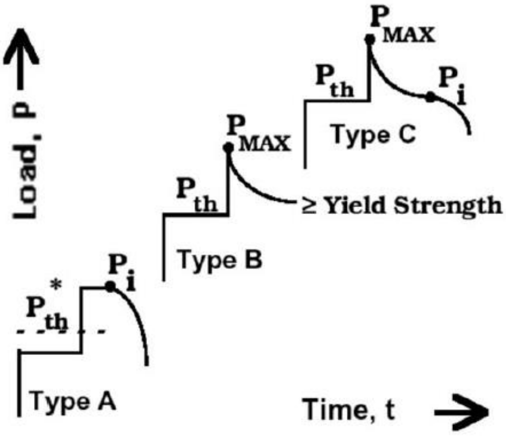

Figure 8.22. Determination of the threshold load value for the onset of crack propagation

Anyway, considering the hydrogen flux related to the X65 steel, from *Figure 8.21* it is possible to note that the incremental step load was applied only when the hydrogen permeation transient exhausted, and the $i_{a,\infty}$ value fluctuated around a quite stable value of 0.20 μA/cm^2. A slight increase in the current value was then detected even in the elastic deformation field; a similar behavior was observed also by Cabrini et al. in their work [133].

A significant effect on the current becomes evident only after 88% TYS. In fact, no perceptible modifications in this steady state value could be recorded in correspondence with the instant stress variations in the elastic field (except for the above-mentioned slight increase). Starting from the subsequent stress variation, from 88% to 94% TYS (from 70% to 75% UTS), the steady state permeation flow manifests a peak at the stress variation instant, followed by a temporary reduction of the hydrogen flux, as already observed in Par. 8.2.3 during the variation of the maximum stress under cyclic loading conditions. After less than 1 hour, this transient exhausted, and the permeation flow returned to the steady state value detected before the stress variation.

Instead, after the overcoming of the YS, and in particular starting from the stress variation from 102% to 108% TYS (from 80% to 85% UTS), the 4-hour duration of the maintenance step was not sufficient for the permeation transient to completely exhaust, and thus to observe an increase of the current to the value of $i_{a,\infty}$ occurring during a longer theoretical stress maintenance in the plastic domain.

On the contrary, in the case of the heat treated material (TT), a relevant increase in the steady state value is observed even at the beginning of the application of the incremental step load profile, when the specimen is still in the elastic domain; a little current response in correspondence of each stress variation is easily visible even in the elastic field.

Despite the significant difference between the two permeation flux values, both the tested specimens came to rupture above 90% UTS in air, and in particular during the loading phase; the X65 steel from 120% to 126% TYS (from 95% to 100% UTS), at a ratio of about 121% TYS (96% UTS), while the heat treated material (TT) at the previous step, from 103% to 109% TYS (from 90% to 95% UTS), at a ratio of about 106% TYS (93% UTS). As a result, a crack propagation during the constant deformation phase in the previous step was not observed.

The failure of both the specimens occurred in a region out from the permeation area, and very far from it. Moreover, the tested specimens came to failure at a stress value very close to that obtained from the test in air, which confirms that neither the sorbitic microstructure of the X65 steel nor the martensitic one, obtained after the afore-mentioned heat treatment, resulted susceptible to HE in accordance to this incremental step load profile.

For example, *Figure 8.23* reports the cathodic surface of the X65 steel, which presents secondary cracks that did not lead to the rupture of the specimen.

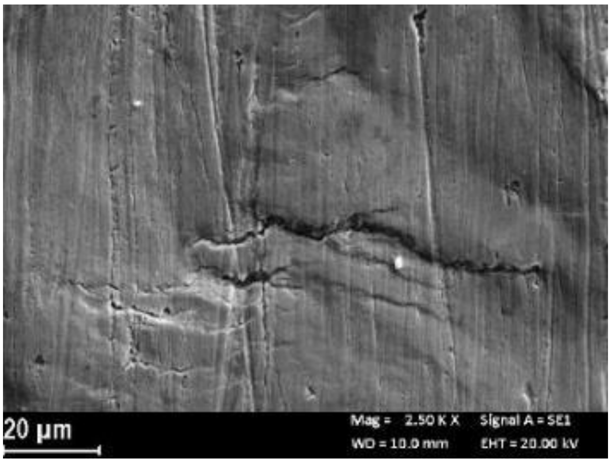

Figure 8.23. Secondary cracks on the cathodic surface of the X65 steel

8.3.6 Background passivity current

Figure 8.24 reports the graph of the effect on i_P determined by the incremental step loading technique, which was performed only on the X65 steel. The dashed grey curve represents again the scheduled load profile required by the reference standard [280].

The load profile reflects again the scheduled load profile up to a stress corresponding to the step around 63% TYS (50% UTS), showing relevant decreases for further increases of the applied stress, which settles later again during the maintenance at the imposed deformation.

In this case, however, the failure of the tested specimen did not occur and, after the achievement of the maximum stress (P_{MAX}) assumed from the tensile test in air (570 MPa), the stress value settles around 121% TYS (96% UTS).

No perceptible modifications in the value of i_P could be recorded (*Figure 8.24*) again in correspondence with the instant stress variations in the elastic field or, more precisely, up to about 88% TYS (70% UTS). Starting from the subsequent stress variation, from 88% to 94% TYS (from 70% to 75% UTS), also i_P manifests a peak at the stress variation instant, followed by a decreasing transient; after less than 2 hours, this transient exhausts, and then i_P can reach again the values before the stress variation.

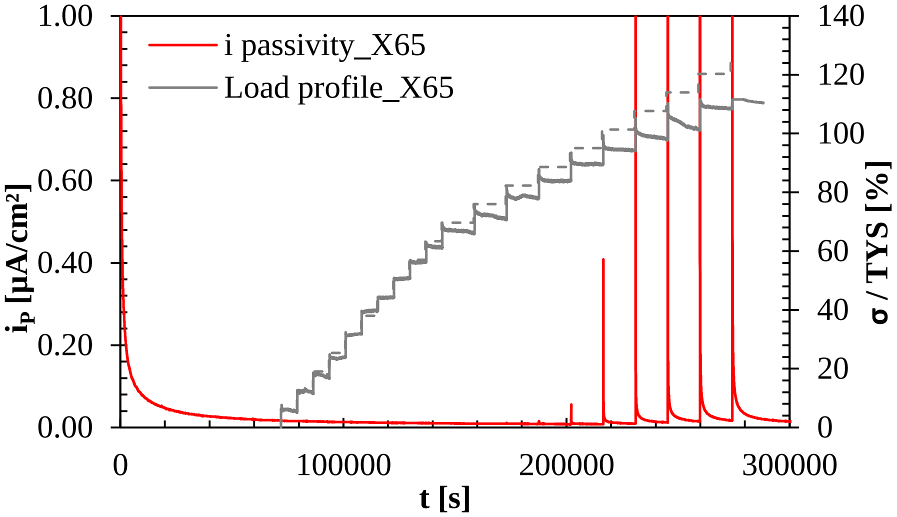

Figure 8.24. Results of the incremental step load test on the background passivity current

The presence of peaks also in the absence of hydrogen, and the instant current variation substantially identical to that induced on $i_{a,\infty}$, allows to confirm also through these tests that the current peak is not due to the presence of diffusing hydrogen, but to the instant local rupture and subsequent reformation of the iron oxide film.

For stress variations closer to the YS, and even beyond this limit, the peak associated to the stress variation increases again, as well as the time necessary for the re-passivation of ever larger and numerous exposed areas of the bare substrate steel, and for the achievement of the passivity values before the stress variation. In particular, after the overcoming of the yield limit, and in this case starting from the variation from 102% to 108% TYS (from 80% to 85% UTS), again the 4-hour duration of the maintenance step was not sufficient for the decreasing transient to completely exhaust. Consequently, the subsequent variation, from 108% to 114% TYS (from 85% to 90% UTS), occurs when the newly exposed areas are not fully re-passivated yet, thus it starts from a higher value of i_P.

9
DISCUSSION

In this chapter, the results deriving from the permeation tests performed on the X65 grade steel in the absence of an applied load and in the presence of different loading conditions, will be discussed.

The need of processing the resulting data for the estimate of the diffusion parameters, such as the apparent diffusivity, the hydrogen concentration and the number of trapping sites, leads necessarily to the use of a suitable processing method.

Therefore, in the first section, the implemented mathematical model for the processing of the experimental permeation curves will be proposed; this processing method allowed to calculate the parameters linked to hydrogen diffusion in a more accurate way than the pure diffusion model, also for the stretched or compressed material and under loading conditions above the yield limit.

In the second section, the analysis will be focused on the effects of the maximum applied stress on the diffusion parameters, of the variation of amplitude (±10/20% TYS) and frequency ($10^{-2} \div 1$ Hz) of the load on both the steady state anodic current ($i_{a,\infty}$) and on the background passivity current ($i_{P,\infty}$) and, finally, of the instant stress variation on $i_{a,\infty}$ under cyclic and incremental step loading conditions.

9.1 Permeation curves processing

9.1.1 First data processing method

The first processing method, extensively reported in Appendix A.2, was implemented by means of the interpolation of the experimental data with the theoretical diffusion curve in non-stationary regime, expressed in terms of the normalized flux (Φ_N) and normalized time (t_N):

$$\Phi_N = \frac{\Phi(t)}{\Phi_\infty} = \frac{i(t)}{i_\infty} \quad ; \quad t_N = \frac{4 \cdot D_{app} \cdot t}{s^2}$$

This pure diffusion curve *(Figure 9.1)* was obtained by means of numerical integration of Fick's second law, considering a thin steel foil of finite thickness (s), and a hydrogen concentration that is constant on one surface (C_0) and null (0) on the other one:

$$\frac{\Phi(t)}{\Phi_\infty} = f(t_N)$$

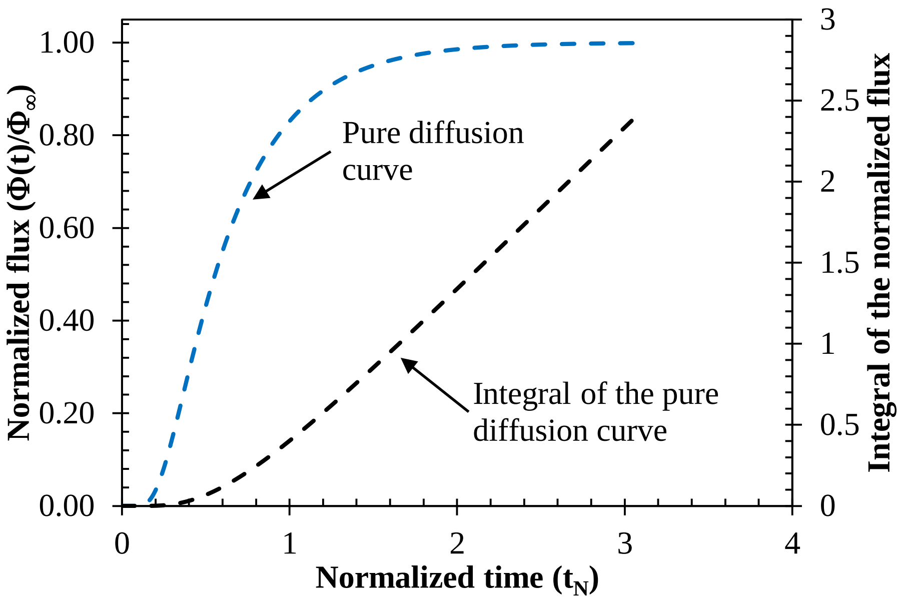

Figure 9.1. Theoretical curve of hydrogen permeation for pure diffusion

After the determination of the average apparent diffusivity (D_{app}) in a specific interval (average value in the interval 63÷80% Φ_∞), the total sub-surface hydrogen concentration (C_{TOT}) was evaluated:

$$C_{TOT} = \frac{s \cdot \Phi_\infty}{D_{app}}$$

Then, the estimation of D_{app} variation from the experimental data was performed, always depending on the adimensional time (t_N):

$$D_{app} = f(t_N)$$

Finally, the aim was that of minimizing the error between the curve of the experimental data and that connected to the numerical solution of Fick's second law, as shown in *Figure 9.2*.

However, especially for low hydrogen concentrations and low values of the normalized flux *(Figure 9.2)*, the existence of reversible and irreversible trapping sites, acting as sources or "sinks" for hydrogen atoms, significantly modifies the trend of the curve during the permeation transient.

Therefore, the processing method based on the pure diffusion model, derived from Fick's second law, is no longer valid to simulate the diffusion process of atomic hydrogen.

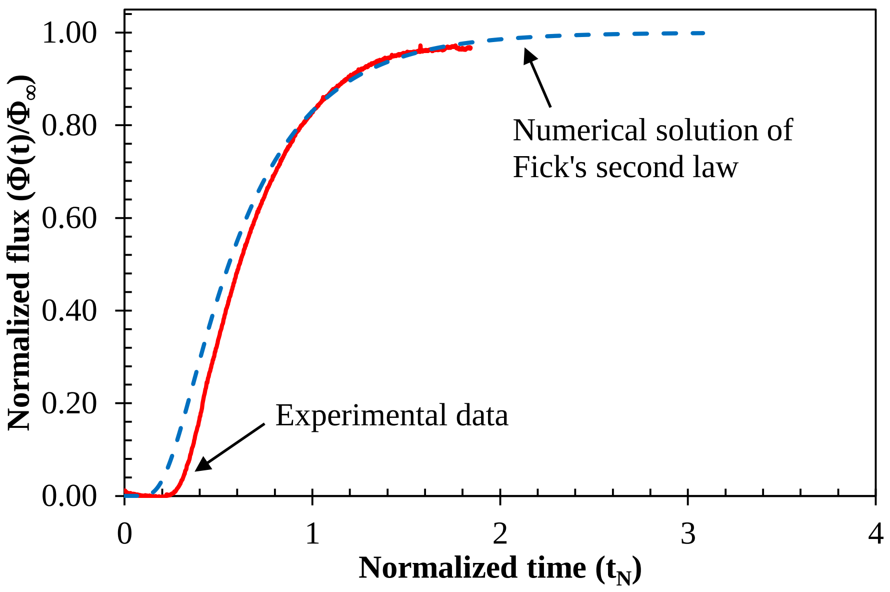

Figure 9.2. Minimization of the error between the pure diffusion and the experimental data curves

As an example, the following graph *(Figure 9.3)* presents the difference between the pure diffusion curve and two of the experimental data curves deriving from the tests, one related to the unloaded material (U) and the other one to the cyclically loaded material at 110% TYS (C_110), respectively. The normalized time ($t_{N'}$) is expressed as a function of the lattice diffusivity (D_l) for bcc-iron, previously determined from the equation proposed by Kiuchi and McLellan [155] at room temperature (T = 23 °C, or 296 K), and equal to: $D_l = 7.2*10^{-9}$ m^2/s.

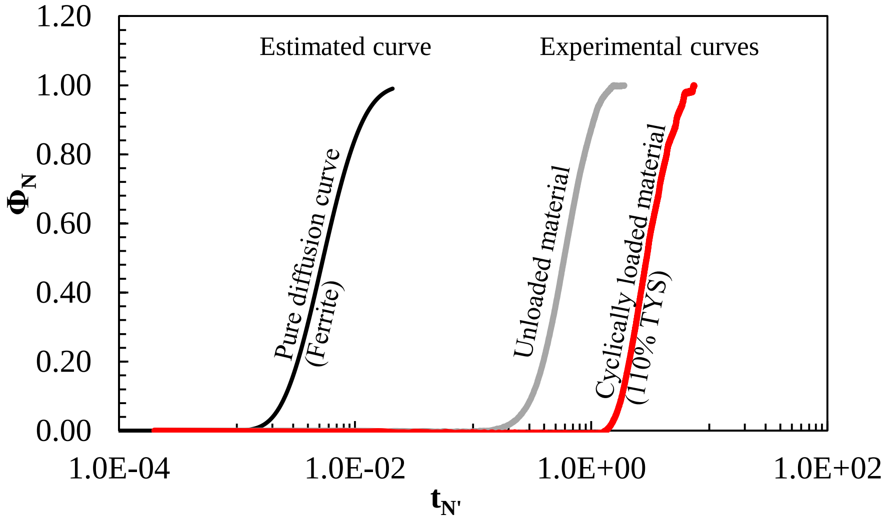

Figure 9.3. Normalization of the permeation curves as a function of the lattice diffusivity

As already said, the lattice activation energy used to calculate D_l was equal to E_l = 5.69 kJ/mol [155] [156] [157], also because many other works suggest to assume a value of activation energy for lattice hydrogen diffusion in bcc-iron ranging from 5 to 8 kJ/mol [174] [299] [300]. Thus, $t_{N'}$ is as follows:

$$t_{N'} = \frac{4 \cdot D_l \cdot t}{s^2}$$

The result is that the experimental permeation curves move to longer times with respect to the pure diffusion curve in the ferrite, calculated with the commonly accepted value of D_l for α-iron [155].

In the absence of an applied stress, i.e. the unloaded material (U, grey curve), the permeation transient maintains a behavior similar to that of the pure diffusion curve, with an increase in the time necessary for hydrogen atoms to diffuse through the material. Instead, in the presence of an applied stress, i.e. the cyclically loaded material at 110% TYS (C_110, red curve), the permeation transient moves to longer times and, in addition, is subject to an increase in the slope for low values of the normalized flux, if compared to the pure diffusion curve, that in *Figure 9.3* is simply translated over time.

Therefore, a second data processing method, based on a more precise mathematical model, must be necessarily applied, in order to consider the presence of trapping sites in the diffusion process.

9.1.2 Second data processing method

The second data processing method implemented, based on the mathematical model proposed by Grabke and Riecke [158], takes into consideration the method implemented by Oriani [153] and integrates it by considering the presence of both reversible (shallow) traps and irreversible (deep) traps. In fact, even if Oriani's model involves the assumption of the presence of only reversible trapping sites, the equations proposed by this author were took as a starting point for the evaluations made by several authors, even many years later [143] [214] [215] [216] [217].

It was found that the equations in the implemented method [158] were a rearrangement of those proposed by Oriani; thus, the values of the parameters related to hydrogen diffusion, with the exception of irreversible trapping sites, calculated with both the methods resulted to be the same. The values presented in the following discussion will be then only those deriving from the equations used by Grabke and Riecke in their work [158].

In accordance to this processing method, extensively reported in Appendix A.3, the above-mentioned delay of the experimental data with respect to the pure diffusion curve is attributable to the presence of reversible trapping sites. Under non-stationary conditions, the diffusion processes in the absence and in the presence of reversible traps are equivalent, but with an apparent diffusion coefficient (D_{app}) connected to the lattice one by a reversible trapping factor (α).

From other results found in the literature, the value of D_{app} in the common structural steels at room temperature is about two orders of magnitude lower than that in the pure ferrite in the annealed state, in which the trapping effect is considered negligible.

Therefore, the obtained permeation curves translate towards longer times due to the presence of reversible traps, which reduce D_{app} proportionally to α, but maintain a behavior similar to pure ferrite.

In this model, the contribution of the irreversible trapping sites is took into consideration by the introduction of a parameter; to an increase in this parameter, an increase in the slope of the modelled permeation curve corresponds, in order to better fit the experimental data curve *(Figure 9.4)*, especially for low hydrogen concentrations and low values of the normalized flux.

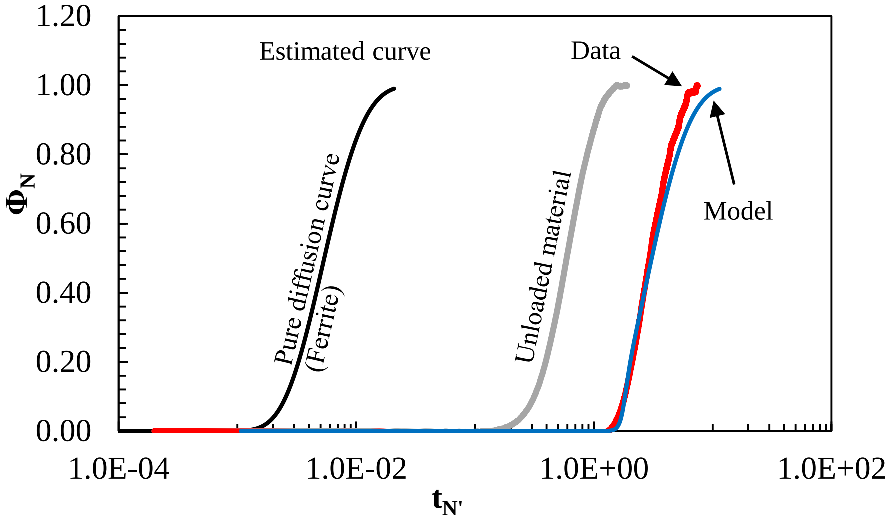

Figure 9.4. Comparison between the modelled permeation curve and the experimental data

The following figures will provide a comparison between the pure diffusion curve in ferrite and the permeation curves obtained by the elaboration of the experimental data with this processing method. *Figure 9.5* shows that, for the stretched/compressed material at 110% TYS (PTC_110), the application of a compressive stress seems to reduce in some way the stress field generated by the previously applied tensile one, even if beyond the yield limit.

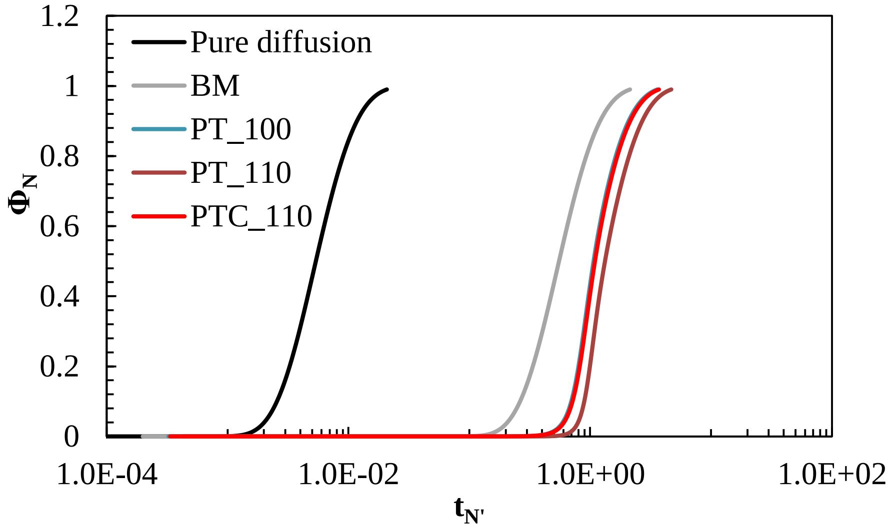

Figure 9.5. Comparison of the modelled permeation curves of the stretched material (PT) and stretched/compressed material (PTC)

Figure 9.6 illustrates that, for the compressed material (PC), the application of a compressive stress determined instead a very slight increase in the number of both reversible and irreversible traps, even beyond the yield limit, which is not as significant as in the previous case, but can be probably included in the uncertainty range of the experimental data.

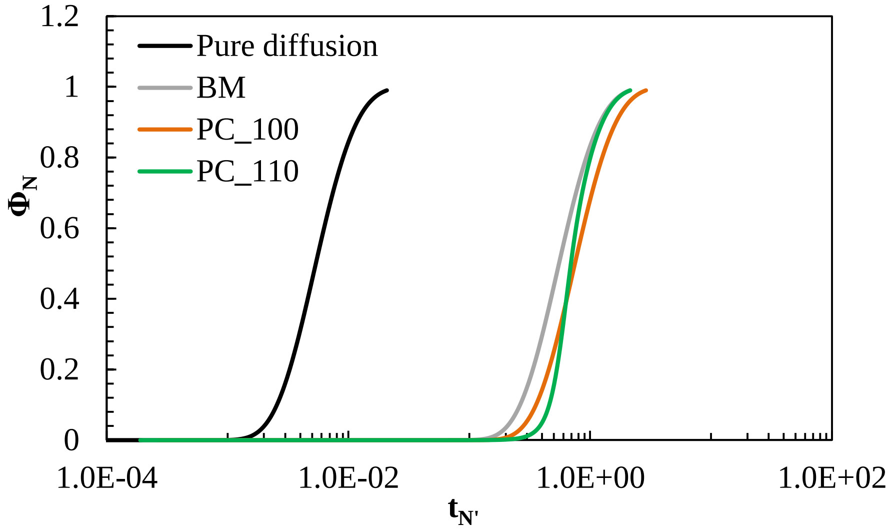

Figure 9.6. Comparison of the modelled permeation curves of the compressed material (PC)

For the cyclically loaded material (C), both the parameters connected to the formation of new reversible and irreversible trapping sites *(Figure 9.7)* tend to increase much more if compared to the stretched material (PT). In this case, it is possible to note how relevant is the contribution given by the presence of irreversible traps, which increase the slope of the permeation curve.

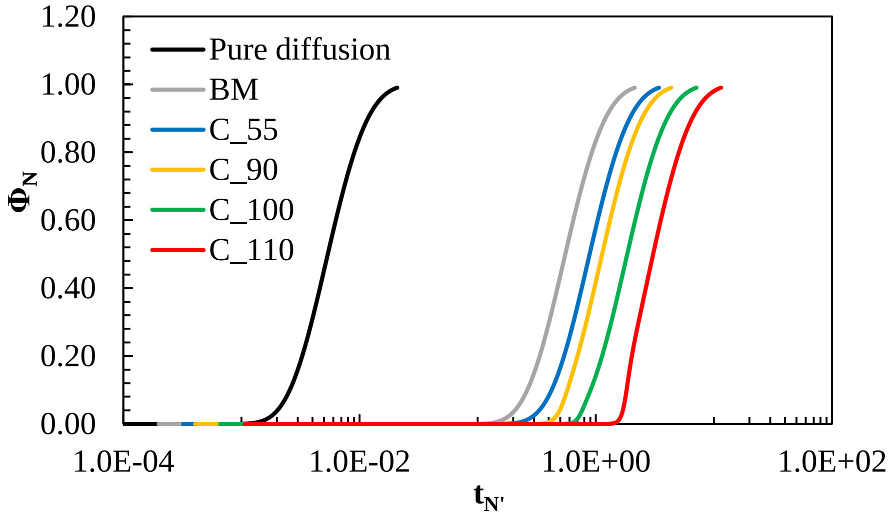

Figure 9.7. Comparison of the modelled permeation curves of the cyclically loaded material (C)

9.2 Effect of the applied maximum stress

The following paragraphs will analyze the effect of the applied maximum stress on the hydrogen diffusion parameters, i.e. apparent diffusion coefficient (D_{app}), number of reversible trapping sites ($N_{t,r}$), total hydrogen concentration (C_{TOT}) and hydrogen concentration in the lattice (C_0), steady state hydrogen permeation current ($i_{H,\infty}$). In the following figures (from *Figure 9.8* to *Figure 9.12*), the applied maximum stress will be expressed as a ratio between the considered stress value and the tensile yield strength (σ/TYS), in percentage, in dependence of the specific loading condition.

As regards the tests performed under cyclic loading conditions, the permeation transient occurred in the presence of the specific applied load, i.e. only after the application of the load sinusoid.

Moreover, every indicator is representative of the average value of the particular parameter, corresponding to the specific maximum applied stress. The error bands of the indicators represent the range of all the obtained values. These error bands were evaluated by considering the errors, both positive and negative, which were determined by the calculation of the difference between the average value and the maximum and minimum values, respectively.

9.2.1 Apparent diffusivity vs. maximum stress

Figure 9.8 shows the correlation between D_{app} and the applied maximum stress (σ/TYS).

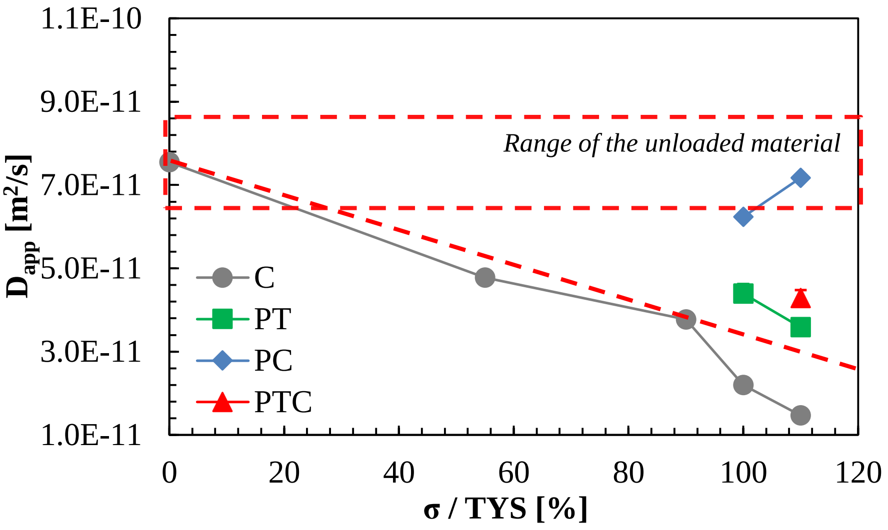

Figure 9.8. Apparent diffusivity (D_{app}) as a function of maximum stress and loading condition

From all the tests performed on the unloaded (U) material (X65 grade steel), D_{app} ranges between a minimum value of $6.2*10^{-11}$ m^2/s and a maximum value of $8.9*10^{-11}$ m^2/s, with an average value of $7.6*10^{-11}$ m^2/s. These results are in line with those found in the literature for this kind of microstructure, for which the order of magnitude of the diffusivity values may be determined by the significant trapping effect. According to Arafin and Szpunar [301] and to Zhao et al. [302], low carbon ferritic-bainitic microstructures (bainitic lath type) are characterized by a significant dislocation density, which seems to act as hydrogen trapping sites.

For the condition of stretched material (PT), D_{app} is subject to a significant decrease beyond the yield limit (green indicators), which is due to the residual plastic deformation occurred after the overcoming of this limit [169] [170] [227]; the average values are equal to 4.4 (100% TYS) and $3.6*10^{-11}$ m^2/s (110% TYS). This phenomenon is similar to that observed by Brass et al. [239] and Dietzel et al. [231]; they documented a linear dependence of hydrogen apparent diffusivity on plastic deformation above a strain level of 0.5%, with a variation in D_{app} (estimated with the t_{lag} method) of more than two orders of magnitude.

On the contrary, the average values (blue indicators) of the compressed material (PC), between 6.2 (100% TYS) and $7.2*10^{-11}$ m^2/s (110% TYS), fall into the range of values in all the tests performed on the unloaded material (U).

However, if a compressive stress is applied after the tensile one (PTC), in this case both equal to 110% TYS, a softening effect seems to occur in the material; thus, D_{app} shifts to a higher value ($4.3*10^{-11}$ m^2/s), as stated by the red indicator in *Figure 9.8*. The softening of the material seems to mitigate the stress field generated by the tensile one.

Since the tensile stress value planned for these tests was equal to or higher than the nominal tensile strength (110% TYS), the observed effect might be referred to the so-called “Bauschinger effect”, which identifies the phenomenon of plasticizing hysteresis in ductile materials and corresponds to a cinematic-type strain-hardening. In this particular case, the expected effect was that of material softening subsequent to the applied compressive stress, and consequent mitigation of the residual plastic strain generated by the previously applied tensile stress.

Under cyclic loading conditions (amplitude = ±10% TYS; frequency = 10^{-2} Hz), it is possible to observe how the application of a tensile stress even in the middle of the elastic domain (55% TYS) determines a slight decrease in D_{app}. With a further increase in the maximum stress, D_{app} significantly decreases beyond the yield limit, with values around $1.5*10^{-11}$ m^2/s for the worst loading condition (110% TYS); the decrease is more relevant if compared to the stretched material (PT).

At this point, the relevant decrease in D_{app} along with an increase in the maximum stress can be related to the increase in the dislocation density with increasing deformation or to the modification of the trap binding energy (E_b).

Kumnick and Johnson [170] suggested that, in deformed specimens, the parameter E_b remains constant. Therefore, for all the performed tests, a constant value of 22.7 kJ/mol for E_b was assumed (see the mathematical assumptions assumed in the model, extensively reported in Appendix A3), which is very similar to that found by Oriani [153] in his research (around 27.2 kJ/mol).

The decrease in D_{app} is already present for maximum stresses fully in the elastic field (55% TYS), although to a lesser extent, and it becomes much more evident when the maximum stress reaches the yield limit.

Therefore, the strong decrease in D_{app} with an increase in the maximum stress is ascribable to the creation of a large quantity of new reversible traps, i.e. new dislocations, with increasing strain [53]. Moreover, provided that the hydrogen diffusion rate in steel is concomitant with the dynamic loading, if compared to the unloaded (U) and stretched (PT) material, it is then possible to affirm that hydrogen trapping phenomena are enhanced under cyclic loading conditions.

9.2.2 Density of reversible traps vs. maximum stress

Figure 9.9 shows the correlation between the parameter related to reversible trapping sites ($N_{t,r}/N_l$) and the applied maximum stress (σ/TYS).

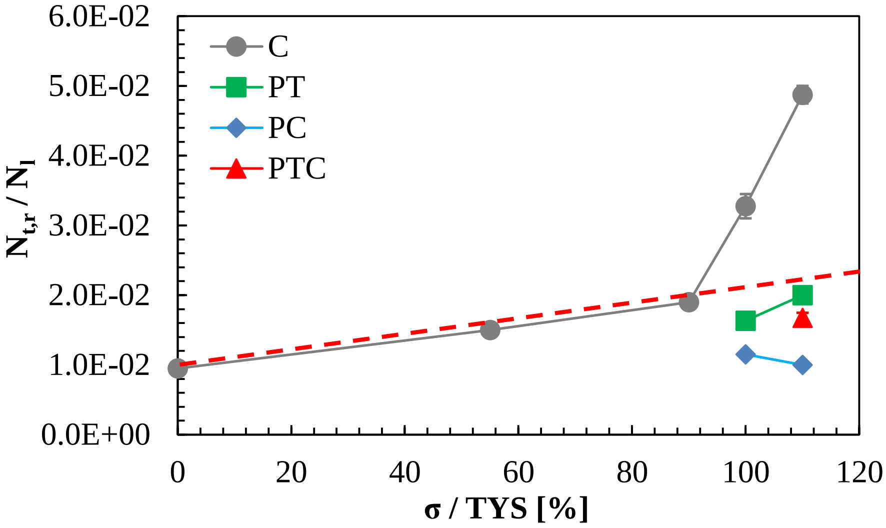

Figure 9.9. Reversible trapping parameter ($N_{t,r}/N_l$) as a function of maximum stress and loading condition

In accordance with the model proposed by Grabke and Riecke [158], the ratio D_{app}/D_l can be assumed as an index for the estimate of the concentration of the reversible trapping sites ($N_{t,r}$) compared to the empty sites of the lattice available for hydrogen permeation (N_l).

From all the tests performed on the unloaded material (U), the ratio $N_{t,r}/N_l$ is characterized by an average value of 0.0095. For the condition of stretched material (PT), $N_{t,r}/N_l$ is subject to a slight increase beyond the yield limit (green indicators); the average values are 0.0165 (100% TYS) and 0.0200 (110% TYS). Instead, the average values (blue indicators) related to the compressed material (PC), between 0.0115 (100% TYS) and 0.0100 (110% TYS), are again similar to the values obtained in all the tests performed on the unloaded material (U).

However, if a compressive stress is applied after the tensile one (PTC) at 110% TYS, the softening effect occurring in the material determines a decrease in the ratio $N_{t,r}/N_l$ down to a value of 0.0170, as represented by the red indicator in *Figure 9.9*.

Under cyclic loading conditions (amplitude = ±10% TYS; frequency = 10^{-2} Hz), it is possible to see that $N_{t,r}/N_l$ starts to slightly increase even in the middle of the elastic field (55% TYS). Between 90% and 100% TYS, and beyond the yield limit, this parameter is subject to a steep increase, and reaches values around 0.0490 for the maximum stress of 110% TYS. Similar results were reported by Brinckmann in his PhD thesis [303], in which he observed an increase in the dislocation density under cyclic loading conditions.

Consequently, the parameter connected to reversible trapping sites increases considerably if compared to the stretched (PT) material and, in the worst loading condition considered (110% TYS), it increases of about 5 times if compared to the unloaded material (U). This sharp increase in the trapping factor is a phenomenon probably due to the contribution of the accumulation of new traps during the application of cyclic loading conditions in the plastic deformation field [170] [226].

In addition, the increase in $N_{t,r}/N_l$ confirms the assumption made in the previous paragraph, according to which the relevant decrease in D_{app}, along with an increase in the applied maximum stress, is connected to an increase in the dislocation density with deformation, and not to a modification of E_b, which is assumed constant for all the performed tests [170].

However, the delaying effect cannot be related only to an increase in the number of reversible traps. The application of a stress in the plastic domain induces not only a further translation of the diffusion process towards longer times, but involves also a significant modification in the behavior of the experimental permeation curve. The latter tends to modify its shape in the initial portion of the transient, with a delay that determines a different initial slope. Such effect is attributable to an increase in the density of irreversible trapping sites; these tend to saturate in the initial phases, before allowing atomic hydrogen to diffuse towards the inner layers of the material, thus subtracting free diffusing hydrogen from the permeation process. Since the extent of the plastic deformation achieved in the performed experimental tests is relatively low, the delaying effect seems to be small if compared to the prevailing one, induced by the multiplication of the reversible trapping sites.

9.2.3 Hydrogen concentration vs. maximum stress

Figure 9.10 shows the correlation between the total hydrogen concentration (C_{TOT}) and the applied maximum stress (σ/TYS).

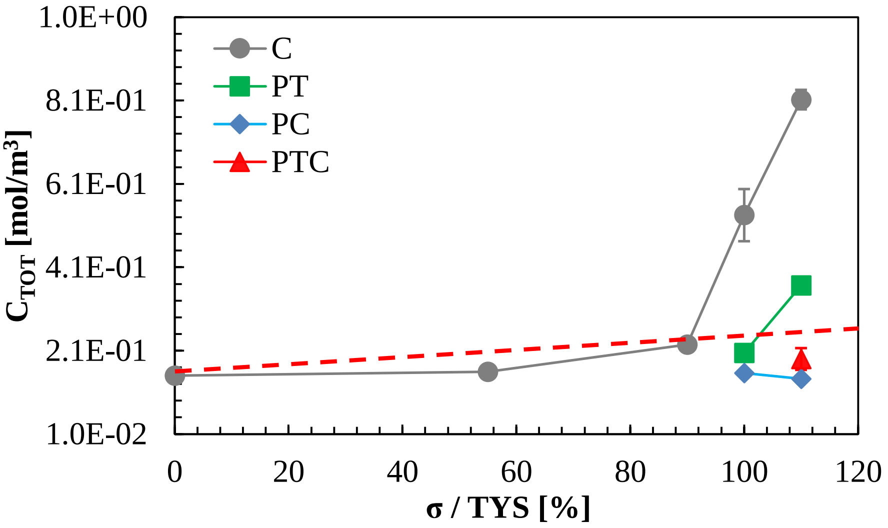

Figure 9.10. Total hydrogen concentration (C_{TOT}) as a function of maximum stress and loading condition

From the tests performed on the unloaded material (U), the average value of C_{TOT} is $1.5*10^{-1}$ mol/m^3. For the condition of stretched material (PT), also C_{TOT} is subject to a significant increase beyond the yield limit (green indicators); the average values are about $2.1*10^{-1}$ (100% TYS) and $3.7*10^{-1}$ mol/m^3

(110% TYS). As stated also by several works in the literature, this effect is connected to the relevant increase in hydrogen solubility beyond the yield limit [231] [232] [233].

Instead, the average values (blue indicators) for the condition of compressed material (PC), between $1.6*10^{-1}$ (100% TYS) and $1.4*10^{-1}$ mol/m^3 (110% TYS), are again similar to the values obtained in the tests on the unloaded material (U). However, if a compressive stress is applied after the tensile one (PTC) at 110% TYS, the softening effect determines a decrease in C_{TOT} down to a value of $1.9*10^{-1}$ mol/m^3, as represented by the red indicator in *Figure 9.10*.

Under cyclic loading conditions, the average value of C_{TOT} remains almost constant up to 55% TYS; between 90% and 100% TYS, and beyond the yield limit, this value drastically increases, as a result of the enhanced hydrogen absorption in the material and filling of an increasing number of trapping sites, intensified by the cyclic load.

The result is that, for the worst loading condition with a maximum stress of 110% TYS, C_{TOT} is nearly one order of magnitude higher ($8.1*10^{-1}$ mol/m^3) than that in the unloaded material (U), and nearly three orders of magnitude higher than the hydrogen concentration in the lattice (C_0), which ranges between a minimum value of $1.2*10^{-3}$ mol/m^3 and a maximum value of $1.8*10^{-3}$ mol/m^3, with an average value of $1.5*10^{-3}$ mol/m^3. Therefore, as also stated by several authors [165] [170] [210] [163], the value of C_{TOT} is significantly higher than the hydrogen concentration in the lattice (C_0).

This latter parameter, instead, remains almost constant with an increase in the applied maximum stress *(Figure 9.11)*, which indicates that, once the equilibrium is restored, the concentration in the lattice is not modified by the application of stresses even beyond the yield limit. Moreover, even if the charging current density, maintained constant during the entire test, is supposed to maintain the sub-surface hydrogen concentration unaltered, the uniform value of C_0 involves that no significant variations in the surface conditions or pollution of the cell environment occurred.

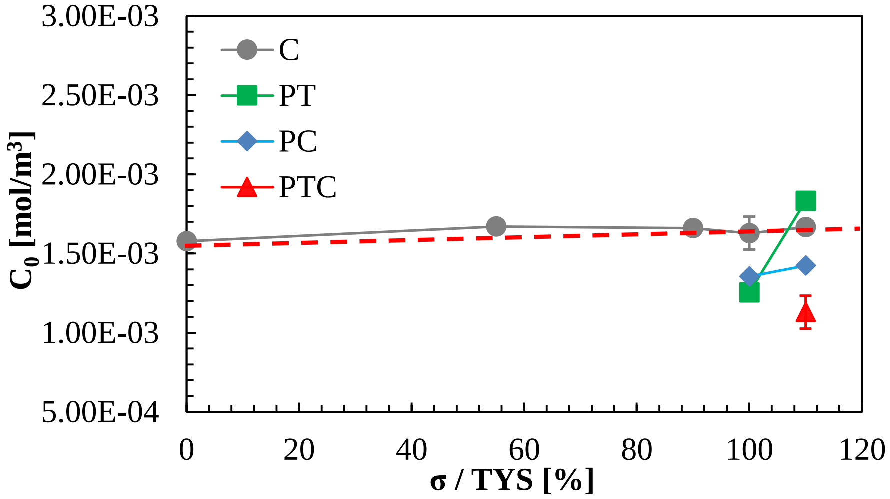

Figure 9.11. Lattice hydrogen concentration (C_0) as a function of maximum stress and loading condition

9.2.4 Steady state permeation current vs. maximum stress

Figure 9.12 shows the relation between the steady state permeation current ($i_{H,\infty}$) and the applied maximum stress (σ/TYS).

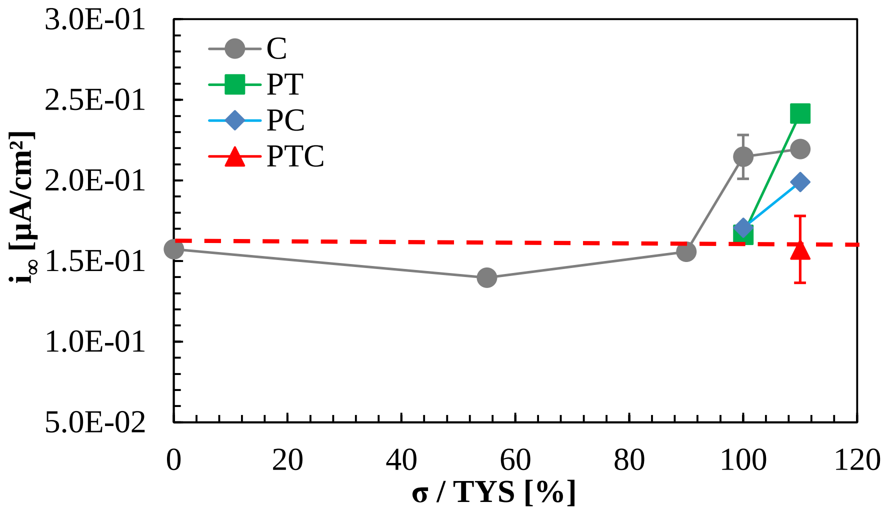

Figure 9.12. Steady state permeation current ($i_{H,\infty}$) as a function of maximum stress and loading condition

The steady state hydrogen flux seems to remain almost constant for maximum stresses fully in the elastic field, up to 90% TYS. This fact is in contradiction to some works in the literature; for example, Cabrini et al. [67] observed that, in the constant load condition, the steady state current in the elastic field was subject to an appreciable increase. Instead, between 90% and 100% TYS, and in the plastic field, $i_{H,\infty}$ is subject to a slight increase, which is about the same for all the loading conditions.

The average value, around $1.5*10^{-1}$ μA/cm^2 for the unloaded material (U) and for maximum stresses in the elastic field, increases and settles around a value of $2.2*10^{-1}$ μA/cm^2 beyond the yield limit.

Again, in the stretched/compressed condition (PTC) at 110% TYS, $i_{H,\infty}$ is subject to a slight lowering, as it returns to the typical values obtained for maximum stresses under 90% TYS.

The explanation of the variation in $i_{H,\infty}$ along with an increase in strain, and the reason of the strong dependence of this parameter from the specific loading condition, is probably related to different factors. In the absence of an applied stress or with applied stresses fully in the elastic field, the measured values of $i_{H,\infty}$ allow to hypothesize that the corresponding flux is mainly due to hydrogen diffusing through the steel matrix. Instead, in pre-straining conditions, in which the achievement of maximum tensile stresses equal to or higher than the yield limit determined the presence of residual plastic stresses, it is possible to affirm that hydrogen reaches the exit surface also by a means different from diffusion, such as the dislocation transport. Thus, as stated also by Frankel and Latanision [237], hydrogen flux is the sum of that transported by the diffusion mechanism and the dislocation transport. Moreover, in the presence of a cyclic load with a maximum stress of 100% TYS, the phenomenon of dislocation transport seems to be enhanced, if compared to the stretched condition (PT).

9.3 Effect of the amplitude and frequency of the load

In this paragraph the effect of the variation of amplitude (±10/20% TYS) and frequency ($10^{-2} \div 1$ Hz) of the load, both on the steady state anodic current ($i_{a,\infty}$) and on the background passivity current ($i_{P,\infty}$), will be analyzed. The load amplitude is again expressed as a ratio between the considered stress value and the tensile yield strength (σ/TYS), in percentage.

Concerning the tests performed on i_P, the load sinusoid was applied only after current density values lower than 0.05 µA/cm^2 were recorded. Instead, for the tests carried out on $i_{a,\infty}$, it must be specified that the permeation transient occurred in the unloaded material (U), thus in the absence of an applied load; the load sinusoid was applied only when the steady state flux value was achieved, with different cyclic loading conditions applied on $i_{a,\infty}$ not depurated from the contribution of $i_{P,\infty}$.

The Fast Fourier Transformation (FFT), reported in *(eq. 112)*, was used to disassemble the current signal and then to reconstruct its waveform, with the Anti-FF Transformation *(eq. 113)*, in order to obtain more precise results of the average value and amplitude of $i_{a,\infty}$ and $i_{P,\infty}$, for each value of the amplitude and frequency of the load.

$$F\{f\}(t) = \hat{f}(t) := \frac{1}{\sqrt{2\pi}} \cdot \int_R f(x) \cdot e^{(-i \cdot x \cdot t)} dx \quad \forall t \in R \qquad \textit{(eq. 112)}$$

$$f(x) = \frac{1}{\sqrt{2\pi}} \cdot \int_R \hat{f}(t) \cdot e^{(i \cdot x \cdot t)} dt \qquad \textit{(eq. 113)}$$

For greater accuracy in the calculation, slightly different values of the load frequency were applied, up to values around 1 Hz. This kind of tests was implemented because recent works, performed on underground pipelines for the transportation of natural gas in the Oil&Gas industry, demonstrated that these pipelines are subject to cyclic loading conditions [304], which can be ascribed to [134]:

- Daily pressure fluctuations during normal service, in the order of ±10% of the nominal operating pressure
- Shutdowns and startups for regular operation or because of an upset condition in which pressure decreases to practically zero, i.e. complete unloading, and then it increases again to the nominal operating value.

From *Figure 9.13* it is possible to observe that an increase in the amplitude (Δσ) and frequency (f) of the load determines an increase in the current response (Δi), both for $i_{a,\infty}$ and $i_{P,\infty}$.

The current variation induced by the considered cyclic loading conditions (two amplitudes of ±10% and ±20% TYS and three significant frequencies of 10^{-2}, 10^{-1}, 1 Hz for each load amplitude) on $i_{a,\infty}$ in the presence of hydrogen is very similar to that induced on i_P in the absence of hydrogen, and with comparable phase shifts *(Figure 9.14)*, i.e. the delay between the load sinusoid and the effect on the current. Therefore, the current variation is not due to the presence of diffusing hydrogen.

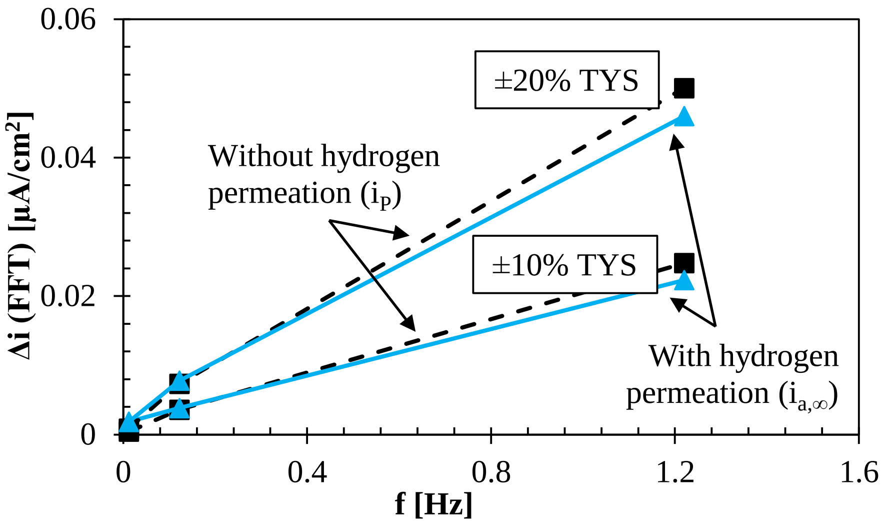

Figure 9.13. Current variation as a function of amplitude and frequency of the load, and comparison between the cases of presence and absence of diffusing hydrogen

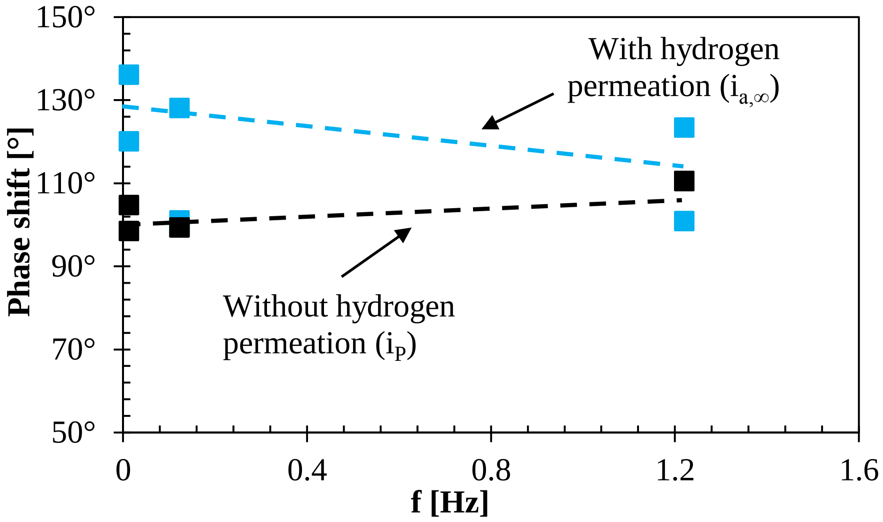

Figure 9.14. Phase shift as a function of amplitude and frequency of the load, and comparison between the cases of presence and absence of diffusing hydrogen

Moreover, a sort of pseudo-impedance parameter (|Z|) was introduced *(Figure 9.15)* to correlate the load amplitude and the current amplitude, represented by the variation induced by the load sinusoid. It is possible to see how this parameter is inversely proportional to the load frequency, as it decreases by two orders of magnitude with an increase in the frequency up to 1 Hz; the larger the load amplitude, the larger the effect on the current.

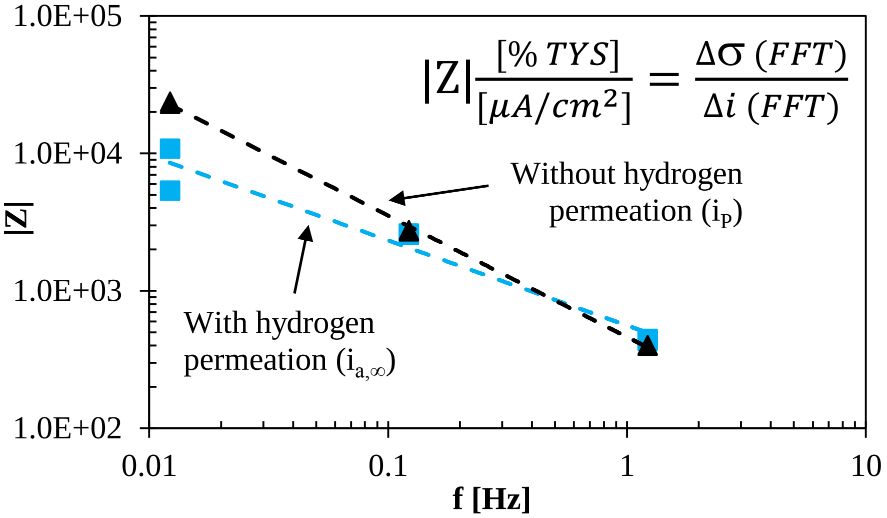

Figure 9.15. Pseudo-impedance parameter (|Z|) as a function of amplitude and frequency of the load, and comparison between the cases of presence and absence of diffusing hydrogen

As a consequence, it is possible to hypothesize that the current variation, observed also on i_P, is linked to a sort of piezoelectric effect related to the dynamic deformation of the iron oxide film.

The maximum stress reached during these tests is around 65% TYS, which is fully in the elastic field and, then, never determined the rupture of the oxide film. In fact, if a failure had occurred, a more significant peak would have been observed in correspondence of the load variation, followed by a transient of re-passivation that would have surely involved longer times than those detected.

Piezoelectricity was experimentally demonstrated for the first time by the Curies in 1880; this phenomenon represents a natural characteristic of the crystal lattice of some materials that, if subject to a mechanical action, produces an electric field as a result of the deformation of their crystal lattice (which is no longer electrically neutral but it becomes polarized).

In particular, piezoelectric materials are a sub-group of ferroelectric materials, which are a part of the largest category of dielectric materials. Ferroelectric materials present an intrinsic polarization (partially ionized atoms) due to a non-uniform distribution of positive and negative electric charges, which can be cancelled by the application of an external electric field, because they arrange themselves in such a way as to counteract the field influence by forming electric dipoles.

As affirmed by some authors [305] [306] [307], the spontaneous polarization in ferroelectric materials is strongly affected by strain; if the mechanical stress is fully included in the elastic domain, the imposed deformation is completely reversible [308] [309]. Piezoelectric materials are then characterized by all the properties of ferroelectric and dielectric materials, with the further characteristic of varying their polarization subsequent to an imposed strain, and vice versa.

In the particular case of the tests performed in this section, the microstructure of the oxide film, formed by anodic polarization in alkaline 0.1 M NaOH solution, is constituted by anhydrous Fe(II) oxide grown at the interface with the base material and hydrated Fe(III) oxide grown superficially. This configuration of the oxide film leads to the possibility of a sort of piezoelectric effect due to the imposed strain. Therefore, the sine waveform assumed by the current is probably due to an electric field induced by the load sinusoid, which cyclically stretches and compresses the iron oxide film.

9.4 Effect of the variation of the maximum stress

As regards the variation of the maximum stress under incremental step loading conditions on the X65 grade steel, a further analysis on i_P *(Figure 9.16)* aimed to compare the first passivation transient (green curve, without an applied load) to the re-passivation transient subsequent to each stress variation (from red to black curve), beginning from that with an appreciable effect on the current, from 70% to 75% UTS (from 88% to 94% TYS). For stress variations closer to the UTS, the related re-passivation transients tend to approach the first passivation curve, evidence of the increasing number of exposed areas of the bare substrate steel that must be re-passivated.

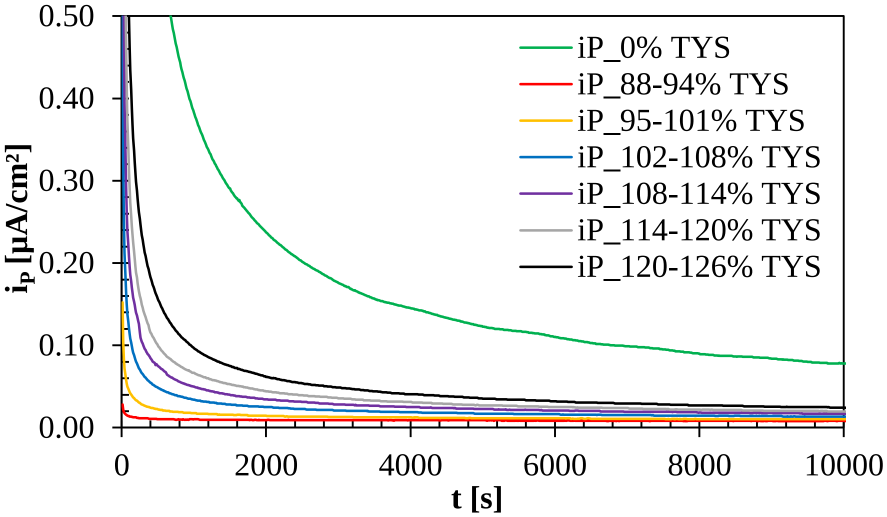

Figure 9.16. Comparison between first passivation and re-passivation transient after each stress variation

A further comparison *(Figure 9.17)*, always on the X65 grade steel, was made on the steady state hydrogen permeation current ($i_{H,\infty}$), between the first hydrogen permeation transient (green curve, without an applied load) and the increasing permeation transient subsequent to each stress variation (from red to grey curve).

As observed also in the case of the maximum stress variation under cyclic loading conditions, the temporary reduction in hydrogen permeation flux is due to an instantaneous reduction of the mobile hydrogen concentration in the lattice, caused by the increase in the number of trapping sites following local plasticization phenomena, which seem to occur even for stress values lower than the TYS.

Considering a steady state current of about 0.19 µA/cm^2, due to the slight increase detected in the elastic deformation field [133], already for the load variation from 95% to 101% TYS (from 75% to

80% UTS) the current value reached after the transient is lower. The subsequent stress variation occurs when the newly generated traps are not fully saturated with hydrogen, because the 4-hour duration of the maintenance step was not sufficient for the permeation transient to exhaust; consequently, the current starts increasing from a value lower than the previous steady state one.

This fact indicates that the duration of the step, even if the specimen was just 1-mm thick, was not sufficient for the permeation transient to completely exhaust and reach again the previous value of $i_{H,\infty}$; thus, the possible occurrence of HE phenomena connected to the filling of new trapping sites could not be evaluated.

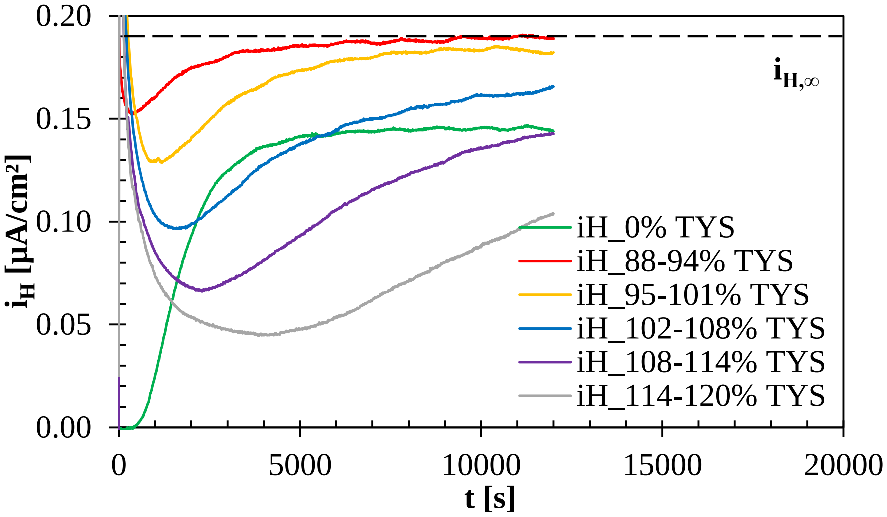

Figure 9.17. Comparison between first and subsequent permeation transient after each load variation

10

CONCLUSIONS

This 3-year PhD Thesis work aimed to analyze hydrogen permeation mechanism in one type of high strength low alloy carbon steel, known as API 5L X65 grade steel, which is probably the mainly utilized in pipelines construction for petroleum and natural gas transportation.

Hydrogen permeation was realized by means of an electrochemical permeation technique, which involved the use of a test device consisting of a modified Devanathan-Stachurski cell, developed in the laboratories of the Department of Engineering and Applied Sciences of the University of Bergamo during this PhD Thesis. Modifications to the original permeation cell and test procedures were applied in order to study hydrogen diffusion in the presence of different applied loading conditions.

The obtained results allowed to better understand the variations in hydrogen transport mechanisms into a commercial pipeline steel in the unloaded condition and in the presence of an applied load or a residual plastic deformation. The conclusions made are listed in the following points:

- No criteria are indicated by the main international and national standards for the determination of the critical limit potential indicated to avoid the occurrence of HE phenomena. This limit should be determined “experimentally” by means of mechanical tests, but no precise indications are provided for the test methods to be adopted
- Apparent diffusivity is characterized by an average value of $7.6 \cdot 10^{-11}$ m^2/s for the X65 grade steel (sorbite). Under cyclic loading conditions, the application of a tensile stress in the middle of the elastic domain determined a slight decrease in D_{app} while, beyond the yield limit, this value drops to values around $1.4 \cdot 10^{-11}$ m^2/s, due to the creation of a large quantity of new reversible and irreversible trapping sites. Hydrogen trapping phenomena are enhanced under cyclic loading conditions. The application of a compressive stress determines a mitigation in the stress field determined by a tensile stress, and a softening effect seems to occur in the material
- Reversible trapping parameter for the unloaded material is characterized by an average value of 0.0095. Under cyclic loading conditions, $N_{t,r}/N_l$ slightly increases even in the middle of the elastic field; between 90% and 100% TYS, and beyond the yield limit, this parameter is subject to a steep increase, and reaches values around 0.0490. In the worst loading condition considered

(110% TYS), $N_{t,r}/N_l$ increases of about 5 times if compared to the unloaded material (U). This sharp increase in the trapping factor is a phenomenon probably due to the contribution of the accumulation of new traps during the application of cyclic loading conditions in the plastic deformation field. The increase in $N_{t,r}/N_l$ confirms the assumption that the relevant decrease in D_{app}, along with an increase in the applied maximum stress, is connected to an increase in the dislocation density with deformation, and not to a modification of E_b, assumed constant for all the performed tests. The delaying effect cannot be related only to an increase in the number of reversible traps, but also to an increase in the density of irreversible traps. The extent of the plastic deformation achieved in the tests is relatively low, thus the delaying effect seems to be small if compared to the multiplication of reversible trapping sites

- Hydrogen concentration in the lattice (C_0) presents an average value of $1.5*10^{-3}$ mol/m^3; this means that no significant variations in the surface conditions or in the cell environment occurred. The average value of the total hydrogen concentration (C_{TOT}) for the unloaded material is around $1.5*10^{-1}$ mol/m^3, which is about two orders of magnitude higher than C_0. Under cyclic loading conditions, C_{TOT} remains almost constant up to 90% TYS; between 90% and 100% TYS, and beyond the yield limit, however, it significantly increases, as a result of enhanced hydrogen absorption and filling of an increasing number of trapping sites. For the worst loading condition (110% TYS), C_{TOT} is nearly one order of magnitude higher than that in the unloaded material, and nearly three orders of magnitude higher than C_0. If a compressive stress is applied after a tensile one, C_{TOT} decreases relevantly, and settles around values very similar to those in the unloaded material; this confirms again the hypothesis of a mitigation in the stress field
- Steady state hydrogen permeation current ($i_{H,\infty}$) is almost constant for stresses fully in the elastic field, with an average value around $1.5*10^{-1}$ µA/cm^2; between 90% and 100% TYS and beyond this limit (110% TYS), instead, this value is subject to a slight increase, common to all the loading conditions, reaching values around $2.0*10^{-1}$ µA/cm^2
- Current response induced on $i_{a,\infty}$ by the alternate component of the load under cyclic loading conditions, even at high frequencies, is very similar to that induced on $i_{P,\infty}$, with comparable phase shifts. Thus, the effect of the load on $i_{a,\infty}$ is not due to the presence of diffusing hydrogen. The current variation is hypothesized to be connected to a sort of piezoelectric effect, related to the dynamic deformation of the iron oxide film on the anodic surface of the specimen. The sine waveform assumed by the current is probably due to an electric field induced by the load sinusoid, which cyclically stretches and compresses the iron oxide film
- Temporary reduction in hydrogen flux, determined by a variation of the maximum stress, may be due to an instantaneous reduction of the mobile hydrogen concentration in the crystal lattice,

caused by an increase in the number of trapping sites following local plasticization phenomena, occurring even for stress values lower than the TYS

- Specimens of X65 grade steel and heat treated material, both tested with an incremental step loading technique prescribed for the evaluation of HE susceptibility of fasteners, came to failure at a stress value very close to that in air. The failure of both the specimens occurred in a region very far from the permeation area, and no crack propagation during the constant deformation phase in the previous step was observed. Therefore, neither the sorbitic microstructure of the X65 grade steel nor the martensitic one, obtained after the heat treatment of water quenching, resulted susceptible to HE in accordance to the analyzed test method. Finally, the duration of the step, even if the specimen was just 1-mm thick, was not sufficient for the permeation transient to completely exhaust and reach again the previous values of $i_{H,\infty}$; thus, the possible occurrence of embrittlement phenomena connected to the filling of new trapping sites could not be evaluated.

REFERENCES

[1] *UNI EN 12954:2002. Protezione catodica di strutture metalliche interrate o immerse.*

[2] *ISO 15589-1:2015. Petroleum, petrochemical and natural gas industries. Cathodic protection of pipeline systems.*

[3] A. Smirnova, *Hydrogen permeation in 13% Cr super martensitic stainless steel and API X70 pipeline steel - PhD thesis,* Norwegian University of Science and Technology, Trondheim, Norway, 2010.

[4] *Energy Institute Document. Guidance for Corrosion Management in Oil and Gas Production and Processing.*

[5] *DNV Offshore Standard. Design of Offshore Steel Structures,* General (LRFD), 2000.

[6] *ISO 19902:2007. Petroleum & Natural Gas Industries, Fixed Steel Offshore Structures.*

[7] *UNI EN 13636:2004. Protezione catodica di serbatoi metallici interrati e delle relative tubazioni.*

[8] *UNI EN 12499:2004. Protezione catodica interna di strutture metalliche.*

[9] *UNI EN ISO 15589-2:2014. Industrie del petrolio, petrolchimiche e del gas naturale - Protezione catodica dei sistemi di tubazioni per il trasporto - Parte 2: Condotte marine.*

[10] *DNV-RP-B401:2010. Recommended Practice - Cathodic Protection Design.*

[11] *UNI EN 13173:2001. Protezione catodica di strutture galleggianti (offshore) di acciaio.*

[12] *UNI EN 12474:2001. Protezione catodica di condotte sottomarine.*

[13] *UNI EN 12495:2002. Protezione catodica per strutture fisse offshore di acciaio.*

[14] *UNI EN 16222:2012. Protezione catodica degli scafi delle navi.*

[15] *UNI EN ISO 13174:2013. Protezione catodica per installazioni portuali.*

[16] *UK Health and Safety Executive, Research report 105, Review of the performance of high strength steels used offshore, 2003.*

[17] *UK Health and Safety Executive, Offshore Technology Report OTH 91351, Hydrogen cracking of legs and spudcans on jack-up drilling rigs, 1993.*

[18] *UNI EN ISO 7539-1:2013. Corrosione dei metalli e loro leghe - Prova di tensocorrosione - Parte 1: Linee guida sulle procedure di prova.*

[19] *UNI EN ISO 7539-11:2015. Corrosione dei metalli e loro leghe - Prova di tensocorrosione - Parte 11: Linee guida per prove di resistenza dei metalli e loro leghe contro l'infragilimento da idrogeno e da cricche indotte da idrogeno.*

[20] *UNI EN ISO 7539-7:2005. Corrosione dei metalli e delle loro leghe - Prova di tensocorrosione - Parte 7: Metodo della prova a deformazione lenta.*

[21] *NACE TM0177-2016. Laboratory testing of metals for resistance to Sulfide Stress Cracking and Stress Corrosion Cracking in H2S environments.*

[22] *ISO 7539-1:2012. Corrosion of metals and alloys - Stress corrosion testing - Part 1: General guidance on testing procedures.*

[23] *UNI 11094:2004. Protezione catodica di strutture metalliche interrate - Criteri generali per l'attuazione, le verifiche e i controlli ad integrazione della UNI EN 12954 anche in presenza di correnti disperse.*

[24] *UNI 10950:2001. Protezione catodica di strutture metalliche interrate - Telecontrollo dei sistemi di protezione catodica.*

[25] *EN 50162:2004. Protection against corrosion by stray current from direct current systems.*

[26] *UNI 10835:1999. Protezione catodica di strutture metalliche interrate - Anodi e dispersori per impianti a corrente impressa - Criteri di progettazione e installazione.*

[27] *EN 14505:2005. Cathodic protection of complex structures.*

[28] *UNI ISO 5256:1987. Tubi ed accessori di acciaio impiegati per tubazioni interrate o immerse. Rivestimento esterno e interno a base di bitume o di catrame.*

[29] *UNI 9099:1989. Tubi di acciaio impiegati per tubazioni interrate o sommerse. Rivestimento esterno di polietilene applicato per estrusione.*

[30] *UNI EN 10289:2003. Tubi e raccordi di acciaio per condotte terrestri e marine - Rivestimenti esterni in resina epossidica e resina epossidica-modificata applicata allo stato liquido.*

[31] *UNI EN 12068:2002. Protezione catodica - Rivestimenti organici esterni per la protezione dalla corrosione delle tubazioni di acciaio interrate o immerse da associare alla protezione catodica - Nastri e materiali termorestringenti.*

[32] *UNI EN 10290:2003. Tubi e raccordi di acciaio per condotte terrestri e marine - Rivestimenti esterni in poliuretano-modificato applicato allo stato liquido.*

[33] S. Taylor, *Short-segment pipeline rehabilitation technology,* Neuilly-en-Thelle, France: CRC-Evans Rehabilitation Systems. Technology Publishing Company, 1998.

[34] *ISO 8501-1:2007. Rust grades and preparation of uncoated steel substrates and steel substrates after overall removal of previous coatings.*

[35] M. Hirscher, Handbook of Hydrogen Storage. New Materials for Future Energy Storage, John Wiley & Sons, 2010.

[36] D. Hardie, E. Charles and A. Lopez, "Hydrogen embrittlement of high strength pipeline steels," *Corrosion Science,* vol. 48, no. 12, pp. 4378-4385, 2006.

[37] R. Iyer, I. Takeuchi, M. Zamanzadeh and H. Pickering, "Hydrogen Sulfide Effect on Hydrogen Entry into Iron—A Mechanistic Study," *Corrosion,* vol. 46, no. 6, pp. 460-468, 1990.

[38] B. Berkowitz and F. Heubaum, "The Role of Hydrogen in Sulfide Stress Cracking of Low Alloy Steels," *Corrosion,* vol. 40, no. 5, pp. 240-245, 1984.

[39] A. Turnbull, "Perspectives on hydrogen uptake, diffusion and trapping," *International Journal of Hydrogen Energy,* vol. 40, no. 47, pp. 16961-16970, 2015.

[40] J. De Luccia, "Electrochemical Aspects of Hydrogen in Metals," in *Hydrogen Embrittlement, Phenomena and Control* , vol. ASTM STP 962, Philadelphia, American Society for Testing and Materials, 1988, pp. 17-34.

[41] L. Cailletet, *Compte Rendu* , p. 327 , 1964.

[42] M. Bodenstein, *Zeitschria fur electrochmie,* vol. 28, p. 517, 1922.

[43] J.-L. Crolet, "Analysis of the various processes downstream cathodic hydrogen charging, I: Diffusion, laboratory permeation and measurement of hydrogen content and diffusion coefficient," *Matériaux & Techniques,* vol. 104, p. 205, 2016.

[44] S. Ewing, "Electrochemical Studies of the Hydrogen Sulfide Corrosion Mechanism," *Corrosion,* vol. 11, no. 11, pp. 51-55, 1955.

[45] W. Johnson, "On some remarkable changes produced in iron and steel by the action of hydrogen acids," *Proceedings of the Royal Society of London,* vol. 23A, pp. 168-179, 1875.

[46] E. Wallaert, T. Depover, B. Pieters, M. Arafin and K. Verbeken, "TDS Evaluation of the Hydrogen Trapping Capacity of NbC Precipitates," in *International Hydrogen Conference (IHC 2012): Hydrogen-Materials Interactions*, 2014, p. Chapter 62.

[47] C. Beachem, "A New Model for Hydrogen-Assisted Cracking (Hydrogen Embrittlement)," *Metallurgical Transactions,* vol. 3, pp. 437-451, 1972.

[48] M. Bernstein and A. Thompson, "Effect of Metallurgical Variables on Environmental Fracture," *International Metal Review,* vol. 21, pp. 269-87, 1976.

[49] S. Lynch, "Mechanisms of Hydrogen Assisted Cracking - A review," in *Hydrogen effects on Materials Behavior and Corrosion Deformation Interactions,* vol. 1, TMS (The Mineals, Metals and materials Society), 2003, pp. 449-466.

[50] S. Zheng, C. Chen and L. Chen, "Influence of S Contents on the Hydrogen Blistering and Hydrogen Induced Cracking of A350LF2 Steel," *Materials Sciences and Applications,* pp. Vol. 2, pp. 917-921, 2011.

[51] T. Hara, H. Asahi and H. Ogawa, "Conditions of Hydrogen-Induced Corrosion Occurrence of X65 Grade Line Pipe Steels in Sour Environments," *Corrosion,* vol. 60, no. 12, pp. 1113-1121, 2004.

[52] M. Lucio-Garcia, J. Gonzalez-Rodriguez and M. Casales, "Effect of Heat Treatment on H2S Corrosion of a Micro-Alloyed C-Mn Steel," *Corrosion Science,* vol. 51, no. 10, pp. 2380-2386, 2009.

[53] H. Ha, J. Ai and J. Scully, "Effects of Prior Cold Work on Hydrogen Trapping and Diffusion in API X-70 Line Pipe Steel During Electrochemical Charging," *Corrosion,* vol. 70, no. 2, pp. 166-184, 2014.

[54] Q. Zhou, L. Qiao, H. Qi, J. Li, J. He and W. Chu, "Hydrogen blistering and hydrogen-induced cracking in amorphous nickel phosphorus coating," *Journal of Non-Crystalline Solids,* vol. 353, no. 44-46, pp. 4011-4014, 2007.

[55] X. Ren, Q. Zhou, G. Shan, W. Chu, J. Li, Y. Su and L. Qiao, "A nucleation mechanism of hydrogen blister in metals and alloys," *Metallurgical and Materials Transactions A,* vol. 39, no. 1, pp. 87-97, 2008.

[56] J. Hirth, "Effects of hydrogen on the properties of iron and steel," *Metallurgical Transactions A,* vol. 11A, pp. 861-890, 1980.

[57] R. Srinivasan and T. Neeraj, "Hydrogen Embrittlement of Ferritic Steels: Deformation and Failure Mechanisms and Challenges in the Oil and Gas Industry," *JOM,* vol. 66, no. 8, pp. 1377-1382, 2014.

[58] G. Razzini, M. Cabrini, S. Maffi, G. Mussati and L. Peraldo Bicelli, "Photoelectrochemical visualization in real-time of hydrogen distribution in plastic regions of low-carbon steel," *Corrosion Science,* vol. 41, no. 1, pp. 203-208, 1999.

[59] J. Kiefner and R. Eiber, *Oil&Gas Journal,* vol. 85, no. 13, pp. 98-100, 1987.

[60] J. Kiefner and R. Eiber, *Oil&Gas Journal,* vol. 85, no. 15, pp. 38-42, 1987.

[61] A. Punker, A. Fikker and G. Venstoen, "Hydrogen-induced stress corrosion cracking on a pipeline," *Material Performance,* vol. 31, no. 6, pp. 24-28, 1992.

[62] A. Mazel, "On stress corrosion cracking of gas pipelines. Reliability and safety of gas pipelines subject to stress corrosion cracking, STP 2-4, p. 11-22," RAO Gazprom, Moscow, 1993.

[63] T. S. B. o. Canada, "Pipeline investigation report. Report No. P94H0003," Hull, Quebec, 1994.

[64] S. Chiovelli, D. Dorling, A. Glover and D. Horsley, *Oil&Gas Journal,* vol. 92, no. 11, pp. 91-100, 1994.

[65] V. Polyakov and V. Kharionovsky, "Statistics of transmission pipeline fractures," in *Structural failure, product liability and technical insurance,* London: E&FN Spon, Rossmanith HP, editor, 1996, pp. 353-361.

[66] T. S. B. o. Canada, "Pipeline investigation report. Report No. P00H0037," Hull, Quebec, 2000.

[67] M. Cabrini, V. Pistone, E. Sinigaglia and M. Tarenzi, "Unique HSC scenario leads to gas line failure," *Oil & Gas Journal,* vol. 98, no. 10, pp. 61-65, 2000.

[68] S. Shipilov and I. Le May, "Structural integrity of aging buried pipelines having cathodic protection," *Engineering Failure Analysis,* vol. 13, no. 7, pp. 1159-1176, 2006.

[69] W. Kim, S. Koh, B. Yang and K. Kim, "Effect of environmental and metallurgical factors on hydrogen induced cracking of HSLA steels," *Corrosion Science,* vol. 50, no. 12, pp. 3336-3342, 2008.

[70] E. Publications, Ed., Corrosion resistant alloys for oil and gas production: guidance on general requirements and test methods for H2S service, Second ed., vol. 17, Maney Publishing.

[71] B. Beidokhti, A. Dolati and A. Koukabi, "Effects of alloying elements and microstructure on the susceptibility of the welded HSLA steel to hydrogen-induced cracking and sulfide stress cracking," *Materials Science and Engineering A,* vol. 507, no. 1-2, pp. 167-173, 2009.

[72] T. Jin, Z. Liu and Y. Cheng, "Effect of non-metallic inclusions on hydrogen-induced cracking of API5L X100 steel," *International Journal of Hydrogen Energy,* vol. 35, pp. 8014-8021, 2010.

[73] E. Publications, Ed., Guidelines on materials requirements for carbon and low alloy steels for H2S-containing environments in oil and gas production, Third ed., vol. 16, Maney Publishing, 2009.

[74] H. Uhlig, Uhlig's Corrosion Handbook, J. W. &. Sons, Ed., Hoboken, New Jersey: R. Winston Revie, 2011.

[75] M. Louthan, in *Hydrogen in metals*, ASM International, Metals Park, Ohio, I. M. Bernstein and A. W. Thompson, eds., 1974, pp. 53-78.

[76] J. Galvele, "Surface mobility mechanism of stress-corrosion cracking," *Corrosion Science,* vol. 35, no. 1-4, pp. 419-434, 1993.

[77] C. Zapffe and C. Sims, "Hydrogen Embrittlement, Internal Stress and Defects in Steel," *American Institute of Mining, Metallurgical, and Petroleum Engineers (AIME),* no. 1307, pp. 1-37, 1941.

[78] F. De Kazinczy, *Journal of the Iron and Steel Institute,* vol. 177, pp. 85-92, 1954.

[79] N. Pitch and P. Stables, "Delayed fracture of metals under static load," *Nature,* vol. 169, p. 842–843, 1952.

[80] A. Griffith, "VI. The phenomena of rupture and flow in solids," *Philosophical Transactions of the Royal Society A,* vol. 221, no. 582-593, 1921.

[81] H. M. J. A. Johnson, "Hydrogen crack initiation and delayed failure in steel," *Transactions of the Metallurgical Society of AIME,* vol. 212, pp. 528-536, 1958.

[82] H. Johnson, J. Morlet and A. Troiano, *TMS-AIME,* vol. 212, no. 29, p. 528, 1958.

[83] E. Steigerwald, F. Schaller and A. Troiano, *TMS-AIME,* vol. 215, no. 35, p. 1048, 1959.

[84] E. Steigerwald, F. Schaller and A. Troiano, "The role of stress in hydrogen induced delayed failure.," *Transactions of the Metallurgical Society of AIME,* vol. 218, pp. 832-841, 1960.

[85] A. Troiano, "The role of hydrogen and other interstitials in the mechanical behaviour of metals," in *Transactions, ASM, Vol. 52,* vol. 12, 1960, pp. 54-80.

[86] L. Pfeil, "The effect of occluded hydrogen on the tensile strength of iron," *Proceedings of the Royal Society A - Mathematical, Physical and Engineering Sciences,* vol. 112, no. 760, pp. 182-195, 1926.

[87] R. Oriani, "Mechanicistic Theory of Hydrogen Embrittlemnt of Steels," *Berichte Der Bunsen-Gesellschaft Fur Physikalische Chemie,* vol. 76, no. 8, pp. 848-857, 1972.

[88] J. Song and W. Curtin, "A nanoscale mechanism of hydrogen embrittlement in metals," *Acta Materialia,* vol. 59, no. 4, p. 1557 – 1569, 2011.

[89] R. Oriani and P. Josephic, "Equilibrium aspects of hydrogen-induced cracking of steels," *Acta Metallurgica,* vol. 22, no. 9, pp. 1065-1074, 1974.

[90] R. Oriani and P. Josephic, "Equilibrium and kinetic studies of the hydrogen-assisted cracking of steel," *Acta Metallurgica,* vol. 25, no. 9, pp. 979-988, 1977.

[91] R. Oriani and P. Josephic, "Hydrogen-enhanced load relaxation in a deformed medium-carbon steel," *Acta Metallurgica,* vol. 27, no. 6, pp. 997-1005, 1979.

[92] W. Gerberich, R. Oriani, M.-J. Lji, X. Chen and T. Foecke, "The necessity of both plasticity and brittleness in the fracture thresholds of iron," *Philosophical Magazine A,* vol. 63, no. 2, pp. 363-376, 1991.

[93] R. Oriani, "Hydrogen: the versatile embrittler," *Corrosion,* vol. 43, no. 7, pp. 390-397, 1987.

[94] A. Oudriss, J. Creus, J. Bouhattate, C. Savall, B. Peraudeau and X. Feaugas, "The diffusion and trapping of hydrogen along the grain boundaries in polycrystalline nickel," *Scripta Materialia,* vol. 66, no. 1, pp. 37-40, 2012.

[95] X. Li, Y. Wang, P. Zhang, B. Li, X. Song and J. Chen, "Effect of pre-strain on hydrogen embrittlement of high strength steels," *Materials Science and Engineering: A,* vol. 616, pp. 116-122, 2014.

[96] A. Stroh, "A Theory of Fracture of Metals," *Advances in Physics,* vol. 6, pp. 418-465, 1957.

[97] A. Cottrell, *Dislocations and Plastic Flow in Crystals,* Oxford: Oxford University Press, 1953.

[98] M. J. Louthan, G. J. Caskey, J. Donovan and D. J. Rawl, "Hydrogen Embrittlement of Metals," *Material Science and Engineering,* vol. 10, pp. 357-368, 1972.

[99] H. Birnbaum and P. Sofronis, "Hydrogen-enhanced localized plasticity - A mechanism for hydrogen-related fracture," *Materials Science and Engineering: A,* vol. 176, no. 1-2, pp. 191-202, 1994.

[100] K. Ichitani and M. Kanno, "Visualization of hydrogen diffusion in steels by high sensitivity hydrogen microprint technique," *Science and Technology of Advanced Materials,* vol. 4, no. 6, pp. 545-551, 2003.

[101] I. Robertson, "The effect of hydrogen on dislocation dynamics," *Engineering Fracture Mechanics,* vol. 68, no. 6, pp. 671-692, 2001.

[102] C. Ayas, V. Deshpande and N. Fleck, "A fracture criterion for the notch strength of high strength steels in the presence of hydrogen," *Journal of the Mechanics and Physics of Solids,* vol. 63, pp. 80-93, 2014.

[103] T. Tabata and H. Birnbaum, "Direct observations of the effect of hydrogen on the behavior of dislocations in iron," *Scripta Metallurgica,* vol. 17, no. 7, pp. 947-950, 1983.

[104] T. Tabata and H. Birnbaum, "Direct observations of hydrogen enhanced crack propagation in iron," *Scripta Metallurgica,* vol. 18, no. 3, pp. 231-236, 1984.

[105] I. Robertson and H. Birnbaum, "An HVEM study of hydrogen effects on the deformation and fracture of nickel," *Acta Metallurgica,* vol. 34, no. 3, pp. 353-366, 1986.

[106] G. Bond, I. Robertson and H. Birnbaum, "The influence of hydrogen on deformation and fracture processes in high-strength aluminum alloys," *Acta Metallurgica,* vol. 35, no. 9, pp. 2289-2296, 1987.

[107] G. Bond, I. Robertson and H. Birnbaum, "Effects of hydrogen on deformation and fracture processes in high-purity aluminium," *Acta Metallurgica,* vol. 36, no. 8, pp. 2193-2197, 1988.

[108] T. Perez and J. Ovejero Garcia, *Scripta Metallurgica,* vol. 16, p. 161, 1982.

[109] M. Nagumo, "Hydrogen related failure of steels – a new aspect," *Materials Science and Technology,* vol. 20, no. 8, pp. 940-950, 2004.

[110] O. Barrera, D. Bombac, Y. Chen, T. Daff, E. Galindo-Nava, P. Gong, D. Haley, R. Horton, I. Katzarov, J. Kermode, C. Liverani, M. Stopher and F. Sweeney, "Understanding and mitigating hydrogen embrittlement of steels: a review of experimental, modelling and design progress from atomistic to continuum," *Journal of Materials Science,* vol. 53, no. 9, pp. 6251-6290, 2018.

[111] J. Ovejero Garcia, "Hydrogen microprint technique in the study of hydrogen in steels," *Journal of Materials Science,* vol. 20, pp. 2623-2629, 1985.

[112] M. Haga, *In situ nanomechanical testing of electrochemical hydrogen permeation membranes - Master thesis,* Norwegian University of Science and Technology, Trondheim, Norway, 2017.

[113] A. Brass and A. Chanfreau, "Accelerated diffusion of hydrogen along grain boundaries in nickel," *Acta Materialia,* vol. 44, no. 9, pp. 3823-3831, 1996.

[114] S. Gahr, M. Grossbeck and H. Birnbaum, "Hydrogen embrittlement of Nb - I. Macroscopic behavior at low temperatures," *Acta Metallurgica,* vol. 25, no. 2, pp. 125-134, 1977.

[115] S. Gahr and H. Birnbaum, "Hydrogen embrittlement of Nb - III. High temperature behavior," *Acta Metallurgica,* vol. 26, no. 11, pp. 1781-1788, 1978.

[116] D. Shih, I. Robertson and H. Birnbaum, "Hydrogen embrittlement of α titanium: In situ TEM studies," *Acta Metallurgica,* vol. 36, no. 1, pp. 111-124, 1988.

[117] N. Paton and J. Williams, "Effect of hydrogen on titanium and its alloys," in *Hydrogen in metals,* Metals park, Ohio, Bernstein, I.M., Thompson, A.W., Editors, 1973, pp. 409-431.

[118] D. Sherman, C. Owen and T. Scott, "The effect of hydrogen on the structure and properties of vanadium," *Transactions of the Metallurgical Society of AIME,* vol. 242, pp. 1775-1784, 1968.

[119] D. Hardie and P. McIntyre, "The low-temperature embrittlement of niobium and vanadium by both dissolved and precipitated hydrogen," *Metallurgical Transactions,* vol. 4, no. 5, pp. 1247-1254, 1973.

[120] R. Dutton, K. Nuttall, M. Puls and L. Simpson, "Mechanisms of hydrogen induced delayed cracking in hydride forming materials," *Metallurgical Transactions A,* vol. 8, no. 10, pp. 1553-1562, 1977.

[121] J. Lufrano, P. Sofronis and H. Birnbaum, "Modeling of hydrogen transport and elastically accommodated hydride formation near a crack tip," *Journal of the Mechanics and Physics of Solids,* vol. 44, no. 2, pp. 179-205, 1996.

[122] J. Lufrano, P. Sofronis and H. Birnbaum, "Elastoplastically accommodated hydride formation and embrittlement," *Journal of the Mechanics and Physics of Solids,* vol. 46, no. 9, pp. 1497-1520, 1998.

[123] H. Birnbaum, "Hydrogen related failure mechanisms in metals," Department of Metallurgy and Mining Engineering, University of Illinois at Urbana-Champaign, Urbana, Illinois 61801 U.S.A., 1989.

[124] D. Porter, K. Easterling and M. Sherif, Phase transformations in metals and alloys - 3rd Edition, Boca Raton, FL: CRC Press, 2009.

[125] J. Crank, The mathematics of diffusion - 2nd Edition, Oxford: Clarendon Press, 1975.

[126] W. Callister and D. Rethwisch, Materials Science and Engineering - 8th Edition, Singapore: John Wiley & Sons Pte Ltd, 2011.

[127] E. Fallahmohammadi, *Diffusion and trapping of hydrogen in pipeline steels - PhD thesis,* University of Milan, 2014.

[128] J. McBreen, L. Nanis and W. Beck, "A method for determination of the permeation rate of hydrogen through metal membranes," *Journal of the Electrochemical Society,* vol. 113, no. 11, pp. 1218-1222, 1966.

[129] G. Herbsleb and W. Schwenk, "The influence of dynamic mechanical parameters on stress corrosion cracking of steel - A review," *Corrosion,* vol. 41, no. 8, pp. 431-437, 1985.

[130] M. Smialowski, Hydrogen in steel. Effect of hydrogen on iron and steel during production, fabrication and use, Oxford, London: Pergamon Press , 1962.

[131] Y. Fukai, Y. Ishii, Y. Goto and K. Watanabe, "Formation of superabundant vacancies in Pd-H alloys," *Journal of Alloys and Compounds,* vol. 313, pp. 121-132, 2000.

[132] A. Krom and A. Bakker, "Hydrogen trapping models in steel," *Metallurgical and Materials Transactions B,* vol. 31, no. 6, pp. 1475-1482, 2000.

[133] M. Cabrini, S. Lorenzi, S. Pellegrini and T. Pastore, "Environmentally assisted cracking and hydrogen diffusion in traditional and high-strength pipeline steels," *Corrosion Reviews,* vol. 33, no. 6, pp. 529-545, 2015.

[134] M. Cabrini and S. Lorenzi, "Pipeline steels: Hydrogen diffusion and Environmentally-Assisted Cracking," in *Encyclopedia of Iron, Steel, and Their Alloys*, Taylor & Francis. Informa UK Limited, 2015, pp. 2547-2559.

[135] L. Tau and S. Chan, "Effects of ferrite/pearlite alignment on the hydrogen permeation in a AISI 4130 steel," *Materials Letters ,* vol. 29, pp. 143-147, 1996.

[136] J. Yang and H. Bhadeshia, "The dislocation density of acicular ferrite in steel welds," *American Welding Journal, Welding Research Supplement,* vol. 69, pp. 305-307, 1990.

[137] S. Serna, H. Martínez, S. López, J. González-Rodríguez and J. Albarrán, "Electrochemical technique applied to evaluate the hydrogen permeability in microalloyed steels," *International Journal of Hydrogen Energy,* vol. 30, no. 12, pp. 1333-1338, 2005.

[138] G. Park, S. Koh, H. Jung and K. Kim, "Effect of microstructure on the hydrogen trapping efficiency and hydrogen induced cracking of linepipe steel," *Corrosion Science,* vol. 50, no. 7, pp. 1865-1871, 2008.

[139] E. Chatzidouros, V. Papazoglou and D. Pantelis, "Hydrogen effect on a low carbon ferritic-bainitic pipeline steel," *International Journal of Hydrogen Energy,* vol. 39, no. 32, pp. 18498-18505, 2014.

[140] H. Xue and Y. Cheng, "Characterization of inclusions of X80 pipeline steel and its correlation with hydrogen-induced cracking," *Corrosion Science,* vol. 53, no. 4, pp. 1201-1208, 2011.

[141] Y. Cheng, "Analysis of electrochemical hydrogen permeation through X-65 pipeline steel and its implications on pipeline stress corrosion cracking," *International Journal of Hydrogen Energy,* vol. 32, no. 9, pp. 1269-1276, 2007.

[142] A. Contreras, A. Albiter, M. Salazar and R. Pérez, "Slow strain rate corrosion and fracture characteristics of X-52 and X-70 pipeline steels," *Materials Science and Engineering A,* vol. 407, no. 1-2, pp. 45-52, 2005.

[143] C. Dong, Z. Liu, X. Li and Y. Cheng, "Effects of hydrogen-charging on the susceptibility of X100 pipeline steel to hydrogen-induced cracking," *International Journal of Hydrogen Energy,* vol. 34, no. 24, pp. 9879-9884, 2009.

[144] C. Dong, K. Xiao, Z. Liu, W. Yang and X. Li, "Hydrogen induced cracking of X80 pipeline steel," *International Journal of Minerals, Metallurgy, and Materials,* vol. 17, no. 5, pp. 579-586, 2010.

[145] C. Dong, X. Li, Z. Liu and Y. Zhang, "Hydrogen-induced cracking and healing behaviour of X70 steel," *Journal of Alloys and Compounds,* vol. 484, no. 1-2, pp. 966-972, 2009.

[146] F. Fassini, M. Zampronio and P. De Miranda, "Design of ion-implanted coatings to impede hydrogen contamination of steel," *Corrosion Science,* vol. 35, no. 1-4, pp. 549-556, 1993.

[147] F. Huang, J. Liu, Z. Deng, J. Cheng, Z. Lu and X. Li, "Effect of microstructure and inclusions on hydrogen induced cracking susceptibility and hydrogen trapping efficiency of X120 pipeline steel," *Materials Science and Engineering A,* vol. 527, no. 26, pp. 6997-7001, 2010.

[148] J. Kittel, V. Smanio, M. Fregonese, L. Garnier and X. Lefebvre, "Hydrogen induced cracking (HIC) testing of low alloy steel in sour environment: Impact of time of exposure on the extent of damage," *Corrosion Science,* vol. 52, no. 4, pp. 1386-1392, 2010.

[149] H. Nykyforchyn, E. Lunarska, O. Tsyrulnyk, K. Nikiforov and G. Gabetta, "Effect of the long-term service of the gas pipeline on the properties of the ferrite-pearlite steel," *Materials and Corrosion,* vol. 60, no. 9, pp. 716-725, 2009.

[150] M. Cabrini, S. Lorenzi, P. Marcassoli and T. Pastore, "Hydrogen embrittlement behavior of HSLA line pipe steel under cathodic protection," *Corrosion Reviews,* vol. 29, no. 5-6, pp. 261-274, 2011.

[151] P. Castaño Rivera, V. Ramunni and P. Bruzzoni, "Hydrogen trapping in an API 5L X60 steel," *Corrosion Science,* vol. 54, pp. 106-118, 2012.

[152] S. Zheng, C. Zhou, P. Wang, C. Chen and L. Chen, "Effects of the temperature on the hydrogen permeation behaviours of L360NCS pipeline steel in 1MPa H2S environments," *International Journal of Electrochemical Science,* vol. 8, pp. 2880-2891, 2013.

[153] R. Oriani, "The diffusion and trapping of hydrogen in steel," *Acta Metallurgica,* vol. 18, no. 1, pp. 147-157, 1970.

[154] A. Turnbull, M. Carroll and D. Ferriss, "Analysis of hydrogen diffusion and trapping in a 13% chromium martensitic stainless steel," *Acta Metallurgica,* vol. 37, no. 7, pp. 2039-2046, 1989.

[155] K. Kiuchi and R. McLellan, "The solubility and diffusivity of hydrogen in well-annealed and deformed iron," *Acta Metallurgica,* vol. 31, no. 7, pp. 961-984, 1983.

[156] A. Turnbull and M. Carroll, "The effect of temperature and H2S concentration on hydrogen diffusion and trapping in a 13% chromium martensitic stainless steel in acidified NaCl," *Corrosion Science,* vol. 30, no. 6-7, pp. 667-679, 1990.

[157] A. Turnbull, "4-Hydrogen diffusion and trapping in metals A2-Gangloff, Richard P. In: Somerday BP, editor.," in *Gaseous hydrogen embrittlement of materials in energy technologies*, Woodhead Publishing, 2012, pp. 89-128.

[158] H. Grabke and E. Riecke, "Absorption and diffusion of hydrogen in steels," *Materials and Technology,* vol. 34, no. 6, p. 331, 2000.

[159] P. Bruzzoni, R. Carranza, J. Collet Lacoste and E. Crespo, "Hydrogen diffusion in α-iron studied using an electrochemical permeation transfer function," *Electrochimica Acta,* vol. 44, no. 16, pp. 2693-2704, 1999.

[160] H. Addach, P. Berçot, M. Rezrazi and M. Wery, "Hydrogen permeation in iron at different temperatures," *Materials Letters,* vol. 59, pp. 1347-1351, 2005.

[161] S. Babu, Z. Feng, M. Santella, S. David, J. Blencoe, L. Anovitz and P. Korinko, "Hydrogen permeability and integrity of hydrogen transfer pipelines - Hydrogen Pipeline R&D, Project Review Meeting," Oak Ridge National Laboratory, Oak Ridge, TN, 2005.

[162] A. McNabb and P. Foster, "A new analysis of the diffusion of hydrogen in iron and ferritic steels," *Transactions of the Metallurgical Society of AIME,* vol. 227, pp. 618-626, 1963.

[163] A. Griffiths and A. Turnbull, "On the effective diffusivity of hydrogen in low alloy steels," *Corrosion Science,* vol. 37, no. 11, pp. 1879-1881, 1995.

[164] D. Ferriss and A. Turnbull, "NPL Report DMM (A)154," 1988.

[165] H. Johnson, "Hydrogen in iron," *Metallurgical Transactions A,* vol. 19, no. 10, pp. 2371-2387, 1988.

[166] G. Pressouyre, "A classification of hydrogen traps in steel," *Metallurgical Transactions A,* vol. 10, no. 10, pp. 1571-1573, 1979.

[167] S. Koh, J. Kim, B. Yang and K. Kim, "Effect of line pipe steel microstructure on susceptibility to sulfide stress cracking," *Corrosion,* vol. 60, no. 3, pp. 244-253, 2004.

[168] R. Wang, "Effects of hydrogen on the fracture toughness of a X70 pipeline steel," *Corrosion Science,* vol. 51, no. 12, pp. 2803-2810, 2009.

[169] S. Xie and J. Hirth, "Permeation of hydrogen, trapping, and damage in spheroidized AISI 1090 steel," *Corrosion,* vol. 38, no. 9, pp. 486-493, 1982.

[170] A. Kumnick and H. Johnson, "Deep trapping states for hydrogen in deformed iron," *Acta Metallurgica,* vol. 28, pp. 33-39, 1980.

[171] M. Kurkela, G. Frankel and R. Latanision, "Influence of plastic deformation on hydrogen transport in 2 1/4 Cr-1Mo steel," *Scripta Metallurgica,* vol. 16, pp. 455-459, 1982.

[172] Y. Huang, A. Nakajima, A. Nishikata and T. Tsuru, "Effect of mechanical deformation on permeation of hydrogen in iron," *The Iron and Steel Institute of Japan,* vol. 43, no. 4, pp. 548-554, 2003.

[173] A. Brass and J. Chene, "Influence of tensile straining on the permeation of hydrogen in low alloy Cr–Mo steels," *Corrosion Science,* vol. 48, pp. 481-497, 2006.

[174] W. Beck, J. O. Bockris, J. McBreen and L. Nanis, "Hydrogen permeation in metals as a function of stress, temperature and dissolved hydrogen concentration," *Proceedings of the Royal Society A,* vol. 290, no. 1421, 1966.

[175] A. Nagao, S. Kuramoto, K. Ichitani and M. Kanno, "Visualization of hydrogen transport in high strength steels affected by stress fields and hydrogen trapping," *Scripta Materialia,* vol. 45, no. 10, pp. 1227-1232, 2001.

[176] T. Zakroczymski, "The effect of straining on the transport of hydrogen in iron, nickel, and stainless steel," *Corrosion,* vol. 41, no. 8, pp. 485-489, 1985.

[177] J. Leblond, D. Nejem, D. Dubois and S. Talbot-Besnard, "Experimental and numerical study of diffusion and trapping of hydrogen in plastically deformed A508.Cl.3 steel at room temperature," *Acta Metallurgica,* vol. 35, no. 7, pp. 1703-1714, 1987.

[178] J. Bockris and P. Subramanyan, "A thermodynamic analysis of hydrogen in metals in the presence of an applied stress field," *Acta Metallurgica,* vol. 19, no. 11, pp. 1205-1208, 1971.

[179] J. Bockris, W. Beck, M. Genshaw, P. Subramanyan and F. Williams, "The effect of stress on the chemical potential of hydrogen in iron and steel," *Acta Metallurgica,* vol. 19, no. 11, pp. 1209-1218, 1971.

[180] S. Kim, D. Yun, H. Jung and K. Kim, "Determination of hydrogen diffusion parameters of ferritic steel from electrochemical permeation measurement under tensile loads," *Journal of the Electrochemical Society,* vol. 161, no. 12, pp. E173-E181, 2014.

[181] S. Charca, O. Uwakweh and V. Agarwala, "Hydrogen transport conditions and effects in cathodically polarized AF1410 steel," *Metallurgical and Materials Transactions A,* vol. 38, no. 10, pp. 2389-2399, 2007.

[182] B. Wilde and C. Kim, "The kinetics of hydrogen absorption and evolution on a carbon-manganese steel exposed to acidified solutions of sodium chloride," *Corrosion,* vol. 37, no. 8, pp. 449-455, 1981.

[183] J. Chene and A. Brass, "Interactions hydrogene-metal en relation avec le processus de corrosion sous contrainte," in *Corrosion sous contrainte - Phenomenologie et mecanismes,* D. Desjardins and R. Oltra, Bombannes, 1990, pp. 159-210.

[184] R. Oriani, J. Hirth and M. Smialowski, "Hydrogen degradation of ferrous alloys," in *Bernstein, I.M.; Pressouyre, G.M.,* Mill Road, Park Ridge, New Jersey 07656, NOYES PUBLICATIONS, 1985, pp. 641-685.

[185] R. Oriani, in *Proceedings of Conference on Fundamental Aspects of Stress Corrosion, R.W. Staehle et al., eds.,* NACE, 1967.

[186] R. Dus and M. Smialowski, *Acta Metallurgica,* vol. 15, pp. 1611-1616, 1967.

[187] J. Laurent, G. Lapasset, M. Aucouturier and P. Lacombe, in *Hydrogen in metals,* ASM International, Metals Park, Ohio, I. M. Bernstein and A. W. Thompson, eds., 1974, pp. 559-574.

[188] G. Pressouyre and I. Bernstein, "A quantitative analysis of hydrogen trapping," *Metallurgical Transactions A,* vol. 9A, pp. 1571-1580, 1978.

[189] W. Robertson, "Measurement and evaluation of hydrogen trapping in thoria dispersed nickel," *Metallurgical Transactions A,* vol. 10, no. 4, pp. 489-501, 1979.

[190] D. Allen-Booth and J. Hewitt, "A mathematical model describing the effects of micro voids upon the diffusion of hydrogen in iron and steel," *Acta Metallurgica,* vol. 22, pp. 171-175, 1974.

[191] M. Martínez-Madrid, S. Chan, J. Charles, J. López and V. Castaño, "Effect of grain size and second phase particles on the hydrogen occlusivity of iron and steels," *Material Research Innovations,* vol. 3, no. 5, pp. 263-270, 2000.

[192] G. Razzini, S. Maffi, G. Mussati and L. Peraldo Bicelli, "The scanning photoelectrochemical microscopy of diffusing hydrogen into metals," *Corrosion Science,* vol. 37, no. 7, pp. 1131-1141, 1995.

[193] J. Tien, A. Thompson, I. Bernstein and R. Richards, "Hydrogen transport by dislocations," *Metallurgical Transactions A,* vol. 7, no. 6, pp. 821-829, 1976.

[194] J. Crolet, "Analysis of the various processes downstream cathodic hydrogen charging, V: Dissolved hydrogen, dislocations and dislocation drag," *Matériaux & Techniques,* vol. 105, p. 202, 2017.

[195] E. Fallahmohammadi, F. Bolzoni, G. Fumagalli, G. Re, G. Benassi and L. Lazzari, "Hydrogen diffusion into three metallurgical microstructures of a Ce Mn X65 and low alloy F22 sour service steel pipelines," *International journal of hydrogen energy* , vol. 39, pp. 13300-13313, 2014.

[196] J. Lee and S. Lee, "Hydrogen trapping phenomena in metals with B.C.C. and F.C.C. crystals structures by the desorption thermal analysis technique," *Surface and Coatings Technology,* vol. 28, p. 301–314, 1986.

[197] E. Villalba and A. Atrens, "SCC of commercial steels exposed to high hydrogen fugacity," *Engineering Failure Analysis,* vol. 15, p. 617–641, 2008.

[198] M. Hashimoto and R. Latanision, "The role of dislocations during transport of hydrogen in hydrogen embrittlement of iron," *Metallurgical Transactions A,* vol. 19, no. 11, pp. 2799-2803, 1988.

[199] J. Ryu, *Hydrogen Embrittlement in TRIP and TWIP Steels,* 2012.

[200] M. Devanathan and Z. Stachurski, "The adsorption and diffusion of electrolytic hydrogen in palladium," *Proceedings of the Royal Society A,* vol. 270, pp. 90-102, 1962.

[201] *ISO 17081:2014. Method of measurement of hydrogen permeation and determination of hydrogen uptake and transport in metals by an electrochemical technique.*

[202] E. Fallahmohammadi, F. Bolzoni, G. Fumagalli, G. Re and L. Lazzari, "Diffusione e intrappolamento di idrogeno negli acciai per condotte," *La metallurgia italiana* , no. 10, pp. 3-13, 2013.

[203] R. Oriani, "The physical and metallurgical aspects of hydrogen in metals," in *ICCF-4 Fourth International Conference on Cold Fusion*, Maui, Hawaii , 1993.

[204] T. Boellinghaus, H. Hoffmeister and A. Dangeleit, "A scatterband for hydrogen diffusion coefficients in micro-alloyed and low carbon structural steels," *Welding in the World,* vol. 35, pp. 83-96, 1995.

[205] T. Zakroczymski, "Electrochemical determination of hydrogen in metals," *Journal of Electroanalytical Chemistry,* vol. 475, no. 1, pp. 82-88, 1999.

[206] T. Zakroczymski, "Adaptation of the electrochemical permeation technique for studying entry, transport and trapping of hydrogen in metals," *Electochemica Acta,* vol. 51, no. 11, pp. 2261-2266, 2006.

[207] H. Johnson and J. Hirth, "Internal hydrogen supersaturation produced by dislocation transport," *Metallurgical Transactions A,* vol. 7, no. 10, pp. 1543-1548, 1976.

[208] A. Turnbull, M. Saenz de Santa Maria and N. Thomas, "The effect of H2S concentration and pH on hydrogen permeation in AISI 410 stainless steel in 5% NaCl," *Corrosion Science,* vol. 29, no. 1, pp. 89-91, 93-104, 1989.

[209] L. Darken and R. Smith, "Behavior of hydrogen in steel during and after immersion in acid," *Corrosion,* vol. 5, no. 1, pp. 1-16, 1949.

[210] V. Olden, A. Saai, L. Jemblie and R. Johnsen, "FE simulation of hydrogen diffusion in duplex stainless steel," *International Journal of Hydrogen Energy,* vol. 39, no. 2, pp. 1156-1163, 2014.

[211] G. Pressouyre and I. Bernstein, "An example of the effect of hydrogen trapping on hydrogen embrittlement," *Metallurgical Transactions A,* vol. 12, no. 5, pp. 835-844, 1981.

[212] A. Turnbull and G. Hinds, "Hydrogen diffusion in corrosion resistant alloys," *NACE International Corrosion, Paper No. 04469,* 2004.

[213] J.-H. Ai, H. Ha, R. Gangloff and J. Scully, "Hydrogen diffusion and trapping in a precipitation-hardened nickel-copper-aluminum alloy Monel K-500 (UNS N05500)," *Acta Materialia,* vol. 61, no. 9, pp. 3186-3199, 2013.

[214] H. Husby, M. Iannuzzi, R. Johnsen, M. Kappes and A. Barnoush, "Effect of nickel on hydrogen permeation in ferritic/pearlitic low alloy steels," *International Journal of Hydrogen Energy,* vol. 43, pp. 3845-3861, 2018.

[215] I. Chattoraj, S. Tiwari, A. Ray, A. Mitra and S. Das, "Investigation on the mechanical degradation of a steel line pipe due to hydrogen ingress during exposure to a simulated sour environment," *Corrosion Science,* vol. 37, no. 6, pp. 885-896, 1995.

[216] A. Haq, K. Muzaka, D. Dunne, A. Calka and E. Pereloma, "Effect of microstructure and composition on hydrogen permeation in X70 pipeline steels," *International Journal of Hydrogen Energy,* vol. 38, no. 5, pp. 2544-2556, 2013.

[217] W. Zhao, T. Zhang, Z. He, J. Sun and Y. Wang, "Determination of the Critical Plastic Strain-Induced Stress of X80 Steel through an Electrochemical Hydrogen Permeation Method," *Electrochimica Acta,* vol. 214, pp. 336-344, 2016.

[218] A. Hauge, *Hydrogen embrittlement in subsea pipelines made from X70: Effect of plastic deformation on hydrogen diffusion - Master thesis,* Norwegian University of Science and Technology, Trondheim, Norway, 2011.

[219] G. Caskey and W. Pillinger, "Effect of trapping on hydrogen permeation," *Metallurgical Transactions A,* vol. 6, no. 3, pp. 467-476, 1975.

[220] P. Thomas and E. Stern, "Efficient numerical modelling of hydrogen diffusion with trapping," *Journal of Materials Science,* vol. 16, no. 11, pp. 3122-3130, 1981.

[221] M. Iino, "A more generalized analysis of hydrogen trapping," *Acta Metallurgica,* vol. 30, no. 2, pp. 367-375, 1982.

[222] M. Iino, "Analysis of irreversible hydrogen trapping," *Acta Metallurgica,* vol. 30, no. 2, pp. 377-383, 1982.

[223] J. Leblond and D. Dubois, "A general mathematical description of hydrogen diffusion in steels - I. Derivation of diffusion equations from Boltzmann-type transport equations," *Acta Metallurgica,* vol. 31, no. 10, pp. 1459-1469, 1983.

[224] J. Leblond and D. Dubois, "A general mathematical description of hydrogen diffusion in steels - II. Numerical study of permeation and determination of trapping parameters," *Acta Metallurgica,* vol. 31, no. 10, pp. 1471-1478, 1983.

[225] Corrosion of metals and hydrogen-related phenomena, Janusz Flis, 1991.

[226] S. Kim and K. Kim, "A review of corrosion and hydrogen diffusion behaviors of high strength pipe steel in sour environments," *Journal of Welding and Joining,* vol. 32, no. 5, 2014.

[227] H. Huang and W. Shaw, "Hydrogen embrittlement interactions in cold-worked steel," *Corrosion,* vol. 51, no. 1, pp. 30-36, 1995.

[228] F. De Kazinczy, in *Jernkort Annlr., Vol. 139*, 1965, p. 885.

[229] R. Oriani, *Transactions of the American Institute of Mining and Metallurgical Engineers,* vol. 236, p. 1368, 1966.

[230] R. Blundy, R. Royce, P. Poole and L. Shreir, "Effect of pressure and stress on permeation of hydrogen through steel," in *Stress Corrosion Cracking and Hydrogen Embrittlement of Iron Base Alloys*, Houston, Texas, NACE-5, R. Staehle, J. Hochmann, R. McCright, J. Slater, eds., 1977, p. 636.

[231] W. Dietzel, M. Pfuff and G. Juilfs, "Hydrogen permeation in plastically deformed steel membranes," *Materials Science,* vol. 42, no. 1, pp. 78-84, 2006.

[232] M. Cabrini and T. Pastore, "Hydrogen diffusion and EAC of pipeline steels under cathodic protection," in *Fracture of Nano and Engineering Materials and Structures*, Dordrecht, Springer, Gdoutos E.E. (eds), 2006, pp. 1005-1006.

[233] V. Olden, A. Hauge and O. Akselsen, "The influence of plastic strain on hydrogen diffusion and trapping in weld simulated heat affected zone of X70 pipeline steel," in *Proceedings of Eurocorr*, Istanbul, Turkey, 2012.

[234] C. Andenna and R. Torella, "A study of hydrogen permeation on API X65 TMCP steel under stress conditions," in *Hydrogen transport and cracking in metals, pp. 240-252. Proceedings of a conference. Editor: Turnbull, A.*, Teddington, UK, 1995.

[235] M. Cabrini, F. Bolzoni, G. Razzini and E. Sinigaglia, "Effect of cathodic potential and strain rate on hydrogen stress cracking of an API 5L X60 pipeline steel," in *Proceedings of the 14th International Corrosion Congress: Co-operation in corrosion control* , Cape Town, South Africa, 1999.

[236] V. Pistone, M. Tarenzi and M. Cabrini, in *Proceedings of EPRG/PRC, 10th Biennial Joint Technical Meeting on Linepipe Research, Paper Number 31* , 1995.

[237] G. Frankel and R. Latanision, "Hydrogen transport during deformation in nickel: Part I. Polycrystalline nickel," *Metallurgical Transactions A,* vol. 17, no. 5, pp. 861-867, 1986.

[238] R. Réquiz, S. Camero and A. Rivas, "Relationship between microstructure and hydrogen permeation of a plastic deformed seamless carbon steel pipe," in *NACE Corrosion Conference and Expo 2010, March 14-18,* San Antonio, Texas, 2010.

[239] A. Brass and J. Chene, "Hydrogen-deformation interactions in iron and nickel base alloys," in *Corrosion deformation interactions CDI '96,* eds. T. Magnin (EFC publication No 21), 1996, p. 198.

[240] H. Kitagawa and Y. Kojima, "Diffusion of hydrogen near an elasto-plastically deformed crack tip," in *Atomistics of Fracture,* New York, Latanision, R.M.; Pickens, J.R., 1983, pp. 799-811.

[241] P. Sofronis and R. McMeeking, "Numerical analysis of hydrogen transport near a blunting crack tip," *Journal of the Mechanics and Physics of Solids,* vol. 37, no. 3, pp. 317-350, 1989.

[242] J. Lufrano and P. Sofronis, "Enhanced hydrogen concentrations ahead of rounded notches and cracks - competition between plastic strain and hydrostatic stress," *Acta Materialia,* vol. 46, no. 5, pp. 1519-1526, 1998.

[243] A. Krom, *Numerical modelling of hydrogen transport in steel - Ph.D. Dissertation,* Delft, The Netherlands: Delft University Press, 1998.

[244] A. Taha and P. Sofronis, "A micromechanics approach to the study of hydrogen transport and embrittlement," *Engineering Fracture Mechanics,* vol. 68, no. 6, pp. 803-837, 2001.

[245] M. Hashimoto and R. Latanision, "Experimental study of hydrogen transport during plastic deformation in iron," *Metallurgical Transactions A,* vol. 19, no. 11, pp. 2789-2798, 1988.

[246] M. Hashimoto and R. Latanision, in *Chemistry and Physics of Fracture,* Latanision, R.M., Jones, R.H., Martinus Nijhoff Publishers, 1987, pp. 505-537.

[247] C. Hwang and I. Bernstein, "Dislocation transport of hydrogen in iron single crystals," *Acta Metallurgica,* vol. 34, no. 6, pp. 1001-1010, 1986.

[248] P. Sofronis, Y. Liang and N. Aravas, "Hydrogen induced shear localization of the plastic flow in metals and alloys," *European Journal of Mechanics - A/Solids,* vol. 20, no. 6, pp. 857-872, 2001.

[249] J. Lufrano, P. Sofronis and D. Symons, "Hydrogen transport and large strain elastoplasticity near a notch in alloy X-750," *Engineering Fracture Mechanics,* vol. 59, no. 6, pp. 827-845, 1998.

[250] C. Wen, C. Ho, B. Boukamp, I. Raistrick, W. Weppner and R. Huggins, "Use of electrochemical methods to determine chemical-diffusion coefficients in alloys: application to "LiAI"," *Journal of International Metals Reviews,* vol. 26, no. 1, pp. 253-268, 1981.

[251] G. Burstein and G. Wright, "Oxidation of atomic hydrogen adsorbed on nickel," *Electroanalytical Chemistry and lnterfacial Electrochemistry,* vol. 50, pp. 399-401, 1974.

[252] T. Zakroczymski and J. Flis, "Impedance characterization of the activation of iron surface for hydrogen entry from alkaline solution," *Electrochimica Acta,* vol. 41, pp. 1245- 1250, 1996.

[253] J. Flis, T. Zakroczymski, V. Kleshnya, T. Kobiela and R. Dus, "Changes in hydrogen entry rate and in surface of iron during cathodic polarisation in alkaline solutions," *Electrochimica Acta,* vol. 44, pp. 3989-3997, 1999.

[254] A. Gajek and T. Zakroczymski, "Long-lasting hydrogen evolution on and hydrogen entry into iron in an aqueous solution," *Journal of Electroanalytical Chemistry,* vol. 578, pp. 171-182, 2005.

[255] S. Duval, R. Antaño-Lopez, C. Scomparin, M. Jerome and F. Ropital, "Hydrogen permeation through Armco iron membranes in sour media," *NACE International Corrosion, Paper No. 04740,* 2004.

[256] H. Addach, P. Berçot, M. Rezrazi and J. Takadoum, "Study of the electrochemical permeation of hydrogen in iron," *Corrosion Science,* vol. 51, no. 2, pp. 263-267, 2009.

[257] V. Ramunni, T. De Paiva Coelho and P. De Miranda, "Interaction of hydrogen with the microstructure of low-carbon steel," *Materials Science and Engineering A,* Vols. 435-436, pp. 504-514, 2006.

[258] J. Kittel, F. Ropital and J. Pellier, "New insight into hydrogen permeation in steel: measurements through thick membranes," *NACE International Corrosion, Paper No. 08409,* 2008.

[259] S. Modiano, J. Carreño, C. Fugivara, A. Benedetti and O. Mattos, "Effect of hydrogen charging on the stability of SAE 10B22 steel surface in alkaline solutions," *Electrochimica Acta,* vol. 51, no. 4, pp. 641-648, 2005.

[260] S. Modiano, J. Carreño, C. Fugivara, R. Torresi, V. Vivier, A. Benedetti and O. Mattos, "Changes on iron electrode surface during hydrogen permeation in borate buffer solution," *Electrochimica Acta,* vol. 53, no. 10, pp. 3670-3679, 2008.

[261] N. Parvathavarthini, S. Saroja, R. Dayal and H. Khatak, "Studies on hydrogen permeability of 2.25% Cr-1% Mo ferritic steel: correlation with microstructure," *Journal of Nuclear Materials,* vol. 288, no. 2-3, pp. 187-196, 2001.

[262] I. Flis-Kabulska, J. Flis and T. Zakroczymski, "Enhanced hydrogen entry into iron from 0.1 M NaOH at definite potentials," *Electrochimica Acta,* vol. 53, no. 7, pp. 3094-3101, 2008.

[263] S. Harada, S. Yokota, Y. Ishii, Y. Shizuku, M. Kanazawa and Y. Fukai, "A relation between the vacancy concentration and hydrogen concentration in the Ni-H, Co-H and Pd-H systems," *Journal of Alloys and Compounds,* Vols. 404-406, pp. 247-251, 2005.

[264] T. Ungár, E. Schafler, P. Hanák, S. Bernstorff and M. Zehetbauer, *Materials Science and Engineering A,* vol. 462, pp. 398-401, 2007.

[265] F. Lewis, J. Magennis, S. McKee and P. Ssebuwufu, "Hydrogen chemical potentials and diffusion coefficients in hydrogen diffusion membranes," *Nature,* vol. 306, pp. 673-675, 1983.

[266] B. Baranowski, "Stress-induced diffusion in hydrogen permeation through Pd81Pt19 membranes," *Journal of the Less Common Metals,* vol. 154, no. 2, pp. 329-353, 1989.

[267] P. Bruzzoni, R. Carranza and J. Collet Lacoste, "A pressure modulation method to study surface effects in hydrogen permeation through iron base alloys," *Electrochimica Acta,* vol. 44, no. 24, pp. 4443-4452, 1999.

[268] J. Wu, "Electrochemical method for studying hydrogen in iron, nickel and palladium," *International Journal of Hydrogen Energy,* vol. 17, no. 12, pp. 917-921, 1992.

[269] D. Li, R. Gangloff and J. Scully, "Hydrogen trap states in ultrahigh-strength AERMET 100 steel," *Metallurgical and Materials Transactions A,* vol. 35, no. 3, pp. 849-864, 2004.

[270] T. Casanova and J. Crousier, "The influence of an oxide layer on hydrogen permeation through steel," *Corrosion Science,* vol. 38, no. 9, pp. 1535-1544, 1996.

[271] C. Gabrielli, G. Maurin, L. Mirkova, H. Perrot and B. Tribollet, "Transfer function analysis of hydrogen permeation through a metallic membrane in a Devanathan cell - I. Theory," *Journal of Electroanalytical Chemistry,* vol. 590, pp. 1-14, 2006.

[272] H. Züchner, L. Opara and H. Barlag, "Multi-layer problems in time-lag measurements applied on metal-hydrogen systems," *Journal of Alloys and Compounds,* Vols. 293-295, pp. 282-288, 1999.

[273] J. Chen, R. Durand and C. Montella, "Étude par spectroscopie d’impédance électrochimique de la diffusion restreinte dans un film bicouche: application à l’insertion de l’hydrogène dans des bifilms Pd/alliage de Pd," *Journal of Chemical Physics,* vol. 91, pp. 383-407, 1994.

[274] S. Chatterjee, B. Ateya and H. Pickering, "Effect of electrodeposited metals on the permeation of hydrogen through iron membranes," *Metallurgical Transactions A,* vol. 9, no. 3, pp. 389-395, 1978.

[275] P. Zoltowski and E. Makowska, "Diffusion coefficient of hydrogen in α-phase palladium and palladium-platinum alloy," *Journal of Physical Chemistry Chemical Physics,* no. 14, 2001.

[276] S. Kim and K. Kim, "Electrochemical hydrogen permeation measurement through high-strength steel under uniaxial tensile stress in plastic range," *Scripta Materialia,* vol. 66, pp. 1069-1072, 2012.

[277] G. Park, H. Jung, S. Koh and K. Kim, in *Proceedings of the 13th International Offshore and Polar Engineering Conference,* Osaka, Japan, 2009.

[278] G. Park, S. Kim and K. Kim, in *Proceedings of the NACE International Conference,* Houston, TX, 2010.

[279] *API 5L: Specification for line pipe. 42nd ed. 1995.*

[280] A. International, *ASTM F1624-12. Standard test method for measurement of hydrogen embrittlement threshold in steel by the Incremental Step Loading technique,* 2012.

[281] A. International, *ASTM STP 543. Hydrogen Embrittlement Testing,* 1974.

[282] A. International, *ASTM G129 - 00. Standard Practice for Slow Strain Rate Testing to Evaluate the Susceptibility of Metallic Materials to Environmentally Assisted Cracking,* 2013.

[283] A. International, *ASTM E8-00b. Standard Test Methods for Tension Testing of Metallic Materials,* 2001.

[284] M. Nagumo, K. Takai and N. Okuda, "Nature of hydrogen trapping sites in steels induced by plastic deformation," *Journal of Alloys and Compounds,* Vols. 293-295, pp. 310-316, 1999.

[285] M. Nagumo, H. Uyama and M. Yoshizawa, "Accelerated failure in high strength steel by alternating hydrogen-charging potential," *Scripta Materialia,* vol. 44, pp. 947-952, 2001.

[286] F. Giraudeau, L. Yang, F. Steward and O. DeBouvier, "Studies on the permeation of hydrogen through steam generator tubes at high temperatures using an electrochemical method," in *Proceedings of the third international steam generator and heat exchanger conference,* Toronto, ON (Canada), 1998.

[287] P. Manolatos, M. Jerome, C. Thual and J. Coze, "The electrochemical permeation of hydrogen in steels without palladium coating. Part I: Interpretation difficulties," *Corrosion Science,* vol. 37, pp. 1773-1783, 1995.

[288] H. Grafen, *Werk. Korros.,* vol. 20, p. 305, 1969.

[289] J. Dünnwald and A. Otto, *Fresenius' Zeitschrift für Analytische Chemie,* vol. 319, p. 738, 1984.

[290] A. Hugot-Le Goff, J. Flis, N. Boucherit, S. Joiret and J. Wilinski, *Journal of the Electrochemical Society,* vol. 137, p. 2684, 1990.

[291] J. Mayne, J. Menter and M. Pryor, *Journal of the Chemical Society,* p. 3229, 1950.

[292] C. Foley, J. Kruger and C. Bechtoldt, *Journal of the Electrochemical Society,* vol. 114, p. 994, 1967.

[293] R. Grauer, *Werk. Korros.,* vol. 32, p. 113, 1981.

[294] L. Schlapbach, in *Hydrogen in Intermetallic Compounds I,* Schlapbach, L., 1988.

[295] E. Protopopoff and P. Marcus, in *Corrosion Mechanisms in theory and practice,* New York, Basel: Marcel Dekker, Inc., Marcus, P., 2002, p. 53.

[296] P. Amiot, A. Besnard and G. Pinard-Legry, "Contribution a I'etude du cloquage des a&r pour constructions soudees," in *Deuxieme Congres International. L'hydrogene dans les metaux,* Paris, 3E8, 1977.

[297] P. Bruzzoni and R. Garavaglia, "Anodic iron oxide films and their effect on the hydrogen permeation through steel," *Corrosion Science,* vol. 33, pp. 1797-1807, 1992.

[298] N. International, *NACE MR0175/ISO 15156. Petroleum and natural gas industries - Materials for use in H2S containing environments in oil and gas production,* Houston, TX, 2009.

[299] N. Quick and H. Johnson, "Hydrogen and deuterium in iron, 49-506°C," *Acta Metallurgica,* vol. 26, no. 6, pp. 903-907, 1978.

[300] H. Kimizuka, H. Mori and S. Ogata, "Effect of temperature on fast hydrogen diffusion in iron: A path-integral quantum dynamics approach," *Physical Review B,* vol. 83, p. 094110, 2011.

[301] M. Arafin and J. Szpunar, "Effect of bainitic microstructure on the susceptibility of pipeline steels to hydrogen induced cracking," *Materials Science and Engineering A,* vol. 528, no. 15, pp. 4927-4940, 2011.

[302] M. Zhao, K. Yang, F. Xiao and Y. Shan, "Continuous cooling transformation of undeformed and deformed low carbon pipeline steels," *Materials Science and Engineering: A,* vol. 355, no. 1-2, pp. 126-136, 2003.

[303] S. Brinckmann, *On the role of dislocations in fatigue crack initiation - PhD thesis,* University of Groningen, 2005.

[304] H. Cialone and J. Holbrook, "Effects of gaseous hydrogen on fatigue crack growth in pipeline steel," *Metallurgical Transactions A,* vol. 16, no. 1, pp. 115-122, 1985.

[305] K. Choi, M. Biegalski, Y. Li, A. Sharan, J. Schubert, R. Uecker, P. Reiche, Y. Chen, X. Pan, V. Gopalan, L. Chen, D. Schlom and C. Eom, "Enhancement of ferroelectricity in strained BaTiO3 thin films," *Science,* vol. 306, pp. 1005-1009, 2004.

[306] J. Wang, J. Neaton, H. Zheng, V. Nagarajan, S. Ogale, B. Liu, D. Viehland, V. Vaithyanathan, D. Schlom, U. Waghmare, N. Spaldin, K. Rabe, M. Wuttig and R. Ramesh, "Epitaxial BiFeO3 multiferroic thin film heterostructures," *Science,* vol. 299, pp. 1719-1722, 2003.

[307] J. Cao and J. Wu, "Strain effects in low-dimensional transition metal oxides," *Materials Science and Engineering R,* vol. 71, pp. 35-52, 2011.

[308] E. Fitzgerald, S. Samavedam, Y. Xie and L. Giovane, "Influence of strain on semiconductor thin film epitaxy," *Journal of Vacuum Science & Technology A,* vol. 15, pp. 1048-1056, 1997.

[309] J. Welser, J. Hoyt and J. Gibbons, "Electron mobility enhancement in strained-Si n-type metal-oxide-semiconductor field-effect transistors," *IEEE Electron Devices Letters,* vol. 15, no. 3, pp. 100-102, 1994.

APPENDIX

A.1 Diffusion laws

A.1.1 Fick's First Law (Stationary Conditions)

Expression *(eq. 114)* in Cartesian coordinates *(Figure A.1)*:

$$\vec{\Phi} = -D \cdot \vec{\nabla} C = -D \cdot \left(\frac{dC}{dx}\vec{i} + \frac{dC}{dy}\vec{j} + \frac{dC}{dz}\vec{k} \right) \qquad \text{(eq. 114)}$$

Expression *(eq. 115)* in cylindrical coordinates *(Figure A.1)*:

$$\vec{\Phi} = -D \cdot \vec{\nabla} C = -D \cdot \left(\frac{dC}{dr}\vec{i}_r + \frac{1}{r}\frac{dC}{d\varphi}\vec{j}_\varphi + \frac{dC}{dz}\vec{k} \right) \qquad \text{(eq. 115)}$$

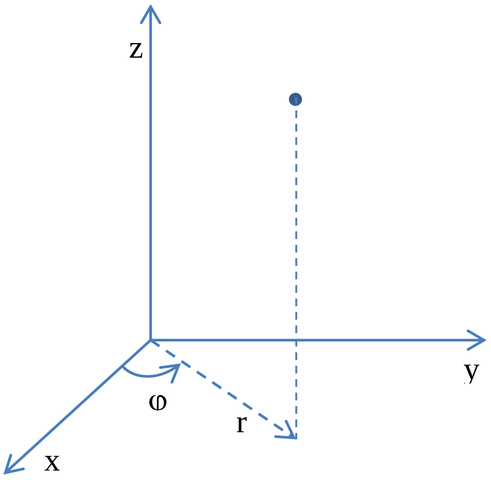

Figure A.1. Reference systems in Cartesian and cylindrical coordinates

In the case of cylindrical symmetry of infinite length (the concentration does not depend on neither the angular coordinate nor the z), the flux in the radial direction is as follows *(eq. 116)*:

$$\Phi_r = -D \cdot \frac{dC}{dr} \qquad \text{(eq. 116)}$$

A.1.2 Fick's Second Law (Non-Stationary Conditions)

Expression *(eq. 117)* in Cartesian coordinates (with constant reaction contribution and diffusivity into the metal):

$$\frac{\partial C}{\partial t} = D \cdot \nabla^2 C = D \cdot \left(\frac{d^2C}{dx^2} + \frac{d^2C}{dy^2} + \frac{d^2C}{dz^2} \right) + R(C) \qquad \text{(eq. 117)}$$

Expression *(eq. 118)* in cylindrical coordinates (with constant reaction contribution and diffusivity into the metal):

$$\frac{\partial C}{\partial t} = D \cdot \nabla^2 C = D \cdot \left[\frac{1}{r}\frac{d}{dr}\left(r\frac{dC}{dr} \right) + \frac{1}{r^2}\frac{d^2C}{d\varphi^2} + \frac{d^2C}{dz^2} \right] + R(C) \qquad \text{(eq. 118)}$$

Or *(eq. 119)*:

$$\frac{\partial C}{\partial t} = D \cdot \left(\frac{d^2C}{dr^2} + \frac{1}{r}\frac{dC}{dr} + \frac{1}{r^2}\frac{d^2C}{d\varphi^2} + \frac{d^2C}{dz^2} \right) + R(C) \qquad \textit{(eq. 119)}$$

In the case of cylindrical symmetry of infinite length (the concentration does not depend on neither the angular coordinate nor the z), the concentration profile in the radial direction is described by the following relation *(eq. 120)*:

$$\frac{\partial C}{\partial t} = D \cdot \left(\frac{d^2C}{dr^2} + \frac{1}{r}\frac{dC}{dr} + \frac{1}{r^2}\frac{d^2C}{d\varphi^2} + \frac{d^2C}{dz^2} \right) + R(C) \qquad \textit{(eq. 120)}$$

A.1.3 Discretization of the diffusion laws

For the numerical solutions of the diffusion laws, the following approximations are assumed (from *(eq. 121)* to *(eq. 123)*):

$$\frac{\partial C}{\partial t} \Rightarrow \frac{\Delta C}{\Delta t} = \frac{C(t + \Delta t, x) - C(t, x)}{\Delta t} \qquad \textit{(eq. 121)}$$

$$\frac{dC}{dx} \Rightarrow \frac{\Delta C}{\Delta x} = \frac{C(t, x + \Delta x) - C(t, x)}{\Delta x} \qquad \textit{(eq. 122)}$$

$$\frac{d^2C}{dx^2} \Rightarrow \frac{\Delta}{\Delta x}\left(\frac{\Delta C}{\Delta x}\right) = \frac{C(t, x + \Delta x) - 2C(t, x) + C(t, x - \Delta x)}{\Delta x^2} \qquad \textit{(eq. 123)}$$

In the case of unidirectional flux, *(eq. 117)* becomes *(eq. 124)*:

$$C(t + \Delta t, x) = C(t, x) + D\frac{C(t, x + \Delta x) - 2C(t, x) + C(t, x - \Delta x)}{\Delta x^2}\Delta t + R(C(t, x))\Delta t \qquad \textit{(eq. 124)}$$

Which is integrable in a stable manner assuming *(eq. 125)*:

$$\Delta \mathrm{t} = \frac{\Delta \mathrm{x}^2}{4D} \qquad \textit{(eq. 125)}$$

In the case of cylindrical symmetry (*(eq. 126)* and *(eq. 127)*):

$$\frac{dC}{dr} \Rightarrow \frac{\Delta C}{\Delta r} = \frac{C(t, r + \Delta r) - C(t, r)}{\Delta r} \qquad \textit{(eq. 126)}$$

$$\frac{d^2C}{dr^2} \Rightarrow \frac{\Delta}{\Delta r}\left(\frac{\Delta C}{\Delta r}\right) = \frac{C(t, r + \Delta r) - 2C(t, r) + C(t, r - \Delta r)}{\Delta r^2} \qquad \textit{(eq. 127)}$$

Therefore, it is possible to discretize *(eq. 124)* as follows *(eq. 128)*:

$$C(t + \Delta t, x) = C(t, x) + D \cdot \left(\frac{C(t, r + \Delta r) - 2C(t, r) + C(t, r + \Delta r)}{\Delta r^2} + \frac{1}{r}\frac{C(t, r + \Delta r) - C(t, r)}{\Delta r} \right)\Delta t + R(C)\Delta t \qquad \textit{(eq. 128)}$$

Which is integrable in a stable manner assuming *(eq. 129)*:

$$\Delta t = \frac{\Delta r^2}{4D} \qquad \textit{(eq. 129)}$$

A.2 Model of hydrogen diffusion in the absence of traps

The interpolation procedure provides the following steps:

1. Estimate of the stationary flux of first attempt (Φ_∞)

2. Normalization of the flux experimental data ($\Phi_{N,i}$):

$$\emptyset_{N,i} = \frac{\emptyset(t_i)}{\emptyset_\infty}$$

3. Estimate of the normalized time ($t_{N,i}$):

$$t_{N,i} = f^{-1}\left(\frac{\emptyset(t_i)}{\emptyset_\infty}\right)$$

4. Estimate of the diffusion coefficient in correspondence of particular values of the normalized flux (D_i):

$$D_i = \frac{s^2 t_{N,i}}{4t_i}$$

5. Estimate of the average value of the diffusion coefficient (D):

$$D = \frac{\sum_{i=1}^{N} D_i}{N}$$

6. Determination of the normalized time related to the experimental data ($t_{N,i}$):

$$t_{N,i} = \frac{4t_i D}{s^2}$$

7. Determination of the expected theoretical values and the expected values on the basis of the following relation:

$$\frac{\emptyset(t)}{\emptyset_\infty} = f(t_N)$$

8. Determination of the absolute error between the experimental data $\left(t_{N,i}; \frac{\emptyset(t)_i}{\emptyset_\infty}\right)$ and the data expected on the basis of the following relation:

$$\frac{\emptyset(t)}{\emptyset_\infty} = f(t_N)$$

9. Reiteration of the calculation with a new value of the stationary flux in order to minimize the error in the interval of the normalized time between 0 and 0.8.

A.3 Model of hydrogen diffusion in the presence of traps

Assumptions:

1. Homogeneous medium
2. Unidirectional geometry (infinite width foil, namely with a thickness much less than its width)
3. Presence of irreversible traps which react with hydrogen present in the metal crystalline matrix
4. Reaction between traps and hydrogen much faster than diffusion, so as to consider in each point that hydrogen concentration in the lattice is in equilibrium with the concentration in the traps
5. Constant superficial concentration (higher than zero) on the entry surface of hydrogen into the metal and concentration equal to zero on the other surface (exit surface).

A.3.1 Equilibrium with reversible traps

The trapping process is described by the reaction *(eq. 130)*:

$$H_l + T_{e,r} \Leftrightarrow R_e + H_{t,r} \qquad \textit{(eq. 130)}$$

The diffusible hydrogen in the lattice (H_l) reacts with an empty reversible trap ($T_{e,r}$) to produce reversibly trapped hydrogen ($H_{t,r}$) and to relief a site in the lattice (L_e). At the equilibrium, the reaction rate in one direction equals that in the opposite direction. From kinetics laws, it is possible to assume that the reaction rate from right to left *(eq. 131)* is proportional to hydrogen concentration in the lattice (C_{Hl}) and to the concentration of the empty reversible traps ($C_{et,r}$):

$$\left(\frac{dC}{dt}\right)_{\mapsto} = k \cdot C_{Hl} \cdot C_{et,r} \qquad \textit{(eq. 131)}$$

The rate in the opposite direction *(eq. 132)* is proportional to hydrogen concentration in the reversible traps ($C_{Ht,r}$) and to the concentration of the empty lattice sites (C_{el}):

$$\left(\frac{dC}{dt}\right)_{\leftarrow} = k' \cdot C_{Ht,r} \cdot C_{el} \qquad \textit{(eq. 132)}$$

Under equilibrium conditions the following relation *(eq. 133)* is valid:

$$k \cdot C_{Hl} \cdot C_{et,r} = k' \cdot C_{Ht,r} \cdot C_{el} \qquad \textit{(eq. 133)}$$

From this equation, the equilibrium constant (K) is derived *(eq. 134)*:

$$K = \frac{k}{k'} = \frac{C_{Ht,r} \cdot C_{el}}{C_{Hl} \cdot C_{et,r}} \qquad \textit{(eq. 134)}$$

With the constant related to the standard molar Gibbs free energy of reaction from the law *(eq. 135)*:

$$K = e^{\left(-\frac{\Delta G^0}{R \cdot T}\right)} \qquad \textit{(eq. 135)}$$

The concentrations reported in *(eq. 134)* can be conveniently expressed in terms of saturation degree of the sites available for hydrogen absorption in the lattice ($\theta_l = N_{Hl} / N_l$) and in the reversible traps ($\theta_{t,r} = N_{Ht,r} / N_{t,r}$), respectively.

From the definition of saturation degree and mole, the following relation can be obtained *(eq. 136)*:

$$C_{Hl} = \theta_l \cdot \frac{N_l}{N_A} \qquad \textit{(eq. 136)}$$

Where: N_A [atoms/mol] = Avogadro's constant = $6.023*10^{23}$. In the same way, it can be written (from *(eq. 137)* to *(eq. 139)*):

$$C_{Ht,r} = \theta_{t,r} \cdot \frac{N_{t,r}}{N_A} \qquad \textit{(eq. 137)}$$

$$C_{el} = (1 - \theta_l) \cdot \frac{N_l}{N_A} \qquad \textit{(eq. 138)}$$

$$C_{et,r} = \left(1 - \theta_{t,r}\right) \cdot \frac{N_{t,r}}{N_A} \qquad \textit{(eq. 139)}$$

By substituting these expressions in *(eq. 135),* the following relation can be derived *(eq. 140)*:

$$K = \frac{k}{k'} = \frac{\theta_{t,r} \cdot (1 - \theta_l)}{\theta_l \cdot \left(1 - \theta_{t,r}\right)} \qquad \textit{(eq. 140)}$$

For θ_l equal to $\theta_{t,r}$, K constant becomes equal to 1 and then ΔG^0 is necessarily equal to zero. In other words, reversible traps would have the same tendency to bond hydrogen, therefore these would not be real traps. Instead, it is possible to hypothesize that the saturation degree of the reversible traps is much higher than that of the lattice. This involves that *(eq. 140)* can be simplified as *(eq. 141)*:

$$K = \frac{\theta_{t,r}}{\theta_l \cdot \left(1 - \theta_{t,r}\right)} \qquad \textit{(eq. 141)}$$

Moreover, it is possible to observe that hydrogen concentration in the lattice is in any case very low at room temperature. For ferrite in contact with an atmosphere of hydrogen at 1 bar, concentrations in the metal in the order of 10^{-6} % are reported, corresponding to a ratio ($R_{Fe/H}$) between hydrogen atoms and iron atoms equal to *(eq. 142)*:

$$R_{Fe/H} = \frac{10^{-6}}{100} \cdot \frac{PA_{Fe}}{PA_H} = \frac{10^{-6}}{100} \cdot \frac{55.85}{1} \cong 6 \cdot 10^{-7} \qquad \textit{(eq. 142)}$$

This ratio becomes four and a half times smaller if the octahedral sites present in the bcc crystal lattice are considered, where hydrogen can preferentially be absorbed (9 sites every 2 iron atoms).

Even for concentrations much higher than this one, assumed around 1 ppm, the saturation degree of the octahedral sites ($1.2^{*}10^{-5}$) is anyway low. For low hydrogen concentrations, it is possible to assume *(eq. 143)*:

$$K = \frac{\theta_{t,r}}{\theta_l} \qquad \textit{(eq. 143)}$$

The ratio between the saturation degree of the reversible traps and that of the lattice sites is therefore equal, under these assumptions, to *(eq. 144)*:

$$\theta_{t,r} = \theta_l \cdot e^{\left(-\frac{\Delta G^0}{R \cdot T}\right)} \qquad \textit{(eq. 144)}$$

At room temperature and for concentrations around 1ppm, the saturation degree of the reversible traps is 10^4 times higher than that of the lattice if ΔG^0 is more negative than 23 kJ/mol, a value in line with those reported in the literature for the reversible traps.

Consequently, *(eq. 134)* can be simplified and differently written as *(eq. 145)*:

$$C_{Ht,r} = C_{Hl} \cdot K \cdot \frac{N_{t,r}}{N_l} \qquad \textit{(eq. 145)}$$

Considering *(eq. 136)* and *(eq. 137)*, *(eq. 141)* can be written in the form *(eq. 146)*:

$$C_{Ht,r} = \frac{K \cdot C_{Hl}}{(1 + K \cdot \theta_l)} \cdot \frac{N_{t,r}}{N_l} \qquad \textit{(eq. 146)}$$

The total hydrogen concentration in each point of the metal (C_H) is given by the sum of hydrogen in the lattice and in the reversible traps *(eq. 147)*:

$$C_H = C_{Hl} + C_{Ht,r} = C_{Hl} \cdot \left(1 + \frac{K}{(1 + K \cdot \theta_l)} \cdot \frac{N_{t,r}}{N_l}\right) \qquad \textit{(eq. 147)}$$

A.3.2 Constitutive equations in the presence of reversible traps

In the presence of reversible traps, the mass balance, at the basis of Fick’s second law, requires that the flux variation in each point is equal to hydrogen accumulation in the lattice and in the reversible traps. Thus, *(eq. 117)* can be then expressed as *(eq. 148)*:

$$\frac{\partial C_{Hl}}{\partial t} + \frac{\partial C_{Ht,r}}{\partial t} = D \cdot \left(\frac{d^2 C_{Hl}}{dx^2} + \frac{d^2 C_{Hl}}{dy^2} + \frac{d^2 C_{Hl}}{dz^2}\right) \qquad \textit{(eq. 148)}$$

It derives that *(eq. 149)*:

$$\frac{\partial C_{Ht,r}}{\partial t} = -R(C) \qquad \textit{(eq. 149)}$$

For derivation of *(eq. 146)*, it can be obtained *(eq. 150)*:

$$\frac{\partial \theta_{t,r}}{\partial t} = \frac{K}{(1 + K \cdot \theta_l)^2} \cdot \frac{\partial \theta_l}{\partial t} \qquad \textit{(eq. 150)}$$

From *(eq. 136)* and from *(eq. 137)* it is possible to write (*(eq. 151)* and *(eq. 152)*):

$$\frac{\partial \theta_l}{\partial t} = \frac{N_A}{N_l} \cdot \frac{\partial C_{Hl}}{\partial t} \qquad \textit{(eq. 151)}$$

$$\frac{\partial \theta_{t,r}}{\partial t} = \frac{N_A}{N_{t,r}} \cdot \frac{\partial C_{Ht,r}}{\partial t} \qquad \textit{(eq. 152)}$$

Finally, it can be obtained (*(eq. 153)* and *(eq. 154)*):

$$\frac{\partial C_{Ht,r}}{\partial t} = \frac{K}{(1 + K \cdot \theta_l)^2} \cdot \frac{N_{t,r}}{N_l} \cdot \frac{\partial C_{Hl}}{\partial t} \tag*{(eq. 153)}$$

$$\frac{\partial \mathrm{C}_{Hl}}{\partial \mathrm{t}} = \frac{D}{\left[1 + \frac{K}{(1 + K \cdot \theta_l)^2} \cdot \frac{N_{t,r}}{N_l}\right]} \cdot \left(\frac{d^2 \mathrm{C}_{Hl}}{dx^2} + \frac{d^2 \mathrm{C}_{Hl}}{dy^2} + \frac{d^2 \mathrm{C}_{Hl}}{dz^2} \right) \tag*{(eq. 154)}$$

The diffusion in the presence of reversible traps, under non-stationary conditions, is equivalent to the case of diffusion in the absence of reversible traps, but with a diffusion coefficient equal to the apparent value (D_{app}), given by the relation *(eq. 155)*:

$$D_{app} = \frac{D_l}{\left[1 + \frac{K}{(1 + K \cdot \theta_l)^2} \cdot \frac{N_{t,r}}{N_l}\right]} = \frac{D_l}{[1 + \alpha]} \tag*{(eq. 155)}$$

In which the reversible trapping factor (α) has been introduced.

Under stationary conditions, reversible traps do not affect the flux (Φ) in any case. In the case of unidirectional diffusion through a foil with thickness s, the following equation *(eq. 156)* is valid:

$$\Phi = D \cdot \frac{C_{Hl}(0) - C_{Hl}(s)}{s} \tag*{(eq. 156)}$$

If the exit flux $C_{Hl}(s)$ is considered equal to 0 and the lattice diffusivity (D_l) is substituted with the apparent diffusivity (D_{app}), the following equation *(eq. 157)* can be obtained:

$$C_{Hl}(0) \cdot \left[1 + \frac{K}{(1 + K \cdot \theta_l)^2} \cdot \frac{N_{t,r}}{N_l}\right] = \frac{\Phi \cdot s}{D_{app}} \tag*{(eq. 157)}$$

The term on the right of this relation, for low hydrogen concentrations in the lattice, tends to the total hydrogen concentration in the metal *(eq. 147)* on the hydrogen entry surface.

From the results in the literature, the apparent diffusivity in the common structural steels at room temperature is about two orders of magnitude lower than the diffusivity in the ferrite lattice in the annealed state (considered with a negligible trapping effect). Therefore, it is possible to estimate the ratio between reversible traps and interstitial sites of the lattice *(eq. 158)*, in the case of defects with a free molar energy of reaction equal to 23 J/mol:

$$\frac{N_{t,r}}{N_l} = \frac{10^2}{K} = 10^{-2} \tag*{(eq. 158)}$$

A.3.3 Irreversible traps

In the case of irreversible traps, the trapping reaction becomes *(eq. 159)*:

$$H_l + T_{e,ir} \Rightarrow R_e + H_{t,ir} \tag*{(eq. 159)}$$

The rate of the reaction is equal to *(eq. 160)*:

$$\left(\frac{dC}{dt}\right)_{\mapsto} = k_{ir} \cdot C_{Hl} \cdot C_{et,ir} \tag*{(eq. 160)}$$

The variation over time of hydrogen in the irreversible traps will be then expressed as *(eq. 161)*:

$$\frac{dC_{Ht,ir}}{dt} = k_{ir} \cdot C_{Hl} \cdot C_{et,ir} \tag*{(eq. 161)}$$

Now it is possible to observe that, from derivation, it can be obtained *(eq. 162)*:

$$\frac{d^2 C_{Ht,ir}}{dt^2} = k_{ir} \cdot C_{et,ir} \cdot \frac{\partial C_{Hl}}{\partial t} + k_{ir} \cdot C_{Hl} \cdot \frac{dC_{et,ir}}{dt} \tag*{(eq. 162)}$$

Then it can be noted that, because *(eq. 163)*:

$$\frac{dC_{Ht,ir}}{dt} = -\frac{dC_{et,ir}}{dt} \tag*{(eq. 163)}$$

The following relation can be obtained *(eq. 164)*:

$$\frac{d^2C_{Ht,ir}}{dt^2}+k_{ir}\cdot C_{Hl}\cdot\frac{dC_{Ht,ir}}{dt}=k_{ir}\cdot C_{et,ir}\cdot\frac{\partial C_{Hl}}{\partial t} \qquad \textit{(eq. 164)}$$

It can be observed that the term on the right is null both in the early stages of diffusion (for t → 0, i.e. when the local concentration has not yet been influenced by diffusion) or in stationary conditions. The following relationship *(eq. 165)* is then obtained:

$$\frac{d^2C_{Ht,ir}}{dt^2}+k_{ir}\cdot C_{Hl}\cdot\frac{dC_{Ht,ir}}{dt}=0 \qquad \textit{(eq. 165)}$$

The integration of this relation, introducing the reaction time: $\tau={}^{1}\!/_{k_{ir}\cdot C_{Hl}}$, leads to the following expression *(eq. 166)*:

$$C_{Ht,ir}=C_{t,ir}\cdot\left(1-e^{\left(-\frac{t}{\tau}\right)}\right) \qquad \textit{(eq. 166)}$$

For very long periods, concentration reaches the (constant) concentration of the irreversible traps while, for very short periods (t<<τ), this can be approximated with the relation *(eq. 167)*:

$$C_{Ht,ir}=C_{t,ir}\cdot\left(\frac{t}{\tau}\right) \qquad \textit{(eq. 167)}$$

In the presence of irreversible traps, the mass balance, at the basis of Fick's second law, requires that the flux variation in each point is equal to hydrogen accumulation in the lattice and in the irreversible traps. Thus, *(eq. 117)* can be then expressed as *(eq. 168)*:

$$\frac{\partial C_{Hl}}{\partial t}+\frac{\partial C_{Ht,ir}}{\partial t}=D\cdot\left(\frac{d^2C_{Hl}}{dx^2}+\frac{d^2C_{Hl}}{dy^2}+\frac{d^2C_{Hl}}{dz^2}\right) \qquad \textit{(eq. 168)}$$

It derives that (*(eq. 169)* and *(eq. 170)*):

$$\frac{\partial \mathrm{C}_{Ht,ir}}{\partial \mathrm{t}}=-R(C) \qquad \textit{(eq. 169)}$$

$$\frac{\partial C_{Hl}}{\partial t}=D\cdot\left(\frac{d^2C_{Hl}}{dx^2}+\frac{d^2C_{Hl}}{dy^2}+\frac{d^2C_{Hl}}{dz^2}\right)-\frac{C_{t,ir}}{\tau}\cdot e^{\left(-\frac{t}{\tau}\right)} \qquad \textit{(eq. 170)}$$

More generally, considering that the concentration of the irreversible traps still empty is equal to the difference between the total concentration of the irreversible traps and that of the traps already occupied by hydrogen, *(eq. 161)* can be written as (*(eq. 171)* and *(eq. 172)*):

$$\frac{dC_{Ht,ir}}{dt}=k_{ir}\cdot C_{Hl}\cdot\left(C_{t,ir}-C_{Ht,ir}\right) \qquad \textit{(eq. 171)}$$

$$\frac{1}{\left(C_{t,ir}-C_{Ht,ir}\right)}\cdot\frac{dC_{Ht,ir}}{dt}=k_{ir}\cdot C_{Hl} \qquad \textit{(eq. 172)}$$

The integration between 0 and t leads to the following relations (from *(eq. 173)* to *(eq. 177)*):

$$\int_0^{C_{Ht,ir}}\frac{1}{\left(C_{t,ir}-C_{Ht,ir}\right)}\cdot dC_{Ht,ir}=\int_0^t k_{ir}\cdot C_{Hl}\cdot dt \qquad \textit{(eq. 173)}$$

$$-ln\left(C_{t,ir}-C_{Ht,ir}\right)=Q(t)=\int_0^t k_{ir}\cdot C_{Hl}\cdot dt \qquad \textit{(eq. 174)}$$

$$C_{Ht,ir}=C_{t,ir}-e^{[-Q(t)]} \qquad \textit{(eq. 175)}$$

$$\frac{\partial C_{Ht,ir}}{\partial t}=k_{ir}\cdot C_{Hl}\cdot e^{[-Q(t)]} \qquad \textit{(eq. 176)}$$

$$\frac{\partial C_{Hl}}{\partial t} = D \cdot \left(\frac{d^2 C_{Hl}}{dx^2} + \frac{d^2 C_{Hl}}{dy^2} + \frac{d^2 C_{Hl}}{dz^2}\right) - k_{ir} \cdot C_{Hl} \cdot e^{[-Q(t)]}$$

(eq. 177)

A.3.4 Simultaneous action of reversible and irreversible traps

$$\frac{\partial \mathrm{C}_{Hl}}{\partial \mathrm{t}} + \frac{K}{(1 + K \cdot \theta_l)^2} \cdot \frac{N_{t,r}}{N_l} \cdot \frac{\partial C_{Hl}}{\partial t} = \mathrm{D} \cdot \left(\frac{d^2 \mathrm{C}_{Hl}}{dx^2}\right) - k_{ir} \cdot C_{Hl} \cdot e^{[-Q(t)]}$$

(eq. 178)

$$\frac{\partial \mathrm{C}_{Hl}}{\partial \mathrm{t}} = \frac{\mathrm{D}}{\left[1 + \frac{K}{(1 + K \cdot \theta_l)^2} \cdot \frac{N_{t,r}}{N_l}\right]} \left(\frac{d^2 \mathrm{C}_{Hl}}{dx^2}\right) - \frac{k_{ir} \cdot C_{Hl}}{\left[1 + \frac{K}{(1 + K \cdot \theta_l)^2} \cdot \frac{N_{t,r}}{N_l}\right]} e^{[-Q(t)]}$$

(eq. 179)

$$\frac{\partial \mathrm{C}_{Hl}}{\partial \mathrm{t}} = D_{app} \cdot \left(\frac{d^2 \mathrm{C}_{Hl}}{dx^2}\right) - \frac{k_{ir}}{[1 + \alpha]} \cdot C_{Hl} \cdot e^{[-Q(t)]}$$

(eq. 180)

A.3.5 Relation for the numerical model, in the presence of reversible and irreversible traps

$$\frac{C(t + \Delta t, x) - C(t, x)}{\Delta \mathrm{t}} = D_{app} \cdot \frac{C(t, x + \Delta x) - 2C(t, x) + C(t, x - \Delta x)}{\Delta \mathrm{x}^2} - \frac{k_{ir}}{[1 + \alpha]} \cdot C(t, x) \cdot e^{[-Q(t)]}$$

(eq. 181)

$$Q(t) = \int_0^t k_{ir} \cdot C(t, x) \cdot dt \Rightarrow k_{ir} \cdot \Delta t \cdot \sum_{i=1}^{n=t/\Delta t} C(i\Delta t)$$

(eq. 182)

$$\frac{C(t + \Delta t, x) - C(t, x)}{\Delta \mathrm{t}} = D_{app} \cdot \frac{C(t, x + \Delta x) - 2C(t, x) + C(t, x - \Delta x)}{\Delta \mathrm{x}^2} - \frac{k_{ir}}{[1 + \alpha]} \cdot C(t, x) \cdot e^{\left[-k_{ir} \cdot \Delta t \cdot \sum_{i=1}^{n=t/\Delta t} C(i\Delta t)\right]}$$

(eq. 183)

$$C(t + \Delta t, x) = C(t, x) + \Delta \mathrm{t} \cdot D_{app} \cdot \frac{C(t, x + \Delta x) - 2C(t, x) + C(t, x - \Delta x)}{\Delta \mathrm{x}^2} - \frac{k_{ir} \cdot \Delta \mathrm{t}}{[1 + \alpha]} \cdot C(t, x) \cdot e^{\left[-k_{ir} \cdot \Delta t \cdot \sum_{i=1}^{n=t/\Delta t} C(i\Delta t)\right]}$$

(eq. 184)